Georgia Water Resources Institute
Annual Technical Report
FY 2009

Introduction

The Georgia Water Resources Institute (GWRI) aims to provide interdisciplinary research, education, technology transfer, and information dissemination, and works collaboratively with various local, state, and federal agencies. At the state and local levels, GWRI collaborates with and supports the Georgia Environmental Protection Division/Georgia Department of Natural Resources, water and power utilities, environmental organizations and citizen groups, and lake associations. At the national level, GWRI collaborative efforts with the California Energy Commission, California Department of Water Resources, National Oceanic and Atmospheric Administration, U.S. Army Corps of Engineers, U.S. Bureau of Reclamation, U.S. Geological Survey, U.S. Environmental Protection Agency, and U.S. Fish and Wildlife Service. Finally, GWRI has a significant international research and educational program in Europe, Africa, China, Middle East, and South America with support from the U.S. Agency for International Development, World Bank, Food and Agriculture Organization of the United Nations, and other international organizations. In all its programs, the Institute strives to bring to bear expertise from a variety of disciplines, including civil and environmental engineering, atmospheric sciences, agriculture, oceanography, forestry, ecology, economics, and public policy. This year's funded activities include:

RESEARCH PROJECTS (1) Multi-Scale Investigation of Seawater Intrusion and Application in Coastal Georgia, Jian Luo PI, Georgia Institute of Technology, sponsored by USGS under grant # 2006P17 (Fund #R9261). (2) Assessing the impacts of a major wildfire in the Okefenokee Swamp on mercury levels in resident Macroinvertebrates and Mosquitofish, Darold Batzer PI, University of Georgia, sponsored by USGS under grant #1266663 (Fund #R7113-G8) (3) Quantification of Vegetative Flow Resistance in Constructed Wetlands, Thorsten Stoesser, Georgia Institute of Technology, sponsored by USGS under grant #1266663 (Fund R7113-G6). (4) Identifying Locations of High Connectivity between Floridan Aquifer Water and Surface Waters at Lineament Intersections with Tributaries of the Lower Flint River, Charles Rhett Jackson, University of Georgia, sponsored by USGS under grant #1266663 (Fund R7113-G7). (5) Water Resources Assessment, Planning, and Management in The Southeast US Using Decision Support System Driven by Climate-based Hydrologic Forecasts NOAA/OGP Climate Prediction Program for the Americas (CPPA), Aris Georgakakos, PI, Georgia Institute of Technology, sponsored by NOAA/OGP Climate Prediction program for the Americas (CPPA) under grant #2006L77.

(6) Integrated Forecast and Reservoir Management (INFORM) for Northern California, Phase II: Operational Implementation, Aris Georgakakos PI, Georgia Institute of Technology, sponsored by California-Nevada River Forecast Center, California Department of Water Resources, California Energy Commission under grant #2006Q15. (7) Performance of the Northern California Water System Under Climate Change: INFORM as an Adaptation Tool, Aris Georgakakos PI, Georgia Institute of Technology, sponsored by Hydrologic Research Center/California Energy Commission under grant #2006P32. (8) Technical Assistance for Water Resources Planning in the State of Georgia, Aris Georgakakos PI, Georgia Institute of Technology, sponsored by Georgia Environmental Protection Division under grant #2006Q13. (9) Operational Multi-scale Forecast and Reservoir Management in Northern California Aris Georgakakos PI, Georgia Institute of Technology, sponsored by NOAA through the Hydrologic Research Center under grant #2006N95

EDUCATIONAL INITIATIVES The Africa Water Resources Institute for Education and Applied Research (AWARE) is a joint institute established by the Georgia Institute of Technology (GT) and the University of Pretoria (UP), through the Georgia Water Resources Institute (GWRI) and the University of Pretoria Water Institute (UPWI). This is the first such initiative between major American and African Universities and focuses on interdisciplinary graduate education, applied research, and technology transfer in the areas of water, energy, and environmental resources planning and management. AWARE was officially launched on June 19, 2008, and is based at the UP campus in Pretoria, South Africa. The first AWARE programs include a Joint Masters Degree Program in Water Resources Management and a Professional Continuing Education

Program for water and hydropower professionals.

PROFESSIONAL AND POLICY IMPACT Georgia: GWRI continues to provide technical assistance to the Georgia Department of Natural Resources in relation to the state water planning process. GWRI's River Basin Planning Tool (RBPT) was developed specifically for this purpose and is now being applied to assess water supply availability and gaps in various Georgia basins. The results are communicated to 12 Water Councils that have been formed across the state. GWRI provides training to state engineers and their contractors who are involved in these assessments. The RBPT is further developed as more specific assessment needs arise in the planning process. In addition to the Georgia Tech River Basin Planning Tool, GWRI has completed a comprehensive study on the impacts of climate change for the Apalachicola-Chattahoochee-Flint River Basin shared with Alabama and Florida.

The study indicates that droughts will most likely intensify having serious implications on water supply, energy generation, and ecological flows. The study was the subject of a series of lectures at various NOAA climate centers and follow-up proposals. California: Similar work, collaboratively with the Hydrologic Research Center in San Diego, has focused on climate change impacts on the Northern California water resources system (including the Sacramento and San Joaquin River basins). While the nature of the changes is different, due to hydrologic significance of snow melt, the findings are equally important regarding the need for mitigation and adaptation measures. With funding from the California Energy Commission and the Department of Water Resources, GWRI and HRC have just initiated a second project phase which aims at finalizing and transferring the forecast-decision tools and evaluating alternative climate and demand change mitigation measures.

International: In January 2009, GWRI staff visited the Democratic Republic of the Congo (DRC) and helped formulate and raise funding for a comprehensive assessment and development program. The program focuses on water, environmental, and energy development, as well as institutional and legal reforms, and is a collaborative effort with the United Nations Development Program and the DRC Ministry of the Environment.

Research Program Introduction

None.

Multi-Scale Investigation of Seawater Intrusion and Application in Coastal Georgia

Basic Information

Title:	Multi-Scale Investigation of Seawater Intrusion and Application in Coastal Georgia
Project Number:	2007GA165G
Start Date:	4/1/2008
End Date:	3/31/2011
Funding Source:	104G
Congressional District:	
Research Category:	Ground-water Flow and Transport
Focus Category:	Groundwater, Hydrology, Models
Descriptors:	
Principal Investigators:	Jian Luo, Jian Luo

Publications

1. Lu, C., Kitanidis, P.K., Luo, J. (2009), Effects of kinetic mass transfer and transient flow conditions on widening mixing zones in coastal aquifers, Water Resour. Res., 45, W12402, doi:10.1029/2008WR007643.
2. Lu, C., Gong, R., Luo, J. (2009), Analysis of stagnation points for a pumping well in recharge areas, J. Hydrol., 373, 442-452.
3. Lu, C., Luo, J. (2010), Boundary condition effects on estimating maximum groundwater withdrawal in coastal aquifers, J. Hydrol., submitted.
4. Lu, C., Luo, J. (2010), Dynamics of freshwater-seawater mixing zone development in dual-domain formations, Water Resour. Res., submitted.
5. Lu, C., Kitanidis, P.K., Luo, J., Mixing enhanced by kinetic mass transfer and dynamic forces in coastal aquifers, Eos Trans. AGU, 90(52), Fall Meet. Suppl., Abstract H32C-05, San Francisco, CA, Dec. 14-18, 2009

Report as of FY2009 for 2007GA165G: “ Multi-Scale Investigation of Seawater Intrusion and Application in Coastal Georgi”

Students Supported

Ph.D. student: Lu, Chunhui

Publications

Lu, C., Kitanidis, P.K., Luo, J. (2009), Effects of kinetic mass transfer and transient flow conditions on widening mixing zones in coastal aquifers, *Water Resour. Res.*, 45, W12402, doi:10.1029/2008WR007643.

Lu, C., Gong, R., Luo, J. (2009), Analysis of stagnation points for a pumping well in recharge areas, *J. Hydrol.*, 373, 442-452.

Lu, C., Luo, J. (2010), Boundary condition effects on estimating maximum groundwater withdrawal in coastal aquifers, *J. Hydrol.*, submitted.

Lu, C., Luo, J. (2010), Dynamics of freshwater-seawater mixing zone development in dual-domain formations, *Water Resour. Res.*, submitted.

Lu, C., Kitanidis, P.K., Luo, J., Mixing enhanced by kinetic mass transfer and dynamic forces in coastal aquifers, *Eos Trans. AGU*, 90(52), Fall Meet. Suppl., Abstract H32C-05, San Francisco, CA, Dec. 14-18, 2009

Report Follows

Chap. 1

Effects of kinetic mass transfer and transient flow conditions on widening mixing zones in coastal aquifers

Abstract

The width of a mixing zone between freshwater and seawater is important primarily because it directly reflects the extent of mixing and the growth and decay of the mixing zone indicates changes of the flow regime and water exchange between freshwater and coastal seawater. Wide mixing zones have been found in many coastal aquifers all over the world. However, the mechanisms responsible for wide mixing zones are not well understood. This work examines the hypothesis that kinetic mass transfer coupled with transient conditions, which create the movement of the mixing zone, may widen mixing zones in coastal aquifers. The hypothesis is tested by conducting two-dimensional numerical simulations based on a variable-density groundwater model for a scaled-tank model and a field-scale model. Periodic water levels, representing periodic tidal motion and freshwater-table fluctuations, are imposed at the seaward and landward boundary, respectively, which cause the movement of the mixing zone. Both the scaled-tank model and the field model show that the combination of the moving mixing zone and kinetic mass transfer may significantly enhance the extent of mixing and create a wider mixing zone than the models without kinetic mass transfer. In addition, sensitivity analyses indicate that a larger capacity ratio (immobile porosity/mobile porosity) of mass transfer leads to a wider mixing zone, and the maximum width of the mixing zone may be reached for a given capacity ratio when the mean retention timescale in the immobile domain (the reciprocal of mass transfer rate) and the period of water-level fluctuations are comparable.

Keywords: Seawater intrusion; Mass transfer; Water-level fluctuation; Mixing zone; Coastal aquifers

1. Introduction

Interaction between groundwater and coastal seawater results in two complementary processes: seawater intrusion and submarine groundwater discharge (SGD). Understanding these processes meets the urgent needs for preserving vital fresh groundwater resources and coastal and offshore environments in highly populated coastal areas worldwide. The mixing zone developed at the freshwater-seawater interface is one of the most important features in complex coastal hydrogeologic systems. As the cumulative effect of many processes and mechanisms, such as periodic tidal activities, seasonal water-table change, groundwater withdrawal, transport processes driven by density gradient, diffusion and dispersion, and properties of geological formations, etc., the growth and decay of the mixing zone can (1) directly reflect the extent of mixing in coastal aquifers; and (2) provide extremely useful information to serve as an indicator for and measure of effective management of groundwater resources and sustainable stewardship of coastal and offshore environments. For example, upconing of the mixing zone generally indicates the occurrence of seawater intrusion subject to excessive groundwater withdrawal [*Bear*, 1972]; and the movement of the mixing zone due to seasonal water-table fluctuation is often associated with the seasonal variations of SGD [*Michael et al.*, 2005]. Thus, gaining a better grasp of mixing-zone development in coastal aquifers within various hydrogeologic settings is a milestone in our efforts to significantly improve our understandings of flow and transport in complex coastal hydrogeologic systems.

In general, two types of mathematical models have been used to describe the mixing-zone development: sharp-interface approximation and miscible-fluid model. In the sharp-interface approximation, it is assumed that there is a stationary and abrupt interface between freshwater and intruding seawater, implying that no mixing takes place between freshwater and seawater. This approach is a major simplification and may allow one to use potential-flow theory for describing interface propagation, and provides a useful tool for developing a variety of analytical solutions [e.g., *Bear and Dagan*, 1964; *Strack*, 1976; *Huppert and Woods* 1995, *Naji et al*., 1998]. The second approach, based on the density-dependent miscible saltwater-freshwater systems, accounts for the presence of a variable-density mixing zone. The latter model is of particular interest in practical applications where one desires to evaluate salt and other species concentrations in coastal aquifers. In this work, we will focus on this model. Due to its practical significance, several numerical models based on miscible-fluid physics have been developed to describe and study the problem of seawater intrusion over the past 20 years [*Voss and Souza*, 1987; *Ataie-Ashtiani et al*., 1999; *Paniconi et al*., 2001; *Zhang et al*., 2004; *Paster* et al., 2006; *Qahman and Larabi*, 2006]. Analytical solutions for seawater intrusion based on miscible-fluid systems are only available for steady-state, simplified cases [*Dentz et al*., 2006; *Bolster et al*., 2007].

Both narrow and wide mixing zones have been observed in numerical, laboratory, and field studies. With a fine discretization and small dispersion, numerical simulations produced narrow mixing zones [e.g., *Benson et al.*, 1998; *Karasaki et al.* 2006]. Laboratory experiments also demonstrated narrow mixing zones in homogeneous media

[e.g., *Zhang et al.*, 2001; *Goswami and Clement*, 2007; *Abarca and Clement*, 2009]. However, many field measurements found wide mixing zones, ranging from hundreds of feet to miles. This finding cannot be simply explained by upscaling small-scale laboratory data. For example, groundwater salinity measurements in Everglades National Park, in Southern Florida, USA, indicated the presence of a wide (6–28 km) seawater mixing zone [*Price et al*., 2003]; in the Floridian aquifer near downtown Brunswick, GA, USA, the mixing zone of seawater and freshwater has been detected across an area of increasing size [*Cherry*, 2006]; *Xue et al*. [1993] reported a wide mixing zone of 1.5-6.0 km in the coastal area of LaiZhou Bay, China, and also found that the increasing extension of the salt water intrusion is a major concern in this area [*Wu et al*., 1993]; *Barlow* [2003] summarized groundwater in freshwater-saltwater environments of the Atlantic Coast, in which wide mixing zones were observed in many coastal aquifers, *e.g.*, the Biscayne aquifer near Miami, Florida, the upper Potomac aquifer in Virginia's Inland Wedge, the Floridan aquifer system in South Carolina, Georgia, and Florida, and the lower Tamiami aquifer in southwestern Florida, etc.

The mechanisms responsible for a wide mixing zone still remain the subject of debate. Local dispersion has been considered as a primary mechanism responsible for the occurrence of the mixing zone. During the movement of the seawater front in either the landward or the seaward direction, elements of each fluid are transferred into the opposite environment by the convection component of dispersion, wherein to a large extent they become inseparably blended with other fluid by mixing and molecular diffusion [*Cooper*, 1959]. *Dagan* [2006] pointed out that transverse dispersion is the main mechanism creating mixing in the seawater-freshwater interface, but the presumed small transverse pore-scale dispersion can only create a narrow mixing layer at the interface. The extent of mixing is also influenced by hydrodynamic fluctuations of the groundwater and seawater levels. *Volker and Rushton* [1982] compared a variety of aquifer parameters and the influence of the flow conditions on the configuration and location of the interface. They concluded that a decrease in the dispersion coefficient leads to the contraction of the dispersion zone for a constant freshwater discharge, while the interface becomes more diffuse as the freshwater discharge decreases provided that the dispersion coefficient keeps invariant. *Ataie-Ashtiani et al*. [1999] numerically examined the effects of tidal fluctuations on seawater intrusion in an unconfined aquifer, and found that the tidal activity created a thicker interface than would occur without tidal effects. However, *Karasaki et al.* [2006] failed to reproduce a wide mixing zone by imposing a time-varying sinusoidal boundary condition without using a large dispersion coefficient. Heterogeneity in the hydraulic conductivity of the formation also contributes to the mixing enhancement. Heterogeneous hydraulic conductivities lead to spatially varying specific-discharge fields and thus to nonuniform advection. As a result, the mixing zone becomes increasingly irregular in shape, enhancing mixing caused by diffusion across its surface. However, *Abarca et al*. [2006] showed that the effects of moderate heterogeneity on increasing the width of mixing zone are small. Thus, the widening of mixing zone width may not simply be attributed to heterogeneity of the formation.

In the present research, we provide an alternative plausible explanation for wide mixing zones observed in coastal aquifers. The hypothesis is that the movement of the mixing zone combined with kinetic mass transfer effects may significantly widen the mixing

zone. This study is motivated by the facts that (1) the mixing zone, in reality, seldom remains stationary, and (2) mass transfer processes, representing mass exchange between relatively mobile phases where advective-dispersive transport occurs and relatively immobile phases including low-permeability zones, stagnation pores, and sorption phases, etc. [*Coats and Smith*, 1964; *van Genuchten and Wierenga*, 1976], occur in almost all fractured and porous heterogeneous media over various scales ranging from pore scale to field scale, and significantly enhance solute mixing [*Michalak and Kitanidis*, 2000]. Previous investigations of the mixing-zone width are mostly based on the steady state or tidal conditions. Under these conditions, the mixing zone is nearly stationary [*Volker and Rushton*. 1982; *Ataie-Ashtiani et al*., 1999; *Robinson et al*., 2007]. In reality, however, mixing zones seldom remain stationary. Large scale recharge into the aquifer as well as withdrawals from it leads to the movement of mixing zone from one position to another. It is now recognized that seasonal oscillations of inland recharge appear to be widespread, clearly indicating that a seasonal mixing-zone movement occurs in coastal aquifers [*Michael et al*., 2005]. On the other hand, the movement of mixing zone can also be caused by the effects from the seaward boundary. *Cartwright and Nielsen* [2003], based on field experiments, indicated that the mixing zone movement can be caused by coastal waves. It is worth noting that the movement of mixing zone has been also observed in many other coastal areas [*Wu et al*., 1993; *Cherry*, 2006]. To the best of our knowledge, no study focusing on the mixing-zone development has considered the combined effect of mass transfer processes and transient conditions. *Langevin et al*. [2003] conducted a simulation of variable-density flow coupled with dual-domain transport for the Henry problem. Without the consideration of mixing-zone movement, they found that the steady-state salinity distribution was roughly the same as the salinity distribution for the classical Henry problem.

2. Numerical model

The proposed hypothesis will be tested by conducting two-dimensional (vertical cross-section) numerical simulations based on the variable-density flow and transport equations for a scaled-tank model and a field-scale model. Transient effects will be introduced by imposing periodic water levels at the seaward and landward boundary. A dual domain transport model with first-order mass transfer will be applied to describe transport processes with kinetic mass transfer between mobile and immobile domains. The numerical model is solved by the density-dependent groundwater flow code SEAWAT-2000 implemented in a graphic user interface software Groundwater Vista 5.20 developed for 3D groundwater flow and transport modeling. SEAWAT-2000 itself was developed by combining MODFLOW and MT3DMS into a single program solving the coupled flow and solute-transport equations. MT3DMS is implemented with an optional, dual-domain formulation for modeling mass transport.

2.1 Governing Equations

The governing equation for saturated variable-density groundwater flow in terms of freshwater head is described by [*Langevin and Guo*., 2006]:

$$\nabla \cdot \left[\rho K_f \left(\nabla \cdot h_f + \frac{\rho - \rho_f}{\rho_f} \cdot \nabla z \right) \right] = \rho S_f \frac{\partial h_f}{\partial t} + \theta_e \frac{\partial \rho}{\partial t} - \rho_s q_s \tag{1}$$

where z [L] is the vertical coordinate directed upward; K_f [LT^{-1}] is the equivalent freshwater hydraulic conductivity; h_f [L] is the equivalent freshwater head; ρ [ML^{-3}] is the fluid density; ρ_f [ML^{-3}] is the freshwater density; S_f [L^{-1}] is the equivalent freshwater storage coefficient; t [T] is the time; θ_e is the effective porosity; and ρ_s [ML^{-3}] and q_s [T^{-1}] are the density and flow rate per unit volume of aquifer of the source/sink, respectively [*Langevin et al*., 2003].

The dual-domain transport model involving advection, molecular diffusion, mechanical dispersion, and first-order mass transfer is described by:

$$\theta_m \frac{\partial C_m}{\partial t} + \theta_{im} \frac{\partial C_{im}}{\partial t} = \nabla \cdot (\theta_m \mathrm{D} \nabla C_m) - \nabla \cdot (\theta_m \mathrm{v} C_m) \tag{2a}$$

$$\theta_{im} \frac{\partial C_{im}}{\partial t} = \xi (C_m - C_{im}) \tag{2b}$$

where θ_m is porosity of the mobile domain and is equal to θ_e; θ_{im} is porosity of the immobile domain; C_m [ML^{-3}] is dissolved concentration in the mobile; C_{im} [ML^{-3}] is dissolved concentration in the immobile; ξ [T^{-1}] is first-order mass transfer rate between the mobile and immobile domain; **D** [L^2T^{-1}] is the hydrodynamic dispersion coefficient tensor; and **v** [LT^{-1}] is the pore water velocity vector.

The relationship between the fluid density and salt concentration is represented by the linear function of state:

$$\rho = \rho_f + \varepsilon C_m \tag{3}$$

where ε is a dimensionless constant with a value of 0.7143 for salt concentrations ranging from zero to 35 kg m^{-3}, a typical concentration value for seawater [*Langevin et al*., 2003]; and ρ is expressed in kg m^{-3}.

2.2 A Scaled Tank Model and Numerical Implementation

A scaled tank model is designed to simulate the mixing-zone development under the considerations of transient conditions and mass transfer effects. *Zhang et al*. [2002] presented an experimental study of a dense contaminant plume in an idealized coastal aquifer based on a tank model, which was numerically studied by *Brovelli et al*. [2007]. Due to its high computational efficiency, this scaled tank model is used here to investigate mass transfer effects on the development of the mixing zone and sensitivity analysis will also be conducted. A schematic representation of the seawater intrusion

problem is shown in Figure 1. The tank is 1.650m long, 0.6m high, and 0.1m wide with a beach slope (vertical/horizontal ratio) 1:6.12. A homogeneous, isotropic hydraulic conductivity of 4×10^{-3} m s^{-1} is assigned to the domain. The mean local longitudinal and transverse dispersivities are measured to be 6.49×10^{-4} m and 1×10^{-4} m, respectively. The total porosity is 0.37. The mean seawater level and the constant freshwater level are 0.439m and 0.463m, respectively. The seawater and freshwater densities are 1025kgm^{-3} and 1000kgm^{-3}, respectively, which represent a salt concentration of 35kgm^{-3} for seawater. The parameters for the scaled tank model are summarized in Table 1.

Rather than only tidal conditions used by *Zhang et al.* [2002] and *Brovelli et al.* [2007], periodic water-level fluctuations are imposed at the seaward and landward boundaries, respectively, to create the movement of the mixing zone. First, a triangular, periodic function with a period of 40 minutes (see Figure 2) is imposed at the seawater boundary to simulate the periodic tidal-like motion, while a constant freshwater level of 0.463m is defined at the landward boundary. The linear variation of water level can be directly implemented based on the variable head boundary condition in SEAWAT by specifying two values of hydraulic head at the beginning and at the end of the stress period, respectively. The software linearly interpolates between the two values according to defined time step. The use of the triangular function instead of a sinusoid function is to minimize the computational effort because much more pressure periods will be needed to reproduce the sinusoid function. Then, another triangular, periodic function with a period of 80 minutes and amplitude of 0.04 m is defined at the landward boundary to simulate the water-table fluctuations, while the seawater level is kept constant at 0.439 m. In reality, the period of the freshwater-table fluctuations may be much greater than that of the tidal motion. Sensitivity analysis will be conducted later to investigate the effects of both periods. A constant salt concentration of 35kgm^{-3} is enforced at the seaward boundary.

The simulation domain is discretized into 9900 cells in order to satisfy the accuracy and convergence requirement for grid spacing in terms of the local Péclet number [*Voss and Souza*, 1987; *Zhang et al*., 2001; *Volker et al*., 2002; *Brovelli et al*., 2007]. The entire model domain is divided into two zones: a surface water zone and an aquifer zone. To simplify the numerical simulation, a large hydraulic conductivity of 0.4ms^{-1}, i.e., 100 times of the saturated aquifer hydraulic conductivity, a constant porosity of 1, and a constant saltwater concentration of 35 kg m^{-3} are assigned to all the cells in free seawater area [*Winter*, 1976; *Anderson et al*., 2002; *Mao et al*., 2006; *Brovelli et al*., 2007; *Robinson et al*., 2007]. In addition, to reproduce the flat surface of the sea, a horizontal strip of cells with a variable-head boundary condition is added onto the seawater surface [*Brovelli et al*., 2007]. Simulations start from steady-state conditions generated by using the mean seawater level and the mean freshwater level. The simulation duration for each case is fifty periods of the corresponding triangular functions, a sufficiently long period for the scaled tank models to reach a dynamic equilibrium state of the concentration distribution, i.e., the tolerance of the maximum concentration variation is satisfied when doubling the computation periods.

2.3 A Field Scale Model and Numerical Implementation

For the field-scale case, we consider a 2D model domain that is 200m long and 35m high with a beach slope 1: 10. The aquifer was assumed to be isotropic and homogeneous with K_f = 20md^{-1}, $n_e = 0.4$, longitudinal dispersivity α_L = 0.5m and transverse dispersivity α_T = 0.05m. Hydraulic conductivity of 1000md^{-1}, $n_e = 1$ and constant salt concentration of 35kgm^{-3} are assigned to the cells in free seawater area so that the entire domain can be solved by SEAWAT. The mean seawater level and the mean freshwater level are 28 m and 29 m, respectively. For field-scale applications, transient effects introduced by periodic tidal motion on the movement of the mixing zone may not be as effective as those introduced by the freshwater-table fluctuations because (1) tidal motion has a much shorter period than freshwater-table fluctuations; (2) the amplitude of freshwater-table fluctuations can be much larger than that of tidal motion because of seasonal precipitation and temperature patterns; and (3) the effects of the freshwater-table change may be enlarged to 40 times on the freshwater-seawater interface according to the Ghyben-Herzberg law based on potential equilibrium [*Bear*, 1972]. In the present research, we impose a triangular, periodic head variation with a period of one year and an amplitude of 1m at the landward boundary, while a constant seawater level of 28m is specified at the seaward boundary. For the numerical simulation, a mesh resolution of 0.5 m was adopted, yielding 28000 cells. This discretization results in a satisfactory *Pe* of 1. The dynamic equilibrium state of the concentration distribution is found after 100 periods, i.e., 100 years.

3. Results of the Tank Model

3. 1 Steady-State Condition

Steady-state cases are first simulated to serve as control cases, which neglect both mass transfer and transient conditions introduced by tidal motion and freshwater-table fluctuations. By assuming a constant seawater level of 0.439 m and a constant freshwater level of 0.463 m, a SEAWAT simulation was first run for steady-state conditions without considering the mass transfer effect. Figure 3 shows the mixing zone, where the contour lines delineate the normalized concentrations 0.1, 0.5, and 0.9. Rather than a sharp interface, a narrow mixing zone is formed due to density gradient and local dispersion. The salinity distribution simulated in our study matches well experimental [*Zhang et al*., 2002] and numerical results [*Zhang et al*., 2001; *Brovelli et al*., 2007] previously obtained based on the same scaled tank model. We also evaluate the mixing zone by including mass transfer but still neglecting transient effects. Similar to the observation by *Langevin et al*. [2003], the resulting mixing zone is almost the same as the one neglecting mass transfer. Thus, for steady-state analyses, mass transfer does not make significant contributions in altering salinity distributions. In fact, by forcing the transient terms in Eq. (2) to be zero, the transport model reduces to the case without mass transfer. That is, the steady-state salinity distributions will become identical for cases with and without mass transfer, although the timescales to reach the steady state may be different.

3.2 Transient and Mass Transfer Effects

Figure 4 shows the mixing zones with the consideration of seawater level oscillations but neglecting mass transfer. A wider mixing zone, particularly at the toe, is observed compared with the mixing zone shown in Figure 3. Furthermore, due to the seawater level oscillations the interface is pushed seaward. This phenomenon is consistent with the simulation results obtained by *Robinson et al*. [2007], who conducted a numerical study on a field-scale domain to investigate the effect of tidal forcing on a subterranean estuary. In addition, their results show that the interface is pushed more seaward with a larger amplitude tide. Seawater-level fluctuation forces the seawater back and forth and, thus, the equilibrium state shown in Figure 3 is disturbed, yielding a transient velocity field and a fluctuated concentration distribution, which result in enhanced mixing and a slightly wider mixing zone due to hydrodynamic dispersion. This phenomenon has been demonstrated by the laboratory experiment of *Zhang et al*. [2002]. *Ataie-Ashtiani et al*. [1999] also showed wider mixing zones caused by tidal motion, but observed that a larger tidal amplitude may force the seawater to intrude further inland. The difference may result from a different domain setting, in which an additional unsaturated zone was assumed above the groundwater table.

However, previous studies including numerical work conducted by *Robinson et al*. [2006, 2007] and *Ataie-Ashtiani et al*. [1999] and field experiments by *Cartwright et al*. [2004] indicate that the mixing zone of the saltwater wedge does not fluctuate over the course of a tidal cycle because the forcing timescale is too short. Hence, the movement of the mixing zone in our study can be attributed to the small tank scale and relatively large timescale of seawater level fluctuation. In reality, however, the mixing zone may be forced landward by a combination of increasing tidal range, wave height and infiltration of wave run-up [*Cartwright and Nielsen*, 2001a,b]. Once the wave forcing decreased the contour gradually moved seaward [*Cartwright and Nielsen*, 2003]. Therefore, the movement of the mixing zone of our scaled tank model may be regarded as a result of complex effects from the seaward boundary.

Figure 4 also shows that the position of the mixing zone varies at different seawater level stages, i.e., the hydraulic gradient determines the position of the mixing zone. Thus, we can only define a dynamic-equilibrium state instead of a steady state for the transient case. As mentioned before, dynamic equilibrium is defined as the state where the mixing-zone position has no significant variations by doubling the simulation duration. In addition, although the position of the mixing zone varies, the width does not change noticeably over the course of one periodic cycle.

Figure 5 shows the mixing zones with the consideration of both mass transfer effects and seawater level oscillations, where both mobile porosity and immobile porosity are set to be 0.185 and the first-order mass transfer rate coefficient is 0.025 min^{-1}. Figure 5 clearly shows that the mass transfer effect leads to significantly wider mixing zones at all stages of the seawater level compared with those shown in Figure 4. In particular, it is more pronounced at the low and falling water level stages. As already mentioned, in the absence of seawater level oscillations, i.e., the mixing zone is stationary, mass transfer has no effect on the steady-state salinity distribution because there is no concentration gradient between the mobile and immobile domains and Eq. (2) can be simplified to the classical advection-dispersion equation, although the timescale to reach the steady state

may be changed. However, in transient cases, the mixing zone is pushed back and forth by complex effects from the seaward boundary, resulting in non-equilibrium in the salt concentrations in the mobile and immobile domains and an enhanced mass exchange between them. The immobile domain here essentially acts as a sink or source for solutes in the mobile zone, determined by the direction of concentration gradient between two domains. Specifically, salts in the mobile domain diffuse into the immobile domain as the mixing zone is dragged inland, while salts are released from the immobile domain to the mobile domain driven by reversed concentration gradients when the mixing zone is towed toward the sea. The disturbed concentration and density gradient field leads to enhanced mixing and a wider mixing zone than would occur in the absence of mass transfer. Moreover, Figure 5 shows that the combination of mass transfer and seawater level fluctuations has greater influences on the high concentration contour lines (see the contour lines of normalized concentration 0.9), which become closer to the seaward boundary.

Freshwater-level fluctuation is observed in many areas, which has been found as a main reason leading to the movement of the mixing zone [*Michael et al*., 2005]. Figure 6 shows the mixing zones under periodic oscillations of the freshwater level without mass transfer effects. Like the effect from seawater level fluctuations shown above, the mixing zone is pushed seaward, and wider mixing zones are formed. However, the mixing zone moves within a broader range due to a larger period of the freshwater-level fluctuation. The width of the mixing zone caused by freshwater variation is expected to increase when the mass transfer effect is taken into account. Figure 7 exhibits the mixing zones with the consideration of both mass transfer and freshwater-level oscillations, where both mobile and immobile porosities are set to be 0.185 and the first-order mass transfer rate coefficient is 0.0125 min^{-1}. Likewise, the introduced mass transfer effect significantly increases the width of the mixing zone, especially at the rising level stages. Similarly, one may expect that a larger fluctuation amplitude will lead to a wider mixing zone.

3.3 Sensitivity Analysis

Parameters of kinetic mass transfer, including mobile and immobile porosity and the first-order rate constant, will be varied in order to investigate the effects of kinetic mass transfer. In order to interpret the results concisely and produce a meaningful generalization, the following dimensionless variables are defined:

$$\tau = \xi^{-1} / T_f \tag{4}$$

$$\beta = \theta_{im} / \theta_m \tag{5}$$

$$w = W / W_{ss} \tag{6}$$

where T_f is the water level fluctuation period; ξ^{-1} represents a characteristic mass transfer time in the immobile domain; β is known as the capacity ratio; W_{ss} is the mixing-zone width under steady-state condition; and W is the width of the mixing zone

under the coupled effect of mass transfer and water-level fluctuation. For simplicity, *W* is represented by the horizontal distance between concentration contour lines of 0.1 and 0.9. Here, we choose the width of the mixing zone at the height of 200 mm at the rising tidal moment to calculate *W*. Similar results will be obtained for the width of the mixing zone at other heights and tidal moments. By assuming a constant total porosity for the mobile and immobile domain, the effects of mass transfer parameters and water level fluctuations on the dimensionless width of the mixing zone, *w*, can be investigated by varying the dimensionless variables, τ and β.

Figure 8 shows the simulated results for the sensitivity analysis for the tank model. The width of the mixing zones formed by varying the freshwater level is somewhat wider than that by seawater-level fluctuation since the period of the former is assumed larger than the latter. For both cases, with a given mean retention time, i.e., a constant first-order mass transfer rate coefficient, the width of the mixing zone increases with the capacity ratio, indicating that a larger immobile domain may cause a wider mixing zone. With a given capacity ratio, i.e., a constant porosity of the immobile domain, the width of the mixing zone is maximized when the retention timescale of the mass transfer and the period of the water-level fluctuation become comparable, i.e., at the same order of magnitude. In such cases, the effects of the capacity ratio will also be maximized. In addition, the left and right tails of the curves shown in Figure 8 (a) and (b) indicate that the mass transfer may not have significant impacts on widening the mixing zone when there is a several orders of magnitude difference between the retention timescale and the water-level fluctuation period. In fact, both the limiting cases of very small and large mass transfer rate coefficients can be simplified to a classical advective-dispersive transport problem. For a small mass transfer rate coefficient, it is equivalent to the transport problem in a medium with a smaller total porosity, i.e., practically no mass transfer occurs within a period. For a large mass transfer rate coefficient, the kinetic mass transfer may be considered as an instantaneous process, which simplifies the two-domain model into a one-domain model with a retardation factor, $1+\beta$. Thus, for both limiting cases, the width of the mixing zone will approach the dynamic equilibrium state in the absence of mass transfer. In our tank model, the mixing zone is significantly widened for τ between 0.1 and 100, and the width reaches maximum for τ to be about 1, i.e., ξ^{-1} is equal to T_f. For example, the width of the mixing zone is approximately 3.7 times as wide as that under steady state condition for the freshwater-level fluctuation case with $\beta = 1$ and $\tau = 1$ (see Figure 8(b)). If other parameters are kept constant, we may expect that the width of the mixing zone will become much larger for a higher β.

4 Field Scale Modeling Results

The field-scale model described in section 2 corroborates the results obtained based on the tank model. Figure 9 shows the mixing zone under steady-state condition, where a narrow mixing zone is generated. With the introduction of freshwater-level fluctuations, the steady-state system is disturbed and the mixing zone is slightly widen (see Figure 10). Mass transfer effect is then introduced, where mobile and immobile porosities both are set to be 0.2, namely, $\beta = 1$. Three mass transfer coefficients including 0.027 d^{-1}, 0.0027

$d^{-1}$and 0.00027 $d^{-1}$are employed, which correspond to dimensionless variable τ as 0.1, 1, and 10, respectively. The corresponding mixing zones at the rising water level stage for these three cases are exhibited in Figure 11, which clearly shows wider mixing zones than those shown in Figure 10. In particular, the mixing-zone width in the case with $\tau = 1$ is maximal, consistent to the result found in the tank model.

In the absence of mass transfer, dispersivities, particularly transverse dispersivity, is considered to be the primary factor affecting the width of the mixing zone [*Ataie-Ashtiani et al*., 1999; *Dagan*, 2006]. In order to reproduce a wide mixing zone in a real case, the common method is to assume a large, perhaps unwarranted, value of dispersivities [*Dagan*, 2006]. In this section, we briefly compare the effects of dispersivities and mass transfer on the mixing-zone width. In addition to the dispersivities assumed in the cases discussed above, two more groups of longitudinal and transverse dispersitivies are adopted in the field-scale model: α_L = 2.5 m and α_T = 0.25 m, and α_L = 0.1 m and α_T = 0.01 m

Figure 12 shows the mixing zones at the rising freshwater level stage with the consideration of the freshwater-level fluctuation alone. It is obvious that larger dispersivities yield a wider mixing zone. However, the maximum mixing zone shown in Figure 12(C) is still not as wide as that in Figure 11(B), although both longitudinal and transverse dispersivities are twenty-five times of those in the previous case. Thus, in order to generate a wider mixing zone, larger dispersivities must be accepted.

Figure 13 shows the results by further introducing mass transfer with $\beta = 1$ and $\tau = 1$ into the three cases with different dispersivities. It is shown that all mixing zones are significantly widened compared with those shown in Figure 12. Furthermore, with the mass transfer effect, all the mixing-zone widths become similar, although different dispersivities are used. The mass transfer effect dominates the mixing-zone width change. Therefore, in our cases, the effect of kinetic mass transfer is more pronounced than the dispersivities on widening the mixing zone.

5 Conclusions

Wide mixing zones have been observed in many aquifers all over the world. However, no agreement has been reached in terms of the responsible mechanisms. In the present work, we propose the hypothesis that kinetic mass transfer combined with movement of mixing zones may significantly widen mixing zones in coastal aquifers. The hypothesis is tested by conducting numerical simulations based on the variable-density groundwater model for both a scaled-tank model and a field-scale model. The movement of the mixing zone may be caused by complex effects from both the seaward boundary (e.g., wave run-up) and the landward boundary (e.g., seasonal fluctuation of fresh groundwater head). In our simulations, the movement of the mixing zone is created by assuming triangular, periodic functions for water-level oscillations at the seawater and landward boundaries, respectively. In the absence of kinetic mass transfer, the created transient effects slightly widen the mixing zone compared with that in steady state. With the introduction of

kinetic mass transfer, mixing zones are significantly widened at all stages within the period.

Furthermore, sensitivity analyses of dimensionless variables based on the tank model yield the following observations: (1) the mixing zone may be significantly widened by the mass transfer effect regardless of which boundary causes the movement of the mixing zone; and (2) a larger capacity ratio of mass transfer leads to a wider mixing zone, and the maximum width may be reached when the mean retention timescale in the immobile domain and the water-level fluctuation period become comparable. Our simulations also investigate the effects of dispersivities on the mixing-zone development. Larger dispersivities always yield wider mixing zones. However, dispersivities may not be as effective as kinetic mass transfer on widening the mixing zone in our cases. More importantly, larger dispersitivies and mass transfer are based on different physical interpretations of the transport processes and formation properties. Large, perhaps unwarranted dispersitivities are often considered as the misrepresentation of aquifer heterogeneities [*Dagan*, 2006]. On the other hand, as is well-known, no natural geological media are truly homogenous, and mass transfer occurs in almost all fractured and porous heterogeneous media over various scales ranging from pore scale to field scale. Our findings provide a plausible explanation for wide mixing zones in coastal aquifers which may consist of low-permeability zones, dead-end pores, porous particles, aggregates, and rock matrix between fractures. In such aquifers, the effects of kinetic mass transfer and the movement of mixing zone caused by tidal motion, freshwater-table fluctuations, groundwater withdrawal, etc., must be considered to evaluate the growth and decay of the variable-density mixing zone. Certainly, other parameters, such as the amplitude of the periodic stimulation, the hydraulic conductivity, the rate of freshwater flow, the heterogeneity of the geological formations, may influence the growth and decay of the mixing zone. The research of effects of these mechanisms on mixing zone development is continuing.

Acknowledgements:

This research was sponsored by the National Institutes of Water Resources (NIWR) and U.S. Geological Survey (USGS) under project ID 2007GA165G. This article has not been reviewed by the agency, and no official endorsement should be inferred. Any opinions, findings, and conclusions or recommendations expressed in this material are those of the authors and do not necessarily reflect the views of NIWR and USGS. We thank David Hochstetler for his comments on a preliminary version of the manuscript. We thank three anomenous reviewers for their constructive comments which significantly improve the manuscript quality.

References:

Abarca, E., and T. P. Clement (2009), A novel approach for characterizing the mixing zone of a saltwater wedge, *Geophys. Res. Lett., 36*, L06402, doi:10.1029/2008GL036995.

Ataie-Ashtiani, B., R. E. Volker, and D. A. Lockington (1999), Tidal effects on sea water intrusion in unconfined aquifers, *J. Hydrol., 216*, 17-31.

Anderson, M. P., R. J. Hunt, J. T. Krohelski, and K. Chung (2002), Using high hydraulic conductivity nodes to simulate seepage lake, *Ground Water, 40*(2), 117-122.

Abarca, E., M. Pool, J. Carrera, and M. Dentz (2006), Can seawater intrusion modeling be simplified, Eos Trans. AGU, 87(52), Fall Meet. Suppl., Abstract H54E-05.

Bear J. (1972), *Dynamics of Fluid in Porous Media*, Elsevier, New York.

Barlow, P.M. (2003), Ground water in freshwater-saltwater environments of the Atlantic coast: U.S. Geological Survey Circular 1262.

Bear, J., and G. Dagan (1964) Some exact solutions of interface problems by means of the hodograph method, *J. Geophys. Res., 69*, 1563-1572.

Benson, D. A., A. E. Carey, and S. W. Wheatcraft (1998), Numerical advective flux in highly variable velocity fields exemplified by saltwater intrusion, *J. Contam. Hydrol., 34*, 207-233.

Brovelli A., X. Mao, and D. A. Barry (2007), Numerical modeling of tidal influence on density-dependent contaminant transport, *Water Resour. Res., 43*, W10426, doi:10.1029/2006WR005173.

Bolster, D. T., D. M. Tartakovsky, and M. Dentz (2007), Analytical models of contaminant transport in coastal aquifers. *Adv. Water Res.*, 30, 1962-1972.

Cherry, G. S. (2006), U.S. Geological Survey Georgia Water Science Center and City of Brunswick-Glynn County Cooperative Water Program - Summary of Activities, July 2005 through June 2006, U.S.G.S. Open-File Report 2006-1368.

Cooper, H. H. (1959), A hypothesis concerning the dynamic balance of fresh water and salt water in a coastal aquifer. J. Geophys. Res. *64*, 461-467.

Cartwright, N., and P. Nielsen (2001a), Groundwater dynamics and salinity in coastal barriers. *Proc. 1st Intl. Conf. on Salt Water Intrusion and Coastal Aquifers-Monitoring, Modeling and Management*, Essaouira, Morocco, April 23-25, CD-ROM.

Cartwright, N., and P. Nielsen (2001b) Groundwater dynamics and salinity in beaches. *Proc. Coasts and Ports 2001, 15th Australasian Coastal and Ocean Engineering Conference*, Gold Coast, Australia, September 25-28, pp 441-446.

Cartwright, N., and P. Nielsen, (2003) Dynamics of the salt-freshwater mixing zone in ocean beaches. 2nd Intl. *Conf. on Salt Water Intrusion and Coastal Aquifers-Monitoring, Modeling and Management*, Merida, Mexico, March 30- April 2.

Cartwright, N., L. Li, and P. Nielsen (2004), Response of the salt-freshwater interface in a coastal aquifer to a wave-induced groundwater pulse: field observations and modelling, *Adv. Water Res., 27*, 297-303.

Coats, K. H., and B. D. Smith (1964). Dead-end pore volume and dispersion in porous media, *Soc. Pet. Eng. J., 4*, 73-81.

Delleur, J. W. (1999), The Handbook of Groundwater Engineering. CRC Press, New York.

Dagan, G. (2006), Transverse Mixing At Fresh-Water Salt-Water Interfaces: An Unresolved Issue. First International Joint Salt Water Intrusion Conference. Tutirials.

Dentz, M., D. M. Tartakovsky, E. Abarca, A. Guadagnini, X. Sanchesz-Vila, and J. Carrera (2006), Variable-density flow in porous media, *J. Fluid Mech., 561*, 209-235.

Goswami, R.R., and T.P. Clement (2007), Laboratory-scale investigation of saltwater intrusion dynamics, Water Resour. Res., *43*, W04418.

Huppert, H. E., and A. W. Woods (1995), Gravity-driven flows in porous layers. *J. Fluid Mech., 292*, 55-69.

Karasaki, K., I. Kazumasa, and K. Maekawa (2006), Simulation of salt water intrusion, Proceedings, TOUGH Symposium, Lawrence Berkeley National Laboratory, Berkeley, California, May 15-17.

Langevin, C. D., and W. Guo (2006), MODFLOW/MT3DMS-based simulation of variable-density ground water flow and transport. *Ground Water, 44*, 339-351.

Langevin, C. D., W. B. Shoemaker, and W. Guo (2003), Modflow-2000, The U.S. Geological Survey modular ground-water flow model Documentation of the Seawat-2000 version with the variable density flow process (VDF) and the integrated MT3DMS transport process (IMT), U.S. Geol. Surv. Open File Rep., 03-426, 43 p.

Michalak, A. M., and P. K. Kitanidis (2000), Macroscopic behavior and random-walk particle tracking of kinetically sorbing solutes, *Water Resour. Res.*, *36*(8), 2133–2146.

Michael, H. A., A. E. Mulligan, and C. F. Harvey (2005), Seasonal oscillations in water exchange between aquifers and the coastal ocean. *Nature, 436*, 1145-1148.

Mao, X., P. Enot, D. A. Barry, L. Li, A. Binley, and D.-S. Jeng (2006), Tidal influence on behavior of a coastal aquifer adjacent to a low-relief estuary, *J. Hydrol., 327*, 110-127, doi: 10.1016/j.jhydrol.2005.11.030.

Naji A., A. H. -D. Cheng, and D. Ouazar (1998), Analytical stochastic solutions of saltwater/freshwater interface in coastal aquifers. *Stoch. Hydrol. Hydraul., 12*, 413-430.

Paster A., G. Dagan, and J. Guttman (2006), The salt-water body in the Northern part of Yarkon-Taninim aquifer: field data analysis, conceptual model and prediction. *J. Hydrol., 323*, 154-167, doi: 10.1016/j.jhydrol.2005.08.018

Paniconi, C., I. Khlaifi, G. Lecca, A. Giacomelli, and J. Tarhouni (2001), Modeling and analysis of seawater intrusion in the coastal aquifer of eastern Cap-Bon, Tunisia. *Transport Porous Med. 43*, 3-28.

Price, R. M., Z. Top, J. D. Happell, and P. K. Swart (2003), Use of tritium and helium to define groundwater flow conditions in Everglades National Park, *Water. Resour. Res., 39*(9), 1267. doi:10.1029/2002WR001929.

Qahman, K., and A. Larabi (2006), Evaluation and numerical modeling of seawater intrusion in the Gaza aquifer (Palestine), *Hydrogeol. J., 14*, 713-728.

Robinson, C., L. Li, and D.A. Barry (2006), Effect of tidal forcing on a subterranean estuary, *Adv. Water Res., 30*, 851-865.

Robinson, C., L. Li, and H. Prommer (2007), Tide-induced recirculation across the aquifer-ocean interface, *Water Resour. Res., 43*, W07428, doi:10.1029/2006WR005679.

Strack, O.D.L. (1976), A single-potential solution for regional interface problems in coastal aquifers. *Water Resour. Res.*, 12, 1165-1174.

Van Genuchten, M. T., and P. J. Wierenga (1976), Mass-transfer studies in sorbing porous-media: 1. Analytical solution, *Soil Sci. Soc. Am. J., 40*, 473-480.

Volker, R. E., and K. R. Rushton (1982), An assessment of the importance of some parameters for seawater intrusion in aquifers and a comparison of dispersive and sharp-interface modelling approaches. *J. Hydrol., 56*, 239-250.

Voss, C. I., and W. R. Souza (1987), Variable density flow and solute transport simulation of regional aquifers containing a narrow freshwater-seawater mixing zone, *Water Resour. Res.*, 23, 1851-1866.

Volker, R. E., Q. Zhang, and D. A. Lockington (2002), Numerical modeling of contaminant transport in coastal aquifers, *Math. Comput. Simul., 59*(1-3), 35-44.

Winter, T. C. (1976), Numerical simulation analysis of the interaction of lakes and groundwater, *U. S. Geol. Surv. Prof.*, 1001.

Wu, J. C., Y. Q. Xue, P. M. Liu, J. J. Wang, Q. B., Jiang, and H. W. Shi (1993), Sea-water intrusion in the coastal area of LaiZhou Bay, China. 2. Sea-water intrusion monitoring. *Ground Water, 31*, 740-745.

Xue, Y.Q., J. C. Wu, P. M. Liu, J. J. Wang, Q. B. Jiang, and H. W. Shi (1993), Sea-water intrusion in the coastal area of LaiZhou Bay, China.1. Distribution of Sea-water Intrusion and its hydrochemical characteristics. *Ground Water, 31*, 532-537.

Zhang Q., R. E. Volker, and D. A. Lockington (2001), Influence of seaward boundary condition on cotaminat transport in unconfined coastal aquifer. *J. Contam. Hydrol*., *49*(3-4), 201-215.

Zhang Q., R. E. Volker, and D. A. Lockington (2002), Experimental investigation of contaminant transport in coastal groundwater. *Adv. Environ. Res.*

Zhang Q., R. E. Volker, and D. A. Lockington (2004), Numerical investigation of seawater intrusion at Gooburrum, Bundaberg, Queensland, Australia. *Hydrogeol. J*., *12*, 674-687.

Table

Table 1 Geometry, hydrogeological, and transport parameters used in the experimental study of *Zhang et al*. [2002]

Parameter	Variable	Value
Domain length, m	L	1.650
Domain height, m	H	0.6
Domain width, m	W	0.1
Beach slope	φ	1 : 6.12
Horizontal saturated hydraulic conductivity, m s-1	K_h	4×10^{-3}
Vertical saturated hydraulic conductivity, m s-1	K_v	4×10^{-3}
Longitudinal dispersivity, m	α_L	6.49×10^{-4}
Transverse dispersivity, m	α_T	1×10^{-4}
Total effective porosity	θ_e	0.37
Mean seawater level, m	h_s	0.463
Constant freshwater level, m	h_f	0.439
Seawater density, kg m-3	ρ_s	1025
Freshwater density, kg m-3	ρ_f	1000
Salt concentration, kg m-3	C_s	35

Figure Captions:

Figure 1. Schematic representation of the seawater intrusion problem.

Figure 2. Transient seawater levels caused by fluctuations. The fluctuation period is 40 minutes. The arrows indicate different water level stages.

Figure 3. The variable-density mixing zone between the freshwater and seawater for steady-state conditions in the absence of water level fluctuation and kinetic mass transfer (tank scale model). The solid lines are the contour lines of normalized salt concentrations.

Figure 4. Mixing zones at different seawater level stages within a fluctuation period with the consideration of seawater level fluctuation alone (tank scale model). (A) low level, (B) rising level, (C) high level, and (D) falling level.

Figure 5. Mixing zones at different seawater level stages within a fluctuation period with the consideration of both seawater level fluctuation and kinetic mass transfer (tank scale model). (A) low level, (B) rising level, (C) high level, and (D) falling level.

Figure 6. Mixing zones at different freshwater level stages within a fluctuation period with the consideration of freshwater level fluctuation alone (tank scale model). (A) low level, (B) rising level, (C) high level, and (D) falling level.

Figure 7. Mixing zones at different freshwater level stages within a fluctuation period with the consideration of both freshwater level fluctuation and kinetic mass transfer (tank scale model). (A) low level, (B) rising level, (C) high level, and (D) falling level.

Figure 8. Sensitivity analysis for the effects of combining mass transfer and movement of the mixing zone which is caused by (a) seawater level fluctuation and (b) freshwater level fluctuation.

Figure 9. The variable-density mixing zone between the freshwater and seawater for steady-state conditions in the absence of water level fluctuation and kinetic mass transfer (field scale model). The solid lines are the contour lines of normalized salt concentrations.

Figure 10. Mixing zones at different freshwater level stages within a fluctuation period with the consideration of freshwater level fluctuation alone (field scale model). (A) low level, (B) rising level, (C) high level, and (D) falling level.

Figure 11. Mixing zones at the rising freshwater level stage with the consideration of both freshwater level fluctuation and kinetic mass transfer (field scale model), in which (A) $\tau = 10$, (B) $\tau = 1$, and (C) $\tau = 0.1$

Figure 12. Mixing zones at the rising freshwater level stage with the consideration of the freshwater level fluctuation alone (field scale model), in which (A) α_L = 0.1 m and α_T = 0.01 m, (B) α_L = 0.5 m and α_T = 0.05 m, and (C) α_L = 2.5 m and α_T = 0.25 m.

Figure 13. Mixing zones at the rising freshwater level stage with the consideration of both freshwater level fluctuation and kinetic mass transfer (field scale model), in which (A) α_L = 0.1 m and α_T = 0.01 m, (B) α_L = 0.5 m and α_T = 0.05 m, and (C) α_L = 2.5 m and α_T = 0.25 m.

Figure 1

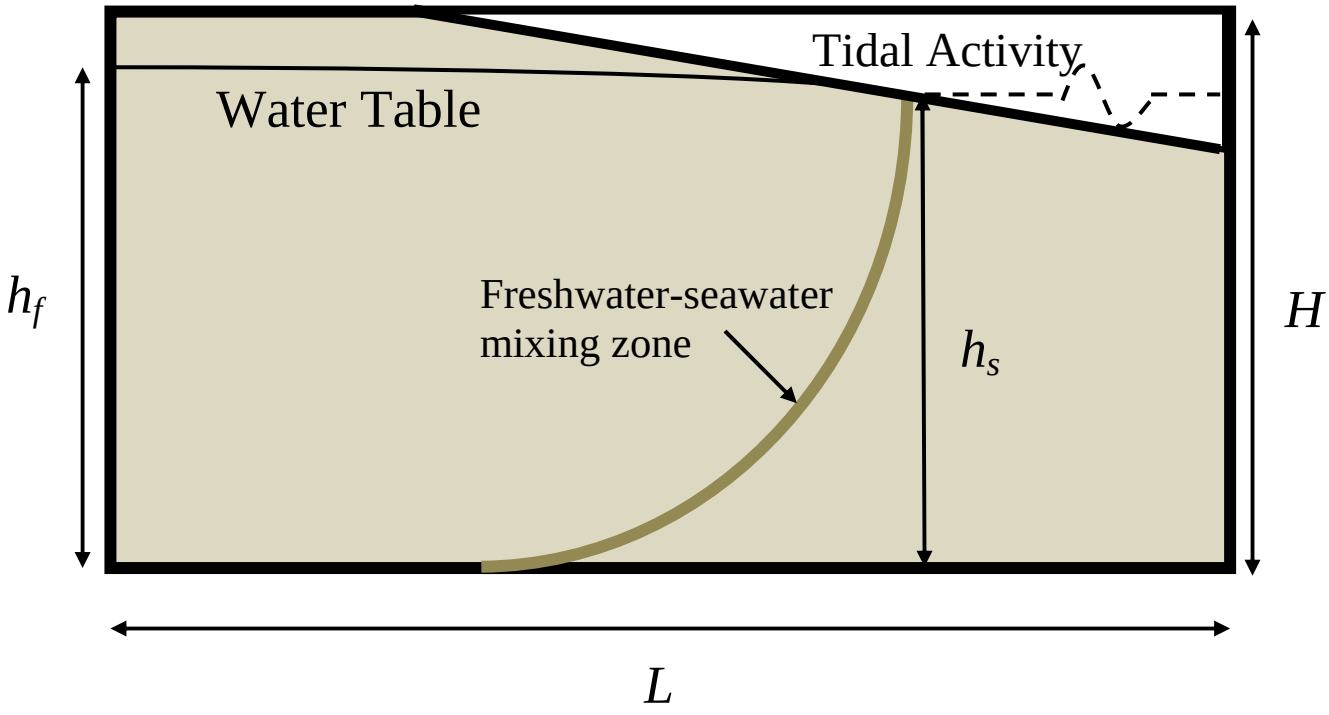
Tidal Activity
Water Table
h_f
Freshwater-seawater
mixing zone
h_s
H
L

Figure 2

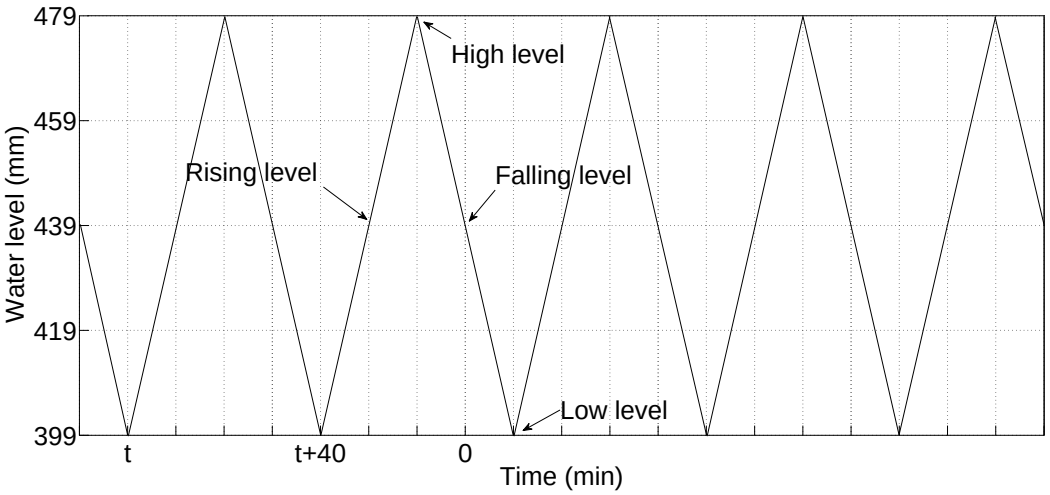

Figure 2. Transient seawater levels caused by fluctuations. The fluctuation period is 40 minutes. The arrows indicate different water level stages.

Figure 3

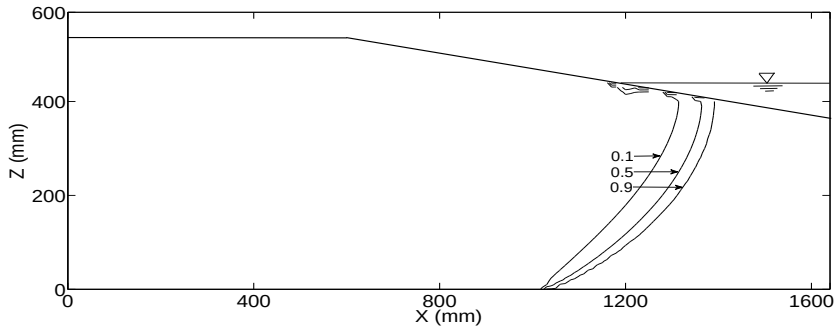

Figure 3. The variable-density mixing zone between the freshwater and seawater for steady-state conditions in the absence of water level fluctuation and kinetic mass transfer (tank scale model). The solid lines are the contour lines of normalized salt concentrations.

Figure 4

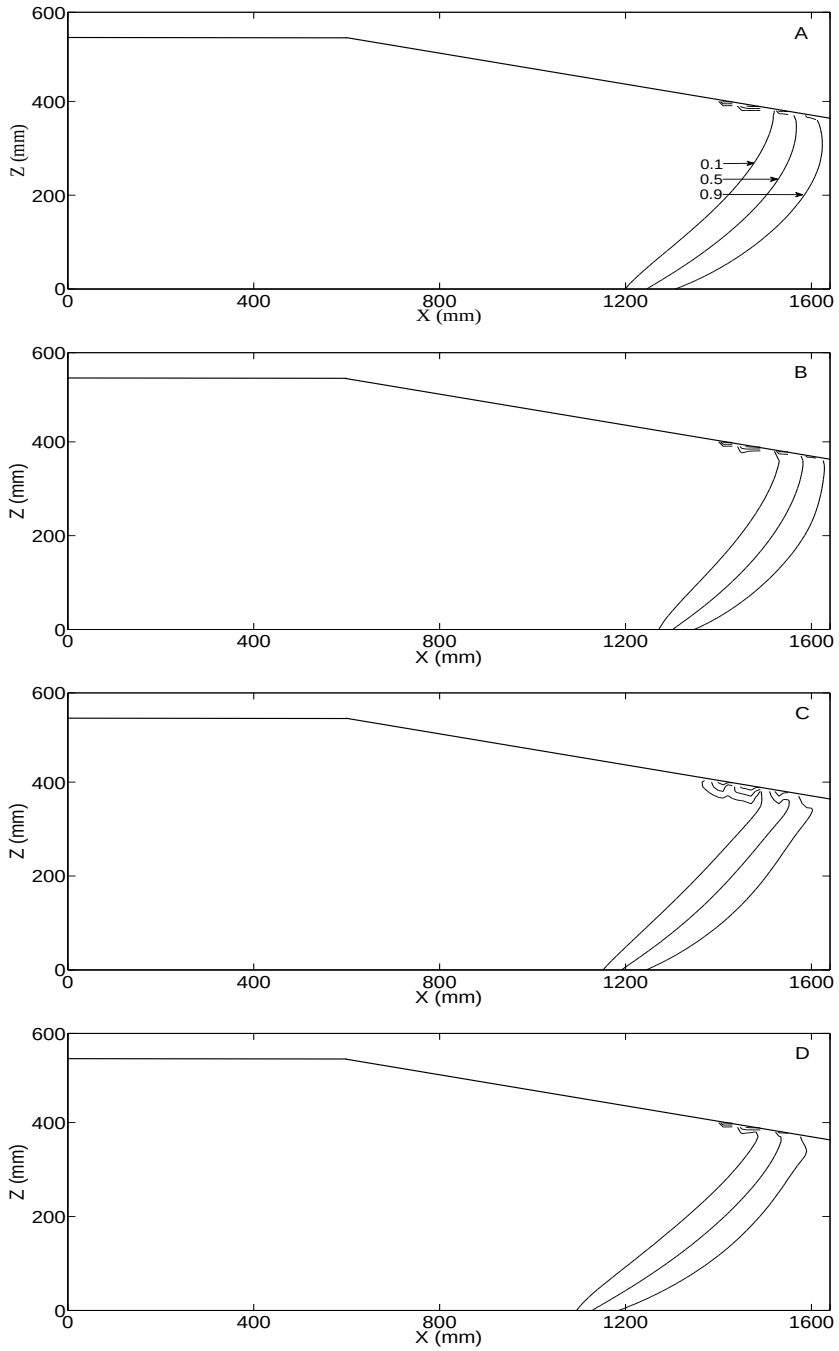

Figure 4. Mixing zones at different seawater level stages within a fluctuation period with the consideration of seawater level fluctuation alone (tank scale model). (A) low level, (B) rising level, (C) high level, and (D) falling level.

Figure 5

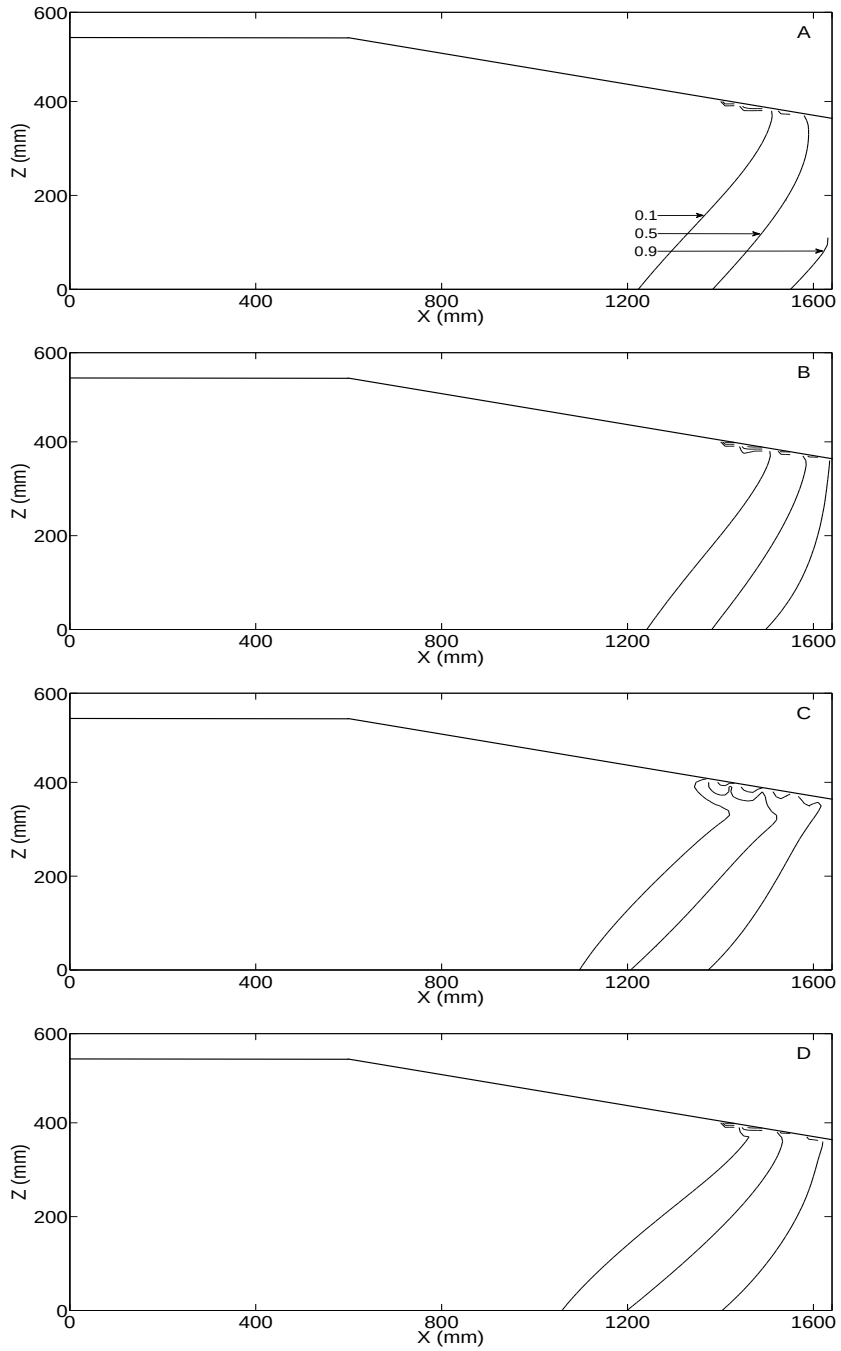

Figure 5. Mixing zones at different seawater level stages within a fluctuation period with the consideration of both seawater level fluctuation and kinetic mass transfer (tank scale model). (A) low level, (B) rising level, (C) high level, and (D) falling level.

Figure 6

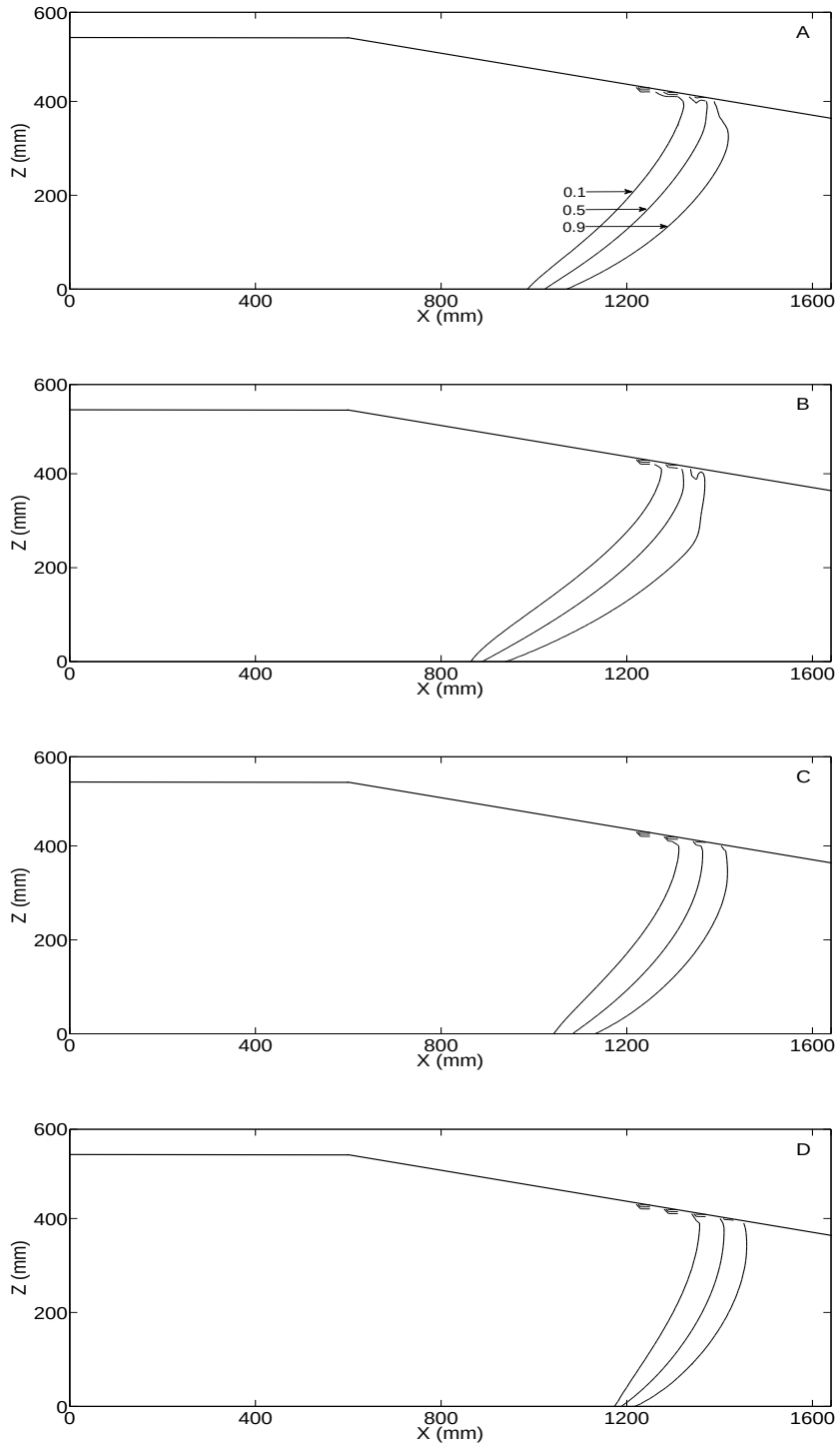

Figure 6. Mixing zones at different freshwater level stages within a fluctuation period with the consideration of freshwater level fluctuation alone (tank scale model). (A) low level, (B) rising level, (C) high level, and (D) falling level.

Figure 7

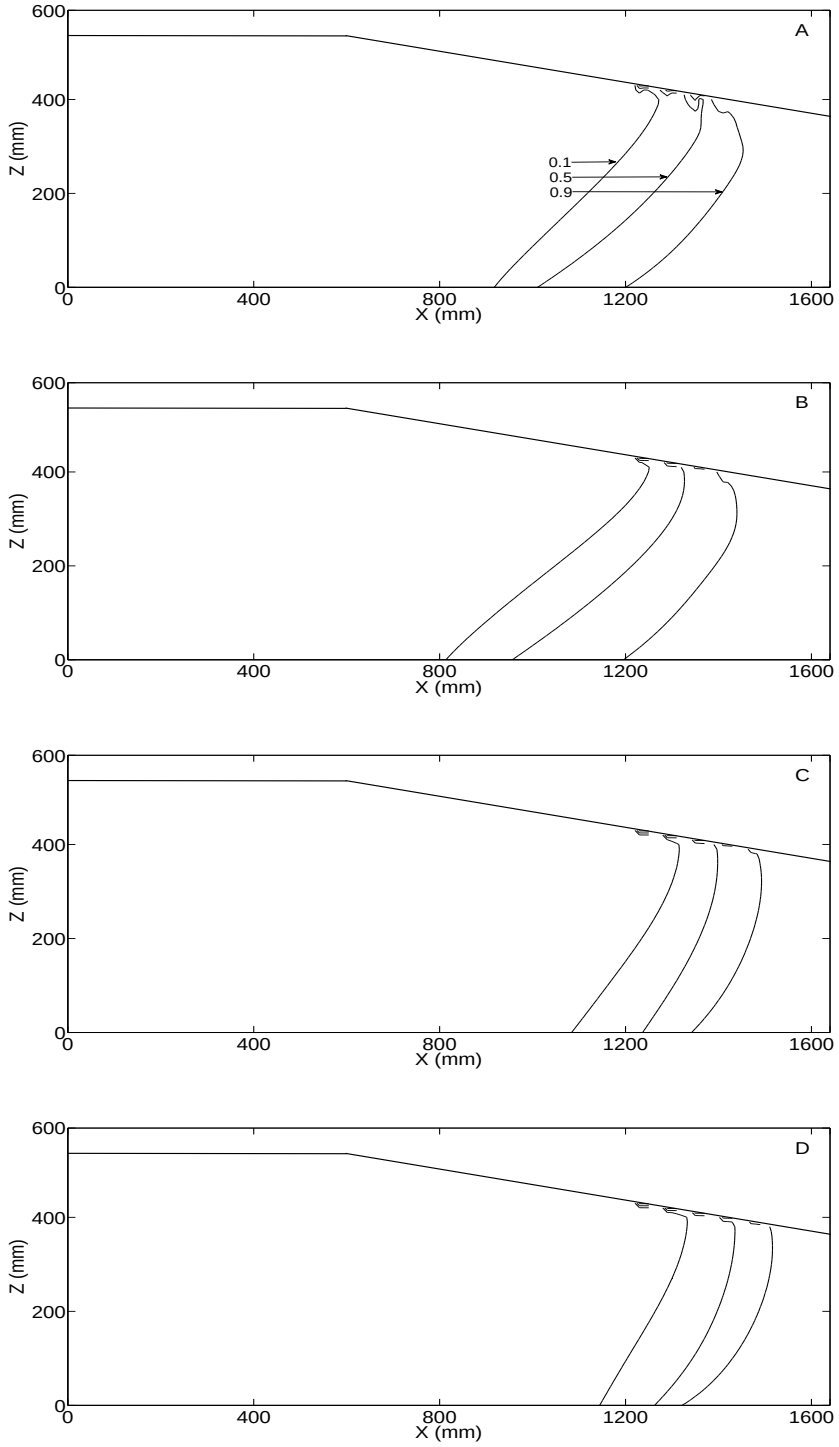

Figure 7. Mixing zones at different freshwater level stages within a fluctuation period with the consideration of both freshwater level fluctuation and kinetic mass transfer (tank scale model). (A) low level, (B) rising level, (C) high level, and (D) falling level.

Figure 8

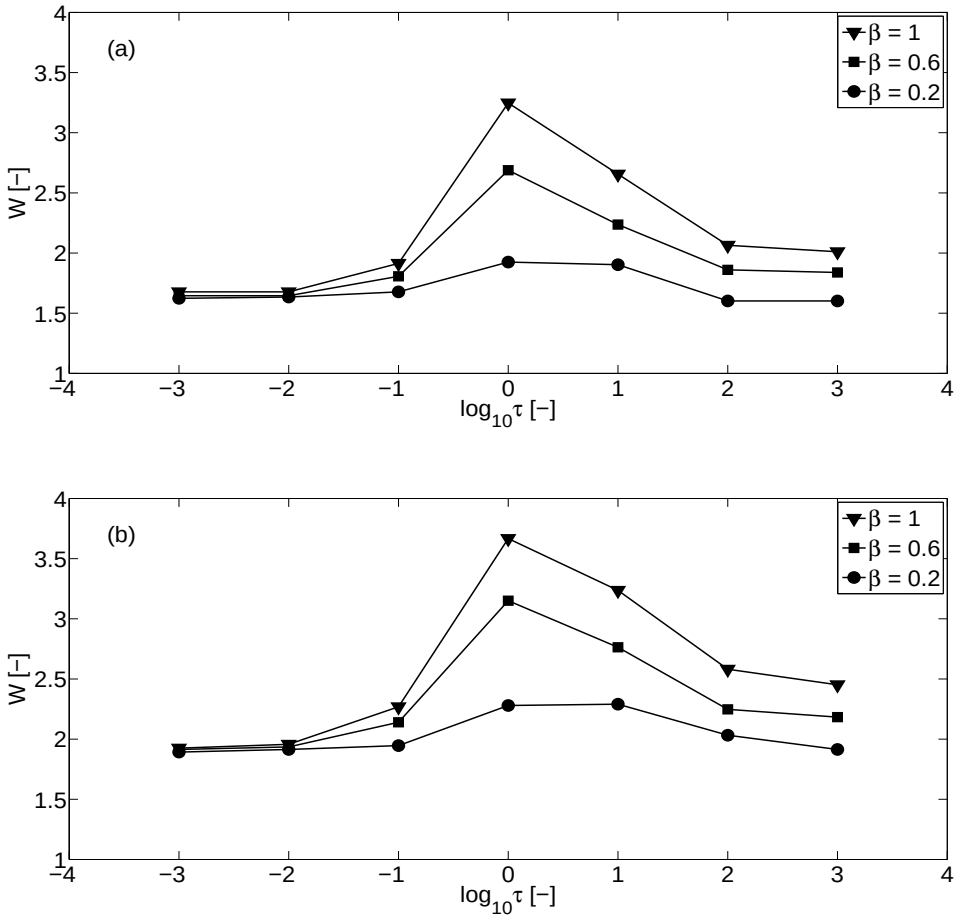

Figure 8. Sensitivity analysis for the effects of combining mass transfer and movement of the mixing zone which is caused by (a) seawater level fluctuation and (b) freshwater level fluctuation.

Figure 9

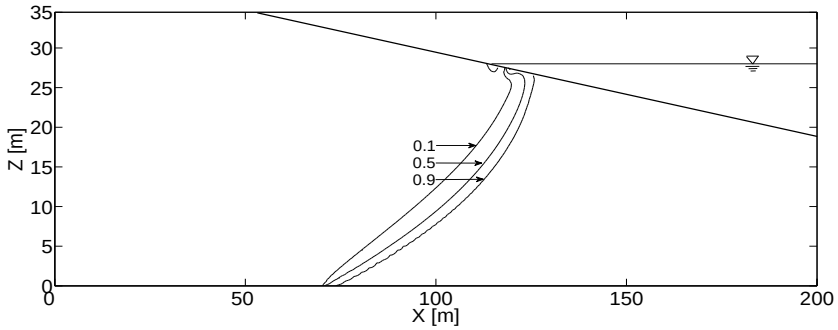

Figure 9. The variable-density mixing zone between the freshwater and seawater for steady-state conditions in the absence of water level fluctuation and kinetic mass transfer (field scale model). The solid lines are the contour lines of normalized salt concentrations.

Figure 10

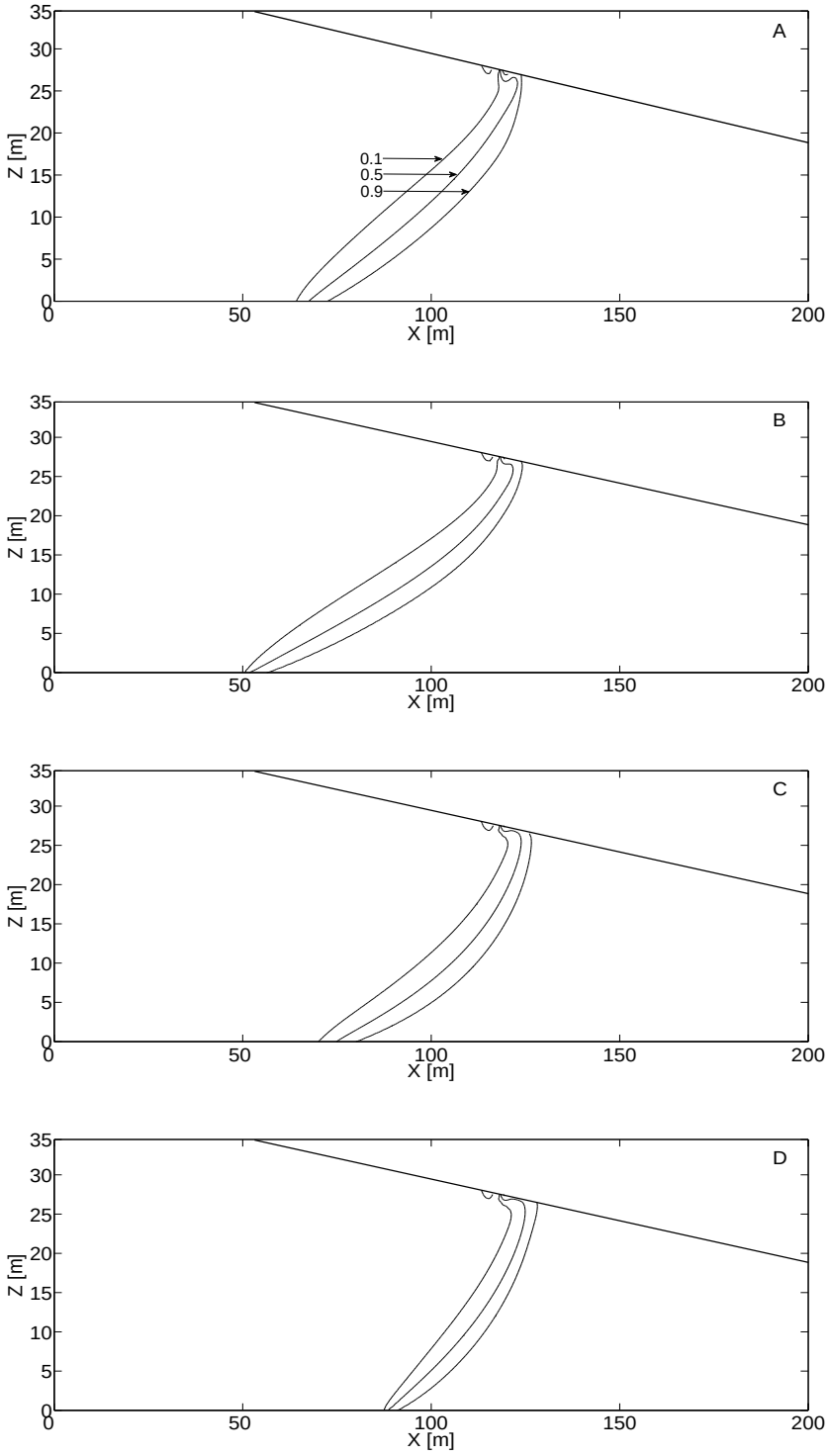

Figure 10. Mixing zones at different freshwater level stages within a fluctuation period with the consideration of freshwater level fluctuation alone (field scale model). (A) low level, (B) rising level, (C) high level, and (D) falling level.

Figure 11

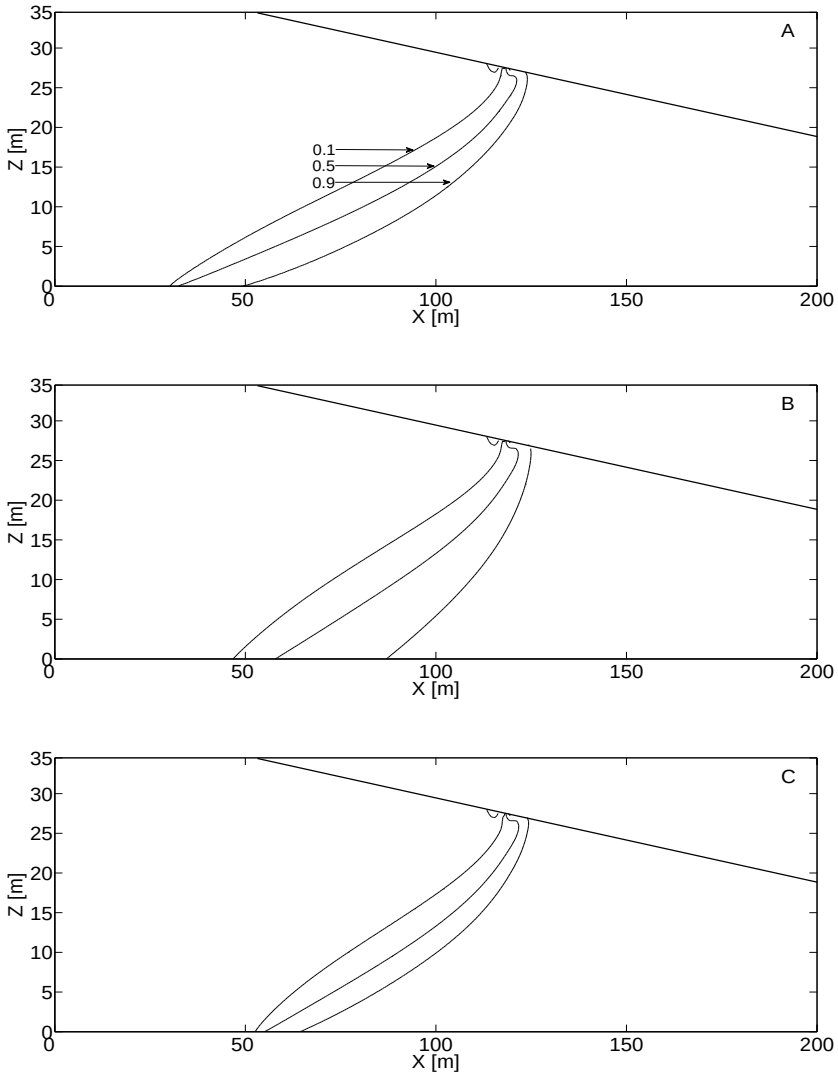

Figure 11. Mixing zones at the rising freshwater level stage with the consideration of both freshwater level fluctuation and kinetic mass transfer (field scale model), in which (A) $\tau = 10$, (B) $\tau = 1$, and (C) $\tau = 0.1$

Figure 12

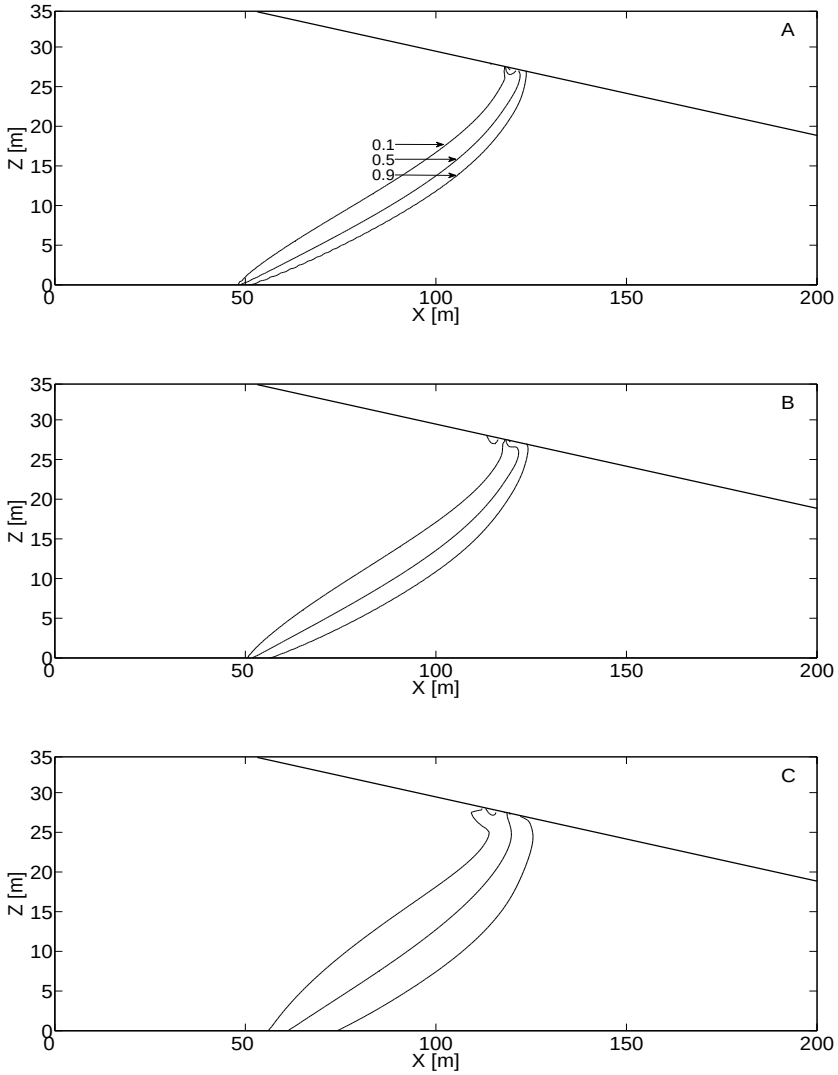

Figure 12. Mixing zones at the rising freshwater level stage with the consideration of the freshwater level fluctuation alone (field scale model), in which (A) α_L = 0.1 m and α_T = 0.01 m, (B) α_L = 0.5 m and α_T = 0.05 m, and (C) α_L = 2.5 m and α_T = 0.25 m.

Figure 13

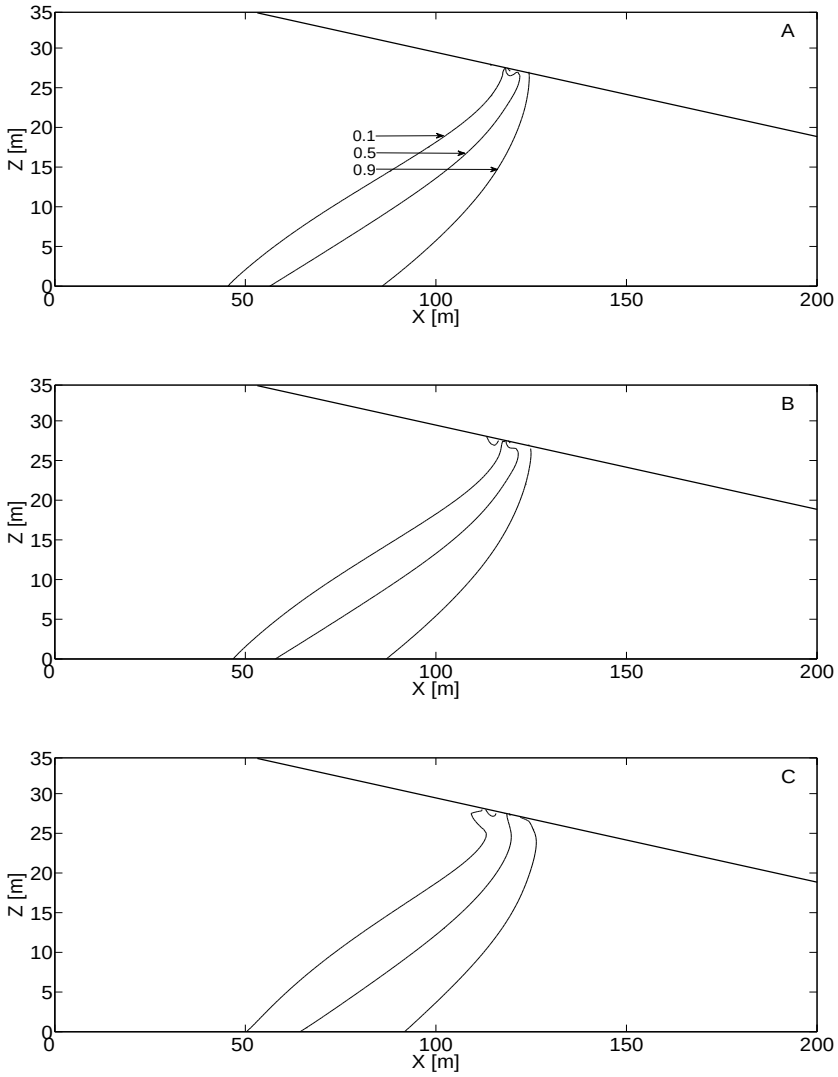

Figure 13. Mixing zones at the rising freshwater level stage with the consideration of both freshwater level fluctuation and kinetic mass transfer (field scale model), in which (A) α_L = 0.1 m and α_T = 0.01 m, (B) α_L = 0.5 m and α_T = 0.05 m, and (C) α_L = 2.5 m and α_T = 0.25 m.

Chap. 2

Dynamics of freshwater-seawater mixing zone development in dual-domain formations

Abstract

The dynamic response of freshwater-seawater mixing zones to seasonal freshwater level fluctuations and the presence of kinetic mass transfer between mobile and immobile domains has been analyzed using numerical models. Mixing zone enhancement is mainly controlled by the unsynchronized behavior of concentration distributions in the mobile and immobile domain. Such behavior is maximized at the aquifer bottom when the retention time scale in the immobile domain is comparable to the period of freshwater level fluctuations, resulting in a thicker mixing zone. Kinetic mass transfer may alter the time tag between periodic freshwater level fluctuations and the movement of the mixing zone, causing the expansion and contraction of the mixing zone. That is, the effect of mixing enhancement by kinetic mass transfer may be nonuniform in the mixing zone, and the mixing zone thickness may vary significantly within a period. By contrast, large dispersion coefficients may create thicker mixing zones, but may not cause such unsynchronized behavior and alter the time lags of different concentration contour lines, i.e., the mixing enhancement is rather uniform in the mixing zone. The dynamics of mixing zone development is sensitive to the flow velocity, which is influenced by the hydraulic conductivity, amplitude of the freshwater level fluctuations, and the capacity ratio of kinetic mass transfer.

1 Introduction

The mixing zone developed at the freshwater-seawater interface is one of the most important features in complex coastal hydrogeologic systems [*Cooper et al.*, 1964]. Across the mixing zone, the salt concentration and fluid density vary between those of freshwater and seawater. The density gradient within the mixing zone causes the rise of diluted saltwater, overlaying seawater, and results in flow circulation as the seawater moves towards the mixing zone to replace the diluted saltwater. Understanding the dynamics of mixing-zone development under various hydrogeologic conditions is essential for designing effective management strategies of groundwater resources and implementing sustainable stewardship of coastal and offshore environments.

The present research aims to numerically investigate the dynamic process of mixing-zone development in a dual-domain subsurface medium. Our previous study has found that kinetic mass transfer between relatively mobile fluids and fluids in stagnant pores combined with periodic movement of the mixing zone may significantly enhance mixing and result in a much thicker mixing zone, shown in Figure 1 [*Lu et al.*, 2009]. Kinetic mass transfer occurs in almost all fractured and porous media over various scales ranging from pore scale to field scale, and has significant implications on coastal groundwater management. For example, the aquifer storage and recovery (ASR) strategy may have a

low freshwater recovery ratio in a dual-domain coastal aquifer due to the mobilization of solutes initially residing in immobile domains [*Eastwood and Stanfield*, 2001; *Culkin et al.*, 2008]. Prior to our finding, thick mixing zones were usually characterized by large dispersion coefficients or assuming highly heterogeneous hydraulic conductivity fields, both of which may not be realistic [*Dagan*, 2003]. In addition, the recharge and tidal fluctuations may only slightly increase the thickness of the mixing zone in the absence of kinetic mass transfer [*Lu et al.*, 2009]. In this note, we conduct numerical experiments to further illustrate the dynamic process of mixing-zone enhancement for a periodically moving mixing zone in the presence of kinetic mass transfer. Specifically, the major questions that have been considered during this work are: how does the distribution of a mixing zone vary in response to variations of hydrogeologic conditions and how are such variations different from those by assuming large dispersion coefficients?

2 Numerical Method

A typical two-dimensional domain (see Figure 1) is set up to represent a cross-shore transect of an unconfined coastal aquifer with a length of 200m, a thickness of 35m, and a beach slope of 0.1, similar to previously reported numerical experiments [*Michael et al.*, 2005; *Robinson et al.*, 2006, 2007; *Lu et al.*, 2009]. For this domain, a base model is first built by defining the following hydrogeologic conditions. The aquifer is isotropic and homogeneous with both mobile and immobile porosities being 0.2. The value of the hydraulic conductivity K is 30m/d. The longitudinal and transverse dispersivity are 0.5m and 0.05m, respectively. Seasonal freshwater level fluctuations are imposed at the landward boundary by defining a triangular, periodic hydraulic head variation with the amplitude A=1m and the period T=360d. The use of the triangular function instead of a sinusoid function is to minimize the pressure periods required to reproduce the periodic function [*Zhang et al.*, 2001; *Brovelli et al.*, 2007]. The first-order mass transfer rate coefficient is $0.0028 d^{-1}$, which implies a retention time scale in the immobile domain, defined as the reciprocal of the rate coefficient, equal to the period of freshwater fluctuations. At the seaward boundary, constant hydraulic head and salt concentration are assigned because tidal activities have a much shorter period and may hardly cause the movement of the mixing zone in a large-scale simulation [*Cartwright et al.*, 2004; *Michael et al.*, 2005]. The mean hydraulic gradient between the landward and seaward boundary is 0.005. The upper boundary in the aquifer is phreatic surface with negligible groundwater recharge, and the bottom is a no-flow boundary.

A miscible fluid model with coupled flow and transport models is applied to simulate the mixing zone development in a dual-domain coastal aquifer. Transport processes include advection, dispersion, and a first-order kinetic mass transfer between the mobile and immobile domain. Flow and transport is coupled by a linear relationship between density and concentration in the mobile domain. The density-dependent groundwater flow code SEAWAT-2000 [*Langevin et al.*, 2003] is used to simulate the groundwater flow and salt transport problem described above. The entire domain is divided into two zones: an ocean zone and an aquifer zone, which are separated by the slanted beach. A high hydraulic conductivity (10^3m/d), an effective porosity $n_e = 1$, and a constant saltwater concentration of $35 kg/m^3$ are assigned to the ocean zone, and a horizontal strip of cells

are added on the tope of the ocean surface to reproduce the flat surface of the ocean [*Brovelli et al.*, 2007; *Robinson et al.*, 2007]. The entire domain is discretized into a uniform grid with a cell size of 0.5m×0.5m, yielding 28000 cells in total. This grid spacing corresponds to a local Peclet number of 1.

The following numerical experiments are conducted: (1) steady-state simulations for the base model with and without mass transfer; (2) transient simulations for the base model with periodic freshwater level fluctuations; and (3) transient simulations by varying a series of parameters, including hydraulic conductivity, dispersion coefficients, amplitude of freshwater fluctuations, and mass transfer coefficients. All transient simulations start from steady-state simulations, and terminate until the salt concentration distributions reaching a dynamic equilibrium state, i.e., the computation duration is sufficiently long so that the tolerance of the maximum concentration variation is satisfied when doubling the computation periods. For simplicity, we use three normalized salt concentration contour lines, 0.1, 0.5 and 0.9, to describe the movement and distribution of the mixing zone.

3 Results and Discussion

Mixing of freshwater and seawater is enhanced primarily due to the unsynchronized behavior of concentrations in the mobile and immobile domain. Two mixing zones may be defined in a dual-domain medium: one in the mobile domain, and the other in the immobile domain. There is an overlap between these two mixing zones, but they do not exactly coincide. The non-equilibrium concentrations in the mobile and immobile domain create the driving force for mass transfer and enhance mixing.

Figure 2 illustrates this process within one period by analyzing the concentration profiles at three points, (70, 0), (90, 0), and (110, 0), all of which are located at the aquifer bottom (Figure 1), where the mixing enhancement is the most significant. At the beginning of the period, non-equilibrium concentrations in the mobile and immobile domains drive mass transfer from the immobile domain to the mobile domain, which result in slowly increasing mobile concentrations and slowly decreasing immobile concentrations. With the decrease of the freshwater level, significant landward movement of the mixing zone causes a fast increasing concentration in the mobile domain, which results in a fast increasing concentration in the immobile domain due to enhanced mass transfer driving forces. Maximum concentrations in the mobile domain occur in the second quarter. After that, the mobile concentration gradually decreases as a result of mass transfer, while the immobile concentration keeps rising until these two become equal. When the hydraulic gradient is reversed as a result of the rise of the freshwater level, seaward movement of the mixing zone causes significant dilution and a fast decreasing mobile concentration. The immobile concentration then decreases due to the reversed mass transfer process. The point at (110, 0), the closest point to the seaward boundary, has the longest period for salt mass transferred from the mobile domain to the immobile domain because the influence by seawater intrusion is more significant than that by freshwater dilution. Contrarily, the point at (70, 0) has the shortest period of mass transfer from the mobile domain to the immobile domain because it is easier to be diluted by the freshwater with the movement of the mixing zone.

Figure 3 illustrates the impacts of hydrogeologic conditions on the dynamics of the mixing zone development by the temporal and spatial distributions of three concentration contour lines, 0.1, 0.5 and 0.9.

Panel A shows the base model results: (1) the movement of different contour lines in response to freshwater fluctuations is unsynchronized due to kinetic mass transfer, resulting in significantly varying moving ranges for different contour lines, by a factor of 4; and (2) a time lag exists between freshwater level fluctuations and the movement of the mixing zone.

Panel B shows that the mixing zone in the case with larger dispersivities (B2) is thicker than that with smaller dispersivities (B1) in the absence of kinetic mass transfer. However, the enhanced thickness of the mixing zone is nearly uniform within a period for both cases without mass transfer. This indicates synchronized behavior for different contour lines in response to freshwater fluctuations, resulting in similar moving ranges for different contour lines. In specific, the 0.5 contour line remains almost at the middle of the mixing zone for the cases without mass transfer, but approaches the 0.1 contour line when the mixing zone expands and the 0.9 contour line when the mixing zone shrinks for the case with mass transfer. Because the freshwater level drops from the mean level at the beginning of a period, one may expect that the maximum landward movement of the mixing zone occurs at the end of the second quarter when the freshwater level rises to the mean level from the lowest level, which implies a three-month time lag between the freshwater level variation and the mixing zone movement. With the consideration of mass transfer, this time lag becomes shorter than a quarter, i.e., the maximum landward movement of the mixing zone occurs within the second quarter. *Michael et al.* [2005] identified a time lag between the seasonal freshwater level fluctuations and the submarine groundwater discharge rate in the absence of mass transfer. Our analysis indicates that the kinetic mass transfer may alter such time lags. In addition, the cases without mass transfer show almost synchronized time lags for different contour lines, while the case with mass transfer shows significant discrepancies in time lags for different concentration contour lines: the 0.9 contour line has the shortest time lag while the 0.1 contour line the longest, resulting in the expansion of the mixing zone. Likewise, similar time lag behavior and movement discrepancies of contour lines are found in the fourth quarter for the seaward movement of the mixing zone, resulting in the contraction of the mixing zone.

Panel C in Figure 3 shows the mixing zone distributions for different hydraulic conductivities: 10 m/d, 30 m/d (base model), and 50 m/d. It is shown that higher hydraulic conductivity causes larger maximum and smaller minimum mixing zone thickness and more unsynchronized responses of various concentration contour lines. Mixing enhanced by mass transfer causes more significantly non-equilibrium concentrations between the mobile and immobile domain for faster flow due to enhanced time scale discrepancies between mass transfer and advection. In addition, higher hydraulic conductivities lead to larger landward and seaward movement. The impact of the amplitude of freshwater level fluctuation is similar to that of the hydraulic conductivity because variations of the amplitude essentially change the hydraulic gradient and the flow velocity. Furthermore, given a constant total porosity, altering capacity ratio,

the ratio between the immobile and mobile porosity, yields different effective mobile porosities and different flow velocities. Thus, the impact of the capacity ratio is also similar to that of hydraulic conductivity and amplitude of freshwater fluctuations.

Panel D in Figure 3 shows the impacts of the first-order mass transfer coefficient. The mass transfer rate coefficient controls how quickly mass is exchanged between the mobile and immobile domain. Our previous study found that when the retention time scale and the period of freshwater level fluctuations become comparable, the mixing-zone thickness is maximized [*Lu et al.*, 2009]. Three time scale ratios are considered: 0.01, 1(base model) and 100. It is shown that narrower mixing zones are developed for the ratios 0.01 and 100, compared with the ratio 1, and their unsynchronized time-lag behavior of the contour lines is similar to the case without kinetic mass transfer. Actually, mass transfer models with very small and large mass transfer rate coefficients may be simplified to a classical advective-dispersive transport problem. For a small time scale ratio, i.e., the mass transfer is approximately equilibrium, the transport equation may be simplified by including a retardation factor. Thus, D1 also shows smaller displacements of the landward and seaward movement of the mixing zone. By contrast, for a large time scale ratio, i.e., the mass transfer is slow, the mass transfer between the mobile and immobile domains may be negligible and the entire system behaves approximately like a single-domain system with the effective porosity approaching the mobile porosity. As a consequence, the decreased porosity effectively speeds up the flow, resulting in a larger moving range of the mixing zone (see D2).

4 Conclusion

Our numerical experiments show that mixing enhancement in a dual-domain coastal aquifer is mainly controlled by the unsynchronized behavior of concentration distributions in the mobile and immobile domain. Such behavior is maximized at the aquifer bottom when the retention time scale in the immobile domain is comparable to the period of freshwater level fluctuations, resulting in nonuniform moving ranges of different concentration contour lines, nonuniform mixing enhancement in the mixing zone, and significantly varying mixing zone thickness during a period. A time lag exists between the freshwater fluctuations and the movement of the mixing zone. This time tag may be altered by kinetic mass transfer. By contrast, large dispersion coefficients may create thicker mixing zones, but may not cause the unsynchronized behavior and alter the time lags of different concentration contour lines, i.e., the mixing enhancement is rather uniform in the mixing zone. The dynamics of mixing zone development is sensitive to the flow velocity, which is influenced by the hydraulic conductivity, amplitude of the freshwater level fluctuations, and the capacity ratio of mass transfer. These findings provide useful insights for understanding the mechanisms responsible for thick mixing zones and identifying key transport processes in coastal aquifers. Field data collection and analysis is underway for verifying these numerical results.

Acknowledgements

This research was sponsored by the National Institutes of Water Resources (NIWR) and U.S. Geological Survey (USGS) under project ID 2007GA165G.

Reference

Brovelli, A., X. Mao, D.A. Barry (2007), Numerical modeling of tidal influence on density-dependent contaminant transport, *Water Resour. Res.*, *43*, W10426, doi:10.1029/2006WR005173.

Cartwright, N., L. Li, and P. Nielsen (2004), Response of the salt-freshwater interface in a coastal aquifer to a wave-induced groundwater pulse: field observations and modeling, *Adv. Water Res.*, *27*, 297-303.

Cooper, H.H., F.A. Kohout, H.R. Henry, and R.E. Glover (1964), Sea water in coastal aquifers, U.S. Geological Water-Supply Paper, 1613-C.

Culkin, S.L., K. Singha, and F.D. Day-Lewis (2008), Implications of rate-limited mass transfer for aquifer storage and recovery, *Ground Water*, *46*, 591-605.

Dagan, G. (2006), Transverse mixing at freshwater saltwater interfaces: An unresolved issue, First International Joint Salt Water Intrusion Conference - Tutorials, Cagliari, Italy.

Eastwood, J.C., and P.J. Stanfield (2001), Key success factors in an ASR scheme, *Q. J. Eng. Geol. Hydrogeol.*, *34*, 399-409.

Langevin, C.D., W.B. Shoemaker, W. Guo (2003), Modflow-2000, The U.S. Geological Survey modular ground-water flow model Documentation of the Seawat-2000 version with the variable density flow process (VDF) and the integrated MT3DMS transport process (IMT), U.S. Geol. Surv. Open File Rep., 03-426.

Lu, C., P.K. Kitanidis, and J. Luo (2009), Effects of kinetic mass transfer and transient flow conditions on widening mixing zones in coastal aquifers, *Water Resour. Res.*, *45*, W12402, doi:10.1029/2008WR007643.

Michael, H.A., A.E. Mulligan, and C.F. Harvey (2005), Seasonal oscillations in water exchange between aquifers and the coastal ocean, *Nature*, *436*, 1145-1148.

Robinson, C., B. Gibbes, and L. Li (2006), Driving mechanisms for groundwater flow and salt transport in a subterranean estuary, *Geophys. Res. Lett.*, *33*, L03402, doi:10.1029/2005GL025247.

Robinson, C., L. Li, and H. Prommer (2007), Tide-induced recirculation across the aquifer-ocean interface, *Water Resour. Res.*, *43*, W07428, doi:10.1029/2006WR005679.

Zhang, Q., R.E. Volker, and D.A. Lockington (2001), Influence of seaward boundary condition on contaminant transport in unconfined coastal aquifer, *J. Contam. Hydrol.*, *49*, 201 -- 215.

Figure Caption

Figure 1

A numerical simulation of freshwater-seawater mixing zone in an unconfined aquifer. (A) steady-state normalized concentration distribution in the absence of kinetic mass transfer; and (B) normalized concentration distribution of a transient simulation with kinetic mass transfer at the time event when the freshwater boundary (left boundary) equals the mean freshwater head. The thick black lines represent the coastal beach with a slope of 0.1. The mixing zones are characterized by three concentration contour lines normalized by the seawater salt concentration: 0.1, 0.5, and 0.9. The stars in (B) represent three observation points at the aquifer bottom.

Figure 2

Temporal profiles of concentrations in the mobile and immobile domain at three observation points: (70,0), (90,0), and (110,0) for the case with kinetic mass transfer and periodic freshwater fluctuations.

Figure 3

The dynamics of mixing zone development influenced by hydrogeologic conditions, including dispersion, hydraulic conductivity, and mass transfer rate coefficient. Temporal and spatial evolution of the mixing zone distribution is characterized by three normalized concentration contour lines at the aquifer bottom (left y-axis) corresponding to periodic freshwater fluctuations (right y-axis). Panel A is the base model with defined parameters: hydraulic conductivity 30m/d, first-order mass transfer rate coefficient $0.0028d^{-1}$, which corresponds to a unitary time scale ratio between the retention in the immobile domain and the period of freshwater fluctuations, and longitudinal and transverse dispersivities 0.5m and 0.05m, respectively. Panel B shows the impact of dispersion, in which B1 is the base model without kinetic mass transfer and B2 is the base model with larger dispersivities (2.5m and 0.25m) and without kinetic mass transfer. Panel C shows the impact of hydraulic conductivity, in which C1 is the base model with hydraulic conductivity 10m/d and C2 50m/d. Panel D shows the impact of mass transfer rate coefficient, in which D1 has a time scale ratio of 0.01 and D.

Figure 1

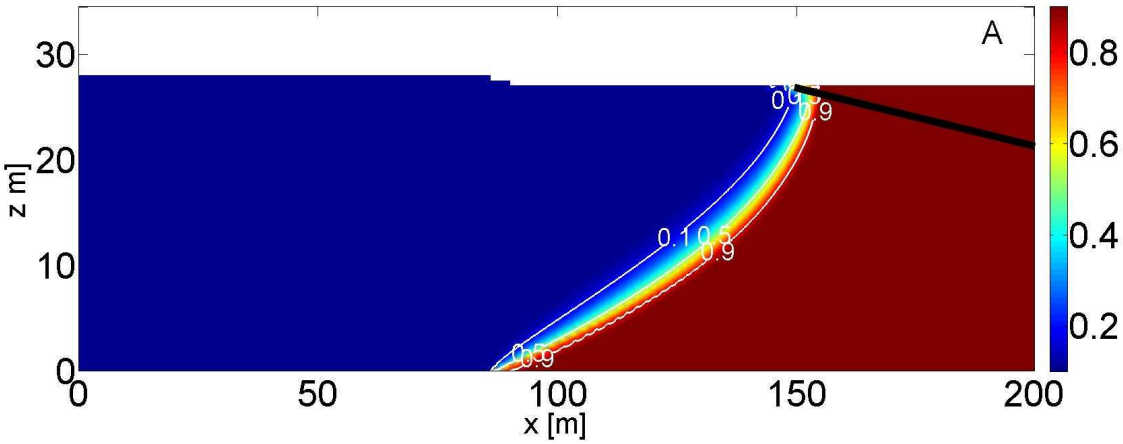

Figure 2

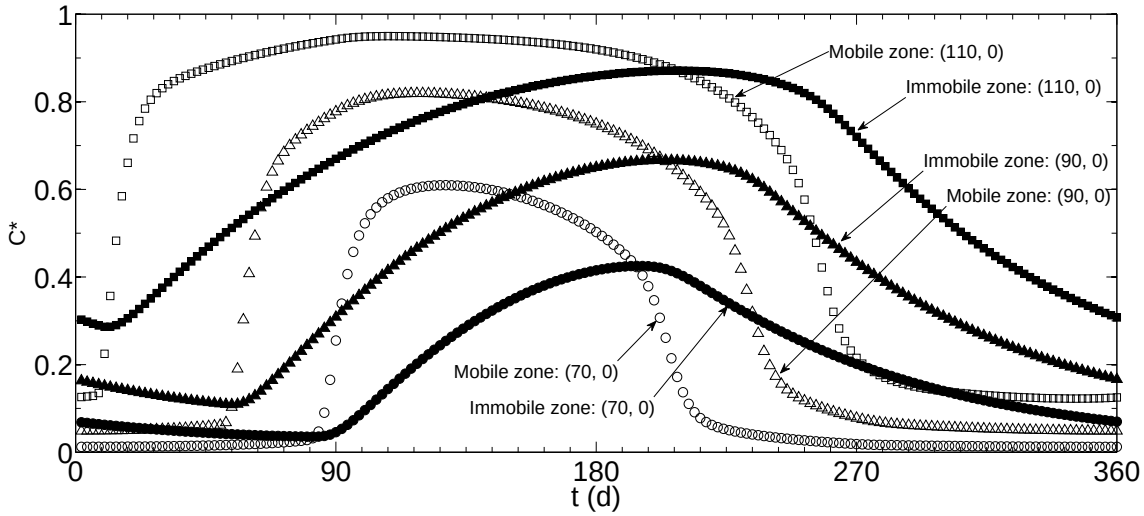
1
0.8
0.6
0.4
0.2
0
C*
0
90
180
270
360
t (d)
Mobile zone: (110, 0)
Immobile zone: (110, 0)
Immobile zone: (90, 0)
Mobile zone: (90, 0)
Mobile zone: (70, 0)
Immobile zone: (70, 0)

Figure 3

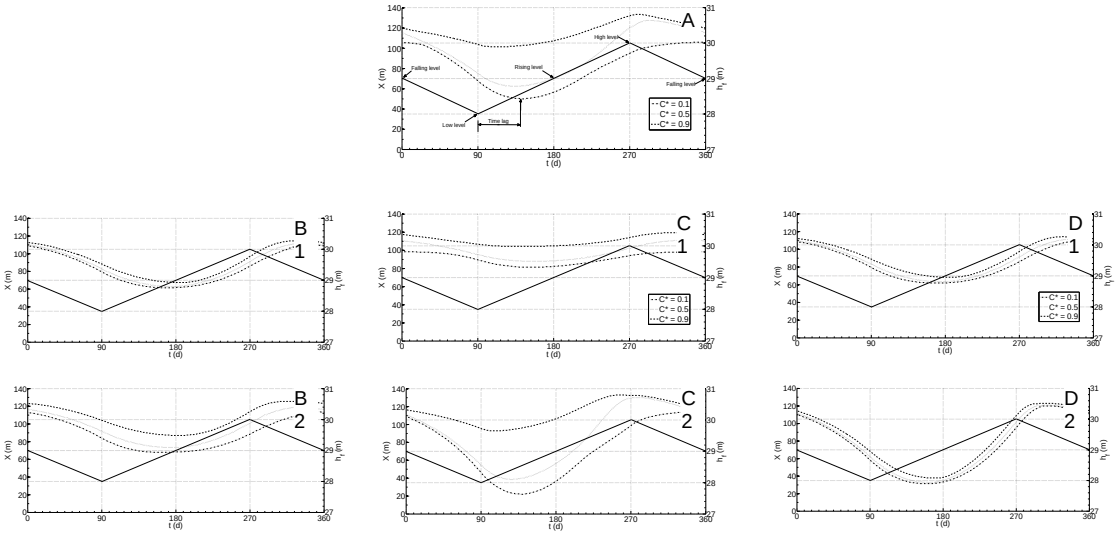
A
B 1
C 1
D 1
B 2
C 2
D 2
High level
Rising level
Falling level
Falling level
Low level
Time lag
C* = 0.1
C* = 0.5
C* = 0.9
X (m)
t (d)

Chap. 3

Boundary condition effects on estimating maximum groundwater withdrawal in coastal aquifers

Abstract

One of the most cost-effective strategies for preventing seawater intrusion in costal aquifers subject to groundwater withdrawal is to optimize well pumping rates by maximizing the water supply while avoiding seawater intrusion. Boundary conditions and the aquifer domain size have significant influences on simulating flow and concentration fields and estimating maximum pumping rates. In this study, an analytical solution is derived based on the potential flow theory for evaluating maximum groundwater pumping rates in a domain with a constant hydraulic head landward boundary, which can also represent coastal hydrogeologic systems containing a surface freshwater body. Comparing with the solution for a constant recharge rate boundary, we find that (1) a constant hydraulic head boundary often yields significantly larger estimations of the maximum pumping rate than a constant recharge rate boundary for the pumping well located more closely to the landward boundary than the coastline, and the difference between these two boundary settings becomes more significant for lower potentials at the toe of saltwater wedge; and (2) when the domain size is five times greater than the distance between the well and the coastline, the effect of setting different landward boundary conditions is not significant. These findings can serve as a preliminary guidance for conducting numerical simulations and designing tank-scale laboratory experiments for studying groundwater withdrawal problems in coastal aquifers with minimized boundary condition effects.

1 Introduction

Groundwater is a vital resource providing water supplies for public potable water, agriculture and industry in coastal areas. To satisfy the increasing demand for freshwater, excessive groundwater withdrawals have upset the long established balance between freshwater and seawater potentials, causing encroachment of salty seawater into the freshwater aquifer, resulting in the well-known seawater intrusion problem (Bear, 1972). Once seawater has intruded into the coastal aquifer to an intolerable distance, the deterioration of the groundwater quality significantly threatens the sustainability of coastal communities and further development of coastal areas. Restoration of groundwater quality in the invaded zones is generally an expensive and ineffective proposition (Bear et al., 1999). Therefore, prevention is considered the most effective approach from the perspective of implementing an integrative groundwater management strategy in coastal areas. One of the most cost-effective prevention strategies is to optimize withdrawal rates, i.e., the management of groundwater extraction in coastal aquifers to maximize the water supply while avoiding seawater intrusion (Shamir et al., 1984; Willis and Finney, 1988; Finney et al., 1992; Hallaji and Yazicigil, 1996; Emch

and Yeh, 1998; Das and Datta, 1999a, 1999b; Cheng et al., 2000; Park and Aral, 2004; Mantoglou et al., 2004; Bhattacharjya and Datta, 2005).

Two types of numerical models have been used in estimating maximum groundwater withdrawal rates in coastal aquifers: the sharp-interface approximation and the miscible flow transport model. By assuming a steady flow in a hydrologically homogeneous porous medium, as well as a sharp interface between the freshwater and the seawater, analytical solutions can be reached for simplified conceptual models by applying potential-flow theories (e.g., Bear and Dagan, 1964; Ozturk, 1970; Collins and Gelhar, 1971; Hunt, 1985; Strack, 1989; Huppert and Woods, 1995; Dagan and Zeitoun, 1998; Naji et al., 1998; Sakr, 1999; kacimov and Obnosov, 2001; Bakker, 2000 and 2006; Kacimov and Sherif, 2006). By contrast, the miscible flow modeling approach is more realistic in that it contains a system of variable-density flow equation and the advection-dispersion equation (e.g., Henry, 1964; Voss and Souza, 1987; Galeati et al., 1992; Fan and Kahawita, 1994; Croucher and O'Sullivan, 1995; Xue et al., 1995; Kolditz et al., 1998; Ackerer et al., 1999; Paniconi et al., 2001; Diersch and Kolditz, 2002; Gotovac et al., 2003; Simpson and Clement, 2003; Simmons, 2005; Langevin and Guo, 2006). In this context, a variable-density mixing zone with a certain thickness, rather than a sharp interface, can be generated, consistent with field observations in coastal aquifers (Barlow, 2003, Cherry, 2006).

Solutions to both sharp-interface and miscible flow models are influenced by boundary condition settings. For a steady state analysis, constant hydraulic heads are usually imposed at the seaward boundary (e.g., Cheng et al., 2000, Park and Aral, 2004), while there are two types of boundary conditions, constant hydraulic head and constant recharge rate, available at the landward boundary (Werner and Simmons, 2009). Constant recharge rate conditions are often used by sharp-interface models, which implicitly assume an infinite large simulation domain (Strack, 1976, 1989; Cheng et al., 2000). By contrast, miscible flow models generally define a sufficiently large domain so that the flow field is not affected by the boundary condition settings. However, no general solution has been given regarding the domain size required for eliminating the boundary condition effects. Moreover, this information is particularly useful for designing tank-scale laboratory experiments to investigate upconing problems, which are sensitive to boundary conditions due to limited equipment size. The present work aims to resolve this issue by investigating the effects of different boundary conditions on estimating the maximum groundwater withdrawal rates from an extraction well in coastal aquifers. In specific, we first derive an analytical solution for the flow field and the maximum groundwater withdrawal rate in a homogeneous domain with constant hydraulic head landward boundary conditions. The derived solutions are then compared with those obtained in a domain with constant recharge rate boundaries to evaluate the effects of different boundary conditions and the domain size required for minimizing the solution variations. The sharp-interface model and potential-flow theories are used to derive the analytical solution and conduct the comparison, which can provide fundamental understanding of the relationships between the rate of freshwater flow or the water table elevations in the vicinity of the coast and the length of the intruding seawater wedge. Finally, a miscible flow transport case is presented to validate the derived results.

2 Mathematical Models

Conceptual Model

Consider a fully-penetrating pumping well in a homogeneous, isotropic costal aquifer. Fig. 1 shows the plan view and cross section of the conceptual model in an unconfined aquifer. The freshwater area within the aquifer is bounded above by a phreatic surface and below by an interface that separates the freshwater from seawater at rest (Zone 1) and the impermeable bed (Zone 2). The horizontal bed of the aquifer is at depth D below the mean sea level. The distance between the phreatic surface and the impermeable bed is h_f. The interface is located at a distance d below the mean sea level. A pumping well is located at a distance x_w away from the coastline with coordinates (x_w, 0) and a pumping rate, Q. q_{x0} is a uniform flow rate of the regional flow to the sea when the well is not present. A similar conceptual model can be developed for a confined aquifer with a uniform aquifer thickness, B.

Two types of boundary conditions are considered for the landward boundary: constant recharge rate q_{x0} and constant hydraulic head. Analytical solutions have bee derived for the former boundary condition (Strack, 1989), which implicitly assumes an infinite domain. For the latter, we assume that a constant head boundary is located at a distance of L from the coastline. This boundary condition setting can also describes coastal hydrogeologic systems containing a surface freshwater body, such as rivers, streams or canals, in coastal regions (Kondolf and Matthews, 1986; Sahoo and Smith, 2009). Such water bodies, especially those parallel to the coastal line, may serve as a barrier for preventing seawater intrusion. For example, at Great Yarmouth, UK, the river Yare flows parallel to the coastal line for several miles with most of the town located on the east side of the river, sandwiched between the sea and the Yare (http://www.thingstodoinnorfolk.co.uk/norfolk/broads/gtyarmouth/southquay/). Bailey and Lear (2006) also indicated that it is very common that a river in coastal areas runs approximately parallel to the sea for some distance before joining it. Therefore, under these field conditions, it is necessary to define a constant hydraulic head boundary for a pumping well located between the sea and the surface water body, and it is important to know how the surface water body affects the maximum allowed groundwater pumping rate. This scenario is also similar to the case with a pumping well located between two parallel rivers (Wilson, 1993; Intaraprasong and Zhan, 2007). However, the seawater-freshwater interface is considered and a constraint that saltwater is not allowed to be extracted must be applied for preventing upconing and seawater intrusion.

Potential-Flow Theory

To apply the potential-flow theory to solve the flow field (Strack, 1976), several assumptions are made: (1) the seawater-freshwater interface is a sharp interface instead of a variable-density mixing zone; (2) the sea level is constant; (3) the Dupuit-Forchheimer assumption is applied to neglect the vertical flow; (4) the Ghyben-Herzberg formula is employed to locate the interface position; and (5) the aquifer storativity is ignored such

that the governing equation is time independent. Based on these assumptions, a potential, ϕ, can be defined for Zones 1 and 2 as (Strack, 1976; Cheng et al., 2000):

Unconfined:

Zone 1: $\phi = \frac{\varepsilon}{2(\varepsilon - 1)}\left(h_f - D\right)^2$

(1a)

Zone 2: $\phi = \frac{1}{2}\left(h_f^2 - \varepsilon D^2\right)$

(1b)

Confined:

Zone 1: $\phi = \frac{1}{2(\varepsilon - 1)}\left(h_f + (\varepsilon - 1)B - \varepsilon D\right)^2$

(2a)

Zone 2: $\phi = Bh_f + \frac{1}{2}(\varepsilon - 1)B^2 - \varepsilon BD$

(2b)

where ε is the seawater and freshwater density ratio (ρ_s / ρ_f). The sharp interface location can be evaluated based on both the potentials in zones 1 and 2 satisfying the Laplace's equation $\nabla \phi^2 = 0$ and the condition of continuity of flow (Strack, 1989). The potential at the toe of saltwater wedge is (Cheng et al., 2000):

Unconfined: $\phi_{toe} = \frac{\varepsilon(\varepsilon - 1)}{2} D^2$

(3)

Confined: $\phi_{toe} = \frac{(\varepsilon - 1)}{2} B^2$

(4)

On the other hand, the freshwater discharge potential for a pumping well located between the sea and the constant freshwater head boundary defined in the conceptual model can be evaluated by superposing an infinite series of imaginary wells (Intaraprasong and Zhan, 2007):

$$\phi = \frac{q_{x0}}{K} x + \frac{Q}{4\pi K} \sum_{n=-\infty}^{\infty} \ln\left[\frac{\left(x - \left(x_w + 2nL\right)\right)^2 + y^2}{\left(x - \left(-x_w + 2nL\right)\right)^2 + y^2} \right]$$

(5)

where n are integers, K is hydraulic conductivity, and $q_{x0}x/K$ is the regional flow potential which reproduces the fixed hydraulic heads at the landward and seawater boundary. Calculating the summation term in Eq. (5) yields (Zhan, 1999):

$$\phi = \frac{q_{x0}}{K}x + \frac{Q}{4\pi K}\ln\left[\frac{\cosh(\pi y/L)-\cos(\pi(x-x_w)/L)}{\cosh(\pi y/L)-\cos(\pi(x+x_w)/L)}\right] \quad (6)$$

Thus, the coordinates of the toe position of saltwater wedge can be found by substituting Eqs. (3) and (4) into (6):

$$\phi_{toe} = \frac{q_{x0}}{K}x + \frac{Q}{4\pi K}\ln\left[\frac{\cosh(\pi y/L)-\cos(\pi(x-x_w)/L)}{\cosh(\pi y/L)-\cos(\pi(x+x_w)/L)}\right] \quad (7)$$

Maximum Pumping Rate

In water resources management, it is of practical interest to predict the maximum pumping rate for an installed well or to design the well location for required pumping rates. In cases where the saltwater does not reach the pumping well, the flow field in Zone 1 is a one-fluid flow system, while in cases with saltwater pumped by the well it becomes a two-fluid flow system. For the latter, the solution of Eq. (6) is not valid. The critical case between these two occurs when the stagnation point created by the pumping well and the toe position of saltwater wedge coincide (Strack, 1976). The seawater-freshwater interface in this critical case is unstable because an infinitesimal increase of the pumping rate may lead to saltwater upconing.

According to the discussion by Intaraprasong and Zhan (2007), there are three possible cases about the stagnation-point location: (1) one stagnation point located between the sea and the well with the same y-coordinate as the well; (2) one stagnation point located at the coastline; and (3) two stagnation points located at the coastline. The latter two represent seawater intrusion into the pumping well. Therefore, only the first case needs to be considered for determining the maximum pumping rate. To facilitate the interpretation of the analysis, the following dimensionless variables are defined:

$$x_w^* = \frac{x_w}{L},\ x_s^* = \frac{x_s}{L},\ Q^* = \frac{Q}{2q_{x0}L}$$

$$\phi_{toe}^* = \frac{\varepsilon(\varepsilon-1)}{2q_{x0}L}KD^2 \text{ (unconfined), and } \phi_{toe}^* = \frac{(\varepsilon-1)}{2q_{x0}L}KB^2 \text{ (confined)} \quad (8)$$

in which x_s is x-coordinate of the stagnation point, and x_w^*, x_s^*, Q^* and ϕ_{toe}^* are dimensionless parameters for the well location, stagnation point location, pumping rate, and potential at the toe. By transforming Eq. (6) into dimensionless formula, taking the

first derivative with respect to *x*, and setting it to be zero, the dimensionless *x*-coordinate of the stagnation point is given by:

$$x_s^* = \frac{1}{\pi}\cos^{-1}(\cos(\pi x_w^*) + Q^* \sin(\pi x_w^*)) \quad (9)$$

which can be expressed as

$$\cos(\pi x_s^*) = \cos(\pi x_w^*) + Q^* \sin(\pi x_w^*) \quad (10)$$

Eqs. (9) and (10) implicitly require that

$$-1 \le \cos(\pi x_w^*) + Q^* \sin(\pi x_w^*) \le 1 \quad (11)$$

Note $Q^* \sin(\pi x_w^*)$ is non-negative because Q^* is non-negative and $0 < x_w^* \le 1$. The monotonically decreasing property of cosine function within the range $[0, \pi]$ indicates that $x_s^* \le x_w^*$, i.e., the stagnation point only exists between the well and the sea.

Fig. 2 shows the position of the stagnation point as a function of the pumping rate and well location. Fig. 2a shows that for a given well location the stagnation point moves towards the sea as the pumping rate increases. A maximum pumping rate may be obtained for x_s^* approaching 0, i.e., the stagnation point reaches the costal line. Certainly, this pumping rate is not the maximum pumping rate allowed in the coastal aquifer because the stagnation point has passed the toe of saltwater wedge. The maximum allowed pumping rate should be less than this rate. Fig. 2b shows that for a given pumping rate the stagnation point moves with the pumping well toward the same direction. Similarly, the well location when x_s^* approaches 0 is not the desirable location to place a pumping well for a given pumping rate. The pumping well should be placed further away from the coastal line.

As discussed above, the critical pumping rate, i.e., the maximum pumping rate that does not cause seawater intrusion, can be evaluated when the stagnation point and the toe of saltwater wedge coincide. By substituting the stagnation point coordinate $(x_s^*, 0)$ given by Eq. (9) into Eq. (7), we obtain:

$$\phi_{toe}^* = \frac{1}{\pi}\cos^{-1}(\cos(\pi x_w^*) + Q_{\max}^* \sin(\pi x_w^*)) + \frac{Q_{\max}^*}{2\pi}\ln\left[\frac{1-\cos(\cos^{-1}(\cos(\pi x_w^*) + Q_{\max}^* \sin(\pi x_w^*)) - \pi x_w^*)}{1-\cos(\cos^{-1}(\cos(\pi x_w^*) + Q_{\max}^* \sin(\pi x_w^*)) + \pi x_w^*)}\right] \quad (12)$$

where $Q_{\max}^*$ is the dimensionless maximum pumping rate.

Eq. (12) is an implicit analytical solution for the maximum pumping rate, which is graphically shown in Fig. 3. Two conclusions can be drawn from Fig. 3: (1) with the increase of the potential at the toe, i.e., a larger vertical distance between the sea level and the aquifer bottom or a thicker aquifer, less water can be extracted from the pumping well because the potential increase results in landward movement of the toe position; and (2) with the increase of x_w^*, i.e., the pumping well is located further from the coastline, more water can be extracted from the pumping well as a result of landward movement of the stagnation point.

Boundary Condition Effects

In this section, we compare the solution for the case with a constant hydraulic head landward boundary derived in the previous section with the solution with a constant recharge rate landward boundary to investigate the effects of different boundary condition settings on estimating the maximum pumping rate in a coastal aquifer defined by the conceptual model. The essential difference between these two is that the constant recharge rate boundary implicitly assumes a sufficiently large aquifer domain so that only one imaginary well needs to be considered to create the seaward boundary. The implicit analytical solution for the maximum pumping rate is given by (Strack, 1976):

$$\phi_{toe}^* = x_w^* \left[\left(1 - \frac{2Q^*}{\pi x_w^*} \right)^{1/2} + \frac{Q^*}{\pi x_w^*} \ln \left[\frac{1 - \left(1 - \frac{2Q^*}{\pi x_w^*} \right)^{1/2}}{1 + \left(1 - \frac{2Q^*}{\pi x_w^*} \right)^{1/2}} \right] \right] \tag{13}$$

Fig. 3 compares the solutions given by Eqs. (12) and (13) for the two different boundary conditions. It clearly shows that the constant hydraulic head boundary often results in significantly enhanced maximum pumping rates for $x_w^* > 0.5$. The deviation becomes more pronounced for lower potentials at the toe of saltwater wedge. However, when $x_w^* < 0.2$, the differences between the two cases with different boundary conditions are not significant. These findings have very important implications for numerical and experimental endeavors for investigating groundwater withdrawal in coastal aquifers. For a fixed domain, the pumping well must be located at $x_w^* < 0.2$ in order to minimize the boundary condition effects. Otherwise, a constant hydraulic head boundary always predicts larger maximum pumping rates allowed for avoiding seawater intrusion than a constant discharge boundary. Similarly, for a fixed well location, the domain size must satisfy $L > 5x_w$ to minimize the boundary condition effects. These findings give experimentalists and modelers a preliminary guidance for designing tank-scale laboratory equipment and delineating a domain for numerical simulations for studying groundwater withdrawal in coastal aquifers with minimized boundary condition effects.

3 Numerical Validation

The findings regarding the boundary condition effects are validated in this section by a numerical field-scale case described by the miscible flow model. Consider a confined costal aquifer with a homogeneous, isotropic hydraulic conductivity K = 8 m/d and a uniform aquifer thickness B = 20 m. The width of the domain is set to be 1000 m, a sufficiently large size for eliminating boundary condition effects at y direction. The longitudinal and transverse dispersivities are assumed to be 0.5 m and 0.05 m, respectively. The effective porosity is 0.4. The density of seawater and freshwater are 1000 kg/m^3 and 1025 kg/m^3, respectively, which corresponds to a salt concentration C_s = 35 kg/m^3. A pumping well is located at 200m from the coastline. For the purpose of investigating the effects of different boundary conditions and domain size on evaluating maximum groundwater withdrawal, two domain lengths L are considered: 400 m and 1000 m. For each domain length, we consider two types of boundary conditions, i.e., constant hydraulic head and constant recharge rate at the landward boundary, both of which represent a constant hydraulic gradient J = 0.005 and q_{x0} = 0.8 m^2/d. The pumping rate at the well in all simulations are 500 m^3/d . Table 1 summarizes the hydrogeologic parameters for this case. The numerical model is solved by the density-dependent groundwater flow code SEAWAT-2000 implemented in a graphic user interface software Groundwater Vista 5.20 developed for 3D groundwater flow and transport modeling.

Figs. 4 and 5 show the steady-state simulation results of the hydraulic head and concentration distributions for the cases with two different domain sizes. It is obvious that, for the domain with L = 400 m, namely, $x_w^* = 0.5$, the hydraulic head and concentration distributions for the two boundary condition settings are significantly different, while for the domain with L = 1000 m, namely, $x_w^* = 0.2$, the simulation results for both hydraulic head and concentration distributions are almost the same as predicted by previous findings. In fact, Fig. 4 shows that for the domain size of L = 400m the predefined pumping rate causes seawater intrusion for the constant recharge rate boundary (see Fig. 4c), while it is still safe for the constant hydraulic head boundary (see Fig. 4d). This is consistent to the finding that the constant hydraulic head boundary often yields higher maximum pumping rates (Fig. 3). By contrast, by increasing the domain size to L = 1000m, Fig. 5 shows that the saltwater wedge has penetrated into the pumping well for both boundary cases. Although there are still small deviations between these two because our findings are based on the sharp-interface approximation and the simulations are based on the miscible flow model, the result definitely have great potential implications in numerical and experimental studies on groundwater withdrawal in coastal aquifers.

4 Conclusion

Optimization of groundwater withdrawal to avoid upconig and seawater intrusion is the most effective prevention strategy for groundwater resources management in coastal aquifers. Boundary conditions and the system domain size have significant influences on simulating the flow and concentration fields and estimating the maximum pumping rates. In this study, we apply the potential-flow theory to investigate the effects of constant hydraulic head and constant recharge rate boundary conditions at the

landward boundary. An analytical solution is derived for the flow field and the maximum groundwater withdrawal rate in a domain with a constant hydraulic head landward boundary condition, which is also capable of simulating coastal hydrogeologic systems involving a surface freshwater body. Comparing with the solution for a constant recharge rate boundary, we find that (1) a constant hydraulic head boundary often yields significantly larger maximum pumping rates for $x_w^* > 0.5$, where x_w^* is a dimensionless well location normalized by the domain length, than a constant recharge boundary condition, and the difference becomes more significant for lower potentials at the toe of saltwater wedge; and (2) for $x_w^* < 0.2$, the differences between the two boundary cases are not significant. These findings can serve as a preliminary guidance for conducting numerical simulations and designing tank-scale laboratory experiments for studying groundwater withdrawal problems in coastal aquifers. One may use the findings to choose the domain size and well locations to minimize the boundary condition effects. For example, in laboratory experiments, it is more convenient to control a constant hydraulic head boundary than a constant recharge rate boundary. By locating the well at $x_w^* < 0.2$, the boundary condition effect may be minimized and there is no need to construct an expensive, large tank-scale equipment. Similarly, with a given well location, modelers may only need to define a domain size satisfying $L > 5x_w$ instead of a much larger simulation domain to minimize the boundary condition effects.

Acknowledgements

This research was sponsored by U.S. Geological Survey (USGS) under project ID 2007GA165G. This article has not been reviewed by the agency, and no official endorsement should be inferred. Any opinions, findings, and conclusions or recommendations expressed in this material are those of the authors and do not necessarily reflect the views of USGS.

References

Ackerer, P., Younes, A., Mose, R., 1999. Modeling variable density flow and solute transport in porous medium: 1. Numerical model and verification. Transport in Porous Media 35 (3), 345-373.

Bear, J., 1972. Dynamics of Fluids in Porous Media. American Elsevier, New York.

Bakker, M., 2000. The size of the freshwater zone below an elongated island with infiltration. Water Resources Research 36, 109-117.

Barlow, P.M., 2003. Ground water in freshwater-saltwater environments of the Atlantic coast: U.S. Geological Survey Circular 1262.

Bakker, M., 2006. Analytical solution for interface flow in combined confined and semi-confined, coastal aquifers. Advances in Water Resources 29 (3), 417-425.

Bear, J., Dagan, G., 1964. Some exact solutions of interface problems by means of hodograph method. Journal of Geophysical Research 69 (8), 1563-1572.

Bhattacharjya, R., Datta, B., 2005. Optimal management of coastal aquifers using linked simulation optimization approach. Water Resources Management 19 (3), 295-320.

Bailey, T.R., Lear, C.H., 2006. Testing the effect of carbonate saturation on the Sr/Ca of biogenic aragonite: A case study from the River Ehen, Cumbria, UK. Geochemistry Geophysics Geosystems 7, Q03019.

Bear, J., Cheng, A.H.D., Sorec, S., Ouazar, D., Herrera, I., 1999. Seawater Intrusion in Coastal Aquifers- Concepts, Methods and Practices. Springer, New York.

Cherry, G.S., 2006. U.S. Geological Survey Georgia Water Science Center and City of Brunswick-Glynn County Cooperative Water Program - Summary of Activities, July 2005 through June 2006, U.S.G.S. Open-File Report 2006-1368.

Collins, M.A., Gelhar, L.W., 1971. Seawater intrusion in layered aquifers. Water Resources Research 7 (4), 971-979.

Croucher, A.E., O'Sullivan, M.J., 1995. The Henry problem for saltwater intrusion. Water Resources Research. 31 (7), 1809-1814.

Cheng A.H.D., Halhal, D., Naji, A., Ouazar, D., 2000. Pumping optimization in saltwater-intruded coastal aquifers. Water Resources Research 36 (8), 2155-2165.

Dagan, G., Zeitoun, D.G., 1998. Seawater-freshwater interface in a stratified aquifer of random permeability distribution. Journal of Contaminant Hydrology, 29 (3), 185-203.

Das, A., Datta, B., 1999a. Development of management models for sustainable use of coastal aquifers. Journal of Irrigation and Drainage Engineering-ASCE 125 (3), 112-121.

Das, A., Datta, B., 1999b. Development of multi-objective management models for coastal aquifers. Journal of Water Resources Planning and Management-ASCE 125 (2), 76-87.

Diersch, H.J.G., Kolditz, O., 2002. Variable-density flow and transport media: approach and challenges. Advances in Water Resources 25 (8-12), 899-944.

Emch, P.G., Yeh, W.W.G., 1998. Management model for conjunctive use of coastal surface water and ground water. Journal of Water Resources Planning and Management-ASCE 124 (3) 129-139.

Fan, Y., Kahawita, R., 1994. A numerical study of variable-density flow and mixing in porous media. Water Resources Research 30 (10), 2707-2716.

Finney, B.A., Samsuhadi, Willis, R., 1992. Quasi-three-dimensional optimization model of Jakarta Basin. Journal of Water Resources Planning and Management-ASCE 118 (1) 18-31.

Galeati, G., Gambolati, G., Neuman, S.P., 1992. Coupled and partially coupled Eulerian-Lagrangian model of freshwater-seawater mixing zone. Water Resources Research 28 (1), 149-165.

Gotovac, H., Andricevic, R., Gotovac, B., Kozulic, V., Vranjes, M., 2003. An improved collocation method for solving Henry problem. Journal of Contaminant Hydrology 64 (1-2), 129-149.

Henry H.R., 1964. Effects of dispersion on salt encroachment in coastal aquifers. Water-Supply Paper 1613-C. US Geological Survey.

Hunt, B., 1985. Some analytical solutions for seawater intrusion control with recharge wells. Journal of Hydrology 80 (1-2), 9-18.

Hallaji, K., Yazicigil, H., 1996. Optimal management of a coastal aquifer in southern Turkey. Journal of Water Resources Planning and Management-ASCE 122 (4) 233-244.

Huppert, H.E., Woods, A.W., 1995. Gravity-driven flows in porous layers. Journal of Fluid Mechanics 292, 55-69.

Intaraprasong, T., Zhan, H., 2007. Capture zone between two streams. Journal of Hydrology 338 (3-4), 297-307.

Kondolf, G.M., Matthews, W.V.G., 1986. Transport of tracer gravels on a coastal California River. Journal of Hydrology 85, 265-280.

Kacimov, A.R., Obnosov, Y., 2001. Analytical solution for a sharp interface problem in sea water intrusion into a coastal aquifer. Proceedings of the Royal Society A 457, 3032-3038.

Kacimov, A.R., Sherif, M.M., 2006. Sharp interface, one-dimensional seawater intrusion into a confined aquifer with controlled pumping: analytical solution. Water Resources Research 42, W06501, doi:10.1029/2005WR004551.

Kolditz, O., Ratke, R., Diersch, H.J.G., Zielke, W., 1998. Coupled groundwater flow and transport. 1. Verification of variable density flow and transport models. Advances in Water Resources 21 (1), 27-46.

Langevin, C.D., Guo, W., 2006. MODFLOW/MT3DMS-based simulation of variable-density ground water flow and transport. Ground Water, 44 (3), 339-351.

Mantoglou, A., Papantoniou, M., Giannoulopoulos, P., 2004. Management of coastal aquifers based on nonlinear optimization and evolutionary algorithms. Journal of Hydrology 297 (1-4), 209-228.

Naji, A., Cheng, A.H.D., Ouazar, D., 1998. Analytical stochastic solutions of saltwater/freshwater interface in coastal aquifers. Stochastic hydrology and Hydraulics 12 (6), 413-430.

Ozturk, Y.F., 1970. Seawater intrusion length in stratified estuaries. Water Research 4 (7), 477-484.

Park, C.H., Aral, M.M., 2004. Multi-objective optimization of pumping rates and well placement in coastal aquifers. Journal of Hydrology 290 (1-2), 80-99.

Paniconi, C., Khlaifi, l., Lecca, G., Giacomelli, A., Tarhouni, J., 2001. Modeling and analysis of seawater intrusion in the coastal aquifer of eastern Cap-Bon, Tunisia. Transport in Porous Media 43 (1), 3-28.

Strack, O.D.L., 1976. A single-potential solution for regional interface problems in coastal aquifers. Water Resources Research 12 (6), 1165-1174.

Strack, O.D.L., 1989. Groundwater Mechanics. Englewood Cliffs, NJ: Prentice-Hall.

Sakr, S.A., 1999. Validity of a sharp-interface model in a confined coastal aquifer. Hydrology Journal 7 (2), 155-160.

Simmons, C.T., 2005. Variable density groundwater flow: From current challenges to further possibilities. Hydrology Journal 13 (1), 116-119.

Shamir, U., Bear, J., Gamliel, A., 1984. Optimal annual operation of a coastal aquifer. Water Resources Research 20 (4), 435-444.

Simpson, M.J., Clement, T.P., 2003. Theoretical analysis of the worthiness of Henry and Elder problems as benchmarks of density-dependent groundwater flow models. Advances in Water Resources 26 (1), 17-31.

Sahoo, D., Smith, P.K., 2009. Hydroclimatic trend detection in a rapidly urbanizing semi-arid and coastal river basin. Journal of Hydrolog 367, 217-227.

Voss, C.I., Souza, W.R., 1987, Variable density flow and solute transport simulation of regional aquifers containing a narrow freshwater-seawater mixing zone, Water Resources Research 23, 1851-1866.

Wilson, J., 1993. Induced infiltration in aquifers with ambient flow. Water Resources Research 29 (10), 3503-3512.

Willis, R., Finney, B.A., 1988. Planning- model for optimal-control of saltwater intrusion. Journal of Water Resources Planning and Management-ASCE 114 (2) 163-178.

Werner, A.D., Simmons, C.T., 2009. Impact of sea-level rise on sea water intrusion in coastal aquifers. Ground Water 47 (2), 197-204.

Xue, Y., Xie, C.H., Wu, J.C., Liu, P.M., Wang J.J., Jiang. Q.B., 1995. A 3-dimensional miscible transport model for seawater intrusion in China. Water Resources Research 31 (4), 903-912.

Zhan, H.B., 1999. Analytical study of capture time to a horizontal well. Journal of Hydrology 217 (1-2), 46-54.

Table

Table 1 Hydrogeologic parameters for the validation numerical case

Parameter	Variable	Value
Domain length, m	L	400, 1000
Domain height, m	H	20
Domain width, m	W	1000
Constant seawater head, m	D	30
Constant hydraulic gradient, -	J	0.005
Homogenous hydraulic conductivity, m d^{-1}	K	8
Longitudinal dispersivity, m	α_L	0.5
Transverse dispersivity, m	α_T	0.05
Effective porosity, -	θ_e	0.4
Seawater density, kg m^{-3}	ρ_s	1025
Freshwater density, kg m^{-3}	ρ_f	1000
Salt concentration, kg m^{-3}	C_s	35
Pumping well location, m	x_w	200
Pumping rate, m d^{-3}	Q	500

Figure Captions

Fig. 1. Plan view and cross section of the conceptual model for a pumping well located in a homogeneous, isotropic, unconfined coastal aquifer.

Fig. 2. Location of stagnation points for a pumping well in coastal aquifers with constant hydraulic head landward boundary. (a) stagnation point vs. pumping rate; and (b) stagnation point vs. well location.

Fig. 3. Comparison of maximum pumping rates for avoiding seawater intrusion in coastal aquifers with different boundary condition settings.

Fig. 4. Comparison of steady-state simulation results of hydraulic head and salt concentration distributions for the domain length L = 400 m with different landward boundary condition settings. (a) hydraulic head distribution (constant discharge rate boundary), (b) hydraulic head distribution (constant hydraulic head boundary), (c) normalized concentration distribution (constant discharge rate boundary), and (d) normalized concentration distribution (constant hydraulic head boundary).

Fig. 5. Comparison of steady-state simulation results of hydraulic head and salt concentration distributions for the domain length L = 1000 m with different landward boundary condition settings. (a) hydraulic head distribution (constant discharge rate boundary), (b) hydraulic head distribution (constant hydraulic head boundary), (c) normalized concentration distribution (constant discharge rate boundary), and (d) normalized concentration distribution (constant hydraulic head boundary).

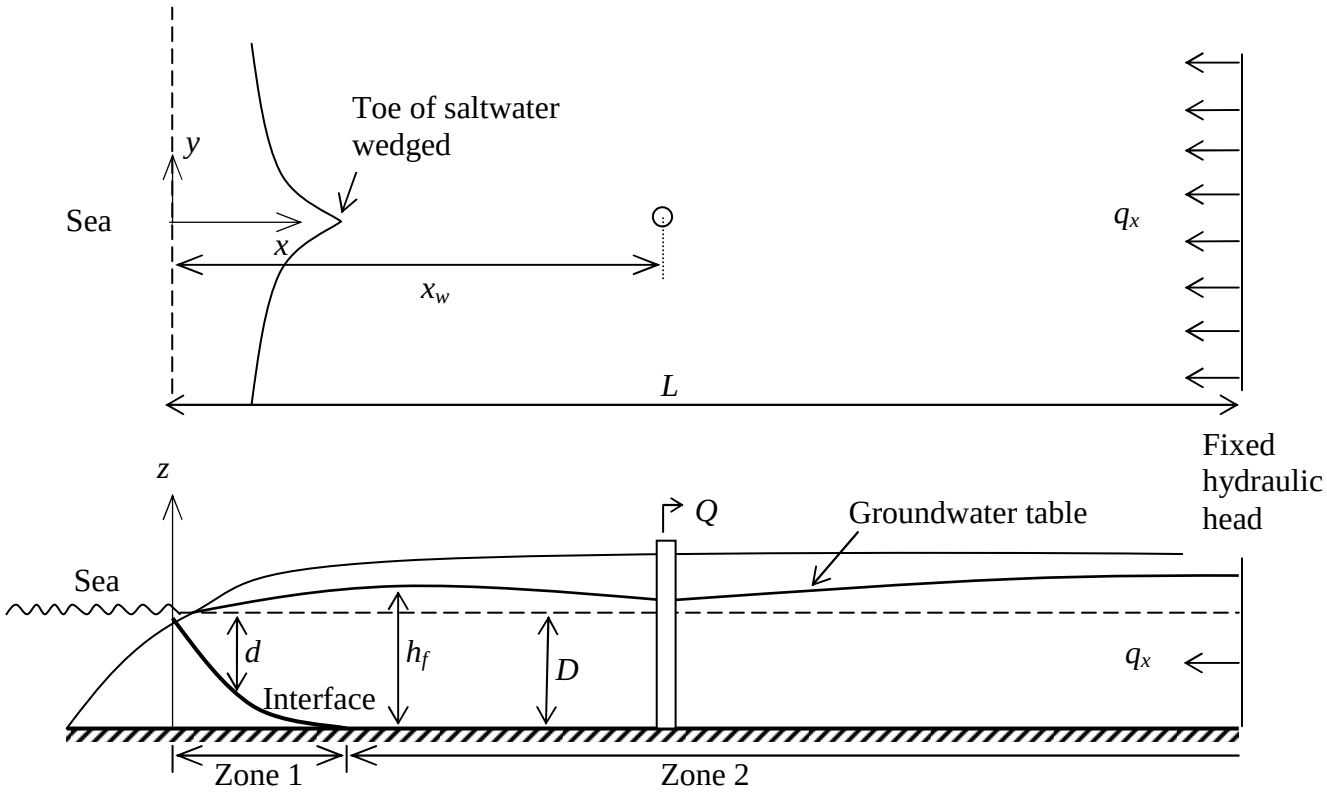

Fig. 1. Plan view and cross section of the conceptual model for a pumping well located in a homogeneous, isotropic, unconfined coastal aquifer.

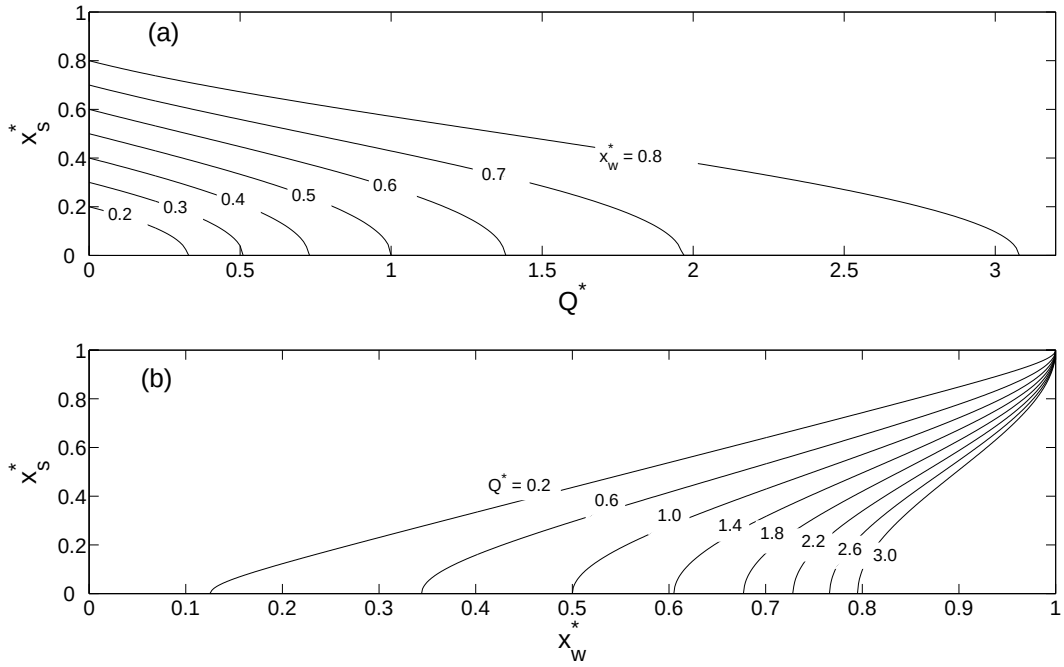

Fig. 2. Location of stagnation points for a pumping well in coastal aquifers with constant hydraulic head landward boundary. (a) stagnation point vs. pumping rate; and (b) stagnation point vs. well location.

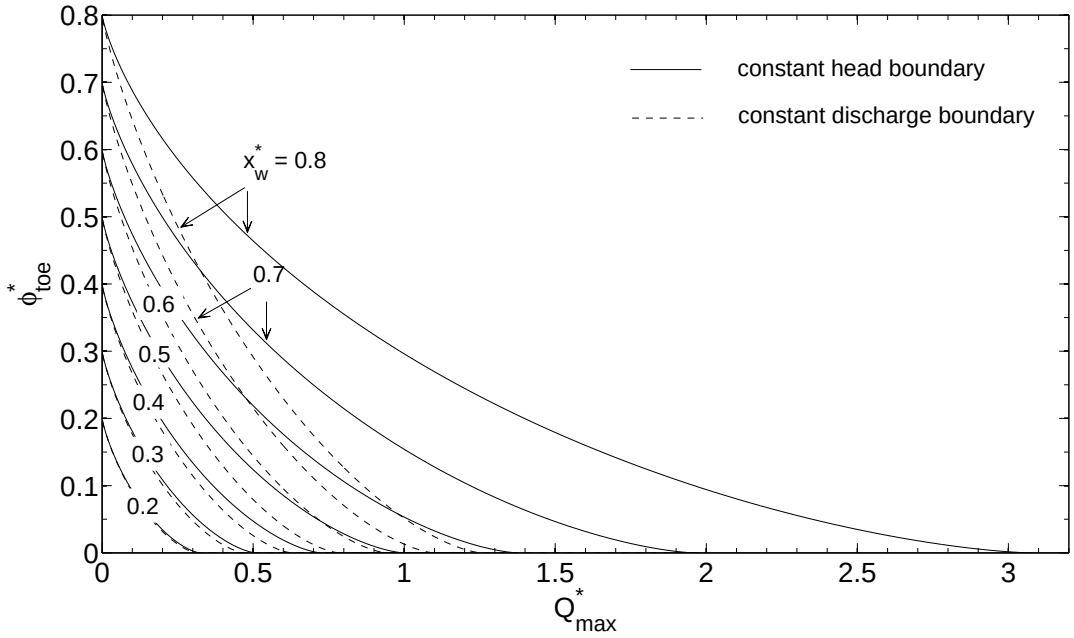

Fig. 3. Comparison of the maximum pumping rates for avoiding seawater intrusion in coastal aquifers with different boundary condition settings.

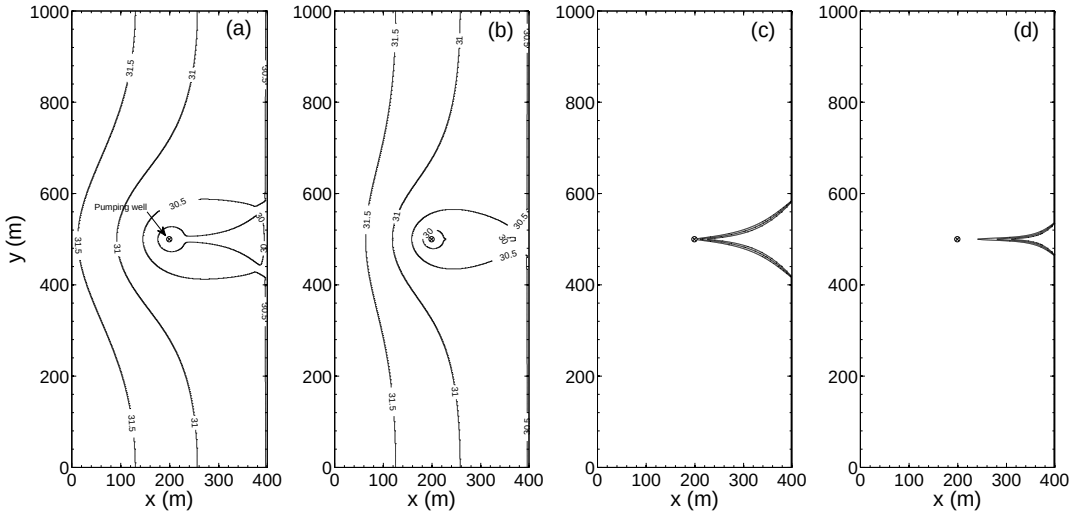

Fig. 4. Comparison of steady-state simulation results of hydraulic head and salt concentration distributions for the domain length L = 400 m with different landward boundary condition settings. (a) hydraulic head distribution (constant discharge rate boundary), (b) hydraulic head distribution (constant hydraulic head boundary), (c) normalized concentration distribution (constant discharge rate boundary), and (d) normalized concentration distribution (constant hydraulic head boundary).

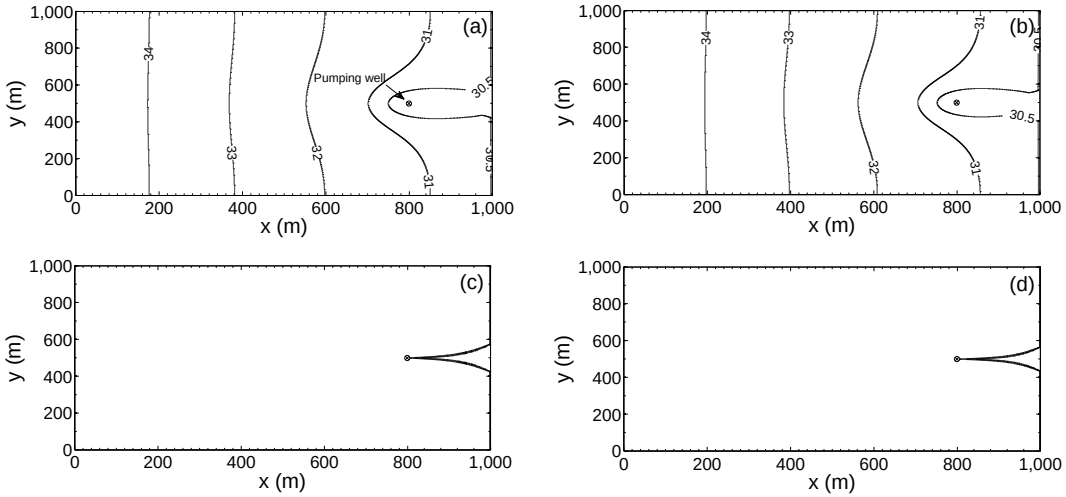

Fig. 5. Comparison of steady-state simulation results of hydraulic head and salt concentration distributions for the domain length L = 1000 m with different landward boundary condition settings. (a) hydraulic head distribution (constant discharge rate boundary), (b) hydraulic head distribution (constant hydraulic head boundary), (c) normalized concentration distribution (constant discharge rate boundary), and (d) normalized concentration distribution (constant hydraulic head boundary).

Chap. 4

Analysis of stagnation points for a pumping well in recharge areas

Abstract

Stagnation points in groundwater flow fields delineate different flow regions by the separation streamlines passing through them. Stagnation-point analysis can hereby provide a useful tool in streamline delineation as well as in hydraulic control. In the present work, we present a stagnation-point analysis for a flow field created by a pumping well in recharge areas. This scenario is of great interest since it is very common in practice for pumping wells to be located inside or near a recharge area. A typical case is that an irrigation system is fed by groundwater pumped from an inside well. By performing stagnation-point analysis, it is found that the behavior of the created flow field under study is not only determined by the magnitudes of specific parameters such as pumping rate, regional flow rate, infiltration rate, recharge area and well location, but also related to the interrelation of these parameters. Applying the properties of the potential Hessian matrix at stagnation points, we also identified the nature of stagnation points (e.g., maximum, minimum, or saddle point) assuming that the pumping well locates at the center of the recharge area. In addition, we delineated the streamlines by tracing streamlines starting from the stagnation points. The orientation of the separation streamlines is determined by the potential Hessian matrix. Generally, for a well with a relatively high pumping rate, there is one, and only one stagnation point outside the recharge area, since all infiltration and partial regional flow are pumped by the well. For a well inside the recharge area with a relatively low pumping rate, however, it is found that there are always three stagnation points, because infiltration is surplus for providing the well extraction, which results in the separation streamlines outside the recharge area and eventually forms a third stagnation point. Under certain field conditions, cases of two stagnation points can occur, and these critical conditions have also been identified.

1 Introduction

Stagnation points are defined as points of zero specific discharge. For two-dimensional potential flow, this condition may be described by

$$\frac{\partial \Phi}{\partial x} = 0 \,,\ \frac{\partial \Phi}{\partial y} = 0 \tag{1}$$

where Φ is discharge potential, and x and y are spatial coordinates. The number, distribution, and type of stagnation points in the flow domain associated with aquifer features determine the flow pattern (Jin and Steward, 2007). A point satisfying Eq. (1) may be a maximum, a minimum, or a saddle point of the potential field (Fienen et al., 2005). The first two cases are possible only when recharge or drainage is involved, and the Poisson equation is satisfied for a homogeneous medium. In the absence of recharge,

Φ is governed by a Laplace equation, and a stagnation point is always a saddle point, by virtue of the mean-value theorem. In all cases, stagnation points can be interpreted as "equilibrium points", where two or more competing forces balance each other. For example, at the stagnation point between two extraction wells, the pull of one well is exactly opposite from the pull of the other. Stagnation points play an important role in groundwater flow because the separation streamlines passing through them delineate different flow regions. As an example, in flow fields manipulated by pumping well systems, separation streamlines passing through stagnation points delineate capture zones of exaction wells, release zones of injection wells, and boundaries of recirculation zones (Fienen et al., 2005).

Stagnation-point analysis and its applications in groundwater flow have continued for many years. Many researchers have made substantial contributions in this field (e.g. Muskat, 1946; Hantush, 1965; Bear, 1979; Javandel and Tsang, 1986; Newsom and Wilson, 1988; Strack, 1989; Wilson, 1993; Bakker and Strack, 1996; Zhan 1999a and 1999b; Christ and Goltz, 2002; Zhan and Zlotnik 2002; Luo and Kitanidis, 2004; Fienen et al., 2005; Intaraprasong and Zhan, 2007). For example, in flow fields created by multiple injection-extraction wells, the difference in the value of stream functions at stagnation points may determine the captured flow rate in the capture zones, recirculated flow rate in the recirculation zones, and the flow rate in release zones. These results can then be used to evaluate the capture-zone width, recirculation ratio, and mean residence time, etc., and help design such multiple-well systems for groundwater remediation (Christ et al., 1999; Cunningham et al., 2004; Luo and Kitanidis, 2004; Luo et al., 2006).

Tracing streamlines from stagnation points is another application of stagnation-point analysis. In a flow field where complex potential or stream function can be defined, one can use the stream function to delineate the separation streamlines through stagnation points based on the definition that the value of the stream function is constant along a streamline (Christ and Goltz, 2002; Shan, 1999). Hence, the separation streamlines are contourlines of the stream function value passing through the stagnation point. In scenarios with internal volumetric sources or sinks, however, this method is complicated because each internal source or sink contributes a branch cut, and thus the stream function is discontinuous. Strack (1989) provided a prediction-correction procedure to track particles using stream functions. When particles pass through a branch cut, the stream function needs to be adjusted with a jump. Accounting for many branch cuts it is complicated. In the numerical approach of Cirpka et al. (1999), the stream function was evaluated only element-wise thus avoiding branch-cuts. In this approach, tracing streamlines was based on finding all points at the edges of the element sharing the same local stream function value. The latter authors determined the location of stagnation points by linear interpolation of the velocity field, and employ additional rules to account for stagnation points at element corners. The approach was applied exclusively to numerical flow fields without recharge or drainage. Bakker and Strack (1996) presented a numerical approach based on an analytic element model for the delineation of capture zones in an isotropic, homogeneous aquifer with recharge by determining starting points for tracing separation streamlines. A forward trace at a possible stagnation point is started to locate two forward and two backward points to determine the saddle stagnation points and generate the separation streamlines. Fienen et al. (2005) developed a novel semi-

analytical method for quick delineation of streamlines in homogeneous aquifer with anisotropic transmissivity. By investigating the behavior of the potential Hessian matrix at stagnation points, starting points of separation streamlines at stagnation points can be exactly determined.

In the present study, we present a thorough stagnation-point analysis for a pumping well in uniform regional flow in the presence of recharge or infiltration, which is an extension of the classical scenario of a pumping well in the absence of recharge. It is known that the resulted flow field by the pumping well and recharge is governed by two equations: inside the recharge area, it is the Poisson Equation, outside the recharge area the Laplace Equation. More than one stagnation point may exist as maximum, minimum, or saddle points. This scenario, essentially, can be considered as a combination of two cases studied by Strack (1989). One is that a pumping well is located at the center of a circular island with rainfall, and the other is local infiltration in the presence of regional flow. However, both cases are relatively simpler than ours because they do not include either the regional flow or the pumping well. By neglecting anyone of them, our cases can be simplified to one of these two cases. This combined scenario is of particular interest because it is very common in practice for pumping wells to be located inside or near a recharge area. A typical case is that an irrigation system is fed by groundwater pumped from an inside well. Pumping groundwater for irrigation in most arid and semiarid regions worldwide has experienced a significant increase over the last four decades since it, compared with traditional surface water irrigation systems, offers more reliable supplies, lesser vulnerability to droughts, and ready accessibility for individual user (Garrido et al., 2006). For example, Spain's groundwater irrigation sector represents 27% of 3.3 M ha total irrigated acreage (Garrido et al., 2006). In Northern Territory, Australia, as much as 89% of water used for irrigation is sourced from groundwater in year of 1996-1997 (http://www.anra.gov.au/topics/irrigation/consumption/nt.html).

2 Flow domain and governing equations

Consider an unconfined homogeneous aquifer with a constant infiltration rate N. Note that the infiltration rate is assumed to be an averaged value over the recharge area. Because a well can be drilled almost anywhere in a high-yielding aquifer, it is common to place it at the pivot point for agriculture irrigation systems (http://www.nespal.org/SIRP/awp/2005.03.Fact_Sheet_04SW.pdf). Without loss of generality, we assume the area with recharge is circular with radius R and centered at the origin. An extraction well inside or near the recharge area with a specific extraction rate Q is arbitrarily located at the x-axis, which is parallel to the regional flow direction. The uniform regional flow is along x direction with intensity q_{x0}. This setup is consistent to the practical scenario, where a well is often the center of an irrigation area or the alignment of wells is parallel to regional flow for optimizing capture zone and containment (Christ and Goltz, 2004).

Fig.1 shows the plane view and cross section of the setup, and the flow filed of the case with recharge, regional flow and no pumping well. It is obvious that the pumped water may come from both the regional flow and the recharge area. For example, if the well locates inside the recharge area with a small pumping rate, it is possible that all

pumped water may come directly from recharge. At a high pumping rate, however, part of water may also be pumped from the surrounding aquifer, supplied by the regional flow.

The problem is simplified to be two-dimensional by ignoring the vertical infiltration processes and assuming steady-state flow field. As described previously, the flow field is governed by two equations: outside the recharge area, the flow field is analytic and governed by a Laplace equation; by contrast, the flow field inside the recharge area is not analytic due to infiltration, and is governed by a Poisson equation. Thus, a complex potential may be defined in the area without recharge, but is not available in the recharge area. We assume that the location of the well is (x_w, 0), and the coordinates of the center of the infiltration are (0, 0). The discharge potential, Φ, can be formulated as

$$\Phi(x,y)=\frac{Q}{4\pi}\ln\left(\frac{(x-x_w)^2+y^2}{R^2}\right)-q_{x0}x+\begin{cases}-\dfrac{x^2+y^2-R^2}{4}N+C & \text{for } x^2+y^2\le R^2\\ -\dfrac{R^2N}{4}\ln\left(\dfrac{x^2+y^2}{R^2}\right)+C & \text{for } x^2+y^2\ge R^2\end{cases} \tag{2}$$

where $\frac{Q}{4\pi}\ln\left(\frac{(x-x_w)^2+y^2}{R^2}\right)$ is the discharge potential for flow created by a pumping well; $-q_{x0}x$ is the regional flow potential; $-\frac{x^2+y^2-R^2}{4}N$ and $-\frac{R^2N}{4}\ln\left(\frac{x^2+y^2}{R^2}\right)$ are the discharge potential inside and outside of the recharge area, respectively; C is a constant.

In order to facilitate the interpretation of the analysis, the following dimensionless variables are defined:

$$x^*=\frac{x}{R},\ y^*=\frac{y}{R},\ x_s^*=\frac{x_s}{R},\ y_s^*=\frac{y_s}{R},\ x_w^*=\frac{x_w}{R},\ y_w^*=\frac{y_w}{R},\ Q^*=\frac{Q}{\pi NR^2},\ q_{x0}^*=\frac{2q_{x0}}{NR},$$
$$H^*=\frac{H}{N},\ \Phi^*=\frac{\Phi}{NR^2} \tag{3}$$

where x^*, y^*, x_s^*, y_s^*, x_w^* and y_w^* are dimensionless coordinates normalized by recharge area radius; x_s and y_s are stagnation point coordinates; Q^* is dimensionless pumping rate; q_{x0}^* is dimensionless regional flow rate; H^* is dimensionless Hessian matrix of the discharge potential; and Φ^* is dimensionless potential, which is expressed as

$$\Phi^*(x^*, y^*) = \frac{Q^*}{4}\ln\left((x^* - x_w^*)^2 + y^{*2}\right) - \frac{q_{x0}^*}{2}x^* + \begin{cases} -\dfrac{x^{*2} + y^{*2} - 1}{4} + C & \text{for } x^{*2} + y^{*2} \le 1 \\ -\dfrac{1}{4}\ln\left(x^{*2} + y^{*2}\right) + C & \text{for } x^{*2} + y^{*2} \ge 1 \end{cases}$$

(4)

3 Stagnation point and critical pumping rate

Stagnation points can be obtained by solving Eq. (1) in dimensionless form

$$0 = \frac{\partial \Phi^*}{\partial x^*} = \frac{Q^*(x^* - x_w^*)}{(x^* - x_w^*)^2 + y^{*2}} - q_{x0}^* + \begin{cases} -x^* & \text{for } x^{*2} + y^{*2} \le 1 \\ -\dfrac{x^*}{x^{*2} + y^{*2}} & \text{for } x^{*2} + y^{*2} \ge 1 \end{cases} \quad (5)$$

$$0 = \frac{\partial \Phi^*}{\partial y^*} = \frac{Q^* y^*}{(x^* - x_w^*)^2 + y^{*2}} + \begin{cases} -y^* & \text{for } x^{*2} + y^{*2} \le 1 \\ -\dfrac{y^*}{x^{*2} + y^{*2}} & \text{for } x^{*2} + y^{*2} \ge 1 \end{cases} \quad (6)$$

Thus, the dimensionless coordinates of the stagnation points are given by:

$$x_s^* = \begin{cases} \left(\frac{x_w^*}{2} - \frac{q_{x0}^*}{2}\right) \pm \sqrt{\left(\frac{x_w^*}{2} - \frac{q_{x0}^*}{2}\right)^2 + \left(Q^* + q_{x0}^* x_w^*\right)} & \text{for } x^{*2} + y^{*2} \le 1 \\ \dfrac{\left(Q^* + q_{x0}^* x_w^* - 1\right) \pm \sqrt{\left(Q^* + q_{x0}^* x_w^* - 1\right)^2 + 4q_{x0}^* x_w^*}}{2q_{x0}^*} & \text{for } x^{*2} + y^{*2} \ge 1 \end{cases}, \quad y_s^* = 0 \quad (7)$$

Eq. (7) indicates that the flow field may have at most four stagnation points, comparing with only one stagnation point without recharge. However, in some cases, the stagnation points may not co-exist or may coincide. Identification of these critical cases may yield critical pumping rates and critical well locations which control the behavior of the flow field. The analysis may also help explain the fate of chemicals and nutrients leached from the field into the groundwater. Detailed analyses about the number and locations of stagnation points can be made based on the dimensionless parameters x_w^*, q_{x0}^*, and Q^*, which are presented in the following sections.

The well locates at the origin

First of all, we consider a special case that the well locates exactly at the origin, namely, $x_w^* = 0$. This will significantly simplify the discussion. According to Eqs. (5) and (6), stagnation points hereby can be obtained by solving

$$0=\frac{\partial \Phi^*}{\partial x^*}=\frac{Q^* x^*}{x^{*2}+y^{*2}}-q_{x0}^*+\begin{cases}-x^* & \text{for } x^{*2}+y^{*2}\le 1\\ -\dfrac{x^*}{x^{*2}+y^{*2}} & \text{for } x^{*2}+y^{*2}\ge 1\end{cases} \tag{8}$$

$$0=\frac{\partial \Phi^*}{\partial y^*}=\frac{Q^* y^*}{x^{*2}+y^{*2}}+\begin{cases}-y^* & \text{for } x^{*2}+y^{*2}\le 1\\ -\dfrac{y^*}{x^{*2}+y^{*2}} & \text{for } x^{*2}+y^{*2}\ge 1\end{cases} \tag{9}$$

Thus, the dimensionless coordinates of the stagnation points are:

$$x_s^*=\begin{cases}-\dfrac{q_{x0}^*}{2}\pm\sqrt{\dfrac{{q_{x0}^*}^2}{4}+Q^*} & \text{for } x^{*2}+y^{*2}\le 1\\ \dfrac{Q^*-1}{q_{x0}^*} & \text{for } x^{*2}+y^{*2}\ge 1\end{cases},\ y_s^*=0 \tag{10}$$

Eq. (10) can not only be used to calculate the dimensionless coordinates of the stagnation points, but also provide a way to determine the dimensionless critical pumping rates by generating the follow inequality set:

$$\begin{cases}a.\ -1\le -\dfrac{q_{x0}^*}{2}-\sqrt{\dfrac{{q_{x0}^*}^2}{4}+Q^*}\le 0\\ b.\ 0\le -\dfrac{q_{x0}^*}{2}+\sqrt{\dfrac{{q_{x0}^*}^2}{4}+Q^*}\le 1\\ c.\ \dfrac{Q^*-1}{q_{x0}^*}\ge 1 \text{ or } \dfrac{Q^*-1}{q_{x0}^*}\le -1\end{cases} \tag{11}$$

which gives:

$$\begin{cases}a.\ \Omega 1:\ Q^*\le 1-q_{x0}^*\\ b.\ \Omega 2:\ Q^*\le 1+q_{x0}^*\\ c.\ \Omega 3:\ Q^*\ge 1+q_{x0}^* \text{ or } Q^*\le 1-q_{x0}^*\end{cases} \tag{12}$$

The solutions derived from the inequality set can be used to evaluate the number and locations of stagnation points for different conditions. For example, for the case of two stagnation points where one exists inside the recharge area, and the other locates outside the recharge area, we can derive the dimensionless pumping rate interval by solving

$$Q^*=\left((\Omega 1\cap\overline{\Omega 2})\cup(\overline{\Omega 1}\cap\Omega 2)\right)\cap\Omega 3 \tag{13}$$

where $\overline{\Omega 1}$ and $\overline{\Omega 2}$ represent complements of $\Omega 1$ and $\Omega 2$, respectively. Then, for a given Q^*, we can obtain the stagnation-point locations by solving Eq. (10).

It should be noted that two dimensionless critical pumping rates, $1+q_{x0}^*$ and $1-q_{x0}^*$ appear in Eq. (12). Physically speaking, $1+q_{x0}^*$ denotes sum of the infiltration rate and equivalent regional flow rate on recharge area, while $1-q_{x0}^*$ represents the difference between these two rates and hereby can be regarded as "over-infiltration rate" on recharge area. Based on the solution set of Eq. (12), the following conclusions about stagnation points can be drawn for different values of Q^*:

1. For $q_{x0}^* \geq 1$:

(a) If $0 < Q^* < 1+q_{x0}^*$, there is only one stagnation point, which is located inside the recharge area.

(b) If $Q^* > 1+q_{x0}^*$, there is only one stagnation point, which is located outside the recharge area.

(c) If $Q^* = 1+q_{x0}^*$, one stagnation point with dimensionless coordinates (1, 0) is obtained, because $-\frac{q_{x0}^*}{2}+\sqrt{\frac{{q_{x0}^*}^2}{4}+Q^*}=\frac{Q^*-1}{q_{x0}^*}=1$.

2. For $q_{x0}^* < 1$:

(a) If $0 < Q^* < 1-q_{x0}^*$, there are three stagnation points. Two of them are located inside the recharge area at $\left(-\frac{q_{x0}^*}{2}\pm\sqrt{\frac{{q_{x0}^*}^2}{4}+Q^*},0\right)$, and one is located outside the recharge area at $\left(\frac{Q^*-1}{q_{x0}^*},0\right)$.

(b) If $1-q_{x0}^* < Q^* < 1+q_{x0}^*$, there is only one stagnation point at $\left(-\frac{q_{x0}^*}{2}+\sqrt{\frac{{q_{x0}^*}^2}{4}+Q^*},0\right)$, which is located inside of the recharge area.

(c) If $Q^* > 1+q_{x0}^*$, there is only one stagnation point at $\left(\frac{Q^*-1}{q_{x0}^*},0\right)$, which is located

outside the recharge area.

(d) If $Q^* = 1 - q_{x0}^*$, there are two stagnation points at (-1, 0) and $\left(1 - q_{x0}^*, 0\right)$, because $-\frac{q_{x0}^*}{2} - \sqrt{\frac{{q_{x0}^*}^2}{4} + Q^*} = \frac{Q^* - 1}{q_{x0}^*} = -1$.

(e) If $Q^* = 1 + q_{x0}^*$, there is only one stagnation point at (1, 0).

The results above show that the number and position of the stagnation points are determined by the pumping rate and relative magnitude between infiltration rate and equivalent regional flow rate on recharge area.

The well does not locate at the origin

In this section, we will extend the stagnation-point analysis for an arbitrarily located pumping well. We assume $x_w^* > 0$, and the case where $x_w^* < 0$ can be similarly derived.

Eq. (7) can be expressed as the following inequality set subject to the constraint that $x_w^* > 0$:

$$\begin{cases} a.\ -1 \le \left(\frac{x_w^*}{2} - \frac{q_{x0}^*}{2}\right) - \sqrt{\left(\frac{x_w^*}{2} - \frac{q_{x0}^*}{2}\right)^2 + \left(Q^* + q_{x0}^* x_w^*\right)} \le 0 \\ b.\ 0 \le \left(\frac{x_w^*}{2} - \frac{q_{x0}^*}{2}\right) + \sqrt{\left(\frac{x_w^*}{2} - \frac{q_{x0}^*}{2}\right)^2 + \left(Q^* + q_{x0}^* x_w^*\right)} \le 1 \\ c.\ \frac{\left(Q^* + q_{x0}^* x_w^* - 1\right) - \sqrt{\left(Q^* + q_{x0}^* x_w^* - 1\right)^2 + 4 q_{x0}^* x_w^*}}{2 q_{x0}^*} \le -1 \\ d.\ \frac{\left(Q^* + q_{x0}^* x_w^* - 1\right) + \sqrt{\left(Q^* + q_{x0}^* x_w^* - 1\right)^2 + 4 q_{x0}^* x_w^*}}{2 q_{x0}^*} \ge 1 \end{cases} \tag{14}$$

Solving these inequalities yields

$$\begin{cases} a.\ \Omega 1:\ Q^* \le \left(1 + x_w^*\right)\left(1 - q_{x0}^*\right) \\ b.\ \Omega 2:\ Q^* \le \left(1 - x_w^*\right)\left(1 + q_{x0}^*\right) \\ c.\ \Omega 3:\ Q^* \le \left(1 + x_w^*\right)\left(1 - q_{x0}^*\right) \\ d.\ \Omega 4:\ Q^* \ge \left(1 - x_w^*\right)\left(1 + q_{x0}^*\right) \end{cases} \tag{15}$$

which provide a tool for calculating the number and locations of stagnation points at a given pumping rate. We define two dimensionless critical pumping rates:

$$Q_{c1} = \left(1 - x_w^*\right)\left(1 + q_{x0}^*\right) \text{ and } Q_{c1} = \left(1 + x_w^*\right)\left(1 - q_{x0}^*\right) \qquad (16)$$

One can observe from the Eq. (15) that $\Omega 1$ and $\Omega 3$ is the same, which means the dimensionless stagnation points at $[-1, 0)$ and $(-\infty, -1]$ co-exist. On the other hand, $\Omega 2 \bigcap \Omega 4 = Q_{c1}$ shows that the dimensionless stagnation points at [0, 1] and $[1, +\infty)$ repel each other, except at the critical pumping rate Q_{c1}, which indicates there is one and only one stagnation point located in these two intervals. The results derived for all cases are given in Table 1. It shows that the number and locations of stagnation points are not only related to the magnitudes of x_w^*, q_{x0}^*, and Q^*, but also dependent on the relative magnitude between x_w^* and q_{x0}^*. As an example, consider $q_{x0}^* \le 1$ and $0 < x_w^* < 1$, the following conclusions about the dimensionless pumping rate, the number and locations of stagnation points can be made.

1. For $x_w^* < q_{x0}^*$:

(a) If $0 < Q^* < Q_{c2}$, there are three stagnation points, and two of them are inside the recharge area and only one stagnation point is outside the recharge area.

(b) If $Q_{c2} < Q^* < Q_{c1}$, there is one stagnation point inside the recharge area, and no stagnation point outside the recharge area.

(c) If $Q^* > Q_{c1}$, there is one stagnation point outside the recharge area, and no stagnation point inside the recharge area.

(d) Consider critical conditions. If $Q^* = Q_{c2}$, there are two stagnation points, $(-1, 0)$ and $\left(\left(\frac{x_w^*}{2} - \frac{q_{x0}^*}{2}\right) + \sqrt{\left(\frac{x_w^*}{2} - \frac{q_{x0}^*}{2}\right)^2 + \left(Q^* + q_{x0}^* x_w^*\right)}, 0\right)$ because $\left(\frac{x_w^*}{2} - \frac{q_{x0}^*}{2}\right) + \sqrt{\left(\frac{x_w^*}{2} - \frac{q_{x0}^*}{2}\right)^2 + \left(Q^* + q_{x0}^* x_w^*\right)} = \frac{\left(Q^* + q_{x0}^* x_w^* - 1\right) - \sqrt{\left(Q^* + q_{x0}^* x_w^* - 1\right)^2 + 4 q_{x0}^* x_w^*}}{2 q_{x0}^*} = -1$.

(e) If $Q^* = Q_{c1}$, there is only one stagnation point, namely (1, 0), located at the perimeter of the recharge circle.

2. For $x_w^* > q_{x0}^*$:

(a) If $0 < Q^* < Q_{c1}$, there are three stagnation points, and two of which are within the recharge area and only one stagnation point is outside the recharge area.

(b) If $Q_{c1} < Q^* < Q_{c2}$, there are also three stagnation points, and one stagnation point is within the recharge and the rest are outside the recharge area.

(c) If $Q^* > Q_{c2}$, there is one stagnation point outside the recharge area, and no stagnation point within the recharge area.

(d) Consider critical conditions. If $Q^* = Q_{c1}$, there are three stagnation points, (1, 0), $\left(\left(\frac{x_w^*}{2} - \frac{q_{x0}^*}{2} \right) - \sqrt{\left(\frac{x_w^*}{2} - \frac{q_{x0}^*}{2} \right)^2 + \left(Q^* + q_{x0}^* x_w^* \right)}, 0 \right)$ and $\left(\frac{\left(Q^* + q_{x0}^* x_w^* - 1 \right) - \sqrt{\left(Q^* + q_{x0}^* x_w^* - 1 \right)^2 + 4 q_{x0}^* x_w^*}}{2 q_{x0}^*}, 0 \right)$.

(e) If $Q^* = Q_{c2}$, there are two stagnation points with coordinates of $\left(\left(\frac{x_w^*}{2} - \frac{q_{x0}^*}{2} \right) + \sqrt{\left(\frac{x_w^*}{2} - \frac{q_{x0}^*}{2} \right)^2 + \left(Q^* + q_{x0}^* x_w^* \right)}, 0 \right)$ and (-1, 0).

3. For $x_w^* = q_{x0}^*$:

(a) If $0 < Q^* < Q_{c1}$, there are three stagnation points. Two symmetrical stagnation points are located inside the recharge area and one is outside the recharge area.

(b) If $Q^* > Q_{c1}$, there is only one stagnation point, which is located outside the recharge area.

(c) If $Q^* = Q_{c1}$, the two stagnation points locate exactly at the recharge boundary, namely, (1, 0) and (-1, 0).

Type of stagnation points

As described in the introduction, stagnation points may be maximum, minimum, or saddle points when recharge or infiltration is considered. Their roles in characterizing flow pattern have been widely studied (Winter TC, 1978; Anderson and Munte, 1981; Anderson, 2002; Bakker and Strack, 1996; Bear and Jacobs, 1965; Cheng and Anderson, 1994; Christ and Goltz, 2002; Erdmann, 1999; Javandel and Tsang, 1986; Nield et. al, 1994; Smith and Townley, 2002; Steward, 1999; Townley and Trefry, 2000; Fienen et. al,

2002; Jin and Steward, 2007). Since the Laplace equation is not satisfied for the recharge area, $x^{*2}+y^{*2}\le 1$, we use the Hessian-matrix method of the discharge potential to identify the type of stagnation points and determine the streamline orientations (Fienen et al., 2005). For the sake of completeness, we summarize the Hessian-matrix method in the Appendix A.1.

For simplicity, we identify the type of stagnation points for the case in which the well locates at the origin. Inside the recharge area, the dimensionless Hessian matrix of the discharge potential is given by

$$H^{*}=\begin{bmatrix} \dfrac{Q^{*}}{2}\dfrac{y^{*2}-x^{*2}}{\left(x^{*2}+y^{*2}\right)^{2}}-\dfrac{1}{2} & \dfrac{-Q^{*}x^{*}y^{*}}{\left(x^{*2}+y^{*2}\right)^{2}} \\ \dfrac{-Q^{*}x^{*}y^{*}}{\left(x^{*2}+y^{*2}\right)^{2}} & \dfrac{Q^{*}}{2}\dfrac{x^{*2}-y^{*2}}{\left(x^{*2}+y^{*2}\right)^{2}}-\dfrac{1}{2} \end{bmatrix} \tag{17}$$

Thus, at the stagnation points,

$$A=-\frac{Q^{*}}{2x_{s}^{*2}}-\frac{1}{2},\ B=0,\ C=\frac{Q^{*}}{2x_{s}^{*2}}-\frac{1}{2} \tag{18}$$

For the stagnation point at $\left(-\dfrac{q_{x0}^{*}}{2}+\sqrt{\dfrac{q_{x0}^{*\,2}}{4}+Q^{*}},0\right)$, we have

$$A<0,\ C>0 \tag{19}$$

The proof of (19) is given in Appendix A.2. According to the properties of the Hessian matrix (see Appendix A.1), this stagnation point is a saddle point and the orientation of the streamlines are x and y direction.

For the stagnation point at $\left(-\dfrac{q_{x0}^{*}}{2}-\sqrt{\dfrac{q_{x0}^{*\,2}}{4}+Q^{*}},0\right)$, we have

$$A<0,\ C<0 \tag{20}$$

The proof of (20) is given in the Appendix A.3. Thus, this stagnation point is a strict maximum, not a saddle point.

Outside the recharge area, the dimensionless Hessian matrix is given by:

$$H^* = \begin{bmatrix} \left(\frac{Q^*}{2} - \frac{1}{2}\right)\frac{y^{*2} - x^{*2}}{\left(x^{*2} + y^{*2}\right)^2} & \left(Q^* - 1\right)\frac{-x^* y^*}{\left(x^{*2} + y^{*2}\right)^2} \\ \left(Q^* - 1\right)\frac{-x^* y^*}{\left(x^{*2} + y^{*2}\right)^2} & \left(\frac{Q^*}{2} - \frac{1}{2}\right)\frac{x^{*2} - y^{*2}}{\left(x^{*2} + y^{*2}\right)^2} \end{bmatrix} \quad (21)$$

Thus, at the stagnation point, $\left(\frac{Q^* - 1}{q^*_{x0}}, 0\right)$, we have:

$$A = -C = \frac{1 - Q^*}{2x_s^{*2}}, \; B = 0 \quad (22)$$

This stagnation point is a saddle point with streamline orientation in x^* and y^* directions.

Consider the critical condition for pumping rate of the well. If $Q^* = 1 + q^*_{x0}$, two stagnation points, $\left(-\frac{q^*_{x0}}{2} + \sqrt{\frac{q^{*\,2}_{x0}}{4} + Q^*}, 0\right)$ and $\left(\frac{Q^* - 1}{q^*_{x0}}, 0\right)$ coincide at (1, 0), and both are saddle points. Applying the dimensionless Hessian matrix inside of the recharge area, i.e., Eq. (17), we obtain:

$$H^* = \begin{bmatrix} -\frac{q^*_{x0}}{2} - 1 & 0 \\ 0 & \frac{q^*_{x0}}{2} \end{bmatrix} \quad (23)$$

On the contrary, using the Hessian matrix outside the recharge area, i.e., Eq. (21), we get:

$$H^* = \begin{bmatrix} -\frac{q^*_{x0}}{2} & 0 \\ 0 & \frac{q^*_{x0}}{2} \end{bmatrix} \quad (24)$$

Thus, the curvatures at this point are discontinuous although both Hessian matrices define this stagnation point as a saddle point. This discontinuity results from the different governing equation used to solve for the discharge potential. Inside the recharge area, the Poisson equation is applied, but outside the recharge area, the Laplace equation is employed. The analytical solution of the dimensionless discharge potential, Eq. (4), is C1-continuous at the perimeter, but not C2-continuous, that is, the potential curvature is discontinuous. At dimensionless coordinates $(1, 0)$, the curvature is continuous in y^* direction because of the identical element $\frac{q^*_{x0}}{2}$ in the dimensionless Hessian matrices,

and discontinuous in x^* direction. Thus, this coincident point can be considered as a transition point between two saddle points, where the potential curvature in direction x^* changes abruptly.

If $Q^* = 1 - q_{x0}^*$ a saddle point $\left(\frac{Q^* - 1}{q_{x0}^*}, 0\right)$ and a maximum point $\left(-\frac{q_{x0}^*}{2} - \sqrt{\frac{q_{x0}^{*\,2}}{4} + Q^*}, 0\right)$ coincide at $(-1, 0)$. This point is also a transition point.

Applying Eq. (17), we obtain:

$$H = \begin{bmatrix} \frac{q_{x0}^*}{2} - 1 & 0 \\ 0 & -\frac{q_{x0}^*}{2} \end{bmatrix} \qquad (25)$$

Because $Q^* = 1 - q_{x0}^* > 0$ gives $q_{x0}^* < 1$, both eigenvalues are negative. Applying Eq. (21), the dimensionless Hessian matrix becomes

$$H^* = \begin{bmatrix} \frac{q_{x0}^*}{2} & 0 \\ 0 & -\frac{q_{x0}^*}{2} \end{bmatrix} \qquad (26)$$

One eigenvalue is positive and the other is negative. Thus, this coincident point is a transition point between a saddle point and a maximum point, where the potential curvature in direction x^* changes abruptly.

4 Case studies and discussion

To demonstrate the theoretical analyses presented above, we assign some specific values for *N*, *R* and q_{x0} to explore the stagnation points and the separation streamlines at different pumping rates for various cases discussed above. We assume that the recharge rate *N* is 5×10^{-6} *m/sec*, *R* is 20 *m*, and the regional flow rate q_{x0} is 10^{-5} m^2/sec. Thus, the value of dimensionless parameter q_{x0}^* is equal to 0.2.

In this case, $q_{x0}^* < 1$, that is, the infiltration rate is larger than equivalent regional flow rate on recharge area, which is more common found in most field conditions. With the changing of well location and pumping rates, the different numbers and locations of stagnation points are obtained, thus forming the different flow fields. The separation streamline are delineated by tracing streamlines from stagnation points, and the detail regarding this approach is given elsewhere (Fienen et al., 2005).

The well locates at the origin

Fig. 2 shows the stagnation points and the separation streamlines for different pumping rates when the well locates exactly at the origin. Dimensionless well pumping rates and coordinates of stagnation points are listed in Table 2. Fig. 2(a) shows if $Q^* < 1 - q_{x0}^*$, which means the pumping rate is smaller than the difference between the infiltration rate and equivalent regional flow rate on recharge area, there are three stagnation points. The transition point separates a saddle point and a maximum point, located outside and inside the recharge area, respectively. Infiltration not only supplies all the well pumping, but acts as a strong injection, which results in the separation streamlines outside the recharge area, thereby forcing the regional flow to travel outside the separation streamlines. Fig. 2(b) shows when $Q^* = 1 - q_{x0}^*$, two stagnation points can be obtained: one is a saddle point, located inside the recharge circle, and the other is a transition point, where a saddle point and a maxima point coincide. The "over-infiltration" is exactly pumped by the well and therefore separation streamlines form a closed cell. Fig. 2(c) shows if $1 - q_{x0}^* < Q^* < 1 + q_{x0}^*$, a saddle point is located inside the recharge area and the separation streamlines cannot contain the recharge circle. Fig. 2(d) indicates if $Q^* = 1 + q_{x0}^*$, that is, all infiltration and regional flow on recharge area are exactly pumped by the well, a saddle point is located at the perimeter of recharge circle and the separation streamlines are tangent to the recharge circle. Fig. 2(e) indicates if $Q^* > 1 + q_{x0}^*$, there is a stagnation point, which is a saddle point, located outside the recharge area and the separation streamlines contain the recharge circle. It can be physically interpreted as the well capturing all the infiltration and some regional flow because its pumping rate is larger than the total recharge and the regional flow received by the recharge circle.

The well does not locate at the origin

Figs. 3-5 delineate the stagnation points and the separation streamlines at different pumping rates for the wells locating at 2 *m*, 4 *m*, and 10 *m*， respectively. Their corresponding dimensionless coordinates are (0.1, 0), (0.2, 0) and (0.5, 0). Well pumping rates and coordinates of stagnation points are listed in Tables 3-5. Inspection of these figures and tables leads to the following conclusions.

1. Fig. 6 shows the relationship between the critical pumping rate and well location.

   As the well moves from the origin to the recharge perimeter, the lower critical pumping rate is linearly increased, and then linearly decreased after passing the well location (0.2, 0), ultimately reaching zero at the perimeter of the recharge area. For the higher critical pumping rate, however, the value is linearly decreased as the well moves from the origin to the dimensionless critical well location (0.2, 0), and then linearly increased after passing this point. Hence, the interval between the higher and lower critical pumping rate initially decreases, and then increases after passing the critical well location. It is noteworthy that at the critical well location, namely the point (0.2, 0), two critical pumping rates are exactly the same being 0.95.
2. An interesting phenomenon can be observed that at the critical well location, namely

$x_w^* = 0.2$, two stagnation points obtained inside the recharge area are symmetrical with respect to the origin under the condition that Q^* is less than the critical pumping rate. For example, at $Q^* = 0.56$, there are two symmetrical stagnation points (0.77, 0) and (-0.77, 0); at $Q^* = 0.88$, two symmetrical stagnation points (0.96, 0) and (-0.96, 0) are found; particularly, at critical pumping rate, two stagnation points locates exactly at the perimeter of the recharge circle.

3. At a low pumping rate, namely, for $x_w^* = 0.1$ and $Q^* < 0.88$, $x_w^* = 0.2$ and $Q^* < 0.95$, and $x_w^* = 0.5$ and $Q^* < 0.60$, there are always three stagnation points for each case, and without exception, one locates outside the recharge area and the rest situate inside the recharge area. Like the case where the well locates at the origin, infiltration not only supplies all the well pumping, but serves as a strong injection, which results in the separation streamlines outside the recharge area, thereby forcing the regional flow to travel outside the separation streamlines. At the same pumping rate Q^* where $Q^* \le 0.60$, as the well moves from the origin to the right, the stagnation point outside the recharge area moves gradually in the negative x^* direction, while two stagnation points inside the recharge area moves in the positive x^* direction.

4. At a high pumping rate, namely, for $x_w^* = 0.1$ and $Q^* > 1.08$, $x_w^* = 0.2$ and $Q^* > 0.95$, and $x_w^* = 0.5$ and $Q^* > 1.2$, there is always only one stagnation point, which locates outside the recharge area. This phenomenon is due to the fact that at a high pumping rate, all infiltration and partial regional flow are served as a supplier for pumping well, thus no additional infiltration acts on regional flow for resulting in the separation streamline outside the recharge area. Besides, for the condition that the well locates inside the recharge area with the same pumping rate Q^* where $Q^* > 1.2$, as the well moves from the origin to the right, the stagnation point outside the recharge area moves gradually in the positive x^* direction.

5. As well location moves from the origin to the infiltration perimeter, comparing the streamlines and stagnation points at $Q^* = 0.95$ for each case, two "tails" outside the recharge area are becoming more and more closer, and then form a closed circle which surrounds the recharge area under the condition that the well locates at the dimensionless critical well location (0.2, 0); eventually the closed cell moves to the right and includes partial regional flow and excludes some recharge area, which results in the separation streamlines outside the recharge area and forms the third stagnation point.

6. With the exception of the case where the well locates at dimensionless point (0.5, 0), there are two stagnation points obtained at the lower critical pumping rate. For the case where the well locates at the point (0.1, 0), one stagnation point locates at (0.90, 0) and the other locates at (-1, 0). For the well located at the critical well location (0.2, 0), two stagnation point locates at (1, 0) and (-1, 0), respectively. However, at

the lower critical pumping rate, as can be seen from Fig. 5(c), there are three stagnation points obtained for the well located at the point (0.5, 0). This may be because the lower critical pumping rate under that condition is so weak that infiltration is surplus for providing the well extraction, which produces the separation streamlines outside the recharge area and eventually forms the third stagnation point. Note that if $x_w^* \geq 0$ and Q^* equals to the lower or higher critical pumping rate, at least one stagnation point locates at the perimeter of recharge circle. On the other hand, except for the well location of (0.5, 0), at the higher critical pumping rate, there is one stagnation point obtained. For the well located at (0.5, 0), however, there are two stagnation points, as can be seen from Fig. 5(d). The closed cell inside the recharge area denotes a dividing curve of pure infiltration and a mixture of infiltration and regional flow, that is, inside the closed cell, there is only infiltration, and outside the curve, there is a mixture of infiltration and regional flow.

7. As analytically shown previously, the stagnation points in $(-\infty, -1)$ and (-1, 0) co-exist, and there is one, and only one stagnation point in $(0, +\infty)$. For example, as $x_w^* = 0.5$, for $Q^* = 0.48$, there are two stagnation points (-0.63, 0) and (-2.95, 0), located in $(-\infty, -1)$ and (-1, 0), respectively. However, for the interval of $(0, +\infty)$, there is only one stagnation, located at (0.93, 0).

Analyses about the case where the well locates at the left of the origin can be made by the similar method presented above. However, for negative value of x_w^*, we have another constraint for the stagnation point located outside the recharge area, namely, $\left(Q^* + q_{x0}^* x_w^* - 1\right)^2 + 4q_{x0}^* x_w^* \geq 0$. In other words, the pumping rate interval derived for stagnation points outside the recharge area should be implicitly subject to this constraint. As an example, we delineate the stagnation points and separation streamlines for the case where the well locates at (-0.5, 0) with a dimensionless critical pumping rate of 0.40, as can be seen in Fig. 7.

5 Conclusion

We have presented a thorough stagnation-point analysis for a single pumping well in recharge areas. For the case where the well locates at the origin, we have performed critical pumping rate analysis and calculated the stagnation points for each critical pumping rate interval. According to the characteristics of the Hessian matrix, we also identified the nature of each stagnation point. For the well arbitrarily located, we also presented the critical pumping rate analysis although it appears to be more complicated than the previous case. By performing the stagnation-point analysis, one can realize that the condition of flow field is determined not only by the magnitude of the single dimensionless parameter such as Q^*, q_{x0}^*, and x_w^*, but also related to the relative magnitude between q_{x0}^* and x_w^*. In the end, we delineated the streamlines for a given case with different well locations and pumping rates. Starting points for tracing separation streamlines are found by offsetting slightly along these directions from the stagnation points. Since the problems that velocity is zero at the stagnation points are

eliminated, the separation streamline can be constructed directly by streamline-tracing methods. In summary, for a well inside the recharge area with a relatively low pumping rate, there are always three stagnation points, because the unpumped infiltration produces the separation streamlines outside the recharge area and eventually forms the third stagnation point. However, for the well with a relatively high pumping rate, there is one, and only one stagnation point outside the recharge area, for all infiltration and partial regional flow are extracted by the well.

Acknowledgements

This work was partially funded by Georgia Water Resources Institute, and partially funded by the National Institutes of Water Resources (NIWR) and U.S. Geological Survey (USGS) under project ID 2007GA165G.. The authors would like to thank Dr. M.N. Fienen for his helpful discussion. The authors are very grateful for the helpful review comments from two anonymous reviewers.

Appendix.

A.1 Hessian matrix method for flow field with recharge or drainage (Fienen et al., 2005)

In the presence of regional infiltration or drainage the discharge potential satisfies the Poisson equation, and the complex potential cannot be used to characterize the flow field. On this condition, we use the discharge potential, $\Phi(x, y)$, rather than complex potential, in order to identify the direction of the streamlines passing through stagnation points.

Consider the symmetric matrix formed by the second derivatives of the discharge potential:

$$H = \begin{bmatrix} \dfrac{\partial^2 \Phi}{\partial x^2} & \dfrac{\partial^2 \Phi}{\partial x \partial y} \\ \dfrac{\partial^2 \Phi}{\partial x \partial y} & \dfrac{\partial^2 \Phi}{\partial y^2} \end{bmatrix} \tag{A1}$$

This matrix is known as the Hessian of $\Phi(x, y)$ and describes the curvature of Φ at a specific point. The larger the absolute value of the second derivative, the more curved the surface $\Phi(x, y)$. The sign determines convexity or concavity. A positive second derivative means convexity, $\cup$, while a negative one means concavity, $\cap$. If the first derivative is zero, then the diagonal elements determine whether we have a maximum, a minimum, or an inflection point along a certain direction.

In order to interpret the application of the Hessian matrix, we choose the origin of the coordinate system at a stagnation point. Then, in the vicinity of the stagnation point, where $\dfrac{\partial \Phi}{\partial x} = \dfrac{\partial \Phi}{\partial y} = 0$, the potential can be approximated by truncated Taylor expansion:

$$\Phi(x, y) = \Phi(0, 0) + \frac{1}{2}\frac{\partial^2 \Phi}{\partial x^2} x^2 + \frac{1}{2}\frac{\partial^2 \Phi}{\partial y^2} y^2 + \frac{\partial^2 \Phi}{\partial x \partial y} xy \tag{A2}$$

$$= \frac{A}{2} x^2 + Bxy + \frac{C}{2} y^2 + D$$

and thus the Hessian matrix is

$$H = \begin{bmatrix} A & B \\ B & C \end{bmatrix} \tag{A3}$$

This matrix has eignvalues

$$\lambda_1 = \frac{A}{2} + \frac{C}{2} + \frac{1}{2}\sqrt{A^2 - 2AC + C^2 + 4B^2} \tag{A4}$$

$$\lambda_2 = \frac{A}{2} + \frac{C}{2} - \frac{1}{2}\sqrt{A^2 - 2AC + C^2 + 4B^2} \tag{A5}$$

with corresponding eigenvectors that define lines with the following slopes:

$$tan(\theta_1) = \frac{A - C + \sqrt{A^2 - 2AC + C^2 + 4B^2}}{2B} \tag{A6}$$

$$tan(\theta_2) = \frac{A - C - \sqrt{A^2 - 2AC + C^2 + 4B^2}}{2B} \tag{A7}$$

Transforming the system if coordinates are different from the *x* and *y* directions to the direction of the eigenvectors, the Hessian matrix becomes a diagonal matrix with eigenvalues λ_1 and λ_2 as entries. Thus, the eigenvalues, λ_1 and λ_2 reveal the nature of the potential at the stagnation point. According to the properties of the Hessian matrix, the following conclusions can be drawn:

1. $\lambda_1 \lambda_2 < 0$: The point is a saddle point.

2. $\lambda_1 < 0$ and $\lambda_2 < 0$: The point is a strict maximum.

3. $\lambda_1 > 0$ and $\lambda_2 > 0$: The point is a strict minimum.

4. $\lambda_1 = 0$ or $\lambda_2 = 0$: The point is an inflection point along the direction of the corresponding eigenvalue.

5. $\lambda_1 = \lambda_2 = 0$: No conclusion about the nature of the potential at the point can be drawn. However, this is a rare case, and is not considered further.

A.2 Proof of Inequality (19)

At the stagnation point $\left(-\frac{q_{x0}^*}{2}+\sqrt{\frac{q_{x0}^{*\,2}}{4}+Q^*},0\right)$,

$$q_{x0}^* < \sqrt{q_{x0}^{*\,2}+4Q^*} \tag{A.8}$$

which can be written as

$$2q_{x0}^{*\,2} < 2q_{x0}^*\sqrt{q_{x0}^{*\,2}+4Q^*} \tag{A.9}$$

Thus,

$$q_{x0}^{*\,2} - 2q_{x0}^*\sqrt{q_{x0}^{*\,2}+4Q^*} + q_{x0}^{*\,2} + 4Q^* < 4Q^* \tag{A.10}$$

Then,

$$\left(-q_{x0}^* + \sqrt{q_{x0}^{*\,2}+4Q^*}\right)^2 < 4Q^* \tag{A.11}$$

and

$$x_s^{*2} = \left(-\frac{q_{x0}^*}{2}+\sqrt{\frac{q_{x0}^{*\,2}}{4}+Q^*}\right)^2 < Q^* \tag{A.12}$$

For element A in the Hessian matrix, $A=-\frac{Q^*}{2x_s^{*2}}-\frac{1}{2}$, is always negative because Q^* and x_s^{*2} are positive. For element C, replacing with inequality (A.12), we have

$$C=\frac{Q^*}{2x_s^{*2}}-\frac{1}{2}>0 \tag{A.13}$$

A.3 Proof of Inequality (20)

At the stagnation point $\left(-\frac{q_{x0}^*}{2}+\sqrt{\frac{q_{x0}^{*\,2}}{4}+Q^*},0\right)$, we have

$$x_s^{*2} = \left(-\frac{q_{x0}^*}{2} + \sqrt{\frac{q_{x0}^{*\,2}}{4} + Q^*} \right)^2 > Q^* \qquad \text{(A.14)}$$

Thus,

$$C = \frac{Q^*}{2x_s^{*2}} - \frac{1}{2} < 0 \qquad \text{(A.15)}$$

References

Aderson, E.I., 2002. An analytic solution representing groundwater-surface water interaction. Water Resour. Res. 39(3), 1071-1078.

Aderson, M.P., Munter, J.A., 1981. Seasonal reversals of groundwater flow around lakes and the relevance to stagnation points and lake budget. Water Resour. Res. 17(4), 1139-1150.

Bear, J., 1979. Hydraulics of Groundwater. New York: McGraw-Hill Book Co.

Bear, J., Jacobs, M., 1965. On the movement of water bodies injected into aquifers. J. Hydrol. 32(5), 1309-1315.

Bakker, M., Strack, O.D.L., 1996. Capture zone delineation in two-dimensional groundwater flow models. Water Resour. Res. 32 (5), 1309-1315.

Bair, E.S., Springer, A.E., Roadcap, G.S., 1991. Delineation of travel-time-related capture areas of wells using analytical flow models and particle-tracking analysis. Ground Water 29 (3), 387-397.

Cheng, X., Anderson, M.P., 1994. Simulating the influence of lake position on groundwater fluxes. Water Resour. Res. 30(7), 2041-2049.

Christ, J.A., Goltz, M.N., 2004. Containment of groundwater contamination plumes: minimizing drawdown by aligning capture wells parallel to regional flow. J. Hydrol. 286, 52-68.

Cunningham, J.A., Hoelen, T.P., Hopkins, G.D., Lebron C.A., Reinhard, M., 2004. Hydraulics of recirculating well pairs for ground water remediation. Ground Water 42(6), 880-889.

Cirpka, O.A., Frind, E.O., Helming, R., 1999. Streamline-oriented grid-generation for transport modeling in two-dimensional domains including wells. Adv. Water Resour. 22 (7), 697-710.

Christ, J.A., Goltz, M.N., Huang, J., 1999. Development and application of an analytical model to aid design and implementation of *in situ* remediation technologies. J. Contam. Hydrol. 37(3-4), 295-317.

Christ, J.A., Goltz, M.N., 2002. Hydraulic containment: analytical and semi-analytical models for capture zone curve delineation. J. Hydrol. 262 (1-4), 224-244.

Cole, B.E., Silliman, S.E., 2000. Utility of simple models for capture zone delineation in heterogeneous unconfined aquifers. Ground water 38 (5), 665-672.

Erdmann, J., 1999. On capture width and capture zone gaps in multiple-well systems. Ground Water 38(4), 497-504.

Fienen, M.N., Luo, J., Kitanidis, P.K., 2005. Semi-analytical homogeneous anisotropic capture zone delineation. J. Hydrol. 312 (1-4), 39-50.

Garrido, A., Martinez-Santos, P., Llamas, M.R., 2006. Groundwater irrigation and its implications for water policy in semiarid countries: the Spanish experience. Hydrol. J. 14(3), 340-349.

Hantush, M.S., 1965. Wells near streams with semipervious beds. J. Geophys. Res. 70, 2829-2838.

Intaraprasong, T., Zhan H., 2007. Capture zone between two streams. 338, 297-307.

Javandel, I., Tsang, C.F., 1986. Capture zone type curves: a tool for aquifer cleanup. Ground water 24 (5), 616-625.

Jin, W., Steward, D.R., 2007. The transition of flow patterns through critical stagnation points in two-dimensional groundwater flow. Adv. Water Resour. 30, 16-28.

Lerner, D.N., 1992. Well catchments and time-of-travel zones in aquifers with recharge. Water Resour. Res. 28 (10), 2621-2628.

Luo J., Kitanidis P.K., 2004. Fluid residence times within a recirculation zone created by an extraction-injection well pair. J. Hydrol. 295(1-4), 149-162.

Luo J., Wu, W.M., Fienen, M.N., Jardine, P.M., Mehlhorn, T.L., Watson, D.B., Cirpka, O.A., Criddle, C.S., Kitanidis P.K., 2006. A nested-cell approach for in situ remediation. Ground Water 44(2), 266-274.

Muskat, M., 1946. The Flow of Homogeneous Fluids through Porous Media. J.W. Edwards, Ann Arbor, USA.

Nield, S.P., Townley, L.R., Barr, A.D., 1994. A framework for quantitative analysis of surface water-groundwater interaction: flow geometry in a vertical section. Water Resour. Res. 30(8), 2461-2475.

Newsom, J.M., Wilson, J.L., 1988. Flow of ground water to a well near a stream-effect of ambient ground-water flow direction. Ground Water 26 (6), 703-711.

Shan, C., 1999. An analytical solution for the capture zone of two arbitrarily located wells. J. Hydrol. 222 (1-4), 123-128.

Steward, D.R., 1999. Three-dimensional analysis of the capture of contaminated leachate by fully penetrating, partially penetrating, and horizontal wells. Water Resour. Res. 35(2),461-468.

Strack, O.D.L., 1989. Groundwater Mechanics. Englewood Cliffs, NJ: Prentice-Hall.

Smith, A.J., Townley, L.R., 2002. Influence of regional setting on interaction between shallow lakes and aquifers. Water Resour. Res. 38(9), 1170.

Schaferperini, A.L., Wilson, J.L., 1991. Efficient and accurate front tracking for two-dimensional groundwater models. Water Resour. Res. 27 (7), 1471-1485.

Townley, L.R., Trefry, M.G., 2000. Surface water-groundwater interaction near shallow circular lakes: flow geometry in three dimensions. Water Resour. Res. 36(4), 935-949.

Winter T.C., 1978. Numerical simulation of steady state three-dimensional groundwater flow near lakes. Water Resour. Res. 4(2), 245-254.

Wilson J.L., 1993. Induced infiltration in aquifers with ambient flow. Water Resour. Res. 29 (10), 3503-3512.

Zhan, H., 1999a. Analytical and numerical modeling of a double-well capture zone. Math. Geol. 31 (2), 175-193

Zhan, H., 1999b. Analytical study of capture time to a horizontal well. J. Hydrol. 217, 46-54.

Zhan, H., Zlotnik, V.A., 2002. Ground water flow to horizontal and slanted wells in unconfined aquifers. Water Resour. Res. 38 (7), 1108, doi: 10.1029/2001WR000401.

Zheng, C., Bennett, G., 2002. Applied Contaminant Transport Modeling, Theory and Practice (Second ed.). New York: John Wiley and Sons, Inc.

Table 1
Well Pumping rates associated with the number and location of the stagnation points.

			Pumping rate Q^*	Location of the stagnation point (x_s^*)						TSP[a]
				$(-\infty,-1)$	-1	$(-1,0)$	$(0,-1)$	1	$(1,-\infty)$	
$q_{x0}^* \le 1$	$0 < x_w^* < 1$	$x_w^* < q_{x0}^*$	$0 < Q^* < Q_{c2}$	x		x	x			3
			$Q^* = Q_{c2}$		x		x			2
			$Q_{c2} < Q^* < Q_{c1}$				x			1
			$Q = Q_{c1}$					x		1
			$Q^* > Q_{c1}$						x	1
		$x_w^* > q_{x0}^*$	$0 < Q^* < Q_{c1}$	x		x	x			3
			$Q = Q_{c1}$	x		x		x		3
			$Q_{c1} < Q^* < Q_{c2}$	x		x			x	3
			$Q^* = Q_{c2}$		x				x	2
			$Q^* > Q_{c2}$						x	1
		$x_w^* = q_{x0}^*$	$0 < Q^* < Q_{c1}$	x		x	x			3
			$Q = Q_{c1}$		x			x		2
			$Q^* > Q_{c1}$						x	1
	$x_w^* \ge 1$		$0 < Q^* < Q_{c2}$	x		x			x	3
			$Q^* = Q_{c2}$		x				x	2
			$Q^* > Q_{c2}$						x	1
$q_{x0}^* > 1$	$0 < x_w^* < 1$		$0 < Q^* < Q_{c1}$				x			1
			$Q = Q_{c1}$					x		1
			$Q^* > Q_{c1}$						x	1
	$x_w^* = 1$		$Q^* > 0$						x	1

[a] TSP = Total number of stagnation points.

Table 2
Dimensionless well pumping rates and coordinates of stagnation points ($x_w^* = 0$)

	Q^*	(x_s^*, y_s^*)
(a). $Q^* < 1 - q_{x0}^*$	0.53	(0.64, 0), (-0.84, 0), (-2.33, 0)
(b). $Q^* = 1 - q_{x0}^*$	0.8	(0.8, 0), (-1,0)
(c). $1 - q_{x0}^* < Q^* < 1 + q_{x0}^*$	0.95	(0.88, 0)
(d). $Q^* = 1 + q_{x0}^*$	1.2	(1, 0)
(e). $Q^* > 1 + q_{x0}^*$	1.44	(2.20, 0)

Table 3
Dimensionless well pumping rates and coordinates of stagnation points ($x_w^* = 0.1$)

	Q^*	(x_s^*, y_s^*)
(a). $Q^* < Q_{c2}$	0.56	(0.71, 0), (-0.81, 0), (-2.33, 0)
(b). $Q^* = Q_{c2}$	0.88	(0.90, 0), (-1, 0)
(c). $Q_{c2} < Q^* < Q_{c1}$	0.95	(0.94, 0)
(d). $Q^* = Q_{c1}$	1.08	(1, 0)
(e). $Q^* > Q_{c1}$	1.44	(2.47, 0)

Table 4
Dimensionless well pumping rates and coordinates of stagnation points ($x_w^* = 0.2$)

	Q^*	(x_s^*, y_s^*)
(a). $Q^* < Q_{c1}$	0.56	(0.77, 0), (-0.77, 0), (-2.43, 0)
(b). $Q^* < Q_{c1}$	0.88	(0.96, 0), (-0.96, 0), (-1.23, 0)
(c). $Q^* = Q_{c1}$	0.95	(1, 0), (-1, 0)
(d). $Q^* > Q_{c1}$	1.08	(1.35, 0)
(e). $Q^* > Q_{c1}$	1.44	(2.73, 0)

Table 5
Dimensionless well pumping rates and coordinates of stagnation points ($x_w^* = 0.5$)

	Q^*	(x_s^*, y_s^*)
(a). $Q^* < Q_{c1}$	0.48	(0.93, 0), (-0.63, 0), (-2.95, 0)
(b). $Q^* = Q_{c1}$	0.60	(1, 0), (-0.70, 0), (-2.50, 0)
(c). $Q_{c1} < Q^* < Q_{c2}$	0.95	(1.73, 0), (-0.89, 0), (-1.45, 0)
(d). $Q^* = Q_{c2}$	1.2	(2.50, 0), (-1, 0)
(e). $Q^* < Q_{c2}$	1.44	(3.40, 0)

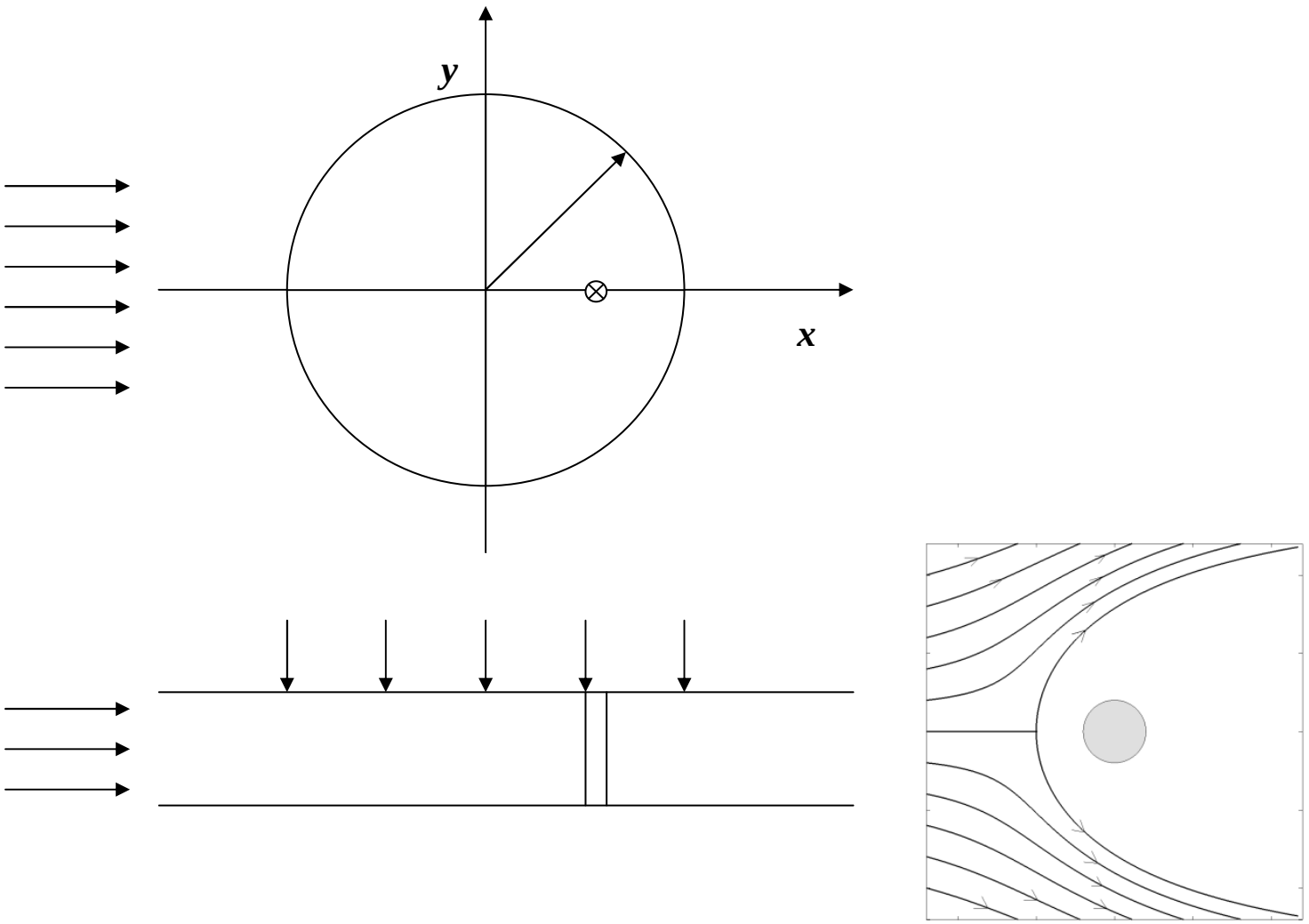

Fig. 1. Plan view and cross section of an extraction well in a uniform regional flow with constant infiltration rate. The right figure shows a flow field with recharge, regional flow and no pumping well. The gray circle represents the infiltration zone.

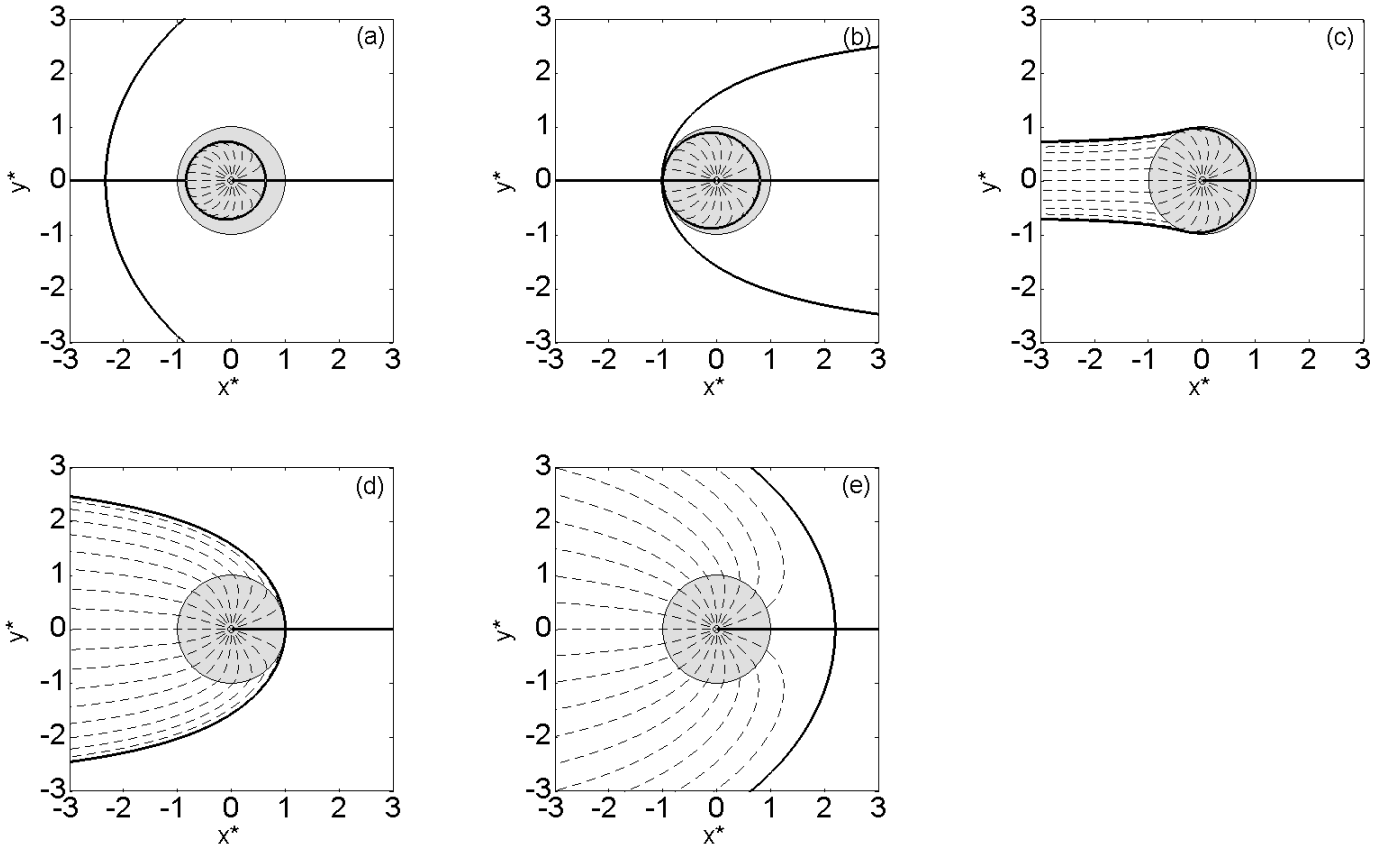

Fig. 2. Stagnation points and separation streamlines for the case where the well locates at the origin. The dark solid lines are separation streamlines, the dashed lines are streamlines plotted by backward tracing from the extraction. The gray circle represents the infiltration zone. (a) Q^* = 0.53, (b) Q^* = 0.8, (c) Q^* = 0.95, (d) Q^* = 1.2, and (e) Q^* = 1.44.

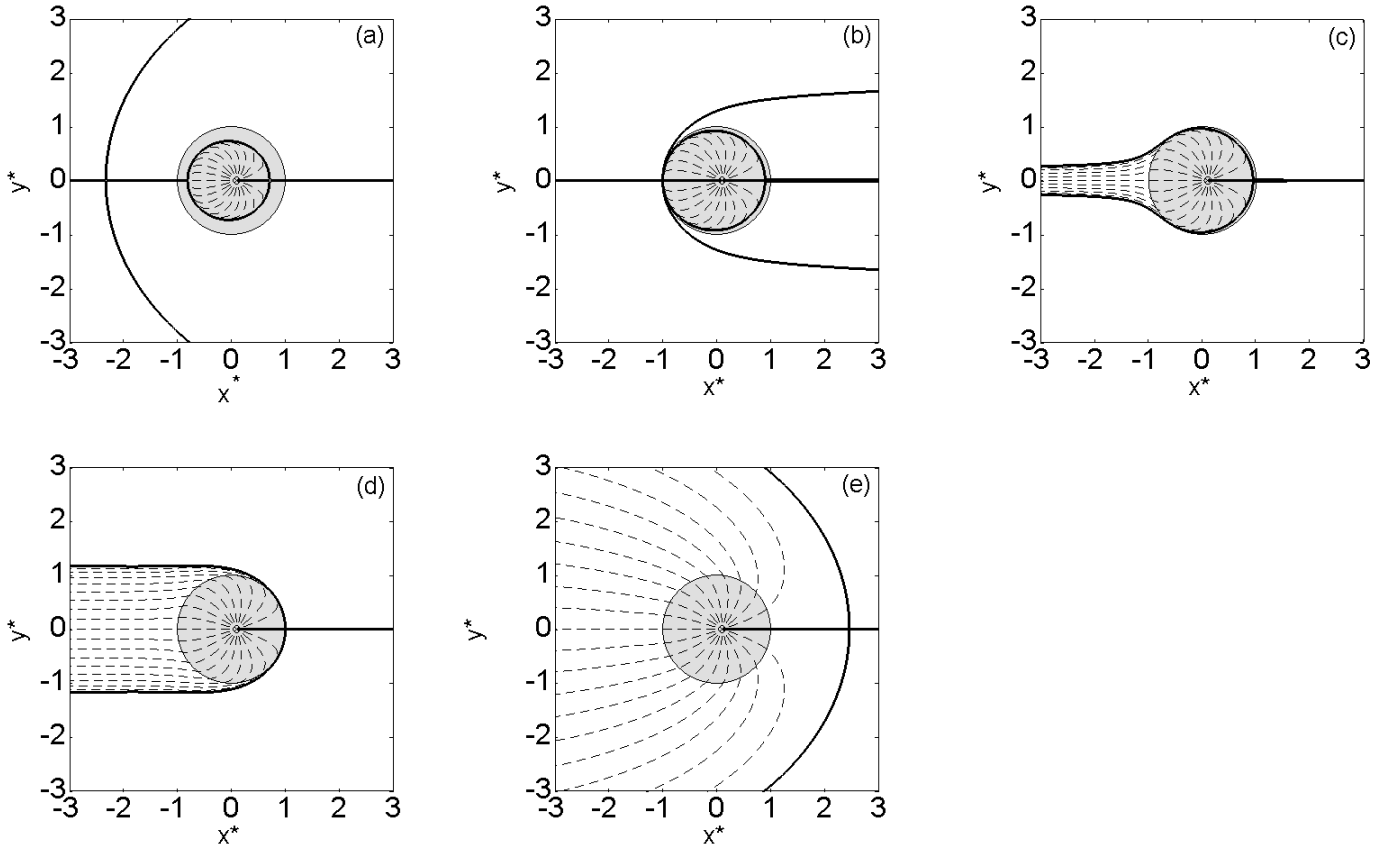

Fig. 3. Stagnation points and separation streamlines for the case where the well locates at the dimensionless point (0.1, 0). The dark solid lines are separation streamlines, the dashed lines are streamlines plotted by backward tracing from the extraction. The gray circle represents the infiltration zone. (a) Q^* = 0.56, (b) Q^* = 0.88, (c) Q^* = 0.95, (d) Q^* = 1.08, and (e) Q^* = 1.44.

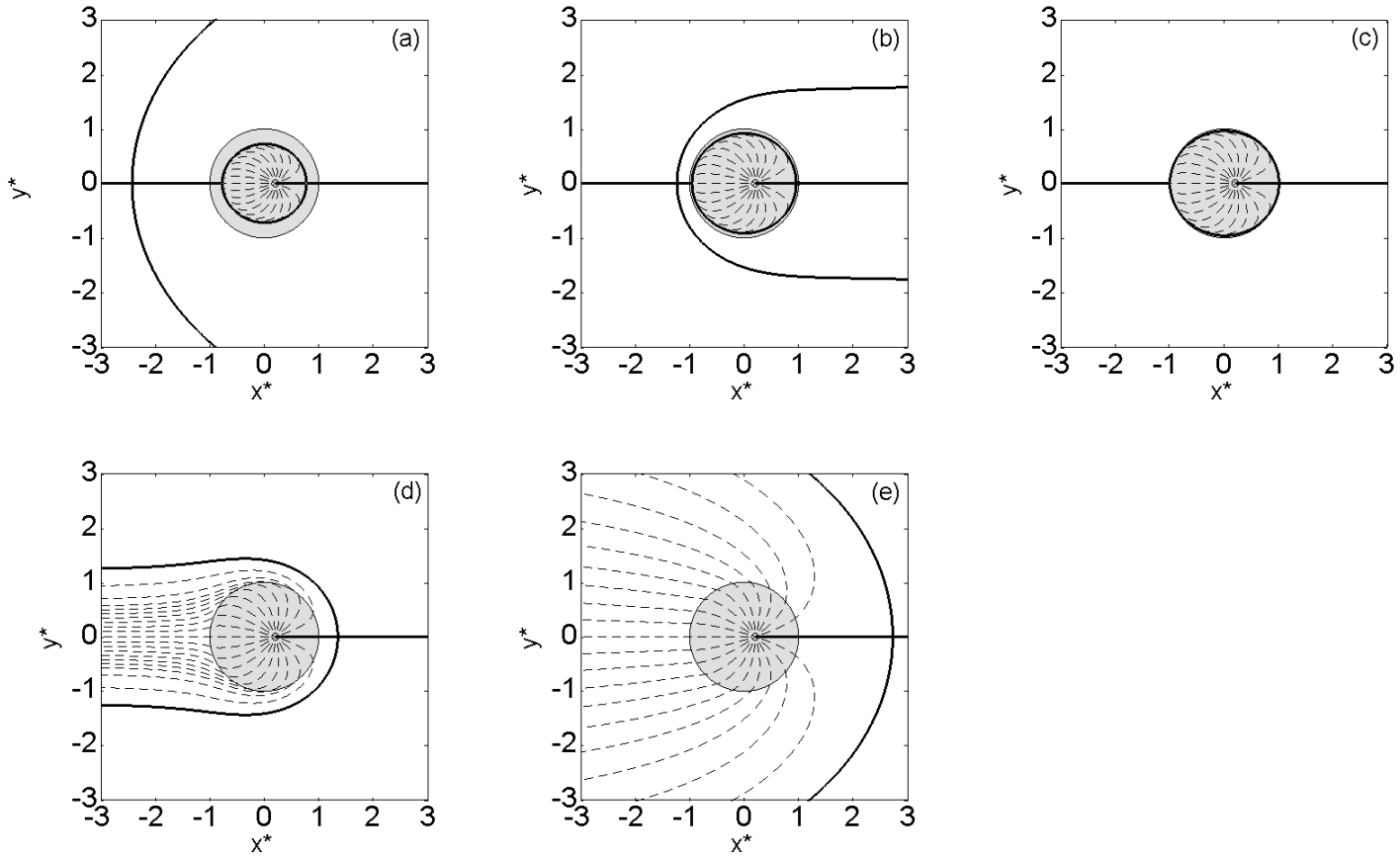

Fig. 4. Stagnation points and separation streamlines for the case where the well locates at the dimensionless point (0.2, 0). The dark solid lines are separation streamlines, the dashed lines are streamlines plotted by backward tracing from the extraction. The gray circle represents the infiltration zone. (a) Q^* = 0.56, (b) Q^* = 0.88, (c) Q^* = 0.95, (d) Q^* = 1.08, and (e) Q^* = 1.44.

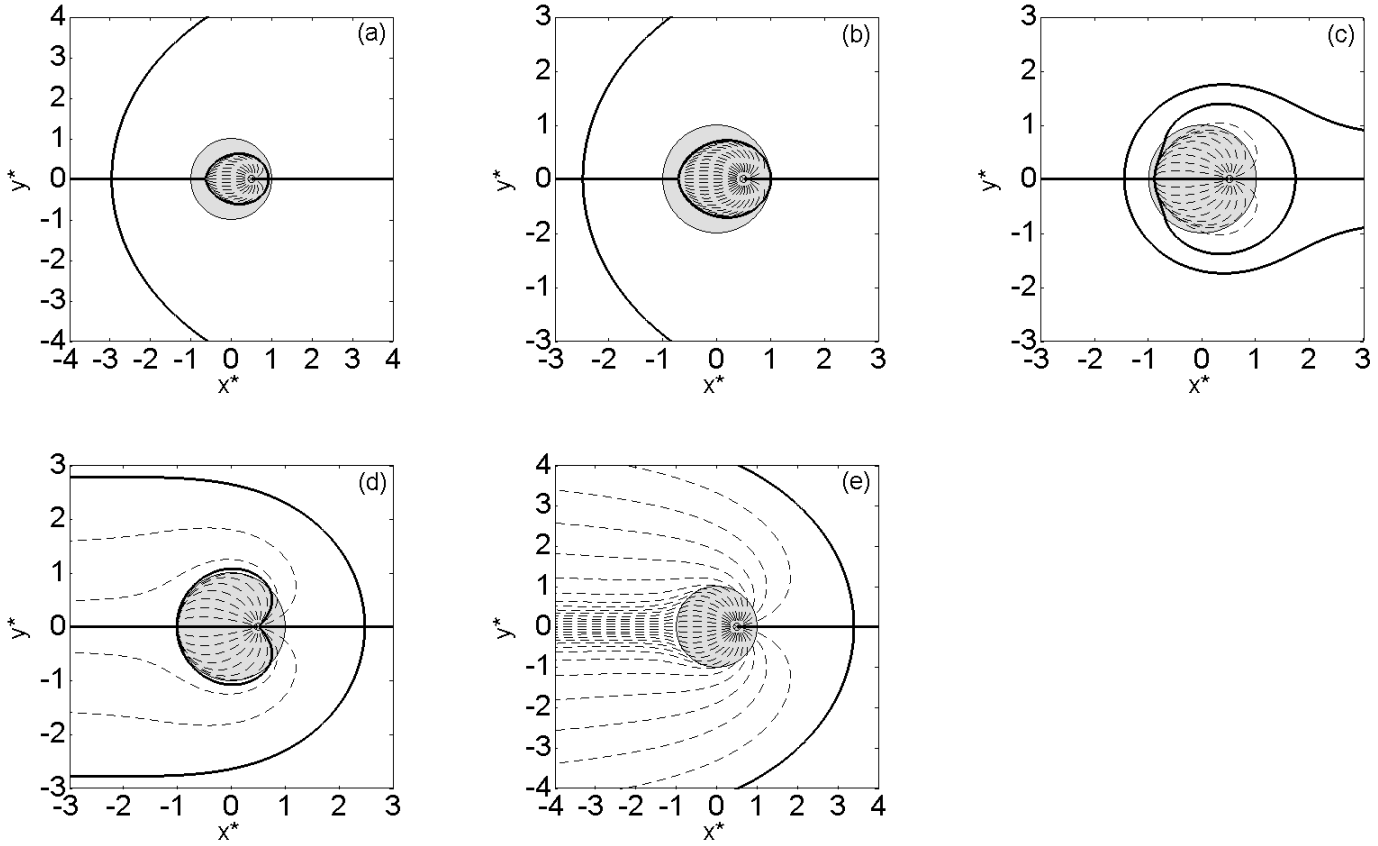

Fig. 5. Stagnation points and separation streamlines for the case where the well locates at the point (10, 0). The dark solid lines are separation streamlines, the dashed lines are streamlines plotted by backward tracing from the extraction. The gray circle represents the infiltration zone. (a) Q^* = 0.48, (b) Q^* = 0.60, (c) Q^* = 0.95, (d) Q^* = 1.2, and (e) Q^* = 1.44.

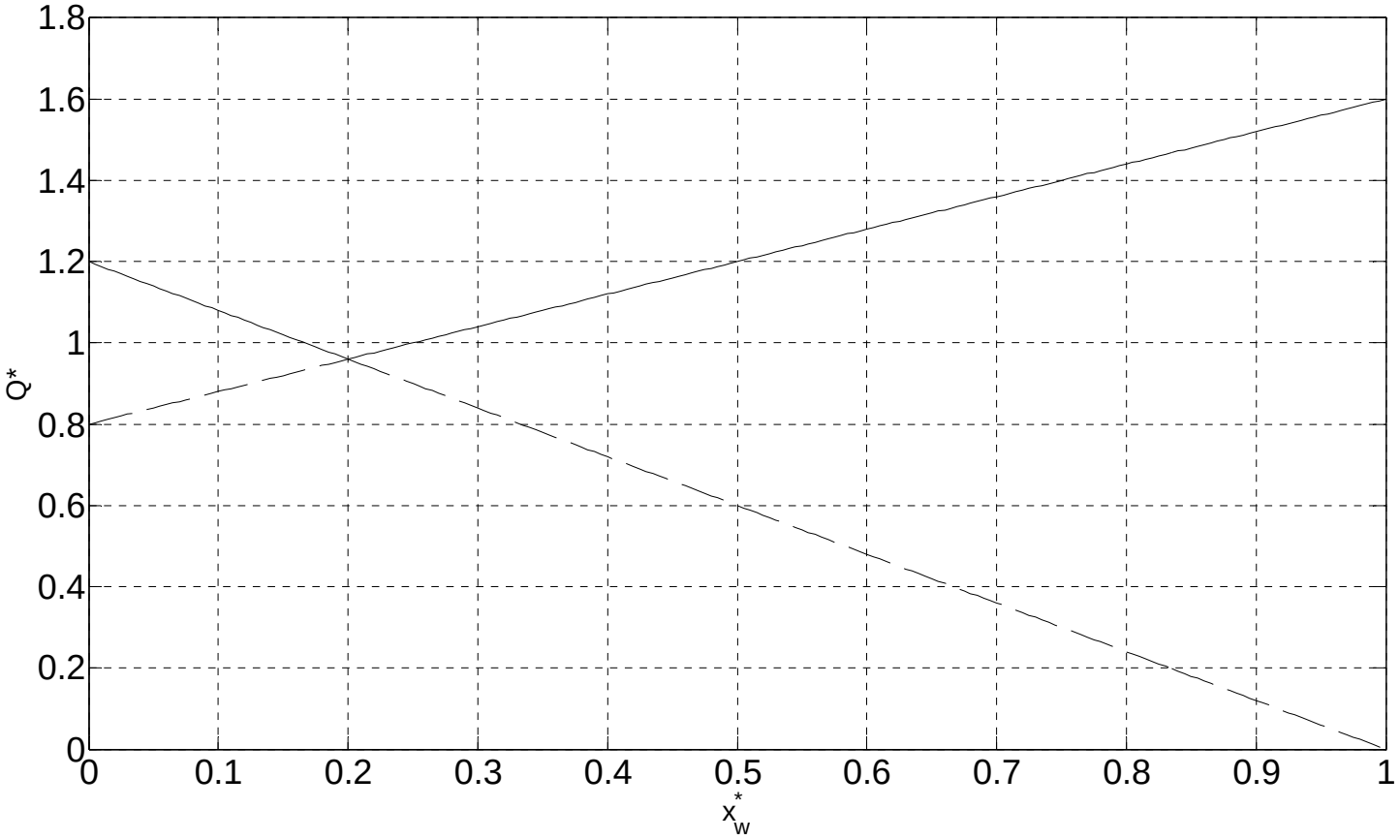

Fig.6. The relationship between the dimensionless critical pumping rate and well location. The dashed line denotes the lower critical pumping rate, and the solid line represents the higher critical pumping rate.

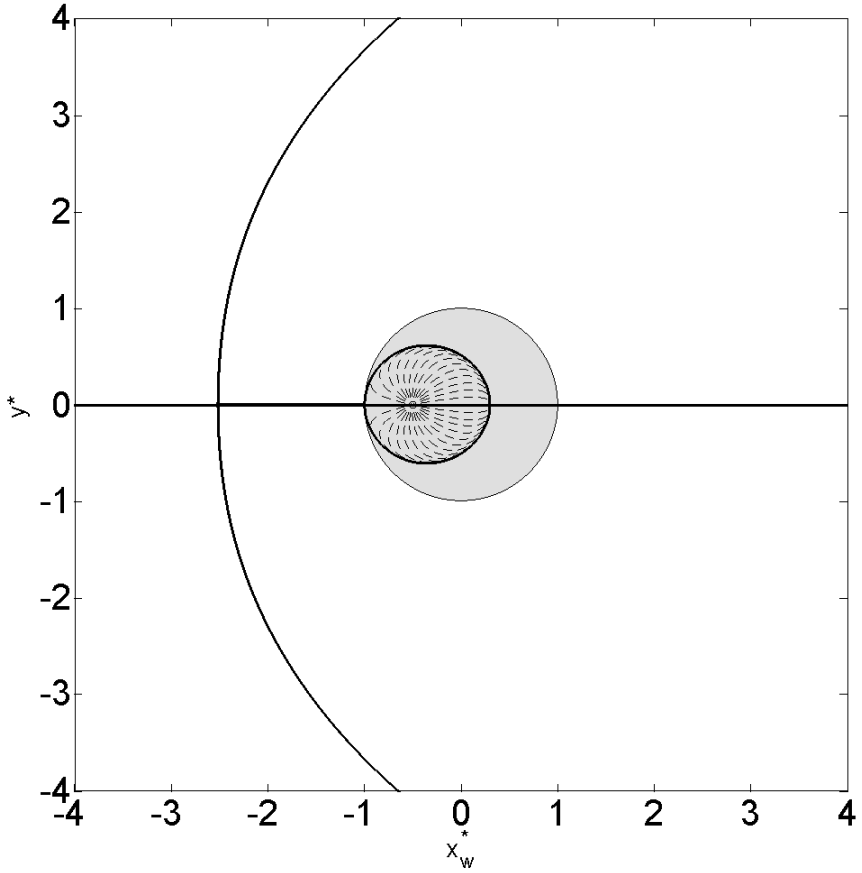

Fig. 7. Stagnation points and separation streamlines for the case where the well locates at the point (-0.5, 0) with a critical pumping arte of 2.5 *L/sec*. The dark solid lines are separation streamlines, the dashed lines are streamlines plotted by backward tracing from the extraction. The gray circle represents the infiltration zone.

Assessing the impacts of a major wildfire in the Okefenokee Swamp on mercury levels in resident macroinvertebrates and mosquitofish

Basic Information

Title:	Assessing the impacts of a major wildfire in the Okefenokee Swamp on mercury levels in resident macroinvertebrates and mosquitofish
Project Number:	2008GA175B
Start Date:	3/1/2009
End Date:	2/28/2010
Funding Source:	104B
Congressional District:	10
Research Category:	Water Quality
Focus Category:	Wetlands, Drought, Toxic Substances
Descriptors:	
Principal Investigators:	Darold Paul Batzer

Publications

1. Beganyi, S. R. 2010. The effects of fire on the community composition and mercury concentrations of aquatic macroinvertebrates in the Okefenokee Swamp, southeast Georgia. MS thesis, University of Georgia, Athens
2. Beganyi, S. R. and D. P. Batzer. 2009. The effects of fire on the community composition and mercury concentrations of aquatic macroinvertebrates in the Okefenokee Swamp, southeast Georgia: Study design. Proceedings of the 2009 Georgia Water Resources Conference, Athens, GA. p. 288-292.

Title: **Assessing the impacts of a major wildfire in the Okefenokee Swamp on mercury levels in resident macroinvertebrates and mosquitofish**

Author: **Darold P. Batzer, Professor of Entomology, University of Georgia, Athens**

Period of Performance: **March 1, 2009 to February 28, 2010**

EXECUTIVE SUMMARY

Fire is an important disturbance in the Okefenokee Swamp. From April–June 2007, wildfire burned 75% of the wetland area. With the existence of extensive pre-fire data sets on community structure and total mercury of invertebrates, the fire presented an opportunity to assess impacts of wildfire on invertebrates from the Okefenokee. Post-fire collection of samples occurred in September, December, and May, 2007–2009. Sample sites included 13 burned and 8 non-burned (reference) sites. Comparisons of data among pre-fire, post-fire reference, and post-fire burned sites permitted assessment of wildfire effects on the community composition of invertebrates and total mercury of select organisms (amphipods, crayfish, odonates, mosquitofish). NMS ordinations and ANOSIM tests suggested that habitat was an important factor; communities in burned cypress differed from reference cypress (driven by certain indicator organisms). Unexpectedly, burned sites had lower mercury concentrations in odonates and crayfish, with variation again being greatest in cypress stands.

LIST OF FIGURES

LIST OF TABLES

Table 2: Two-way crossed ANOSIM tests for burn category and time, or habitat suggest that habitat is a significant factor. Asterisks indicate significant p-values (<0.05).

PROJECT SCOPE AND OBJECTIVES

Wildfire is noted as a significant disturbance in many ecosystems; it can dynamically change ecosystem structure and function. The significance of fire has been well studied in terrestrial systems, but comprehensive studies in aquatic systems are long overdue. Fire can directly and indirectly affect aquatic systems and it may take years to recover from fire (Gresswell, 1999; Minshall, 2003). Studies suggest changes after fire include a shift in the dominant invertebrate taxa after fire (Minshall, 2003; deSzalay & Resh, 1997), increases in nutrient levels (Scrimgeour et al., 2001), and releases of mercury into the water column for uptake by biota (Kelly et al., 2006). Many wetlands in the United States burn regularly (Middleton, 1999); however, little emphasis has been placed on the impacts of wildfire in wetland systems and even less on how fire affects macroinvertebrate community composition and mercury levels in aquatic organisms.

Wildfire near streams in Yellowstone National Park caused a shift of the invertebrate community toward dominance by disturbance adapted organisms with foodwebs containing a greater number of generalists in burned streams when compared to reference streams (Minshall, 2003). Recently burned Canadian Shield lakes had greater total benthic macroinvertebrate biomass and Chironomidae biomass than in reference lakes (Scrimgeour et al., 2001). Multiple studies (Kelly et al., 2006; Scrimgeour et al., 2001) found fire associated nutrient releases into the water column.

Today, some wetlands are managed with prescribed fire to promote aquatic invertebrate communities and plant species important to waterfowl (de Szalay & Resh, 1997; Davis & Bidwell, 2008). Prescribed burn areas supported more water boatmen, dytiscid and hydrophilid beetles, midges, and oligochaetes when compared to control sites (de Szalay & Resh, 1997). This study provides some insight into wetland fires, however, experimental and prescribed burns are usually less intense than wildfires and may have different impacts on aquatic systems (Gresswell, 1999).

Mercury is of particular concern in wetlands because wetlands with high temperatures, low dissolved oxygen, and fluctuating water levels are conducive to the production of methylmercury (Zillioux et al., 1993; Richardson, 1999). Methylmercury is capable of entering the foodweb and binds tightly to animal tissues (Horvat, 1996). Many wetland plants are also capable of mercury uptake (Casagrande & Erchull, 1977), and others (Sigler, 2003; Biswas et al., 2007) noted a release of mercury into the atmosphere from forest fires. Zilloux et al. (1993) suggested that disturbed wetlands are capable of producing more methylmercury than undisturbed wetlands. Since mercury is of special concern in wetlands, it is important to understand how disturbance such as fire may affect the cycling of mercury through the food web.

The purpose of this study was to examine the effects of wildfire on macroinvertebrate community composition and the total mercury concentrations of select organisms. We analyzed the invertebrate community composition and total mercury concentrations of amphipods, odonates, crayfish and *Gambusia* (mosquitofish) in burned and reference sites and compared these to pre-fire data sets. We hypothesized that (1) wildfire would shift the community structure

of invertebrates toward a community of generalists. We predicted that samples from the pre-fire data and the post-fire reference sites would have similar community compositions, but would both differ from the post-fire burned sites. In addition to community differences, we predicted that burned sites might have a greater Chironomidae biomass. We also hypothesized that (2) total mercury concentrations would be higher in organisms from the burned sites than reference sites because of fire-induced releases of mercury into the water column and that total mercury concentrations of select organisms would be higher post-fire. And lastly, in a nutrient poor system such as the Okefenokee Swamp (Flebbe, 1982), fire may function to release nutrients into the water column for use by organisms (Yin, 1993). We hypothesized that (3) a fire induced release of nutrients would cause burned sites to have higher total nitrogen and total phosphorous levels than reference sites.

METHODS

Study Site

The Okefenokee Swamp is located in southern Georgia and part of northern Florida and is one of the largest wetlands in North America. Although in earlier years, humans influenced the landscape through the input of canals, logging, fire suppression and the creation of water control structures, today most (80%) of the Okefenokee is managed as a National Wilderness Area. The Okefenokee is a southern blackwater swamp that is generally nutrient poor with high amounts of humic substances (Flebbe, 1982). Water inputs to the swamp include precipitation (61%) and surface drainage (39%) (Patten & Matis, 1984). Water outputs include evapotranspiration (80%) and streamflow (20%) through the Suwanne River and St. Mary's River (Rykiel, 1984).
The swamp supports a variety of plants; the primary wetland habitat types are scrub-shrub thickets, cypress stands and sedge prairies (Hamilton, 1982). The swamp is a host to many vertebrates including the American alligator (*Alligator mississippiensis*), numerous fishes, and birds. The aquatic invertebrate community is moderately diverse, supporting 103 different taxa, dominated by midges (Chironomidae and Ceratapogonidae) and water mites (Hydrachnidia) (Kratzer & Batzer, 2007). Kratzer & Batzer (2007) found that invertebrate communities are fairly homogenous across the Okefenokee, in spite of a mosaic of habitat types.

Mercury contamination in the Okefenokee is a concern, and the Georgia Department of Natural Resources has issued fish consumption advisories for *Amia calva* (bowfin), *Centrarchus macropterus* (flier), and *Esox niger* (chain pickerel). Moderately high levels of mercury have been found in many aquatic organisms of the Okefenokee (Jagoe et al., 1998; George & Batzer, 2008). Mercury in the Okefenokee is most likely due to atmospheric fallout (Winger & Lasier, 1997).

Fire has been recognized as an important ecological disturbance in the swamp and in part helps structure the plant habitats. It is suggested that prairie formation occurs during extreme fires that burn peat and roots completely, preventing the woody vegetation from re-establishing (Cypert, 1961). Historically, most wildfires of the Okefenokee started during the summer months when thunderstorms with lightning moved through the area. The upland longleaf pine and wiregrass systems of the Okefenokee are fire dependent and before human settlement, fires occurred every 1-3 years. Post-settlement fire suppression has reduced the frequency of fire to once every 20-30 years (Cypert, 1961), with records of large fires (burning more than 50% of the area) occurring every 100 years (Yin, 1993).

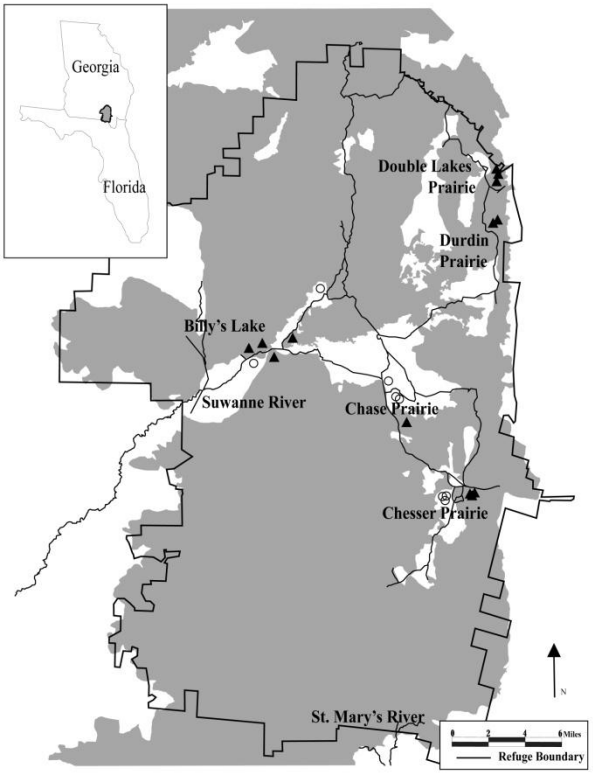

Figure 1: Map of the Okefenokee showing burned areas (shaded) with burned sites (triangles) and non-burned areas (white) with reference sites (circles). Modified map: original courtesy of the USFWS and the Okefenokee NWR.

From April to June 2007, a complex of wildfires moved through the swamp burning about 75% of the total area and leaving only small unburned pockets. This recent fire presented a unique opportunity to assess the impacts of fire on aquatic invertebrates and mercury accumulation because most areas previously sampled for invertebrate community composition (Kratzer & Batzer, 2007) and mercury content (George & Batzer, 2008) burned.

Areas of interest for our study included burned as well as non-burned reference sites that were in close proximity to burned areas. Overall we selected 21 sites: 13 burned sites and 8 reference sites (Figure 1). The sites were composed of a mixture of the three dominant vegetative habitats of scrub-shrub thickets, cypress stands, and sedge prairies and were in the same general areas as those sampled by Kratzer & Batzer (2007) and George & Batzer (2008). Sites were centered in the following sub-regions: Chesser Prairie, Chase Prairie, Billy's Lake, Double Lakes, and Durden Prairie.

Sampling Methods

In order to assess the differences between pre-fire and post-fire data sets, it was necessary to replicate the sampling programs of Kratzer & Batzer (2007) and George & Batzer (2008). A two-year data set was collected (September 2007–August 2009). Collection of samples occurred three times per year (September, December, and May), which parallels pre-fire sampling regimes.

Macroinvertebrate Community Composition

As in Kratzer & Batzer (2007), samples for macroinvertebrates were comprised of three 1-m long sweeps (1-mm mesh size) through the vegetation and water column, collected randomly along a representative transect, in each of the sampling sites (e.g., Chase Prairie, cypress stand, December 2007). Water depth was less than 50cm at most sites which resulted in all or most of the water column sampled with the D-net with each sweep. Sweep nets are useful to sample the water column, emergent vegetation, and along the substrate (Turner & Trexler, 1997; Batzer et al., 2001). Among the various sampling devices used in wetlands, sweep nets have been found to capture the greatest richness and are therefore useful in community studies (Turner & Trexler, 1997; Batzer et al., 2001). Samples were stored in 95% ethanol in plastic bags. Fluctuating water levels allowed sampling at most sites on most dates; however, if a site was dry, a sample was not taken.

In the lab, community sweep net samples were filtered through a 250 µm sieve, sorted under a dissecting microscope, and organisms were re-preserved in 95% ethanol. Macroinvertebrates were identified to the lowest taxonomic level using standard references (Thorp & Covich, 1991; Epler, 1996; Merritt et al., 2008). When possible, organisms were identified to genus, but due to small instars or a lack of expertise, some taxa were identified only to family (Ancylidae, Ceratapogonidae, Chironomidae, Crambidae, Lymnaeidae, and Pyralidae) or order (Oligochaeta). Individuals from the family Chironomidae were measured to the nearest millimeter and published length-mass relationships were used to calculate biomass (Benke et al., 1999).

Total Mercury of Select Organisms

We repeated sampling protocols from the previous study (George & Batzer, 2008) to permit pre and post fire comparisons. For mercury analyses, odonates (Libellulidae and Corduliidae), crayfish (Cambaridae), amphipods (*Crangonyx*), and mosquitofish (*Gambusia*), were gathered, from each site using nets and dip pans. Sampling was conducted for at least 1 person/ hour or until approximately 1 g of mass was collected, whichever happened first (George & Batzer, 2008). Mosquitofish were euthanized with MS222 buffered with calcium carbonate in accordance with the UGA Animal Care and Use Compliance. Samples were stored on ice, and then frozen until analysis. Amphipods, odonates and crayfish were collected from December 2007 – December 2008. Beginning in May 2009 we sampled mosquitofish and continued to collect odonates and crayfish until August 2009. We chose to sample mosquitofish because they were ubiquitous throughout the sampling sites.

The University of Georgia Agricultural and Environmental Services Laboratory analyzed the samples for total mercury using USEPA Method 3052 (1996) for digestion and USEPA Method 245.6 (1991) for the determination of mercury in tissues by cold vapor atomic absorption spectrometry (CVAAS) with detection limits of 0.008 ppb wet weight. The lab follows a stringent quality control protocol and calibrates instruments every 20 samples using certified reference materials. According to Horvat (1996), CVAAS is one of the leading and most reliable methods for mercury determination available.

Water Chemistry

Basic water quality parameters were measured at each of the sampling sites. Temperature (°C; HM Digital COM-100, Oakton WD-35607-10), dissolved oxygen (mg/L; YSI Model 57), pH (Oakton pH Testr 2), and electrical conductivity (µS/cm; HM Digital COM-100, Oakton WD-35607-10) readings were measured in the field on all sampling dates. Total nitrogen (TN; mg/L) and total phosphorus (TP; mg/L) samples were collected for the following sample dates: December 2007, May 2008, September 2008, and May 2008. A bottled water sample was filled in the field and kept on ice until TN (mg/L) and TP (mg/L) were analyzed by the University of Georgia Agricultural and Environmental Services Laboratory using methods developed by the USEPA (TN; 1984) and APHA (TP; 1999).

Statistical Analyses

Macroinvertebrate Community Composition

To determine any patterns in community structure, burned and reference data were log (x+1) transformed and analyzed using a Non-metric Multidimensional Scaling approach (NMS; PC-ORD 5). A Bray-Curtis Similarity distance measure was used on the slow-and-thorough autopilot option in PC-ORD 5. McCune and Grace (2002) suggest that NMS is the most effective ordination method for community data because it allows the user to view the strongest suggested structure of the community based on chosen factors. NMS ordinations are useful to view community structures and possible groupings among factors; however, these analyses do not include formal testing of significant differences among groups (Clarke & Warwick, 1994). Therefore, an Analysis of Similarity (ANOSIM; Primer 6) was used to verify significant factors. To determine what taxa were driving differences in community structures, an indicator species analysis (PC-ORD 5) was used. The indicator species analysis determines the abundance of each taxa within each chosen group and assigns an indicator value accordingly. Indicator values combine information on the abundance of the species within each group and the faithfulness (always present in the group and exclusive to that group) of occurrence (McCune & Grace, 2002). Then, a Monte Carlo test of significance (5000 permutations) was used to determine significant indicator taxa. We log (x+1) transformed Chironomidae biomass values and used a multi-way ANOVA (Proc GLM; SAS 9.2) to assess differences in biomass among burn category, habitat, and time.

Total Mercury of Select Organisms

Non-parametric Kruskal-Wallis tests (SAS 9.2) were used to assess differences in total mercury concentrations by organism type, among the burn categories, and habitats. The Kruskal-Wallis test is a ranked test that is useful for non-normal data (Dowdy et al., 2004). When results were significant, Wilcoxon two sample tests were used for multiple comparisons; we used a Bonferroni corrected global alpha when multiple tests were run in series.

Water Chemistry

Multi-way ANOVAs (Proc GLM; SAS 9.2) were used to determine if any of the water chemistry measures differed among burn category, habitat, and time.

RESULTS

Macroinvertebrate Community Composition

A total of 31,864 individuals were collected in 109 samples. Eighty two taxa were identified; from 15 orders, 39 families and 72 genera. The most common families included: Chironomidae 74%, Ceratopogonidae 7%, Crangoncytidae 5%, Hydroptilidae 3%, and Dytiscidae 2%.

Pre-fire and Post-fire Community Composition

NMS community analysis of pre-fire, post-fire reference, and post-fire burned sites suggested a three dimensional solution with moderately high stress (18.66) that explained 76% of the variability. NMS ordinations illustrated slight groupings of community structures among the three burn categories (Figure 2), confirmed by a one-way ANOSIM (Table 1; overall p = 0.0002). Pre-fire communities and post-fire burned communities differed most (p=0.0001), and post-fire reference and post-fire burned sites were marginally different (p=0.063). Pre-fire and post-fire reference communities were similar (p=0.092).

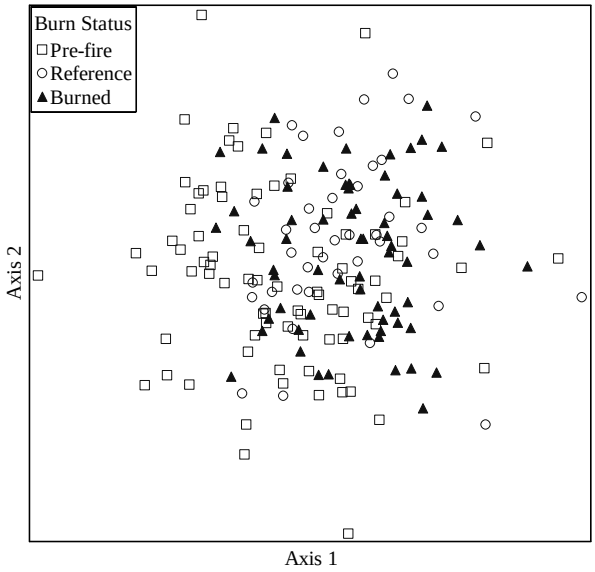

Figure 2: NMS ordination of pre-fire, post-fire burned, and post-fire reference sites. The plot is comprised of Axis 1 (r^2=0.266), Axis 2 (r^2=0.248), and Axis 3 (not shown, r^2=0.241) that explained 76% of the variability; overall stress for NMS analysis = 18.66.

Table 1: One-way ANOSIM test suggested significant differences among burn categories (overall p=0.0002); pairwise tests are given in the table below and suggest that reference sites are intermediary to pre-fire and post-fire burned sites. Asterisks indicate significant p-values (<0.05).

Burn Category Groupings	p
Pre-fire & Post-fire Burned	0.0001*
Pre-fire & Post-fire Reference	0.092
Post-fire Burned & Post-fire Reference	0.063

Post-fire Community Composition: Burned and Reference Sites

While analyses including the pre-fire data set suggest an impact of fire, contrasts are complicated by potential temporal effects unrelated to fire. Thus, we focused on the post-fire data. NMS analysis of post-fire burned and post-fire reference sites suggested a three-dimensional solution with moderately high stress (18.43) that explained 75% of the variability. However, NMS ordinations did not illustrate clear groupings of community structures between burned and reference sites, and a one-way ANOSIM contrasting burned and reference sites was marginally non-significant (p=0.066).

To determine if the effect of burn status was modified by other spatial (habitat) or temporal (sample date) factors, we conducted two-way crossed ANOSIMs with burn status and either sample date or habitat as the second factor. We detected significant impacts of fire after factoring for habitat but not sample date (Table 2).

Table 2: Two-way crossed ANOSIM tests for burn category and time, or habitat suggest that habitat is a significant factor. Asterisks indicate significant p-values (<0.05).

Burn Category and Other Factors	Differences between burn category groups (across other factors)	Differences among factor groups (across all burn category groups)
Burn Status & Time	0.599	0.524
Burn Status & Habitat	0.049*	0.001*

In prairie and scrub-shrub habitats, the community structure of burned and reference sites did not significantly differ. However, in cypress habitats, burned and reference sites were different (p=0.025). NMS ordination of the community structure in cypress sites only showed separation between burned sites and reference sites (Figure 3). Indicator analysis suggested that *Ischnura* (Coenagrionidae; p=0.046) and *Oecetis* (Leptoceridae; p=0.039) were indicators of reference sites, and *Sigara* (Corixidae; p=0.039) was an indicator of burned sites.

A multi-way ANOVA of Chironomidae biomass did not reveal differences among burn status, habitat, time, nor interactions between factors (overall p=0.4688).

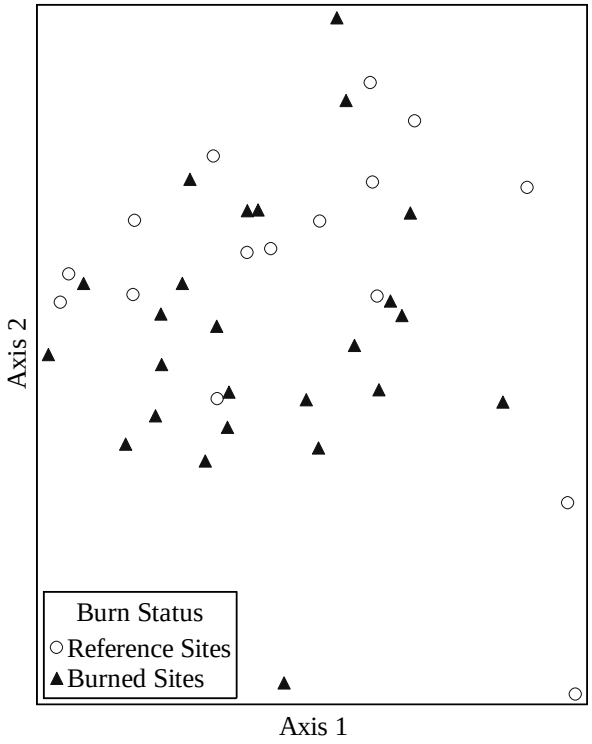

Figure 3: NMS ordination of cypress habitat sites showing groupings of burned and reference sites. Plot comprised of Axis 1 (r^2=0.279), Axis 2 (r^2=0.272), and Axis 3 (not shown, r^2=0.232) that explained 78% of the variability; overall stress for NMS analysis = 16.43. One-way ANOSIM suggested that the groupings were significantly different (p = 0.025).

Total Mercury of Select Organisms

Pre- and Post-fire Comparison of Mercury

Total mercury concentrations from the 1998–2000 study were considerably higher than the concentrations found in the post-fire study. All organisms had lower total mercury concentrations post-fire. Wilcoxon two-sample tests indicated that pre-fire values were significantly higher than post-fire values for all organisms (amphipods: H=57.15, d.f.=1, p<0.0001; odonates: H=52.94, d.f.=1, p<0.0001; crayfish: H=23.71, d.f.=1, p<0.0001).

Post-fire Comparison of Mercury: Reference and Burned Sites

Kruskal-Wallis tests indicated that concentrations in odonates and crayfish were lower in burned than reference sites (odonates: H=7.24, d.f.=1, p=0.0072; crayfish: H=4.21, d.f.=1, p=0.0401), while concentrations in amphipods and mosquitofish did not differ between burned and reference sites (Figure 4). Kruskal-Wallis test with multiple comparisons revealed that crayfish and odonates did not differ in total mercury, but were lower than levels from amphipods and mosquitofish, which also did not differ from each other (reference sites: H=25.38, d.f.=3, overall p<0.0001; burned sites: H=47.25, d.f.=3, overall p<0.0001).

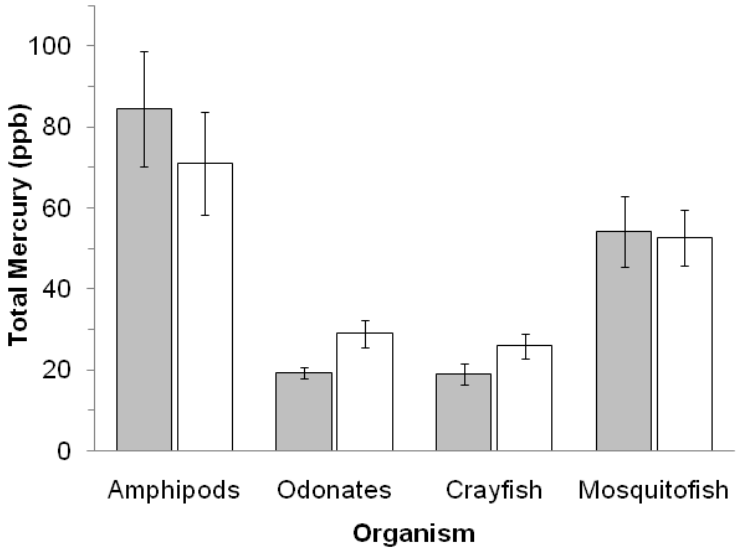

Figure 4: Total mercury concentrations of amphipods (n=67 samples), odonates (n=73 samples), crayfish (n=60 samples), and Gambusia (n= 25 samples) of the Okefenokee Swamp. Open bars indicate means from reference sites and shaded bars indicate means from burned sites; error bars represent ±1SE. Wilcoxon two sample tests suggest that concentrations in odonates and crayfish were lower in burned sites than reference sites (odonates: H=7.235, d.f.=1, p=0.0072; crayfish: H=4.2123, d.f.=1, p=0.0401)

Conducting separate comparisons for individual habitat types for each organism only revealed that mercury in odonates from burned cypress habitats was lower than in reference cypress habitats (H=9.59, d.f.=1, p=0.0020). All other organism and habitat combinations were not significant. In some cases (e.g., crayfish), differences between overall and habitat specific results may have been related to smaller sample sizes.

Water Chemistry

Total phosphorus was higher in burned sites (0.51 mg/l) than in reference sites (0.19 mg/l) ($F_{1,54}$=6.03, p=0.0174). Total nitrogen (1.23mg/l – 49.8mg/l) was not affected by any factors. Multi-way ANOVAs for temperature (11.3°C – 67.1°C), pH (3.3-7.23), conductivity (28.0µS – 191.4µS), and dissolved oxygen (0.6mg/l – 11.6mg/l) varied temporally (all $p<0.0001$), but not by burn category or habitat.

CONCLUSIONS AND RECOMMENDATIONS

Macroinvertebrate Community Response to Wildfire

We hypothesized that wildfire would shift the macroinvertebrate community composition toward a community of disturbance adapted generalists. We predicted that pre-fire data samples and post-fire reference sites should have similar community compositions, but both would differ from the post-fire burned sites. While the data suggested community differences among the three burn categories (pre-fire, post-fire burned and post-fire reference), factors other than fire may be responsible for variation between pre- and post-fire periods such as natural temporal changes in the Okefenokee Swamp. Therefore, most of my discussion focuses on the post-fire differences between reference and burned sites.

There were only marginal differences in overall community composition (p=0.063) between burned and reference sites and NMS analyses did not illustrate clear groupings. However, when habitats were examined individually, we found that macroinvertebrates in cypress habitats were most affected by fire. Most differences could be attributed to three indicator organisms: *Sigara* was associated with burned sites; and *Oecetis* and *Ischnura* were associated with reference sites. Responses by these taxa support the hypothesis that burning would induce a community dominated by disturbance adapted organisms.

Corixidae water boatmen, such as *Sigara,* are often associated with disturbed wetlands. A study of prescribed burn in a California marsh found a greater density of corixids in burned areas than reference areas (deSzalay & Resh, 1997). In bioassessment, corixids have frequently been found dominating anthropogencially impacted wetlands (Helgen & Gernes, 2001; Hartzell et al., 2007). *Sigara* corixids may be able to exploit disturbed habitats in part because they are generalist herbivore feeders (Merritt et al., 2008), and this may explain their abundance in burned areas. The increased phosphorous levels in burned sites might have increased algal food supplies benefitting *Sigara*; we observed dense algal blooms in burned sites, although algal biomass was not quantified.

Trichoptera (caddisflies) are commonly used as indicators of stream quality, and although not found in large numbers in wetlands, they can also be useful in determining wetland condition (Burton et al., 1999; Helgen & Gernes, 2001; Wilcox et al., 2002; Hartzell et al., 2007). We found three genera of Trichoptera in our samples. Numbers of Trichoptera genera did not vary between burned and non-burned reference areas, but we found that the genus *Oecetis* was more prominent in reference cypress habitats when compared to burned cypress habitats. *Oecetis* is considered an intolerant taxon and it tends to be absent in disturbed wetlands (Helgen & Gernes, 2001). *Oecetis* is predaceous (Merritt et al., 2008), and it may be sensitive to changes at lower trophic levels induced by fire. Alternatively, they may be intolerant of post-fire physic-chemical conditions in cypress stands.

Odonata (dragonflies and damselflies) are another taxonomic group commonly used as indicators of disturbance in wetlands (Burton et al., 1999; Helgen & Gernes, 2001; Wilcox et al., 2002; Hartzell et al., 2007). Indicator analysis suggested that the damselfly, *Ischnura* (Coenagrionidae) is sensitive to fire because it was an indicator of reference sites. *Ischnura*, like *Oecetis* is predaceous (Merritt et al., 2008) and environmentally sensitive. Both *Ischnura* and *Oecetis* might respond similarly to fire.

We were surprised to find that fire did not affect biomass of Chironomidae (another disturbance adapted organism) as it had in other studies (deSzalay & Resh, 1997, Scrimgeour et al., 2001). However, these studies used different sampling techniques (benthic corer, Eckman-Birge grab), while our study used a D-net to sample. Davis & Bidwell (2008) found that fire impacted Chironomidae biomass sampled benthically with a corer, while Chironomidae biomass sampled epiphytically with a D-net were not affected. D-nets sample midges living epiphytically more efficiently than those living benthically (Henke 2005), so we may have underestimated responses of benthic midges in my study.

Our study suggests that macroinvertebrate communities in cypress stands of the Okefenokee were more impacted by fire than those in sedge prairies or scrub-shrub thickets. Perhaps burn intensity was greater in the cypress stands. Future studies of wildfire in wetlands should take habitat conditions and burn intensity into consideration.

Total Mercury of Select Organisms after Wildfire

We hypothesized that fire would increase total mercury levels in aquatic organisms. However, our study found lower rather than higher total mercury concentrations post-fire, albeit only in select organisms. When comparing our results with those collected several years before the fire (George & Batzer, 2008), levels declined in all taxa sampled including a 97% decline in *Crangonyx* (Amphipoda), 90% in odonates (Corduliidae and Libellulidae), and 78% in crayfish (Cambaridae). This post-fire decline occurred in both burned and non-burned areas, suggesting either that fire had a pervasive effect, even beyond the areas burned directly, or that the decline was caused by factors other than fire. Thus, as for community analyses, we focus our discussion on post-fire burned and reference sites.

Odonates and crayfish both had lower levels of total mercury in burned sites than reference sites overall. When focusing on individual habitats, we only found that total mercury levels in odonates living in burned cypress areas were lower than those living in nonburned cypress. This indicates that impacts on total mercury were greatest in burned cypress, as was the case with macroinvertebrate community responses. Analyzing total mercury in habitats individually reduced sample size and may have obscured some trends in other organisms or habitats. However, increased burn intensity in forested habitat versus shrub or herbaceous vegetation seems a likely reason for pronounced responses in cypress.

Results also contradict results from another study. Kelly et al. (2006) found that after the catchment for Moab Lake partially burned, fish methylmercury increased 5-fold post-fire when compared to reference lakes. They attributed the differences to a shift in the fish diets and increased mercury inputs (Kelly et al., 2006); i.e., increases in lake productivity caused food chains to be longer, which affected the structure of aquatic communities and concentrations of mercury. The mosquitofish in the Okefenokee, which did not respond, occupy a fairly low position in food chains. Perhaps larger, piscivorous fish in the Okefenokee might respond differently.

Other studies have reported responses more similar to our results. Allen et al. (2005) found that levels of methylmercury decreased by 43% in *Gammarus lacustris* amphipods and 32% in *Cordulia shurtleffi* odonates in Canadian lakes after a major fire. This same study also found that mean body sizes and $\delta 15N$ of some organisms were different between the pre-fire and post-fire time periods suggesting differences in the diets of these organisms between the two treatment times. Pickhardt et al. (2002) demonstrated that algal blooms can reduce methylmercury concentrations in zooplankton via biodilution. As mentioned, we found higher levels of total phosphorous and observed algal blooms in burned sites. Perhaps these algal blooms caused biodilution of mercury in burned areas of the Okefenokee, and levels of mercury in some macroinvertebrates thus declined. Another study by Garcia & Carnignan (1999) failed to find differences in methylmercury levels in zooplankton from burned and reference lakes after the catchments partially burned. They attributed this to changes in soil mercury speciation, loss of

mercury through volatilization, and nutrient pulses following fire that diluted mercury levels available to biota. In our study, neither amphipods nor mosquitofish had significantly different total mercury levels in burned versus reference sites. Besides being habitat specific, responses also appear to be organism specific.

Horvat (1996) describes how many factors can affect mercury levels in organisms (e.g. diet and age of organism, physical attributes of the surrounding system), and suggests that mercury cycling will not be similar in all aquatic systems or aquatic organisms. Others have suggested that variation in burn intensity and total area burned could also affect mercury cycling in aquatic systems (Allen et al., 2005). Since mercury cycling depends on many factors and studies provide conflicting conclusions it seems likely that post-fire changes in mercury cycling in aquatic systems will be difficult to predict.

Conclusion

To our knowledge, this the first study to examine the effects of natural wildfire on macroinvertebrate communities and total mercury levels of organisms in a wetland. In the Okefenokee, fire impacts on both macroinvertebrate community structure and mercury levels were particularly pronounced in cypress habitats. Longer-term monitoring will focus on cypress habitats, and select indicator organisms (including the Odonata).

The results of this study and future studies can be important for the management of wetland ecosystems. The Okefenokee is managed to protect populations of birds, waterfowl, fishes and endangered and threatened species. Knowing how fire affects mercury concentrations and aquatic macroinvertebrate communities can help managers make more informed management decisions regarding fire in the Okefenokee Swamp and other managed wetlands.

REFERENCES CITED

Allen, E.W., E.E. Prepas, S. Gabos, W.M.J. Strachan & W. Zhang. 2005. Methyl mercury concentrations in macroinvertebrates and fish from burned and undisturbed lakes on the Boreal Plain. Canadian Journal of Fisheries and Aquatic Science 62: 1963–1977.

American Public Health Association. 1999. Standard methods for the examination of water and wastewater, 20th Edition, American Water Works. Washington, DC, USA.

Batzer, D.P., A.S. Shurtleff & R.B. Rader. 2001. Sampling invertebrates in wetlands. In R. B. Rader, D. P. Batzer & S. A. Wissinger (eds), Bioassessment and management of North American freshwater wetlands. John Wiley and Sons Inc., New York, NY: 339–354.

Benke, A.C., A.D. Huryn, L.A. Smock & J.B. Wallace. 1999. Length-mass relationships for freshwater macroinvertebrates in North America with particular reference to the southeastern United States. Journal of the North American Benthological Society 18: 308–343.

Biswas, A., J. D. Blum, B. Klaue & G. J. Keeler. 2007. Release of mercury from Rocky Mountain forest fires. Global Biogeochemical Cycles, 21: GB1002.

Burton, T.M., D.G. Uzarski, J.P. Gathman, J.A. Genet, B.E. Keas & C.A. Stricker. 1999. Development of a preliminary invertebrate index of biotic integrity for Lake Huron coastal wetlands. Wetlands 19: 869–882.

Casagrande, D.J. & L.D. Erchull. 1977. Metals in plants and waters in the Okefenokee Swamp and their relationship to constituents found in coal. Geochimica et Cosmochimica Acta 41:1391–1394.
Clarke, K.R. & R.M. Warwick. 1994. Similarity-based testing for community pattern: the two-way layout with no replication. Marine Biology 118:167–176.
Cypert, E. 1961. The effects of fires in the Okefenokee Swamp in 1954 and 1955. American Midland Naturalist 66:485–503.
Davis, C. A. & J. R. Bidwell. 2008. Response of aquatic invertebrates to vegetation management and agriculture. Wetlands 28:793–805.
de Szalay, F. A. & V. H. Resh. 1997. Responses of wetland invertebrates and plants important in waterfowl diets to burning and mowing of emergent vegetation. Wetlands 17:149–156.
Dowdy, S., S. Weardon & D. Chilko. 2004. Statistics for research 3rd edition. John Wiley and Sons Inc., Hoboken.
Epler, J. H. 1996. Identification Manual for the Water Beetles of Florida. State of Florida Department of Environmental Protection, Tallahassee, Florida.
Flebbe, P.A. 1982. Biogeochemistry of carbon, nitrogen and phosphorus in the aquatic subsystem of selected Okefenokee swamp sites. Ph.D. Dissertation. University of Georgia, Athens, GA, USA.
Garcia, E. & R. Carignan. 1999. Impact of wildfire and clear-cutting in the boreal forest on methyl mercury in zooplankton. Canadian Journal of Fisheries and Aquatic Science 56:339–345.
George, B. M. & D. P. Batzer. 2008. Spatial and temporal variations of mercury levels in Okefenokee invertebrates: Southeast Georgia. Environmental Pollution 152: 484–490.
Gresswell, R. E. 1999. Fire and aquatic ecosystems in forested biomes of North America. Transactions of the American Fisheries Society 128: 193–22.
Hamilton, D. B. 1982. Plant succession and the influence of disturbance in the Okefenokee Swamp, Georgia. Ph.D. Dissertation. University of Georgia, Athens, GA, USA.
Hartzell, D., J.R. Bidwell & C.A. Davis. 2007. A comparison of natural and created depressional wetlands in central Oklahoma using metrics from indices of biological integrity. Wetlands 27: 794–805.
Helgen, J.C., and M.C. Gernes. 2001. Monitoring the condition of wetlands: indexes of biological integrity using invertebrates and vegetation. In D.P. Batzer, R.B.Rader and S.A. Wissinger (eds), Invertebrates in Freshwater Wetlands of North America: Ecology and Management. John Wiley & Sons, Inc., New York, NY, USA: 167–184.
Henke, J. A. 2005. Assessing the efficacy of different sampling methods and determining length-mass relationships for wetland invertebrates. M.S. Thesis University of Georgia, Athens, Georgia.
Horvat, M. 1996. Mercury analysis and speciation in environmental samples. In W. Baeyens, R. Ebinghaus & O. Vasiliev (eds), Global and Regional Mercury Cycles: Sources, Fluxes and Mass Balances. Kuwer Academic Pulishers, Dordrecht, Netherlands 1–31.
Jagoe, C.H., B. Arnold-Hill, G.M. Yanochko, P.V. Winger & I.L. Brisbin. 1998. Mercury in alligators (Alligator mississippiensis) in the southeastern United States. The Science of the Total Environment 213: 255–262.
Kelly, E. N., D. W. Schindler, V. L. St. Louis, D. B. Donald & K. E. Vladicka. 2006. Forest fire increases mercury accumulation by fishes via food web restructuring and increased mercury inputs. Proceedings of the National Academy of Sciences 103:19380–19385.

Kratzer, E. B. & D. P. Batzer. 2007. Spatial and temporal variation in aquatic macroinvertebrates in the Okefenokee swamp Georgia, USA. Wetlands 27:127–140.

McCune, B. & J.B. Grace. 2002. Nonmetric multidimensional scaling. In Analysis of Ecological Communities. MjM Software Design, Gleneden Beach, OR: 125–142.

Merritt, R. W., K. W. Cummins & M. B. Berg. 2008. An Introduction to the aquatic insects of North America, 4th edition. Kendall Hunt, Dubuque, IA.

Middleton, B. 1999. Wetland Restoration, Flood Pulsing, and Disturbance Dynamics. John Wiley & Sons, Inc., New York, New York.

Minshall, G. W. 2003. Responses of stream benthic macroinvertebrates to fire. Forest Ecology and Management 178:155–161.

Patten, B.C. & J.H. Matis. 1984. The macrohydrology of Okefenokee Swamp. In A.D. Cohen, D.J. Casagrande, M.J. Andrejko & G.R. Best (eds), The Okefenokee Swamp: Its Natural History, Geology, and Geochemistry. Wetland Surveys, Los Alamos, NM: 246–263.

Pickhardt, P.C., C.L. Folt, C.Y.Chen, B. Klaue & J. D. Blum. 2002. Algal blooms reduce the uptake of toxic methylmercury in freshwater food webs. Proceedings of the National Academy of Sciences 99: 4419–4423.

Richardson, C. J. 1999. Plenary Session Presentation: Ecological Functions of Wetlands in the Landscape. In M. A. Lewis, F. L. Mayer, R. L. Powell, M. K. Nelson, S. J. Klaine, M. G. Henry & G. W. Dickson (eds). Ecotoxicology and risk assessment for wetlands. SETAC Press: 9-25.

Rykeil, E. J. 1984. General hydrology and mineral budgets for Okefenokee Swamp. In A.D. Cohen, D.J. Casagrande, M.J. Andrejko & G.R. Best, (eds), The Okefenokee Swamp: Its Natural History, Geology, and Geochemistry. Wetland Surveys, Los Alamos, NM: 212–222.

Scrimgeour, G. J., W. M. Tonn, C. A. Paszkowski & C. Goater. 2001. Benthic macroinvertebrate biomass and wildfires: evidence for enrichment of boreal subarctic lakes. Freshwater Biology 46:367–378.

Sigler, J.M., X. Lee & W. Munger. 2003. Emission and long-range transport of gaseous mercury from a large-scale Canadian boreal forest fire. Environmental Science & Technology, 37: 4343–4347.

Thorp, J. H. & A. P. Covich. 1991. Ecology and classification of North American freshwater invertebrates. Academic Press, Inc., San Diego, CA.

Turner, A.M. & J.C. Trexler. 1997. Sampling aquatic invertebrates from marshes: evaluating the options. Journal of the North American Benthological Society 16:694–709.

U.S. Environmental Protection Agency. 1984. Methods for chemical analysis of water and wastes. EPA–600/4–79–020. Cincinnati, OH, USA.

U.S. Environmental Protection Agency. 1991. Methods for the determination of metals in environmental samples. EPA–600/4-91–010. Cincinnati, OH, USA.

U.S. Environmental Protection Agency. 1996. Method 3052: Microwave assisted acid digestion of siliceous and organically based matrices, rev. 0. U.S. Gov. Print. Office, Washington, D.C.

Wilcox, D.A., J.E. Meeker, P.L. Hudson, B.J. Armitage, M.G. Black & D.G. Uzarski. 2002. Hydrologic variability and the application of index of biotic integrity metrics to wetlands: a great lakes evaluation. Wetlands 22: 588–615.

Winger, P.V. & P.J. Lasier. 1997. Fate of airborne contaminants in Okefenokee National Wildlife Refuge. USGS-BR Division, Athens, Georgia.

Yin, Z. 1993. Fire regime of the Okefenokee Swamp and its relation to hydrological and climatic conditions. International Journal of Wildland Fire 3:229–240.
Zillioux, E.J., D.B. Porcella & J.M. Benoit. 1993. Mercury cycling and effects in freshwater wetland ecosystems. Environmental Toxicology and Chemistry 12: 2245–2264.

Quantification of Vegetative Flow Resistance in Constructed Wetlands

Basic Information

Title:	Quantification of Vegetative Flow Resistance in Constructed Wetlands
Project Number:	2009GA197B
Start Date:	3/1/2009
End Date:	2/28/2010
Funding Source:	104B
Congressional District:	
Research Category:	Engineering
Focus Category:	Wastewater, Wetlands, Drought
Descriptors:	None
Principal Investigators:	Thorsten Stoesser

Publications

1. Stoesser, T., Kim, S. J., and Diplas, P. (2010). Turbulent flow through idealized emergent vegetation, ASCE, Journal of Hydraulic Engineering (in press).
2. Kim, S. J. and Stoesser, T. (2010). The effect of drag coefficient on 3D numerical modeling of open-channel flow with emergent vegetation, 8th International Symposium on Ecohydraulics 2010, Seoul, Korea, Sep. 12-16, 2010.
3. Kim, S. J., Reuter, E. R., Harris, B., and Stoesser, T. (2010). Quantification of vegetative flow resistance in a constructed wetland in Georgia, U.S.A., River Flow 2010, International Conference on Fluvial Hydraulics, Braunschweig, Germany, Sep. 8-10, 2010.

Quantification of Vegetative Flow Resistance in Constructed Wetlands

Final Report

by

Thorsten Stoesser, Ph.D.,
Su Jin Kim, Grad. Res. Asst.,
Brandon Strellis, Brandon Harris, Emma Reuter, and Ingrid Duque,
Undergrad. Students

School of Civil and Environmental Engineering
Georgia Institute of Technology
Atlanta, GA 30332

May, 2010

ABSTRACT

Field work, laboratory experiments, and numerical simulations were conducted to identify and quantify the relevant drag force parameters for natural vegetation. The study was motivated by the need to develop better methods for calculating the headloss in constructed wetlands.

Measurements of the natural plant densities and geometric characteristics of *Typha* (Cattail), one of the most common types of vegetation in natural and constructed wetlands, were taken during field research at the Clayton County Water Authority's constructed wetland systems.

Laboratory experiments were then designed and conducted using wooden dowels (acting similarly than *Typha*) that were placed in a tilting flume at the same density as *Typha*. Water surface profiles were measured for the two different wetland cells as well as for the flume experiments. In addition, the flow in an alternative pattern of marsh zone and deep zone, which is common in treatment wetlands, was also investigated in the flume. The flow resistance calculated from laboratory measurements were compared with field observations and analyzed to acquire the respective drag coefficients. The results describe the relationship between the drag coefficient and Reynolds number well.

Numerical simulations were also performed to investigate the hydrodynamics in both constructed wetlands and laboratory flume by employing a numerical analysis tool, SSIIM.

TABLE OF CONTENTS

Page

1. INTRODUCTION

1.1 Background and motivation

As the record drought across Georgia continues, new and effective ways of wastewater purification are urgently needed. The ability of wetland ecosystems to improve water quality naturally has been historically recognized and natural and engineered wetlands are emerging as important treatment systems for wastewater and agricultural run-off (Lin et al., 2003). Wetlands are effective at decreasing the concentrations of BOD, TSS, nutrients, metals, pathogens, and trace organics (Bachand and Horne; 2000, Reilly et al., 2000; Debusk et al., 1996; Kadlec and Knight, 1996; Webb et al., 1998; Schulz and Peall, 2001; O'Loughlin and Burris, 1999).

Greater reliance on wetlands treatment and optimization of existing wetlands operations require a better understanding of the hydraulic factors that govern treatment efficiency. A precondition for studying wetlands hydraulics is detailed knowledge of the flow through vegetation and the quantification of the prevailing flow resistance.

Quantification of vegetative flow resistance is essential for simulating the hydrodynamic behavior of constructed wetlands. Better representation of vegetative effects on flow resistance, in terms of parameters that describe the flow/vegetation interaction are sought to improve numerical models. These models are required for the design and/or performance optimization of constructed wetlands for efficient wastewater treatment.

Recent research on vegetative resistance in open channel flows has been motivated by the need to develop better methods for evaluating flow and transport processes through vegetated channels, floodplains, and wetlands. State-of-the-art approaches for the characterization of vegetative flow resistance in Computational Fluid Dynamics (CFD) models are using a drag force term in the momentum equations to model the stem drag imposed by plants which project through a significant amount of the water depth (Fischer-Antze et al., 2001). In doing so the primary aim is to move away from lumped, and often unknowable, friction parameterizations (such as Mannings n) to physically-based laws describing each component contributing to the energy loss source term in the Navier-Stokes equations. This approach reduces the ability to subsume under-represented processes and data uncertainties in the calibration process which are inherent in roughness closures using a bed friction term.

However, the drag force formulation is based on a cylinder analogy where vegetation is treated as rigid, round, free-standing cylinders with the drag coefficient mostly specified to be uniform corresponding to fully turbulent and undisturbed approach flow conditions. This of course does not hold for a stand of natural plants and has been only assumed due to the lack of detailed knowledge about the individual drag coefficients of the diverse wetland vegetation species. Furthermore, the drag force approach assumes pressure drag to be dominating over viscous drag, which in the case of dense wetlands and low Reynolds numbers does not necessarily hold.

Constructed wetland systems are operated by the Clayton County Water Authority (CCWA) and were initially chosen by the CCWA due to their ability to treat large volumes of effluent while minimizing land area requirements.

The CCWA Shoal Creek system includes the 2.1-mgd Shoal Creek Water Reclamation Facility, a storage reservoir, a pump station, and constructed wetlands, consisting of approximately 360 acres (including approximately 150 acres of sprayfields) with a permitted capacity of 1.1 mgd. Owing to the increasing demand additional wetlands are being added since the year 2000 and provide 3.0 mgd of additional capacity, and encompass about 55 wetland acres subdivided into 22 separate cells. The reclaimed water from the wetlands is collected and returned to the Shoal Creek Reservoir, eventually flowing to the J.W. Smith Reservoir to augment potable water supply.

Observations of hydraulic headloss in existing constructed wetlands of the Clayton County Water Authority (CCWA) versus design projections have resulted in undesired disparities. Evidently, the flow resistance of the vegetation in the wetlands as specified during the design phase is not longer valid for the prevailing conditions. The proposed study aims at identifying factors involved in flow resistance of natural vegetation leading to more accurate predictions of system headloss through constructed wetlands. The primary goal is to accomplish an accurate quantification of the flow resistance for some of the most common vegetation types (e.g. Typha and Scirpus) found in the constructed wetlands of the Clayton County Water Authority (CCWA). Quantification of flow resistance for these types will allow the development of an adequate approach for characterizing vegetative flow resistance to be implemented into a practically deployable CFD model. With this model accurate predictions of hydrodynamics and water levels as well as residence times can be accomplished. Ultimately, design optimization of future wetlands and operational guidelines for existing wetlands can be provided.

1.2 Literature review

Constructed Systems for Wastewater Treatment

Constructed wetlands are shallow detention systems which are typically extensively vegetated with emergent aquatic macrophytes (Persson et al., 1999). Wetlands have been used as convenient wastewater discharge sites for more than 100 years in some regions and many natural systems that use the ability of plant species in uptaking or degrading the pollutants were developed (Sundaravadivel and Vigneswaran, 2001). In 1953, Dr. Seidel of Max Planck Institute in Plon, Germany, first reported about the possibility to lessen the overfertilization, pollution, and silting up of inland waters through appropriate plants (Brix, 1994). Natural and constructed treatment wetlands offer effective and reliable treatment to wastewater in a simple and inexpensive manner. Major advantages of wetlands being used for water treatment include (Sundaravadivel and Vigneswaran, 2001):

- Wetlands achieve high levels of treatment with little or no maintenance, making them especially appropriate in locations where no infrastructure support exists;

- Wetlands are relatively tolerant to shock hydraulic and pollutant loads that ensures the reliability of treated wastewater quality;
- Wetland vegetation generate oxygen and consume carbon dioxide, thereby help improving air quality and fight global warming; and
- Wetland vegetation provide indirect benefits such as green space, wildlife habitats, and recreational and educational areas.

The presence of vegetation in wetlands considerably reduces the bulk flow velocities of the water, promoting better conditions for sedimentation of suspended solids. The reduction of turbulence and the prevailing uniform vertical velocity profile in vegetated areas hinder resuspension of settled material and thereby improve the removal of suspended solids by sedimentation. Many of such systems have been constructed however mostly without proper hydrodynamic design due to the lack of detailed knowledge about the water-plant-sediment interaction processes. Reliable and accurate models are necessary to enable wetland design in order to achieve their expected performance (Persson et al., 1999).

Predicting Flow through Vegetation Using Computational Fluid Dynamics Models

Enabled by the continually growing computational speed and storage capacity, Computational Fluid Dynamics (CFD) models have been developed to solve the 3D steady or unsteady Reynolds-averaged-Navier-Stokes (RANS/URANS) equations, which resolve local flow and turbulence features of the temporally averaged turbulent flow field. Presently, steady RANS models are the most practical approaches allowing reasonable predictions of the time-averaged turbulent flow field over or through vegetation by adding an additional source term to the RANS and turbulence transport equations to account for vegetative drag effects. Petryk and Bosmajian (1975) addressed the problem that the Manning's friction coefficient is a function of flow depth and vegetation density. The latter researchers used a force-equilibrium approach where they postulated that the gravity force is equal to the boundary shear stress and the drag forces induced on the emergent vegetation. The drag force on F_D can be expressed as:

$$F_D = \rho \frac{U^2}{2} C_D A \tag{1}$$

where U is the approach flow velocity, C_D is the drag coefficient and A representing the projected area of a single plant in streamwise direction. The drag coefficient can be determined from experiments or evaluated for simple geometries from the plants' base shape and the Reynolds number. For conditions where the energy losses due to vegetation dominate, the drag force increases as the square of the flow velocity. However Fathi-Maghadam and Kouwen, 1997, through their experimental work on non-submerged pine and cedar saplings and branches have directly measured the drag force for a variety of flow conditions. They have found that the relationship between drag force and flow velocity is probably linear for natural vegetation species that is subject to bending. This is similar to the findings from Wilson and Horritt (2002) for a flexible grass canopy where the drag force per unit area was calculated from a force-equilibrium approach. Dunn *et al.* (1996) simulated a rigid emergent plant canopy using vertical cylinders set in a

staggered arrangement with variable density. The drag coefficient calculated from a force-equilibrium approach was found to be a function of the vertical distance from the bed reaching a maximum value at one third of the flow depth and a mean value close to $C_D = 1.13 \pm 0.15$.

Numerical methods that include the drag force approach for multi-dimensional flow problems have been developed by Shimizu and Tsujimoto (1994), Lopez and Garcia (1998, 2001), Neary (2000), Fischer-Antze et al. (2001) using two-equation turbulence closure models to simulate rigid and emergent vegetation in simple-section and compound-section channel arrangements. Modified k-ε or k-ω turbulence closure models were used, introducing drag-related sink terms into the turbulent transport equations. Laboratory experiments by Dunn et al. (1996), Tsujimoto and Kitamura (1998), Fairbanks and Diplas (1998), or Pasche and Rouve *(*1985) were used to validate the models. For idealized conditions i.e. where the vegetation is approximated by rigid cylinders application of the drag force approach resulted in fairly accurate predictions of flow velocities and turbulence quantities.

Previous experimental and numerical studies confirm the complexity of vegetation-flow interaction and highlight why this particular area of hydraulics has for so long defied effective treatment. Vegetative roughness and flow vegetation interaction is, clearly, an area where current hydraulic understanding is still limited, yet it is central to many problems of practical interest to environmental engineers including the hydraulic performance of constructed wetlands. The treatment of vegetative flow resistance in numerical models needs further improvements.

2. OBJECTIVES

A combination of field work, laboratory experiments and high resolution numerical simulations is proposed to quantify pressure and viscous drag forces specifically for *Typha* and *Scirpus*, the two most common vegetation in natural and constructed wetlands. The main objective of the proposed project is to identify and quantify the relevant drag force parameters for natural vegetation. Knowledge of these parameters will improve the current approach for characterizing vegetative flow resistance considerably. The major contribution of doing so is that these parameters will have both physical meaning and be easily measurable. For instance, using the drag force approach requires knowledge about three parameters i.e. the vegetation density, the projected area A_p and the drag coefficient C_D of the plants. Whereas the first parameter can be determined from field measurements or from reaped field specimens the latter can only be determined from a combination of detailed laboratory experiments and high resolution numerical simulations. Through analysis of vegetation-flow interaction, and in particular the energy losses generated, the various components (pressure/viscous drag, friction) of hydraulic resistance of the selected vegetation types can be unpacked yielding to accurate and transferable C_D values. This process is considered a physically based roughness closure scheme driven by

physically measurable plant parameters using input parameters which require no calibration.

3. FIELD WORK

3.1 Vegetation properties and quantification

This study was conducted in a constructed wetland system operated by the Clayton County Water Authority (CCWA) in Georgia, USA. The wetlands were selected due to the ability to treat large volumes of effluent while minimizing land area requirements.
The CCWA Shoal Creek system includes the 7,950 m^3/day Shoal Creek Water Reclamation Facility, a storage reservoir, a pump station, and constructed wetlands, consisting of approximately 1,457,000 m^2 (including approximately 607,000 m^2 of sprayfields) with a permitted capacity of 4160 m^3/day. Owing to the increasing demand additional wetlands are being added since the year 2000 and provide 11,360 m^3/day of additional capacity, and encompass about 222,600 m^2 wetland acres subdivided into 22 separate cells. The reclaimed water from the wetlands is collected and returned to the Shoal Creek Reservoir, eventually flowing to the J.W. Smith Reservoir to augment potable water supply.

The study area for the field work included of two cells of the CCWA constructed wetlands. These are Cell I-1 (Figure 1(a)) and Cell H (Figure 1(b)) and were selected for the following reasons. First of all, the geometry is relatively simple and the flow is expected to be one-dimensional (so that the flow can be reproduced in a straight laboratory flume). Secondly, the state of the vegetation in the two cells is monoculture consisting of 99% Cattail (*Typha Latifolia*). This allows investigation of the flow resistance of this species exclusively. Thirdly, the density of the vegetation is different in both cells so that the influence of the density on the hydrodynamics and the flow resistance can be investigated also. Each cell consists of two marsh zones and three deep zones arranged in an alternating fashion. A schematic side view of a longitudinal cross-section through the cells is shown in Figure 2.

(a) Cell I-1 (b) Cell H

Figure 1. Location of the samples for the quantification of vegetation

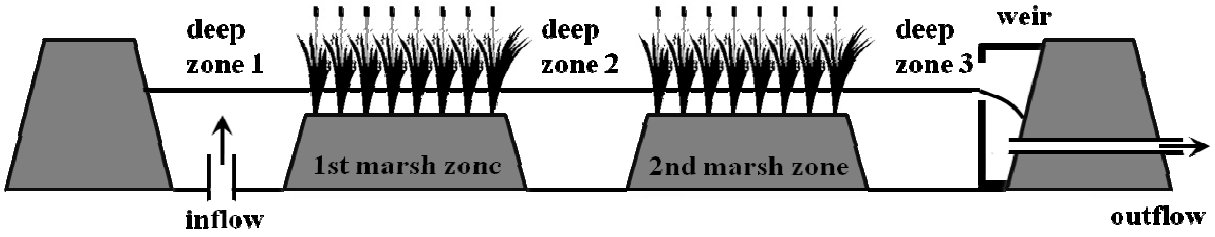

Figure 2. Schematic side view of a longitudinal cross-section through the cells (not to scale)

(a) (b) (c)

Figure 3. Typical stands of *Typha* (Cattail) in the CCWA constructed wetlands

The prevailing vegetation of these two cells is Typha latifolia (Cattail). Typha latifolia is generally acknowledged as an erect, rhizomatous, perennial aquatic growing to 3 m tall, with creeping rhizomes up to 70 cm long and from 0.5 to 3 cm in diameter. The fibrous roots develop from soft, white rhizomes. The linear pale or grayish-green leaves are flat, sheathing, 80 to 120 cm long, and 8 to 20 mm wide (Mitich, 2000). The collected Cattail in March and November is shown in Figure 3(a) and 3(b), respectively.

Quantification of the size and density of the vegetation was carried out three times in May, June, and November, 2009, a several locations in each of the two marsh zones of Cells I and H. In total, 12 representative locations in the four marsh zones were selected, at which a 1 m x 1 m square was marked out. Within the square each plant was identified

and several geometric parameters including the diameter of each individual plant and the relative distances between the plants were measured. The example sketch in Figure 4a (upper part) shows which quantities were measured for each plant. The lower part of Figure 4b shows the sampled vegetation arrangement in one of the squares. All results of 12 measurements are attached in Appendix 1.

In the past many empirical techniques were developed for plant density quantification (Cottam and Curtis, 1956; Dix, 1961; Elzinga et al., 1998; Lyon, 1968; and Mueller-Dombois and Ellenberg, 1974). In doing so, empirical formulas were developed that convert average area around a plant individual to traditional terms of density that more easily are employed in a laboratory setting. Herein three of those empirical methods were used to convert the observed plant densities into values better predicting the natural, random growth of plants, and are as follows: The Closest Individual method, the Point-Centered Quartet method, and the Nearest Neighbor method.

1) Closest Individual Method (CIM)

This technique requires a series of virtual and stagnated sample points established within a 1m square area, A. Then the distance, s from a sample point to the closest individual is measured. The estimate density form CIM is

$$\boldsymbol{m} = \frac{\boldsymbol{A}}{(\boldsymbol{2s_{ave}})^2} \tag{2}$$

, in which m = density or number of individuals per specified area, save = average distance measured from point to plant, respectively. In this study, 36 sample points were used.

2) Nearest Neighbor Method (NNM)

For the NNM, the distance from a selected plant to its nearest plant (neighbor) is measured. Then the average distance to each one's nearest plant neighbor is calculated as follows.

$$\boldsymbol{m} = \frac{\boldsymbol{A}}{(\boldsymbol{1.67s_{ave}})^2} \tag{3}$$

, in which a coefficient of 1.67 was used based on past field studies describing the random growth and sporadic placement of plants in nature.

3) Point-Centered Quarter (PCQ)

This method also requires a series of sample points within the sample area. Quadrants are established for each point with the associated point at the center. It is equivalent to laying a "cross" or "plus" shaped guide over each point. The distance from the reference point to the nearest plant in each of the four quadrants is measured. The density is evaluated using

the averaged distance of each averaged distance of the four values from each of a quadrant.

$$m = \frac{A}{(s_{ave})^2} \tag{4}$$

The distance between vegetation and the diameter were analyzed for the four different samples for each cell.

Field Measurement Datasheet 1/3

Sample No.	1
Date	5-May-09
Member	Su Jin Kim, Brandon Harris, Brandon Strellis, Ingrid Duque
Measuring location	(check or sketch the location on the picture below)

Cell I-1

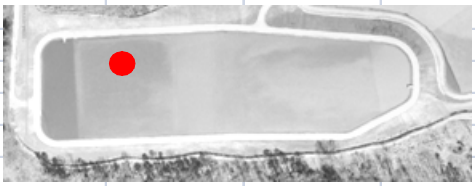

Cell H

Discharge		(cfs or cms)
Numbers of cattail in 1m x 1m	32	

Sketch of 1m x 1m zone with distance between vegetion (1grid = 2.5 cm x 2.5 cm)

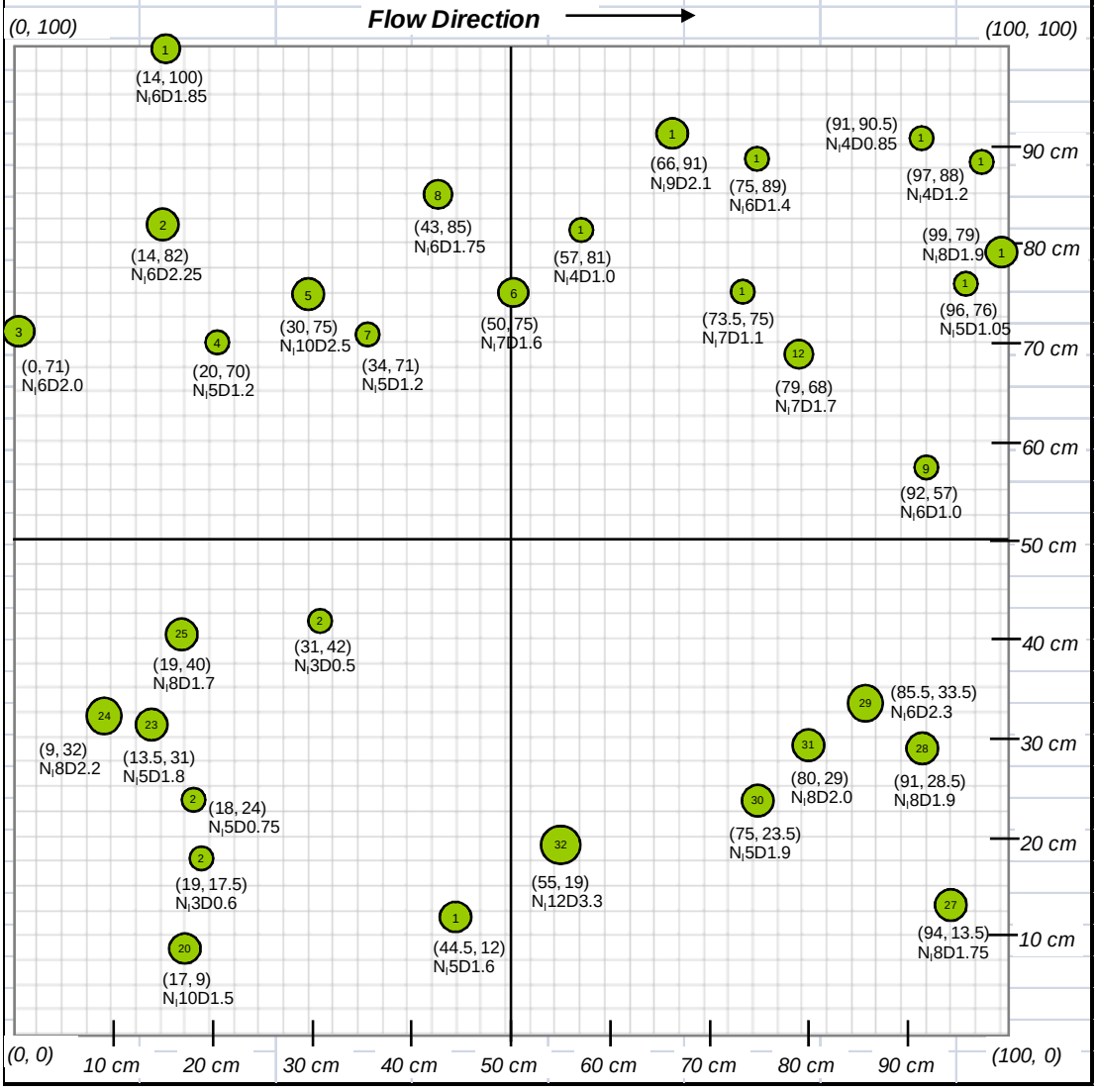

Figure 4a. Fieldwork datasheet and the example of the record

Field Measurement Datasheet 2/3

Sample No. 1

Sample datail

$$A_{front} = D(h-a) + \frac{(D+b)}{2}a$$

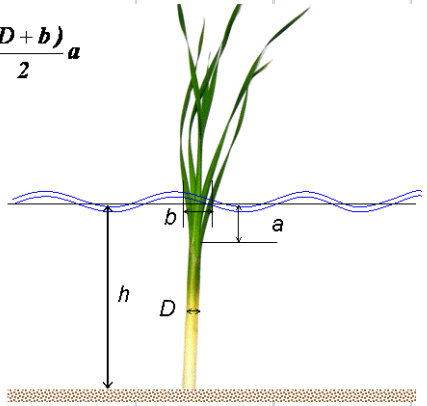

sample number	N_L, number of leaves	D, thickness of cattail (cm)	dx, x distance from left down corner (cm)	dy, y distance from left down corner (cm)	*h, height bottom to surface (cm)*	a, height between branch and water-surface (cm)	b, frontal length at water-surface (cm)
1	6	1.85	14	100			
2	6	2.25	14	82			
3	6	2.00	0	71			
4	5	1.20	20	70			
5	10	2.50	30	75			
6	7	1.60	50	75			
7	5	1.20	34	71			
8	6	1.75	43	85			
9	6	1.00	92	57			
10	5	1.05	96	76			
11	8	1.90	99	79			
12	7	1.70	79	68			
13	4	1.20	97	88			
14	4	0.85	91	90.5			
15	7	1.10	73.5	75			
16	4	1.00	57	81			
17	9	2.10	66	91			
18	6	1.40	75	89			
19	5	1.60	44.5	12			
20	10	1.50	17	9			
21	3	0.60	19	17.5			
22	5	0.75	18	24			
23	5	1.80	13.5	31			
24	8	2.20	9	32			
25	8	1.70	19	40			
26	3	0.50	31	42			
27	8	1.75	94	13.5			
28	8	1.90	91	28.5			
29	6	2.30	85.5	33.5			

Figure 4b. Fieldwork datasheet and the example of the record

The summary of the vegetation quantification data analysis is detailed in Tables 1, 2, and 3. Statistical analysis is performed for each sample (Table 2 for samples in Cell I-1, and Table 3 for samples in Cell H), and then it extends to the unit of marsh zones, cells and total (Table 1). In total, the mean diameter of the Cattail results in 0.027 m as known in common. After the average distance between vegetation at each sample is analyzed, it is used to calculate the number of vegetation in $1m^2$. The average number of individuals in 1m X 1m is 44. From the results of average distance between vegetation and the number of vegetation which is density of Cattail, the volume fraction of vegetation is also determined.

For the numerical simulation of the field scale in Chapter 5, the mean values of the measurement and the three estimations are adopted. The adopted values of each cell are listed in Table 4.

Table 1. Summary of the vegetation quantification data analysis

	Method	*I-1st*	*I-2nd*	*Cell I*	*H-1st*	*H-2nd*	*Cell H*	*total*
Diameter, D (m)		0.021	0.022	0.021	0.037	0.029	0.033	0.0271
Area, $A=\pi(D^2)/4$ (m^2)		0.00035	0.00036	0.00036	0.00109	0.00065	0.00085	0.00058
Average distance between vegetation, d (m)	*CIM*	0.109	0.099	0.104	0.108	0.092	0.100	0.1020
	NNM	0.109	0.087	0.098	0.090	0.091	0.091	0.0943
	PCQM	0.184	0.157	0.171	0.174	0.169	0.172	0.1711
	Mean	0.134	0.114	0.124	0.124	0.117	0.121	0.122
Number of vegetation in $1m^2$, m (m^{-2})	*Count*	37	46	42	43	50	46	44
	CIM	21.42	27.59	24.50	25.31	30.00	27.65	26.08
	NNM	39.96	48.98	44.47	50.72	53.69	52.20	48.34
	PCQM	59.56	61.96	60.76	51.13	59.91	55.52	58.14
	Mean	39.57	46.13	42.85	42.46	48.40	45.43	44.14
Volume fraction of vegetation area, φ (-)	*Count*	0.0130	0.0167	0.0148	0.0464	0.0325	0.0396	0.0254
	CIM	0.0074	0.0100	0.0087	0.0275	0.0195	0.0236	0.0151
	NNM	0.0139	0.0178	0.0158	0.0551	0.0349	0.0446	0.0279
	PCQM	0.0207	0.0225	0.0216	0.0556	0.0389	0.0474	0.0336
	Mean	0.0137	0.0167	0.0152	0.0461	0.0315	0.0388	0.0255

Table 2. Vegetation quantification data analysis of each sample in Cell I-1

	Method	*I1*	*I2*	*I3*	*I4*	*I5*	*I6*
Diameter, D (m)		0.016	0.017	0.023	0.025	0.024	0.023
Area, $A=\pi(D^2)/4$ (m^2)		0.00020	0.00023	0.00040	0.00049	0.00046	0.00040
Average distance between vegetation, d (m)	*CIM*	0.104	0.090	0.122	0.084	0.101	0.123
	NNM	0.094	0.082	0.157	0.102	0.074	0.078
	PCQM	0.183	0.158	0.203	0.135	0.168	0.177
	Mean	0.127	0.110	0.161	0.107	0.114	0.126
Number of vegetation in $1m^2$, m (m^{-2})	*Count*	32	48	37	53	43	37
	CIM	22.94	30.93	16.78	35.22	24.55	16.60
	NNM	40.65	53.05	14.50	34.39	64.74	59.50
	PCQM	46.14	51.45	39.98	65.83	92.57	68.60
	Mean	35.43	45.86	27.06	47.11	56.21	45.42
Volume fraction of vegetation area, φ (-)	*Count*	0.0065	0.0109	0.0150	0.0260	0.0199	0.0147
	CIM	0.0047	0.0070	0.0068	0.0173	0.0114	0.0066
	NNM	0.0083	0.0120	0.0059	0.0169	0.0300	0.0237
	PCQM	0.0094	0.0117	0.0162	0.0323	0.0429	0.0273
	Mean	0.0072	0.0104	0.0110	0.0231	0.0261	0.0181

Table 3. Vegetation quantification data analysis of each sample in Cell H

	Method	*H1*	*H2*	*H3*	*H4*	*H5*	*H6*
Diameter, D (m)		0.023	0.020	0.022	0.022	0.067	0.045
Area, A=π(D²)/4 (m²)		0.00042	0.00031	0.00037	0.00038	0.00350	0.00156
Average distance between vegetation, d (m)	*CIM*	0.095	0.083	0.083	0.095	0.147	0.098
	NNM	0.079	0.084	0.072	0.070	0.120	0.120
	PCQM	0.164	0.145	0.147	0.151	0.211	0.211
	Mean	0.112	0.104	0.101	0.105	0.159	0.143
Number of vegetation in 1m², m (m⁻²)	*Count*	47	57	60	58	21	35
	CIM	27.91	35.93	36.40	27.95	11.61	26.13
	NNM	57.71	51.24	69.52	73.23	24.94	36.59
	PCQM	59.15	75.92	71.86	69.27	22.37	34.54
	Mean	47.94	55.02	59.44	57.11	19.98	33.06
Volume fraction of vegetation area, φ (-)	*Count*	0.0199	0.0177	0.0220	0.0218	0.0736	0.0544
	CIM	0.0118	0.0112	0.0133	0.0105	0.0407	0.0406
	NNM	0.0244	0.0159	0.0255	0.0276	0.0874	0.0569
	PCQM	0.0250	0.0236	0.0263	0.0261	0.0784	0.0537
	Mean	0.0203	0.0171	0.0218	0.0215	0.0700	0.0514

Figures 5, 6, and 7 present the results from the data analysis using the three different methods for each sample, marsh zone, and cell. In the figures upper cases show the analysis of vegetation in Cell I-1 and lower cases present one in Cell H. Figure 5 shows the analysis of distance between vegetation. The uniformity of the vegetation is apparent and similar results were obtained from each of the methods, with the PCQ method tending to give the highest values. From the average distance by three different methods, the densities of vegetation in each sample, marsh zone, and cell were calculated. Both number of vegetation per 1 m^2 and volume fraction of vegetation indicate the vegetation densities. Figure 5 shows the results of number of vegetation per 1 m^2 and Figure 6 shows the ones of volume fraction of the vegetation area when using the averaged diameter of plants. The difference between those two indexes for indicating vegetation densities is whether the average diameter of vegetation is considered in the calculation or not. The vegetation density is slightly higher in Cell H from volume fraction of vegetation.

The volume fraction of vegetation is defined as follows

$$\varphi = m\frac{\pi D^2}{4} \tag{5}$$

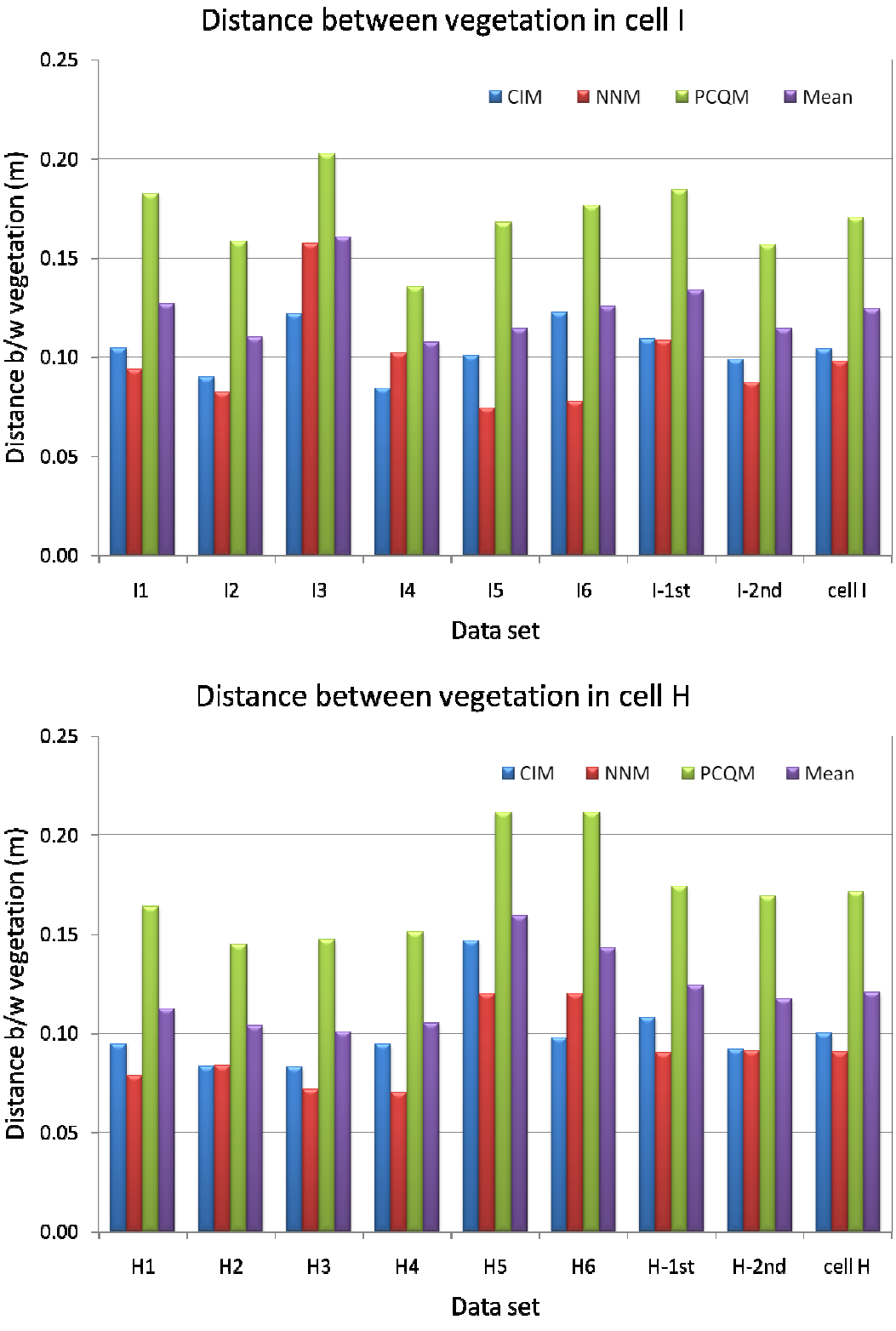

Figure 5. Data analysis for distance between vegetation of CCWA Cell I-1 (top) and Cell H (bottom)

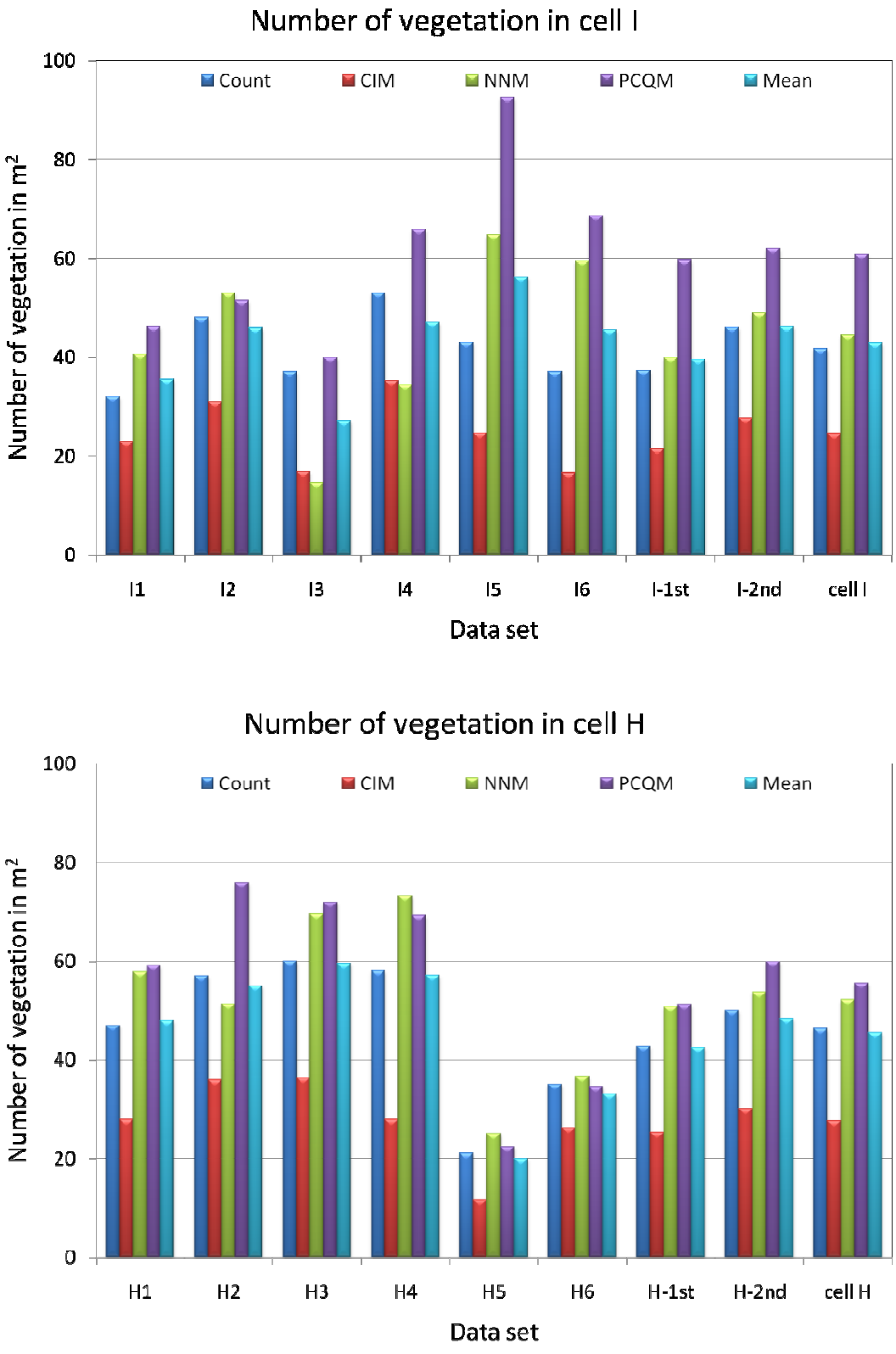

Figure 6. Data analysis for number of vegetation of CCWA Cell I-1 (top) and Cell H (bottom)

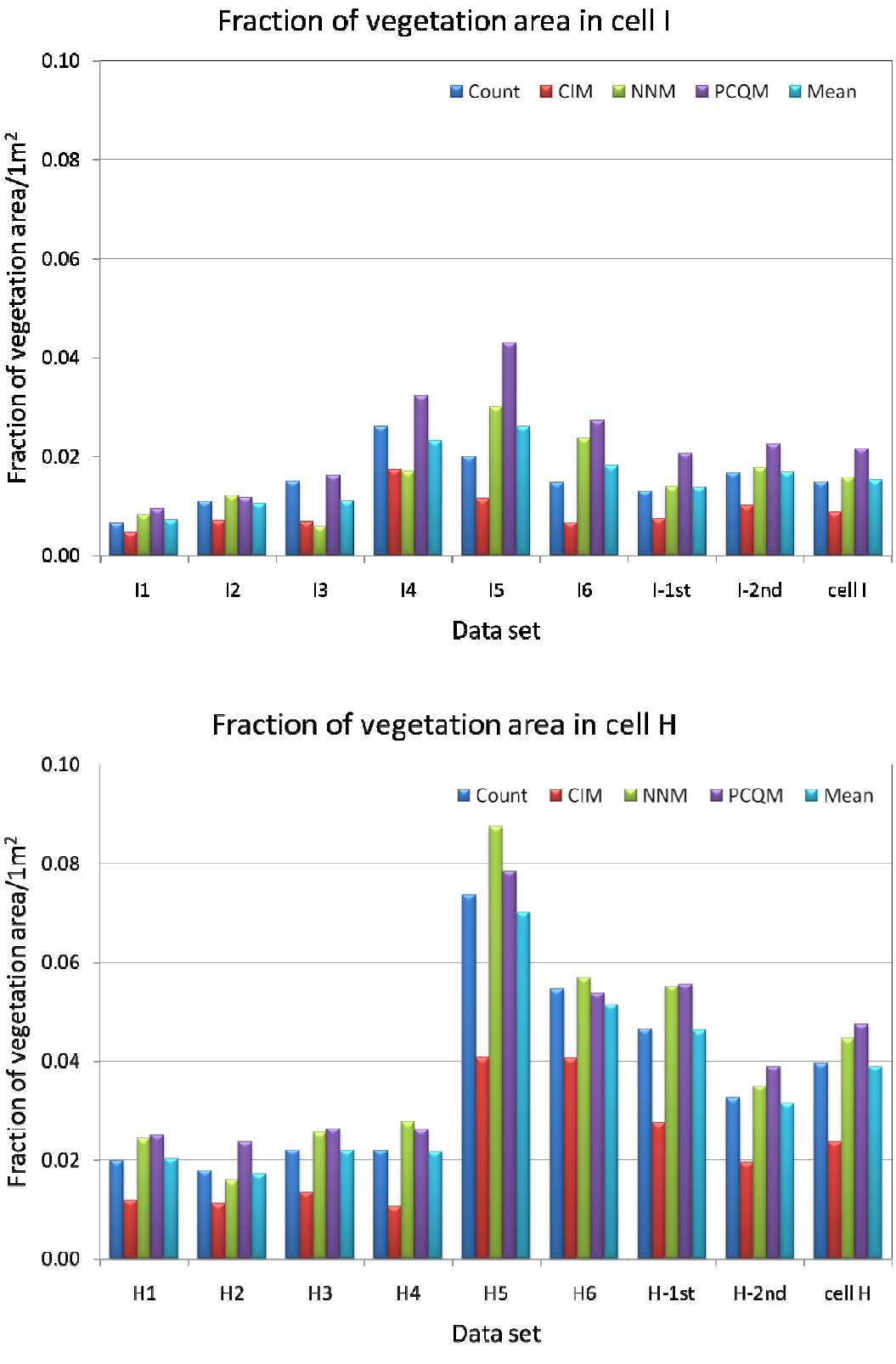

Figure 7. Data analysis for area fraction of vegetation of CCWA Cell I-1 (top) and Cell H (bottom)

3.2 Water depth measurements

Several water surface profiles and water depth measurements were conducted using pre-installed stakes in deep zones. Figure 8 shows the water surface profiles taken on May 29, 2009 for Cells I and H and the locations of measurement is described as well. All datasheets are presented in Appendix 2. Water depth measurements were carried out with help of pre-installed stakes shown in Figure 9. Figure 10 shows the weirs in Cells I and H, respectively.

Field Measurement Datasheet

				No.			1
Date	29-May-09						
Member	Su Jin Kim, Brandon Harris						
Cell I-1				Cell H			
time	10:00 ~11:00 am			time	11:00 ~12:00 pm		
Survey Point ID	reference elevation	Water Level	Water depth (m)	Survey Point ID	reference elevation	Water Level	Water depth (m)
Sfe_113	278.26						
I-1	277.17	276.86	1.32	H-1	255.53	255.22	1.94
I-2	277.16	276.86	1.32	H-2	255.52	255.22	1.93
I-3	277.17	276.86	1.32	H-3	255.52	255.22	1.94
I-4	277.16	276.86	1.32	H-4	255.54	255.23	1.94
I-5	277.15	276.86	1.32	H-5	255.52	255.22	1.93
I-6	277.15	276.85	1.31	H-6	255.51	255.22	1.93
I-7	277.16	276.85	1.31	H-7	255.51	255.22	1.93
I-8	277.08	276.80	1.26	H-8	255.45	255.15	1.86
I-9	277.09	276.81	1.27	H-9	255.44	255.15	1.86
I-10	277.08	276.80	1.26	H-10	255.44	255.15	1.86
I-11	277.08	276.80	1.26	H-11	255.44	255.15	1.86
Pell	278.60	276.71	crest	Peh1	256.64	255.09	crest
	H=	0.09			H=	0.05	
	P=	1.170432			P=	1.801368	
bottom elev	275.54	m		bottom elev	253.29	m	

Figure 8. Location of measurement position in the two cells and example of the datasheet of the water depth measurements

Figure 9. Measurement point

Figure 10. Weir

Water surface profiles in Cell I and Cell H are illustrated in Figure 11 and 12, respectively. The plotted water levels are from measurement dates, May 29, June 12, June 26, and November 6, and the numbers in round brackets show the inflow at each date. The inflow data was provided by CCWA. As confirmed in the figures, the water surface profiles in Cell I are proportional to the daily inflow data. However, the water surfaces in Cell H do not exhibit consistency with the inflow data. For instance the water surface profile for Q=0.0354 is the maximum discharge but does not show the highest waterlevels. Therefore, the results affect the flow resistance analysis and numerical simulation.

The water surface profiles of each marsh zone was used for the head loss calculations. Zero slope was observed for the deep zones, which could be expected due to the very low velocities and the relatively smooth bed. Though the vegetation density doesn't vary much between first and second marsh zone, the water surface slopes in each of the marsh zone differs quite dramatically (i.e. S_{upper} = 0.008 % and S_{lower}= 0.034 % for Cell I; and S_{upper} = 0.006 % and S_{lower}= 0.047 % for Cell H). This is rather surprising given the fact that the marsh zones are relatively long for Cell H (i.e. L_{upper} = 137 m, L_{lower} = 129 m). The flow resistance analysis below will provide evidence that

flow non-uniformity seems to be the dominating factor for the steep slopes, observed in particular in the second, downstream marsh zones.

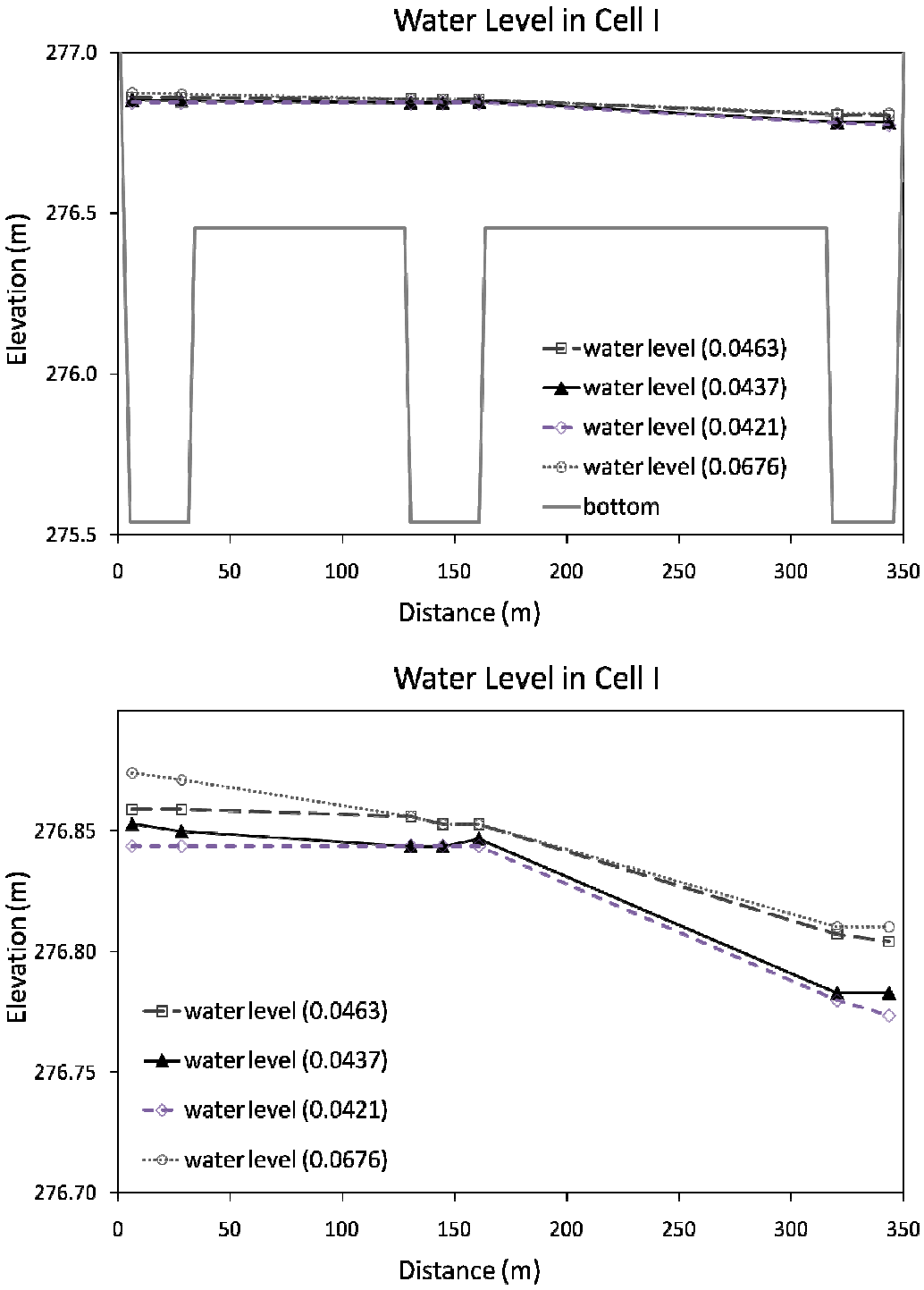

Figure 11. Water surface profile of Cell I with bottom elevation (top) and zoomed in profiles (bottom)

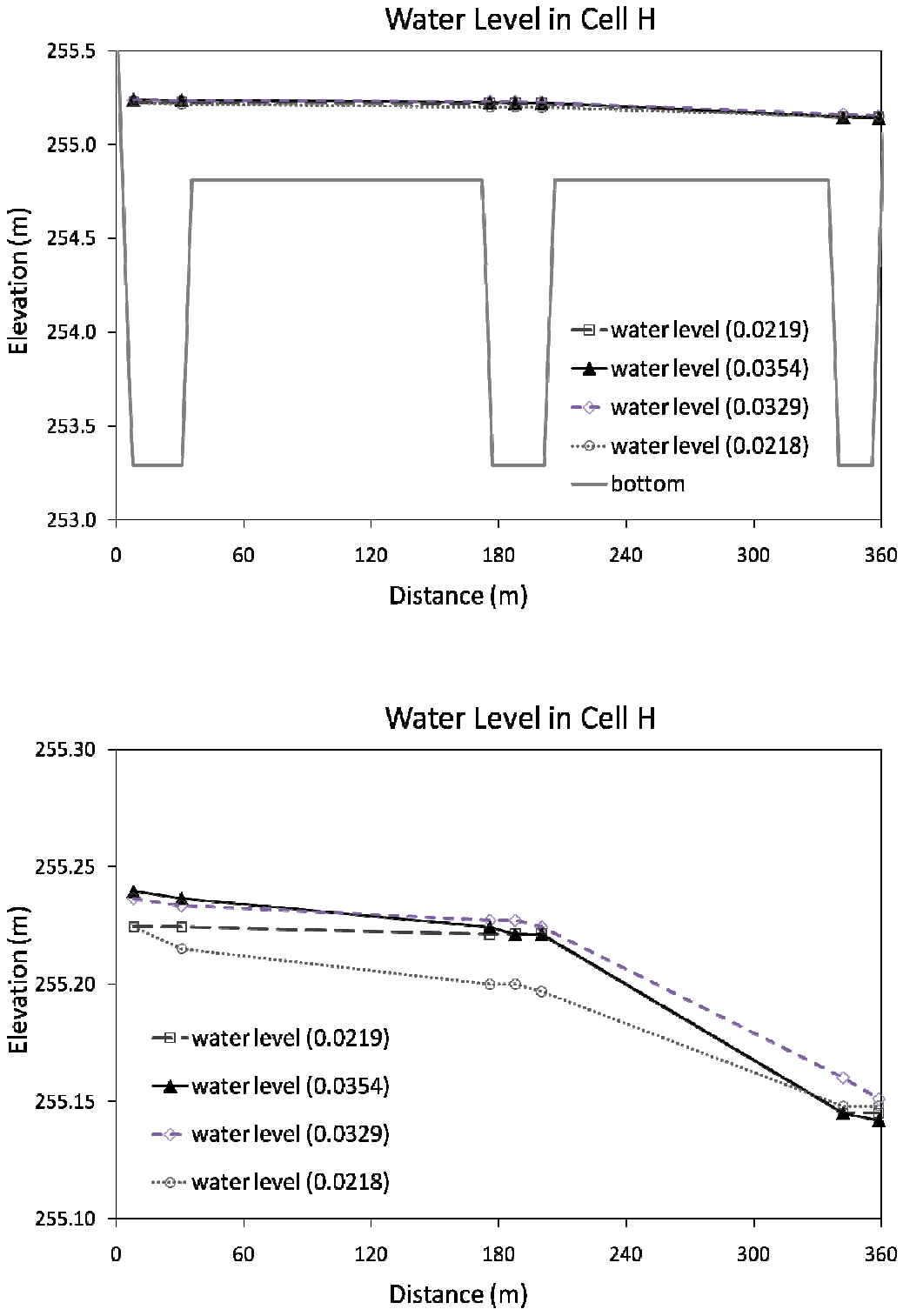

Figure 12. Water surface profile of Cell H with bottom elevation (top) and zoomed in profiles (bottom)

3.3 Hydraulic resistance and head loss

To calculate head loss and the drag forces on the marsh zone, the record of the influent of both cells given by CCWA is used from May 1 to December 3 in 2009. The average and maximum influent flows of Cell I during the period are 0.0463 and 0.0677 m^3/s, respectively, and 0.0222 and 0.0359 m^3/s for Cell H. Both first and second marsh zones are considered for the analysis. The flow of first marsh zone in the both cells is affected by influent flow, and the flow of second marsh zone is affected by the downstream control of weir. The length of the first marsh zone, L is 93.3 and 136.6 m, and the length of the second marsh zone, 151.8 and 128.9 m for Cells I and H, respectively. The bed levels of Cells I and H are 275.54 and 253.29 m, in that order. The bottom levels of each marsh zone are 0.91 and 1.524 m higher than the bed levels of Cells I and H, respectively. For the analysis, the diameter of vegetation, D and the solid volume fraction, φ are used of averaged values for each marsh zone, respectively, as shown in Table 4. The approaches for quantification of hydraulic resistance are three.

1) Friction factor, f

From extended Bernoulli equation (energy equation), head loss due to second marsh zone is calculated as follows (Figure 13)

$$z_1 + y_1 + \alpha_1 \frac{V_1^2}{2g} = z_2 + y_2 + \alpha_2 \frac{V_2^2}{2g} + h_L \tag{6}$$

, in which z = bed level from datum, y = water depth, V = velocity, g= gravity, h_L = head loss, and α is a kinetic energy flux correction coefficient and was assumed as 1. Subscripts 1 and 2 denotes the across section upstream and downstream, respectively. For laminar flow the head loss can be expressed by Darcy-Weisbach friction factor, f as shown below

$$h_L = f \frac{L}{4R} \frac{V^2}{2g} \tag{7}$$

, in which L = channel length, R = hydraulic radius, respectively.

Hence, the friction factor can be calculated from the head loss as follows

$$f = h_L \frac{4R}{L} \frac{2g}{V^2} \tag{8}$$

2) Manning's n

From the water surface profile, the energy gradient, S_e can be calculated and Manning's roughness coefficient can also be evaluated by it

$$S_e = -\frac{dy}{dx}\left(1 - F^2\right) + S_0 \tag{9}$$

$$n = \frac{K_n}{V} R^{\frac{2}{3}} S_e^{\frac{1}{2}} \tag{10}$$

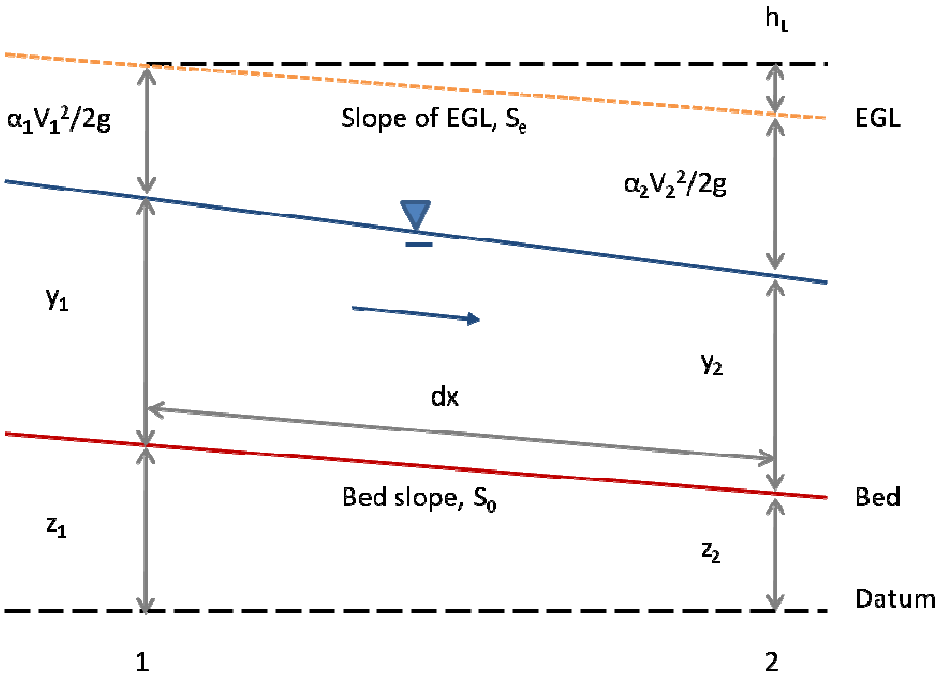

Figure 13. Definition sketch for Bernoulli equation

3) Drag force approach

As suggested by Wilson and Shaw (1977), a drag related force term can be included into the Navier Stokes equations in order to account for the flow resistance of vegetation. A sub-grid drag force per fluid mass unit in a finite volume cell F_D is calculated with the definition of plant density as in Figure 14 below (Wilson et al., 2004)

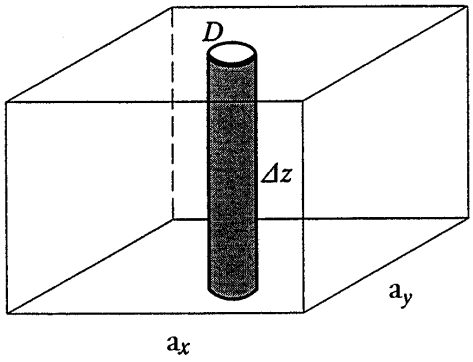

$$F_D = \rho \frac{u^2}{2} C_D \lambda$$

with:

cD = drag coefficient

λ = vegetative coefficient, defined as:

$$\lambda = \frac{projected\,area\,of\;plant}{total\,volume} = \frac{D\,\Delta z}{a_x\,a_y\,\Delta z}$$

Figure 14. Definition of drag force in a FV cell

Finally, the drag coefficient, c_D is evaluated by comparing total shear stress, F_g exerted on the flow region with total forces exerted on the vegetation, F_D,

$$F_g = F_D \tag{11}$$

$$\rho g h S_e = \frac{1}{2} \rho c_D A_p u^2 m \tag{12}$$

$$c_D = \frac{g h S_e}{\frac{1}{2} A_p u^2 m} \tag{13}$$

in which m is the number of individual vegetation per m^2, indicated in Table 4.

The result of the analysis for the hydraulic resistance is summarized in Table 5, and the relations of the results from each analysis are described in Figure 15.

From Table 5 and Figure 15, respectively it is apparent that the obtained values for hydraulic resistance parameters are unphysically high, regardless of the method. For instance flows around single or multiple cylinders (see Figures 16 and 17) exhibit drag coefficients that are dependent on both Re number and vegetation density. As Figure 17 indicates a uniform flow at low Re through very dense vegetation (e.g. phi=0.27) may exhibit largely increased drag coefficients, however for the conditions studied here maximum values of c_D=20 might be typical. Computed values of c based on the field measurements deviate by factor 40 – 600 (!!).

Obviously, all methods employed herein were developed for uniform flow conditions, which is not the case in neither of the marsh zones under consideration. Even though geometric as well as vegetation conditions in the two marsh zones are almost identical the headloss exhibits significant differences between first and second marsh zones which leads to enormous differences in the roughness coefficients. This reflects the rather large contribution of flow uniformity to the flow resistance parameters.

Table 4. Summary of the geometric properties of cells

Channel	*Marsh zone*	*D (m)*	*Volume fraction φ*	*m (#/m²)*	*Length (m)*	B_{ave} *(m)*	m_{total}= *m*LB*
Cell I	*1st*	0.021	0.0137	39.57	93.3	97.84	361286
Cell H		0.037	0.0461	42.46	136.6	99.97	579584
Cell I	*2nd*	0.022	0.0167	46.13	151.8	91.44	640422
Cell H		0.029	0.0315	48.40	128.9	96.01	599130

Table 5. Summary of the hydraulic resistance analysis

Date	*Marsh zone*	*Influent* (m^3/s)	d_1 (m)	d_2 (m)	dy (m)	u_{ave} (m/s)	Re_D	S_e	h_L (m)	n	f	c_D
5/29	*Cell I (1st)*	0.0463	0.405	0.402	-0.003	0.0012	25	0.00003	0.003	2.53	682	512
6/12		0.0437	0.396	0.390	-0.006	0.0011	24	0.00006	0.006	3.63	1416	1090
6/26		0.0421	0.390	0.390	0.000	0.0011	23	0.00000	0.000	0.00	0	0
11/6		0.0676	0.417	0.403	-0.014	0.0017	35	0.00015	0.014	3.97	1672	1236
5/29	*Cell H (1st)*	0.0219	0.411	0.409	-0.003	0.0005	20	0.00002	0.003	4.71	2348	914
6/12		0.0354	0.423	0.412	-0.011	0.0008	32	0.00008	0.011	6.00	3789	1448
6/26		0.0329	0.420	0.415	-0.006	0.0008	29	0.00004	0.006	4.58	2205	843
11/6		0.0218	0.402	0.387	-0.014	0.0006	21	0.00011	0.014	9.92	10560	4269
5/29	*Cell I (2nd)*	0.0463	0.398	0.355	-0.044	0.0013	29	0.00029	0.044	6.53	4652	3138
6/12		0.0437	0.392	0.331	-0.061	0.0013	28	0.00040	0.061	7.66	6475	4549
6/26		0.0421	0.389	0.328	-0.061	0.0013	28	0.00040	0.061	7.83	6795	4814
11/6		0.0676	0.399	0.358	-0.041	0.0020	42	0.00027	0.041	4.35	2062	1385
5/29	*Cell H (2nd)*	0.0219	0.405	0.336	-0.069	0.0006	18	0.00054	0.069	19.32	40910	19978
6/12		0.0354	0.405	0.336	-0.069	0.0010	29	0.00054	0.069	11.94	15627	7631
6/26		0.0329	0.409	0.351	-0.058	0.0009	26	0.00045	0.058	12.29	16425	7830
11/6		0.0218	0.382	0.338	-0.044	0.0006	18	0.00034	0.044	14.78	24170	12153

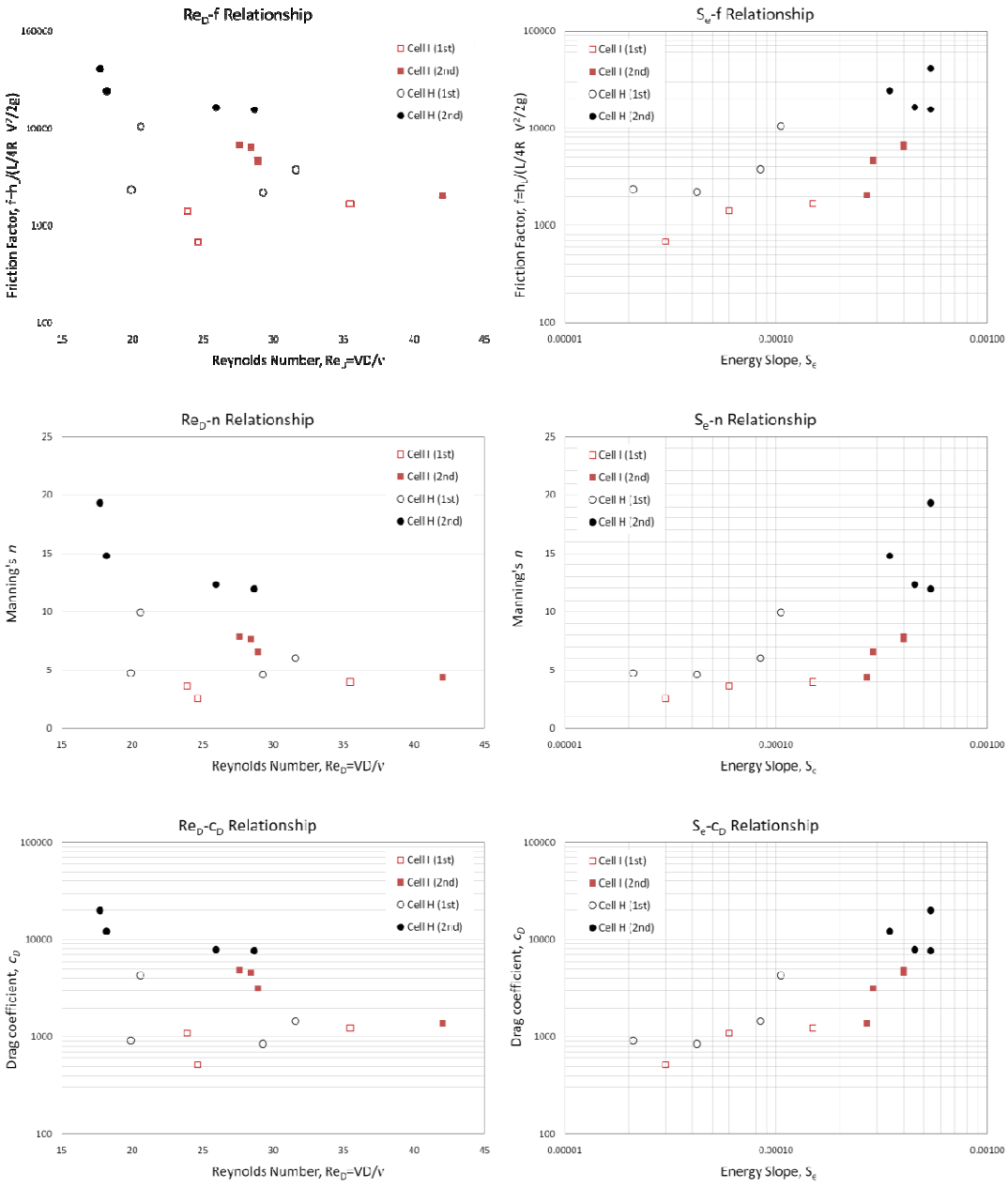

Figure 15. Summary of the quantification of hydraulic resistance using three methods

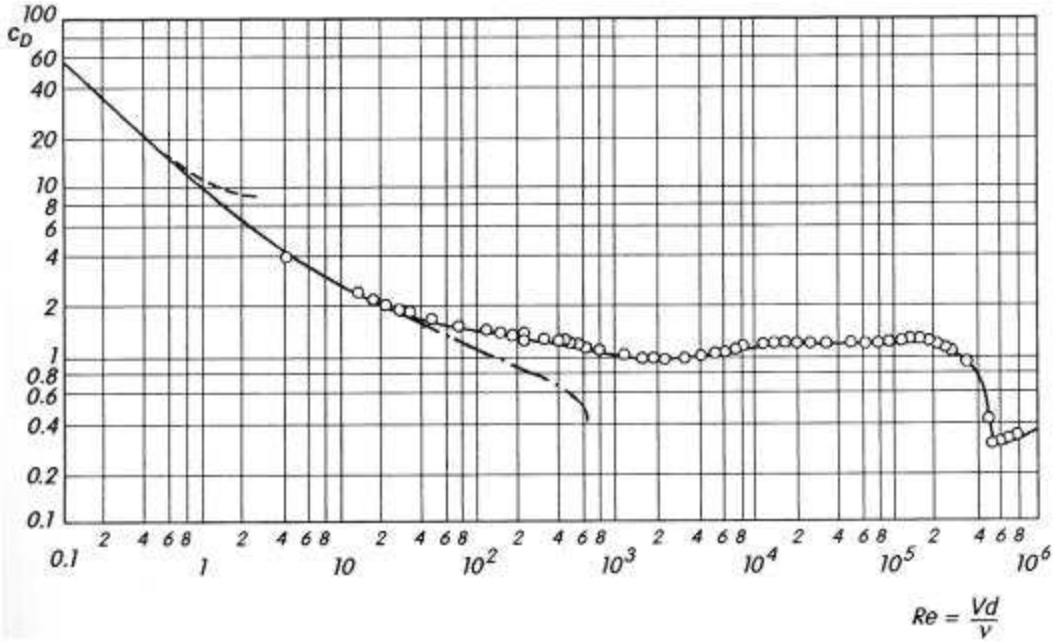

Figure 16. The drag coefficient c_D of flow around a cylinder, as function of the Reynolds number Re (Schlichting and Gersten, 2000).

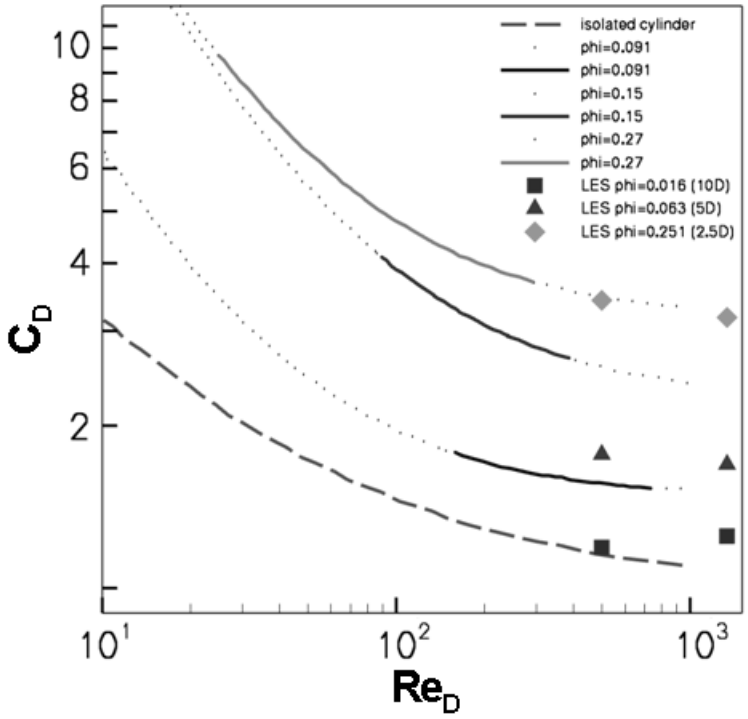

Figure 17. Drag coefficient c_D as a function of the Reynolds number for various vegetation densities (Kim and Stoesser, 2009)

4. LABORATORY EXPERIMENTS

4.1 Design of experimental setup

The experiments were carried out in a 8m long, 1m wide flume in the hydraulic laboratory at the Georgia Institute of Technology in order to recreate the flow conditions in the wetland cells, at the measured vegetation densities. The experiment was designed as a Re model based on the average diameter of the vegetation from analysis (Table 1) at a 1:2.7 scale. Two different vegetation densities were modeled using thin, wooden dowels. The dowels were arranged in staggered array and the distance, s was determined based on the ratio to the cylinder diameters, D, s = 8.5D and 4.25D. The diameter of the vegetation for the model was given as 0.01 m. The average diameter of the cattail stems in the field was found to be 0.027 m. Table 6 gives the physical model data including the length and width of the flume. Two cases of the distance between vegetation are subscribed as M1 and M2 in Table 6.

Figure 18 shows the setup in the flume and gives an impression of the vegetation density (here the 8.5D case) of the experiments. The dowels covered a length of 4.88 m of the flume. A third experiment was carried out during which the dowels in a section of the flume were cleared out for 0.6 m in order to mimic the alternating marsh zone / deep zone scenario in the wetlands.

Table 6. Experimental model scales

Properties	*Symbols and values*
Diameter of stem	D = 0.01 m
Distance between stems	s_{M1} = 8.5D s_{M2} = 4.25D
Channel width	W = 1 m
Channel length covered by stems	L = 4.88 m

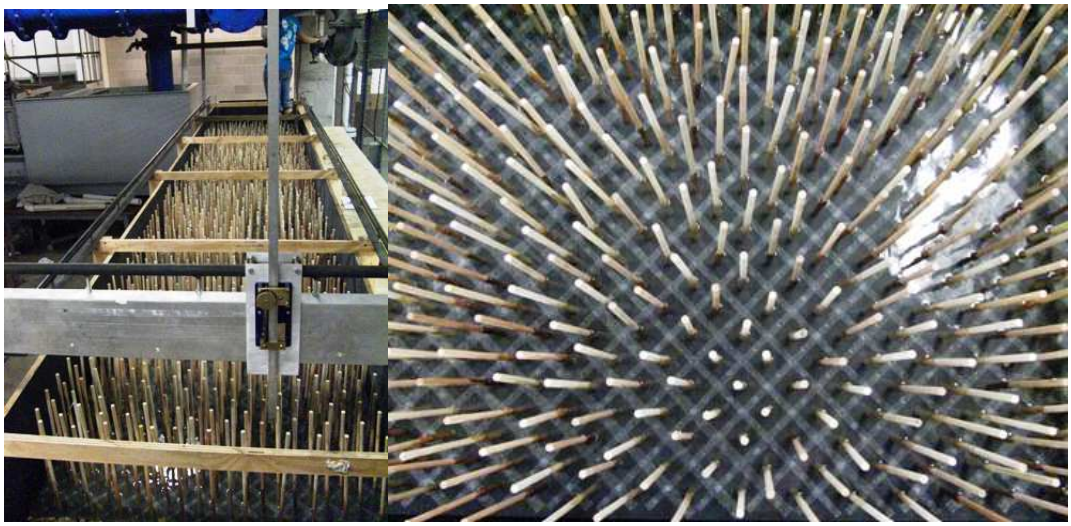

Figure 18. Vegetated channel of the experiment and the cylinders

Figure 19. Upstream (left) and downstream (right) of the channel

4.2 Water surface profile and analysis

Water surface elevations were taken at 33cm intervals along the length of the flume using a point gage. Figure 20 presents the water surface profiles for 8.5D case and Figure 21 exemplary shows the water surface profiles for two different cases. The vegetation density in both experiments was the one of the 4.25D cases, but the vegetation distribution was different; one was fully vegetated, and another had no vegetation in a 0.6m section. In the figure, the result of the latter case is denoted with w.e.z. (abbreviates with empty zone).

The original case which was 4.25D and fully vegetated flume showed monotonically decreasing depth due to the vegetation while the experiments with the emptied portion of the flume showed backwater between vegetated zones. As a result, the water surface profile exhibits lower values for the slope in upstream marsh zone and higher values of the water surface slope in the second marsh zone. Even though in the experiments it is not as pronounced as in the field the same trend as the water surface profile of the CCWA wet land cells can be observed. There are three reasons why the flume experiments only show a trend but could not entirely reproduce the profiles observed in the field.

1) The flume in the GT hydraulic lab has a slope of 0.6% while the wetland cells of the CCWA have no bed slope. Hence, the effect of non-uniformity is less pronounced in the flume.
2) The empty zone in the flume is not deep in contrast to the wetland cells of the CCWA. This deep zone magnifies the effect of non-uniformity which could not be reproduced in the laboratory.

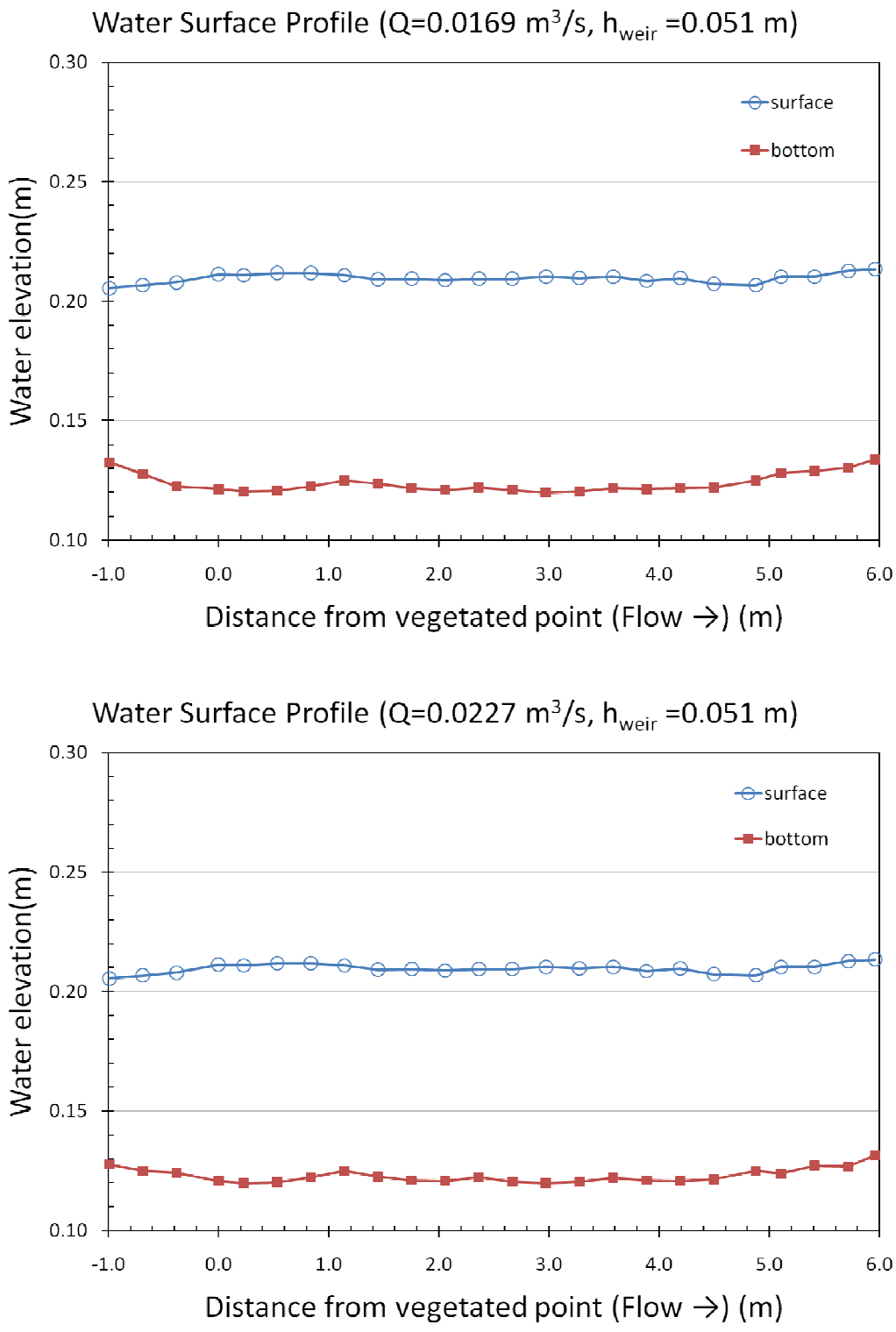

Figure 20. Water surface profile of experiments (8.5D, top-case 9 and bottom-case 12)

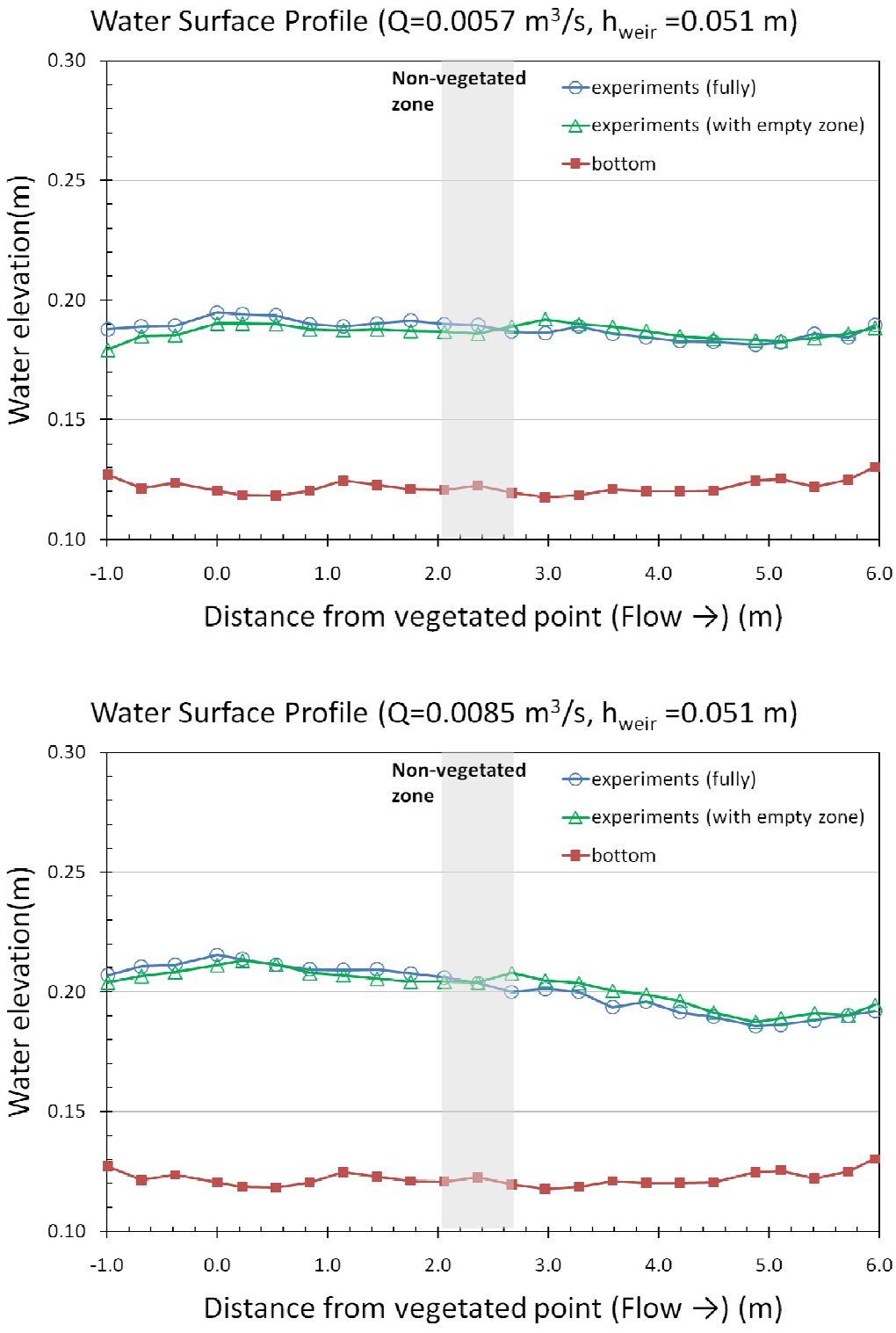

Figure 21a. Water surface profile of experiments (4.25D & 4.25D with empty zone, top-case 2 vs. 21 and bottom-case 3 vs. 22)

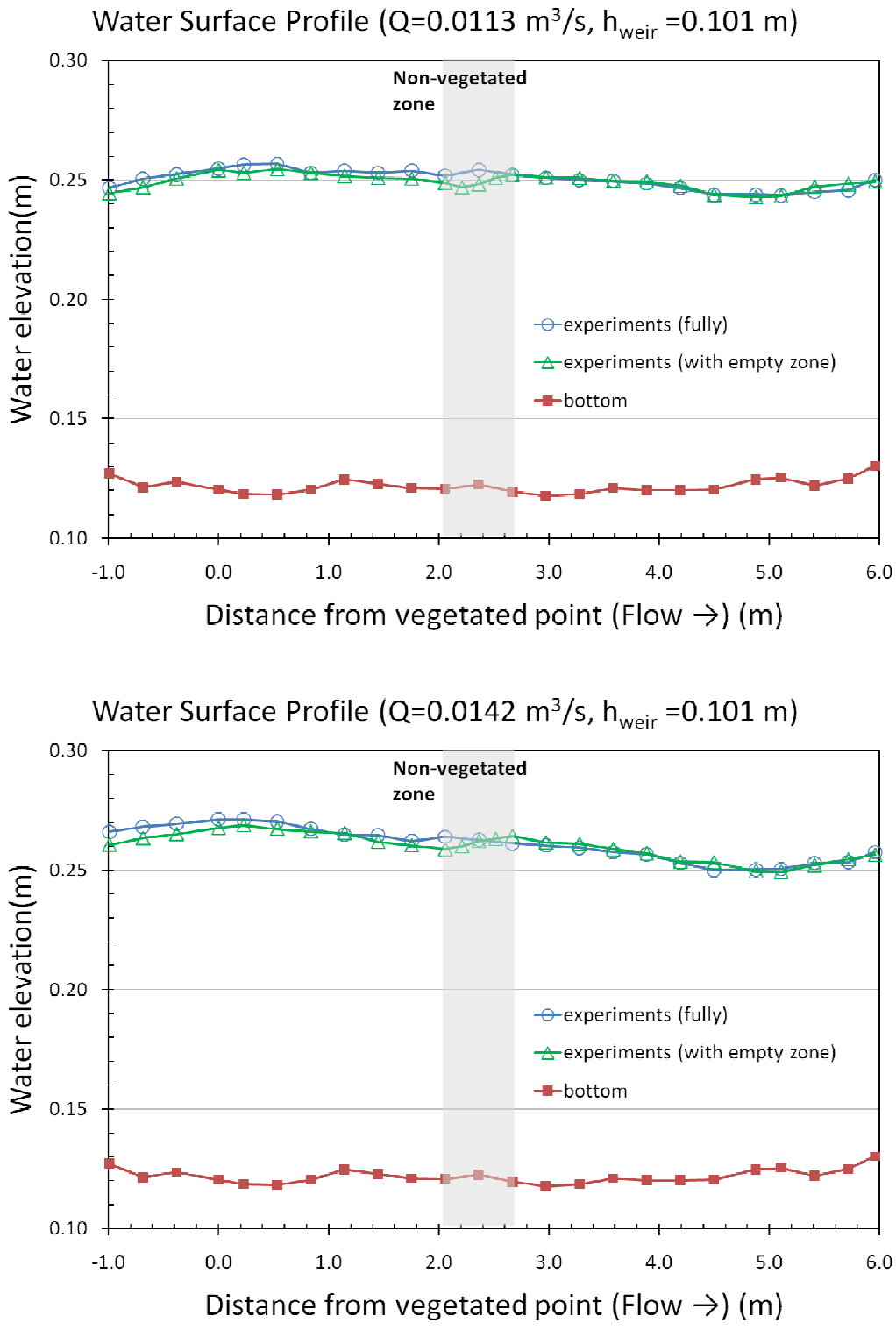

Figure 21b. Water surface profile of experiments (4.25D & 4.25D with empty zone, up-case 14 vs. 23 and down-case 15 vs. 24)

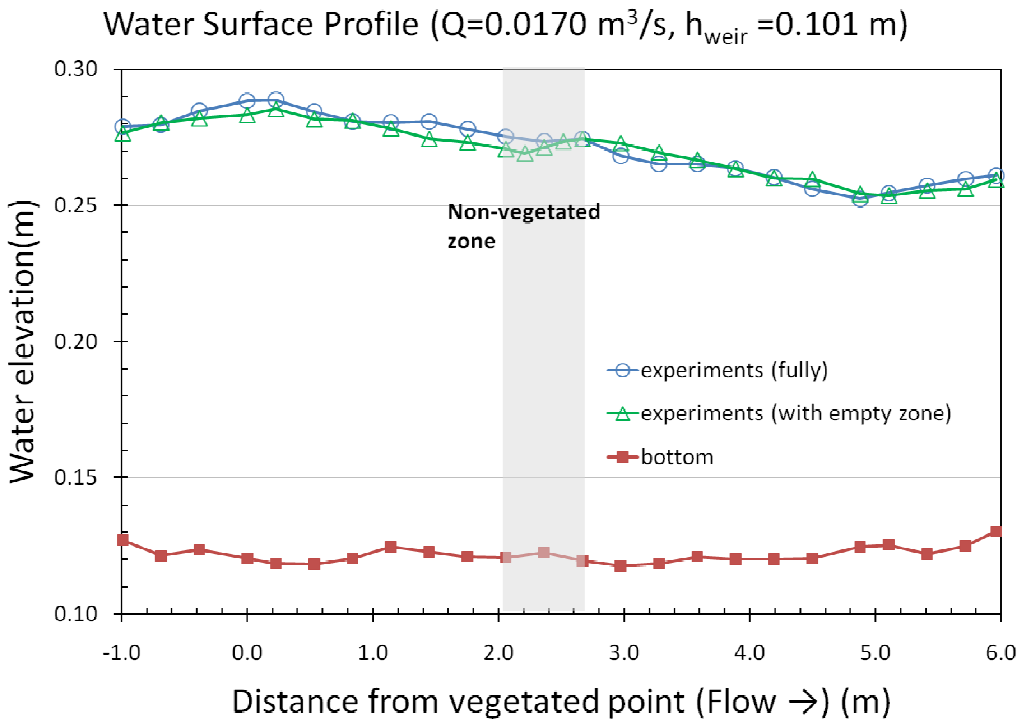

Figure 21c. Water surface profile of experiments (4.25D & 4.25D with empty zone, case 16 vs. 25)

4.3 Resistance analysis and discussions

The analysis of hydraulic resistance of the experimental cases is carried out with the three methods that were used for the field measurement data. The summary of experimental conditions and the results of the analysis are detailed in Tables 7, 8, and 9 for 8.5D, 4.25D, and 4.25D (w.e.z), respectively.

The flow resistance of the laboratory experiments was quantified by calculating the slope of the energy gradient line. The results of the series of the experiment of three cases were plotted together in Figures 22 to 24. As expected the 4.25D cases showed a greater energy slope as the 8.5D cases, which unambiguously and not surprisingly confirms that the higher density of vegetation results in higher flow resistance. Figure 22 presents the slope of the energy gradient line (EGL) as a function of cylinder Reynolds number. While the 8.5 D vegetation density shows a relatively weak influence of the Re_D number on the headloss, the EGL of the 4.25D increases exponentially with $Re_{D.}$

For the cases with the empty zone, the slope of the energy gradient line was calculated for each section separately and also for the entire length. Interestingly, the cases with the empty zone resulted in a lower energy slope for the total energy slope, but the energy slope in the second marsh zone was greater than the one under uniform conditions. This is in agreement with what has been observed from the field measurements, and provides evidence of strong non-uniformity of the flow being created by the deep zones.

For the experimental conditions, drag coefficients were calculated and are plotted versus the slope of energy gradient line and cylinder Reynolds number in Figures 23 and 24, respectively. At the same slope of energy gradient line 8.5D and 4.25D cases exhibit different drag coefficients. The drag coefficients for the 8.5D and 4.25D were in range of 1.22 to 1.44 and 1.83 to 2.37, respectively. The c_D values are compared to drag coefficient of the experimental study of Tanino and Nepf (2008) and the Large-Eddy Simulations of Kim and Stoesser (2009) in Figure 25.

Figures 22 to 25 confirm that the drag coefficient dependent on both the vegetation density and the cylinder Re number, in particular at lower Re numbers.

Table 7. Summary of the experiments and the analysis of 8.5D cases

Case	*d*	*Q* (m^3/s)	*weir h* (*m*)	h_{ave} (*m*)	u_{bulk} (*m/s*)	Re_D	S_e	H_L (*m*)	*f*	*n*	c_D
4	*8.5D*	0.0027	0.102	0.096	0.028	284	0.001	0.006	10.3	0.24	11.57
5		0.0056		0.102	0.055	548	0.002	0.009	4.2	0.15	4.46
6		0.0076	0.146	0.152	0.050	502	0.002	0.007	5.4	0.18	4.23
7		0.0059	0.051	0.053	0.113	1126	0.004	0.017	1.0	0.07	1.99
8		0.0114		0.072	0.159	1594	0.005	0.026	1.0	0.07	1.49
9		0.0168		0.088	0.193	1934	0.008	0.037	1.2	0.08	1.44
10		0.0027		0.043	0.064	639	0.001	0.006	1.0	0.06	2.25
11		0.0042		0.048	0.089	889	0.002	0.011	1.0	0.07	2.02
12		0.0227		0.099	0.231	2309	0.009	0.045	1.1	0.08	1.22
13		0.0027	0.122	0.115	0.024	235	0.001	0.004	10.8	0.25	10.44
14		0.0042		0.120	0.036	358	0.001	0.006	7.8	0.21	7.28
15		0.0057	0.146	0.145	0.040	395	0.001	0.006	7.1	0.21	5.69
16		0.0113		0.159	0.072	720	0.002	0.009	3.2	0.14	2.41
18		0.0227	0.122	0.164	0.140	1398	0.004	0.021	2.1	0.12	1.55

Table 8. Summary of the experiments and the analysis of 4.25D cases

Case	*d*	*Q* (m^3/s)	*weir h* (*m*)	h_{ave} (*m*)	u_{bulk} (*m/s*)	Re_D	S_e	H_L (*m*)	*f*	*n*	c_D
1	*4.25D*	0.0027	0.051	0.048	0.056	562	0.006	0.028	6.2	0.17	3.20
2		0.0057		0.068	0.085	846	0.010	0.047	6.2	0.18	2.37
3		0.0085		0.082	0.105	1050	0.013	0.063	6.5	0.18	2.08
4		0.0113		0.096	0.120	1195	0.016	0.077	6.9	0.20	1.95
5		0.0142		0.113	0.127	1266	0.019	0.090	8.3	0.22	2.05
6		0.0170		0.125	0.138	1378	0.020	0.096	8.1	0.22	1.83
7		0.0184		0.132	0.141	1412	0.022	0.109	9.1	0.23	1.99
8		0.0198		0.138	0.145	1454	0.024	0.119	9.7	0.24	2.04
9		0.0212		0.145	0.148	1476	0.025	0.123	10.2	0.25	2.05
10		0.0227		0.152	0.150	1502	0.027	0.133	11.1	0.26	2.14
11		0.0027	0.101	0.096	0.028	283	0.002	0.008	13.3	0.27	3.73
12		0.0057		0.108	0.053	530	0.005	0.025	12.6	0.27	3.20
13		0.0085		0.119	0.072	719	0.007	0.032	9.6	0.24	2.25
14		0.0113		0.131	0.087	875	0.009	0.045	9.8	0.24	2.14
15		0.0142		0.141	0.102	1016	0.011	0.055	9.4	0.24	1.93
16		0.0170		0.152	0.113	1130	0.014	0.069	10.2	0.25	1.98
17		0.0184		0.158	0.118	1177	0.014	0.070	9.8	0.25	1.84
18		0.0198		0.164	0.122	1222	0.016	0.077	10.2	0.25	1.87
19		0.0212		0.169	0.127	1268	0.017	0.083	10.5	0.26	1.87
20		0.0227		0.175	0.130	1305	0.018	0.086	10.5	0.26	1.83

Table 9. Summary of the experiments and the analysis of 4.25D with empty zone cases

Case	*d*	*Q* (m^3/s)	*weir h* (*m*)	h_{ave} (*m*)	u_{bulk} (*m/s*)	Re_D	S_e	H_L (*m*)	*f*	*n*	c_D
21	*4.25D with empty zone (total)*	0.0057	0.051	0.066	0.086	860	0.008	0.040	5.2	0.16	2.27
22		0.0085		0.082	0.104	1042	0.012	0.057	6.0	0.18	2.19
23		0.0113	0.101	0.129	0.089	885	0.009	0.045	9.4	0.24	2.37
24		0.0142		0.140	0.102	1021	0.011	0.051	8.7	0.23	2.05
25		0.0170		0.151	0.114	1138	0.013	0.062	8.9	0.23	1.99
26		0.0170	0.146	0.197	0.087	870	0.009	0.043	12.9	0.29	2.35
27		0.0184		0.201	0.093	925	0.010	0.051	13.7	0.30	2.48
28		0.0198		0.206	0.097	972	0.011	0.053	13.2	0.30	2.34
29		0.0212		0.210	0.102	1021	0.012	0.057	12.9	0.29	2.25
30		0.0227		0.215	0.106	1064	0.013	0.061	13.0	0.30	2.24
21	*4.25D with empty zone (1st)*	0.0057	0.051	0.067	0.086	856	0.008	0.017	5.1	0.16	1.95
22		0.0085		0.087	0.099	990	0.010	0.020	5.9	0.18	1.80
23		0.0113	0.101	0.131	0.087	874	0.009	0.018	9.5	0.24	2.08
24		0.0142		0.143	0.100	997	0.011	0.022	9.4	0.24	1.91
25		0.0170		0.157	0.109	1091	0.012	0.025	9.7	0.25	1.83
26		0.0170	0.146	0.198	0.086	864	0.010	0.021	14.9	0.31	2.37
27		0.0184		0.203	0.092	916	0.012	0.024	15.8	0.32	2.48
28		0.0198		0.209	0.096	956	0.012	0.025	15.2	0.32	2.34
29		0.0212		0.214	0.100	1003	0.012	0.025	14.4	0.31	2.18
30		0.0227		0.221	0.104	1037	0.012	0.025	13.4	0.30	1.98
21	*4.25D with empty zone (2nd)*	0.0057	0.051	0.067	0.086	859	0.011	0.024	6.7	0.18	2.59
22		0.0085		0.078	0.110	1100	0.017	0.038	7.5	0.20	2.51
23		0.0113	0.101	0.128	0.089	894	0.013	0.028	12.6	0.27	2.79
24		0.0142		0.137	0.105	1045	0.015	0.033	11.5	0.26	2.41
25		0.0170		0.145	0.118	1184	0.017	0.038	10.9	0.26	2.19
26		0.0170	0.146	0.196	0.088	876	0.011	0.025	16.3	0.33	2.62
27		0.0184		0.199	0.093	934	0.015	0.032	18.7	0.35	2.98
28		0.0198		0.203	0.099	988	0.015	0.032	16.9	0.34	2.66
29		0.0212		0.206	0.104	1039	0.015	0.033	16.0	0.33	2.47
30		0.0227		0.210	0.109	1091	0.018	0.039	17.1	0.34	2.63

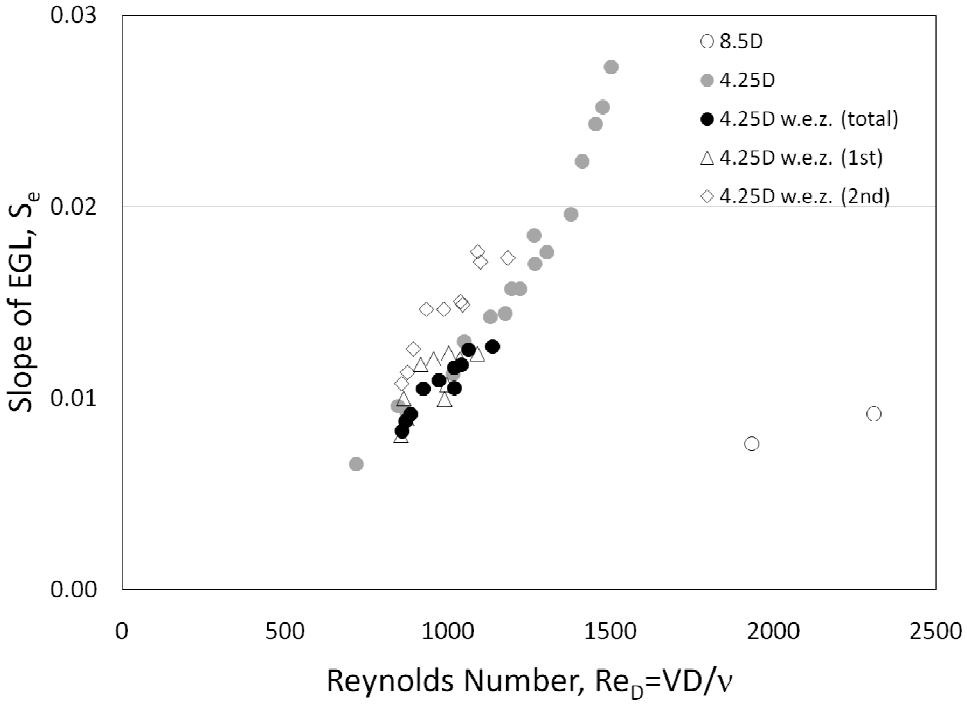

Figure 22. Slope of energy gradient line and cylinder Reynolds number relationships

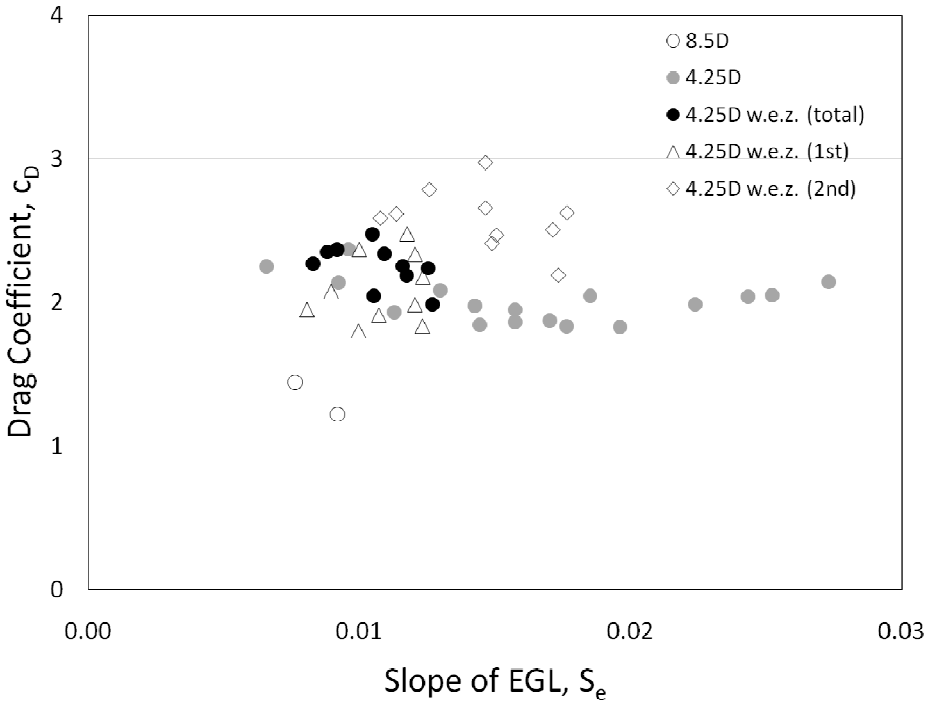

Figure 23. Drag coefficient and slope of energy gradient line relationships

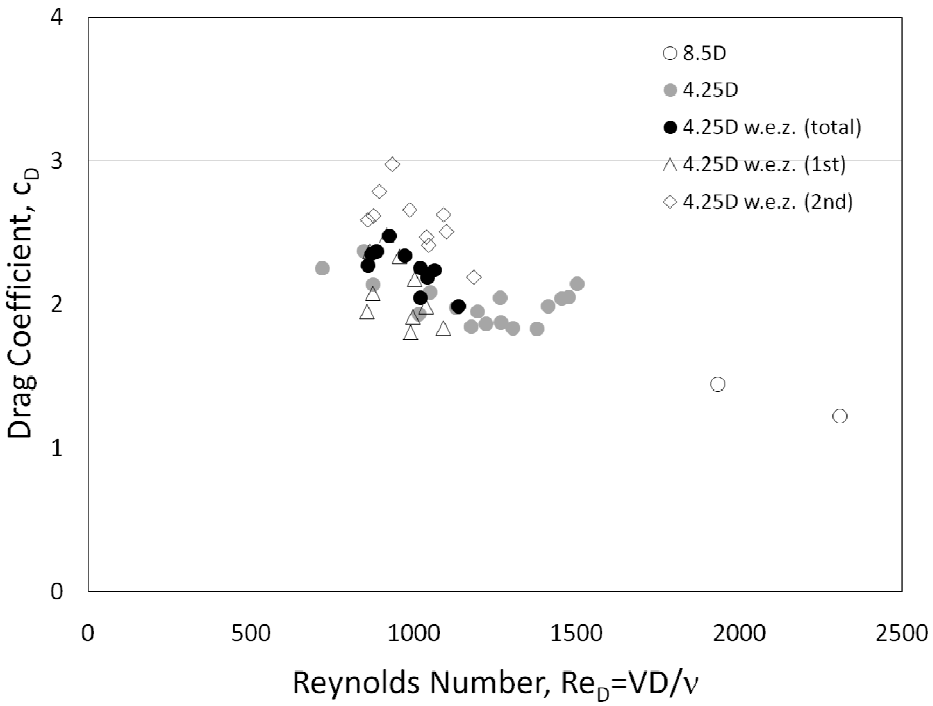

Figure 24. Drag coefficient and cylinder Reynolds number relationships for experiments

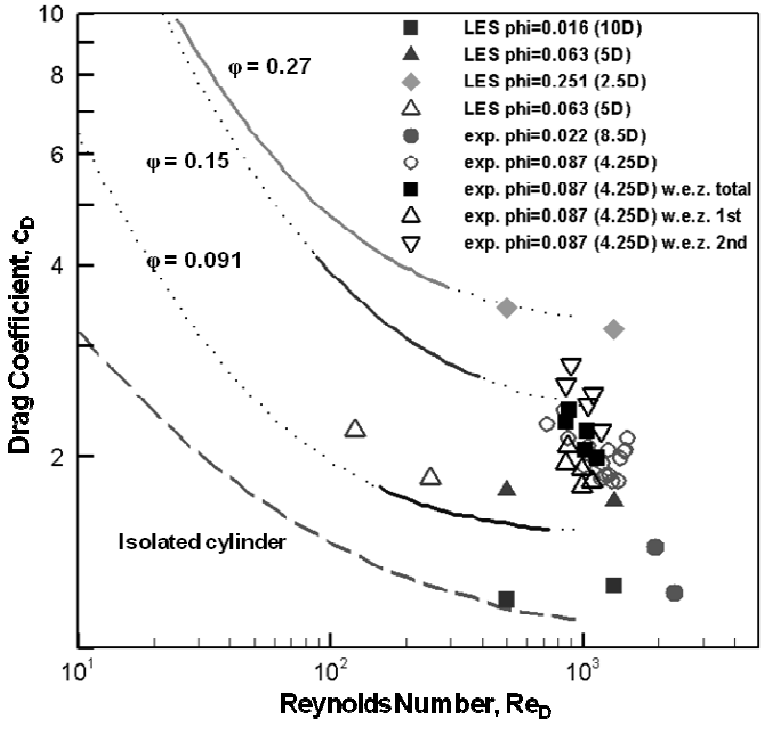

Figure 25. Drag coefficient c_D as a function of the cylinder Reynolds number for present experiment with previous studies (Tanino and Nepf, 2008; Kim and Stoesser, 2009).

5. NUMERICAL SIMULATIONS

5.1 Reynolds averaged Navier-Stokes model with a standard k-ε turbulence model

The program SSIIM (Sediment Simulation In Intakes with Multiblock option) is employed to perform the numerical simulations for both laboratory experiments and field works. This program solves the RANS equations with the finite-volume approach on a structured non-orthogonal grid. The SIMPLE method couples the pressure to the velocity field and the standard k-ε turbulence closure approximates the Reynolds Stresses appearing in the RANS formulation of the Navier Stokes equations. A second-order upwind scheme is employed to model the convective terms in the Navier-Stokes equations, whereas diffusive terms are approximated with a central differencing scheme. Details of the model are available in Olsen (2005). The vegetation is included as a sink term in the momentum equations according to relationship presented in Figure 14.

5.2 Simulation of the laboratory experiments

Selected comparison of the numerical results with water depth profiles is shown in Figure 26 and Figure 27 for 8.5D and 4.25D (fully vegetated case and partially vegetated case which has empty zone are plotted together), respectively. It is apparent that for several of the simulated cases the match between observations and simulations is good while for others there are obvious discrepancies. In particular the simulations for which uniform flow conditions prevail the match is favourable (particularly obvious in the two 8.5D cases), while for the non-uniform flows the computed water levels deviate from the measured, especially in the upstream regions. This trend again reflects that the non-uniformity plays a role and that this has to be accounted for in the model.

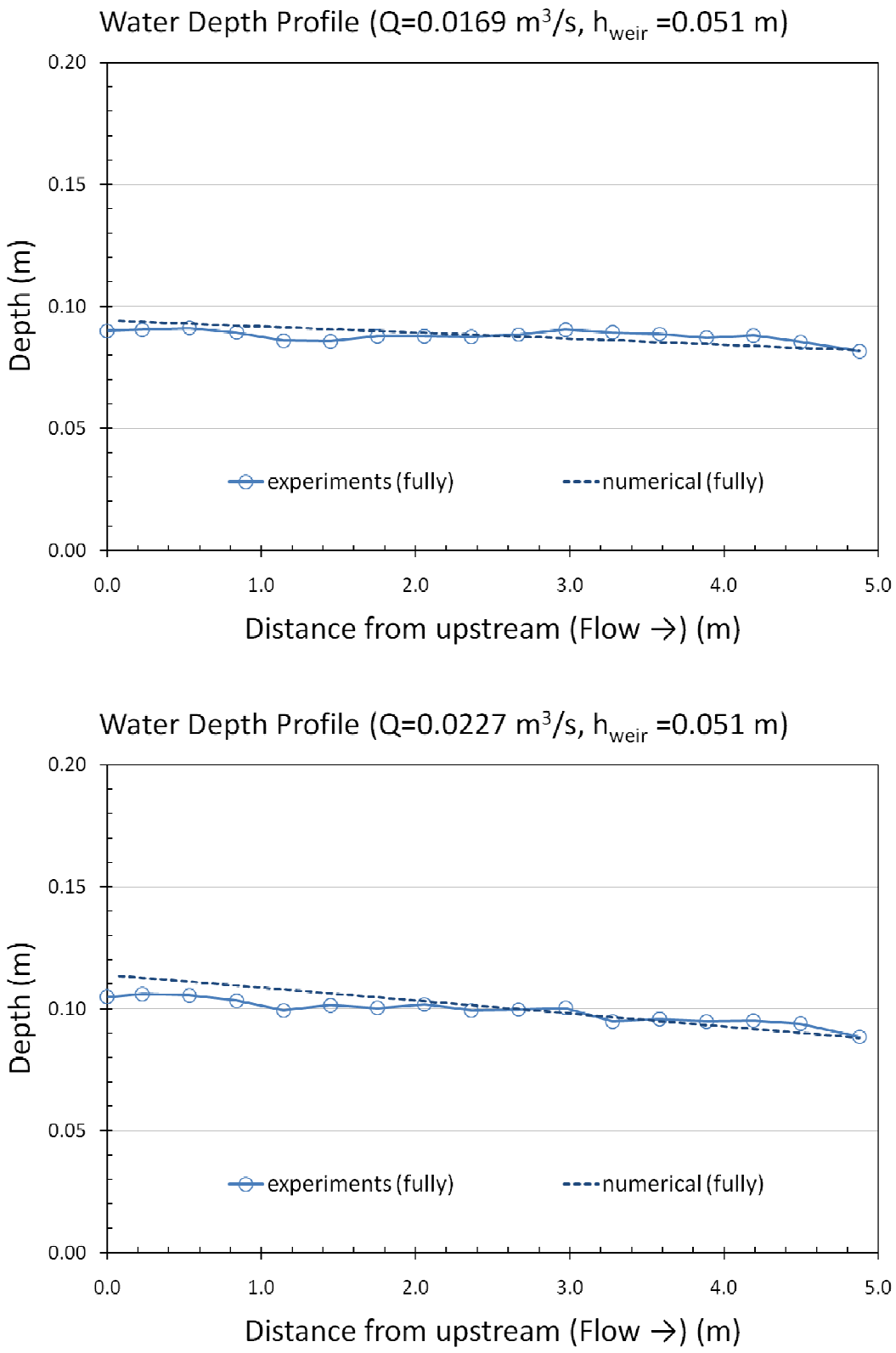

Figure 26. Comparison of water surface profile of experiments and numerical results (8.5D, top-case 9 and bottom-case 12)

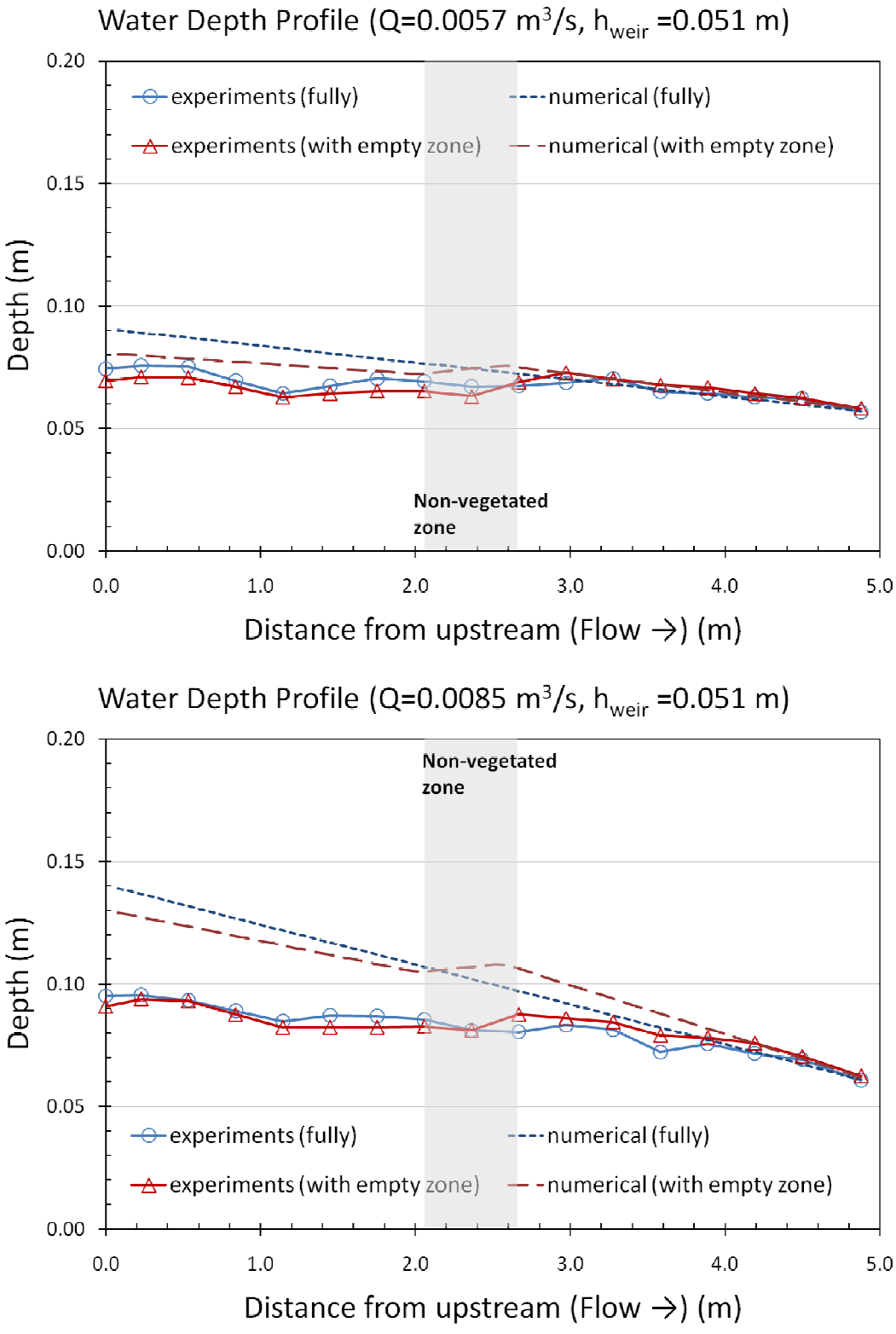

Figure 27a. Comparison of water surface profile of experiments and numerical results (4.25D & 4.25D with empty zone, top-case 2 vs. 21 and bottom-case 3 vs. 22)

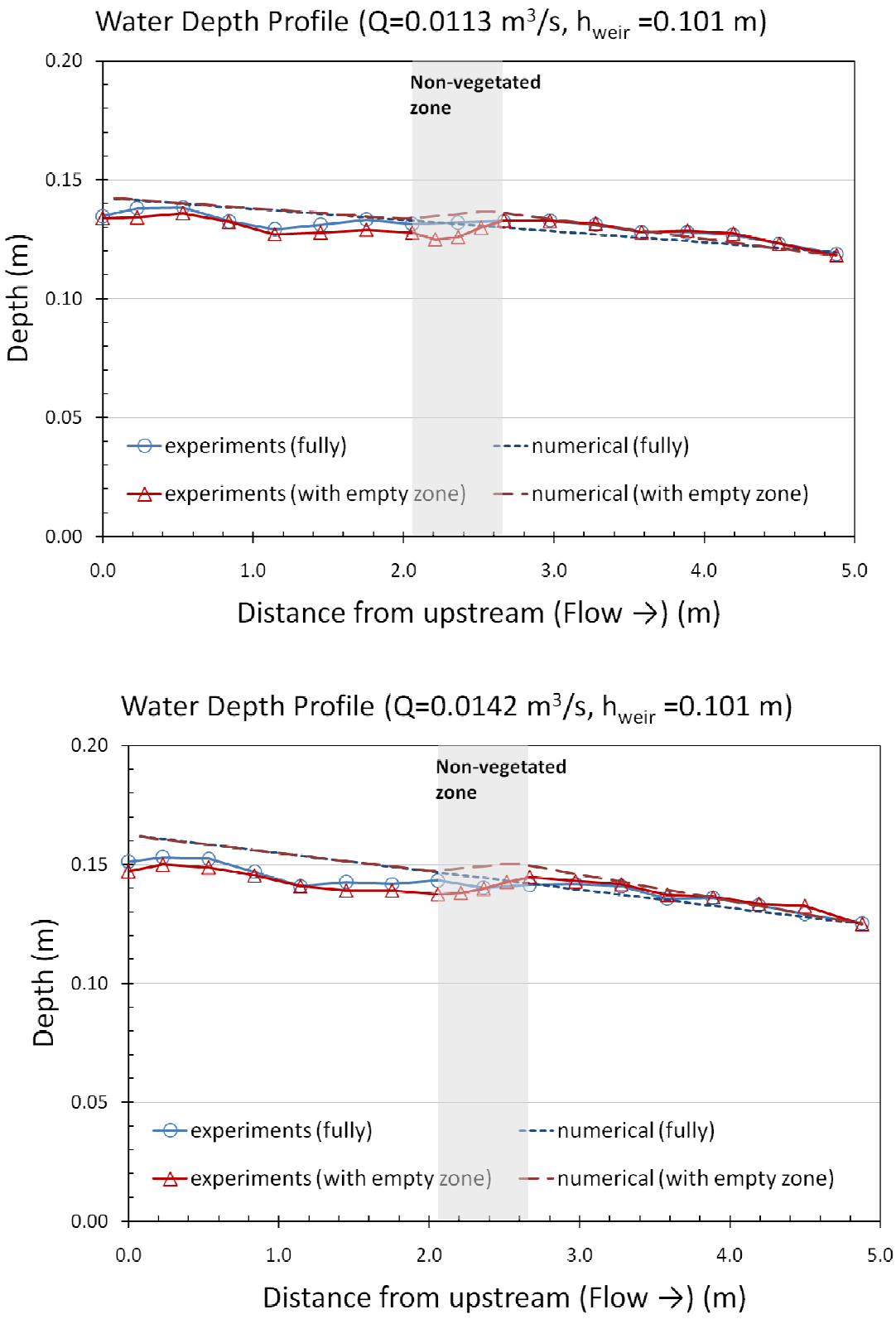

Figure 27b. Comparison of water surface profile of experiments and numerical results (4.25D & 4.25D with empty zone, top-case 14 vs. 23 and bottom-case 15 vs. 24)

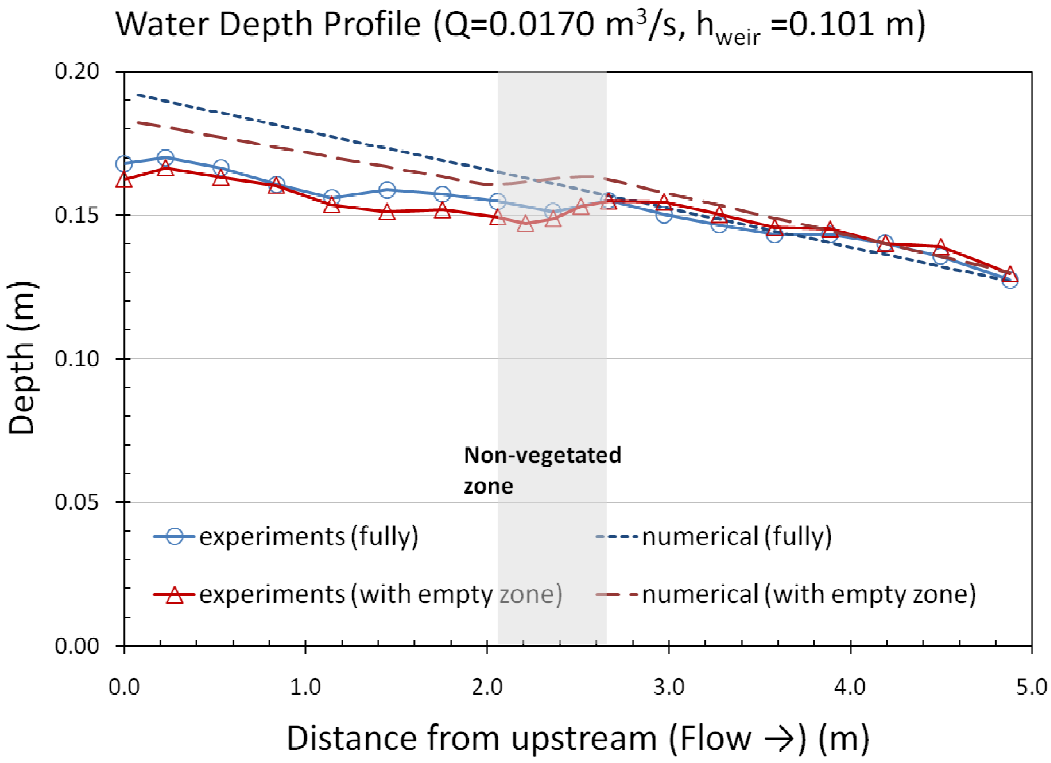

Figure 27c. Comparison of water surface profile of experiments and numerical results (4.25D & 4.25D with empty zone, 16 vs. 25)

5.3 Simulation of the flow in Cells I-1 and H

Numerical simulation of the CCWA wetland cells is performed by using SSIIM as well. For the numerical simulation of the field scale, the found geometrical values of the vegetation parameters for each cell is listed in Table 4 are used as input parameters for the flow resistance calculations. The geometry of the wetland cells is idealized to be of rectangular planview as flows are expected to be unidirectional. The length of the numerical domain is according to the length of each of the two cells and the average width of 95 m and 98 m for Cells I and H, are used as domain width. Figure 28 shows the computational mesh used in numerical simulation for Cell I (top) and Cell H (bottom). Like the schematic side view of constructed cells shows in Figure 2, the inflow is set up at the bottom of the 1st deep zone, and the outflow is set up at the location of the weir. Figures 29 and 30 show calculated velocities in Cells I and H, respectively. Streamlines are also depicted indicating the direction of the flow in the figures.

The water surface profiles are calculated from the pressure gradient using the relationship for hydrostatic pressure. The values for the drag coefficient c_D as provided in Table 5 are adopted. Calculated water level of each case is compared with measured water surface profile and the results are plotted in Figures 31 and 32. Clearly calculated and measured waterlevels exhibit a pretty good match, confirming the ability of the numerical model to predict water surface profiles in constructed wetlands. However, the waterlevels were obtained by a calibrated roughness coefficient which was previously obtained from measurements. This is undesirable because it minimizes the methods ability to be used as a design tool. This of course is true for all flow resistance methods because neither provided parameters that were within physical bounds.

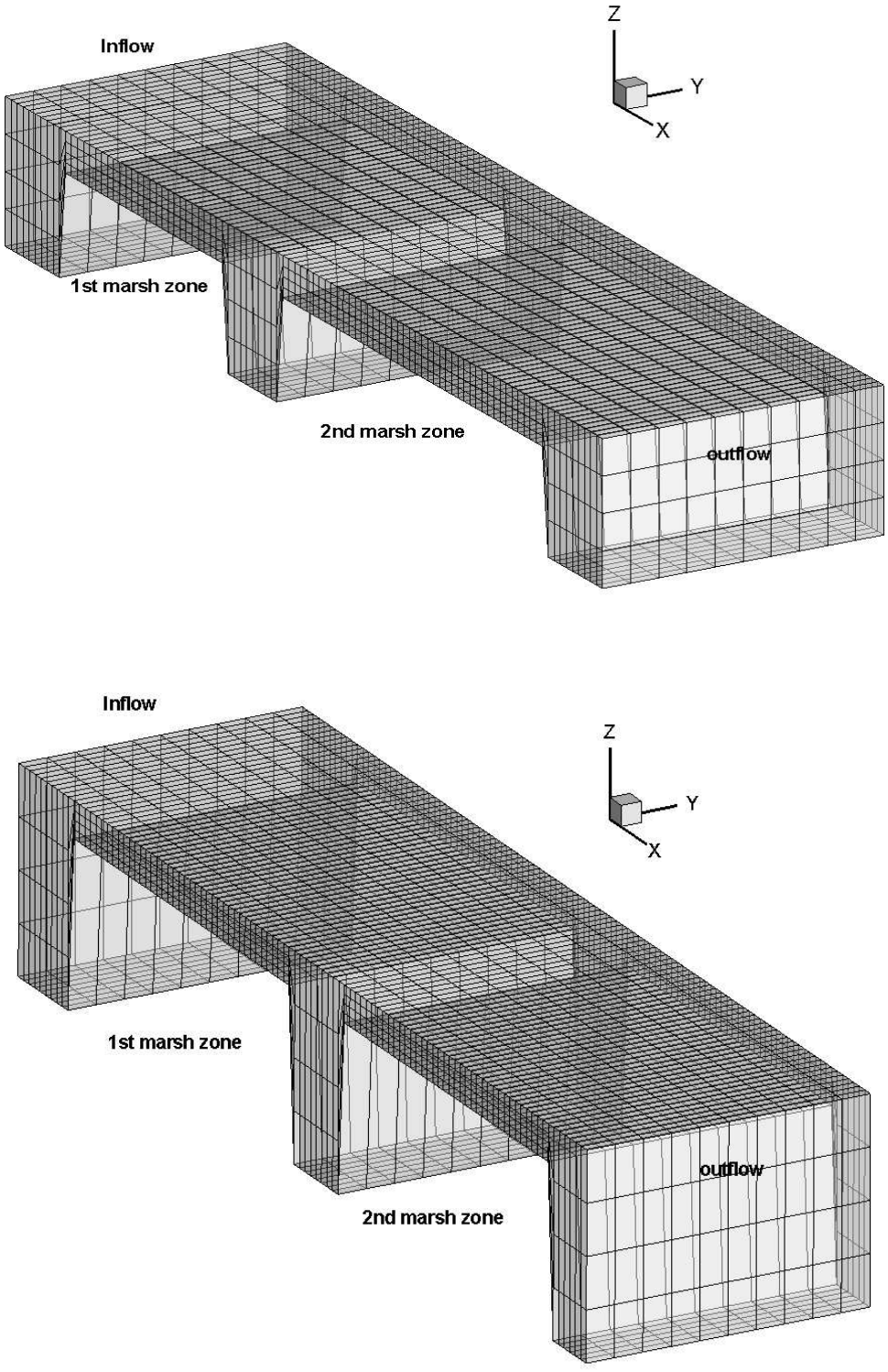

Figure 28. Mesh and grid of numerical models of Cell I-1 (top) and Cell H (bottom)

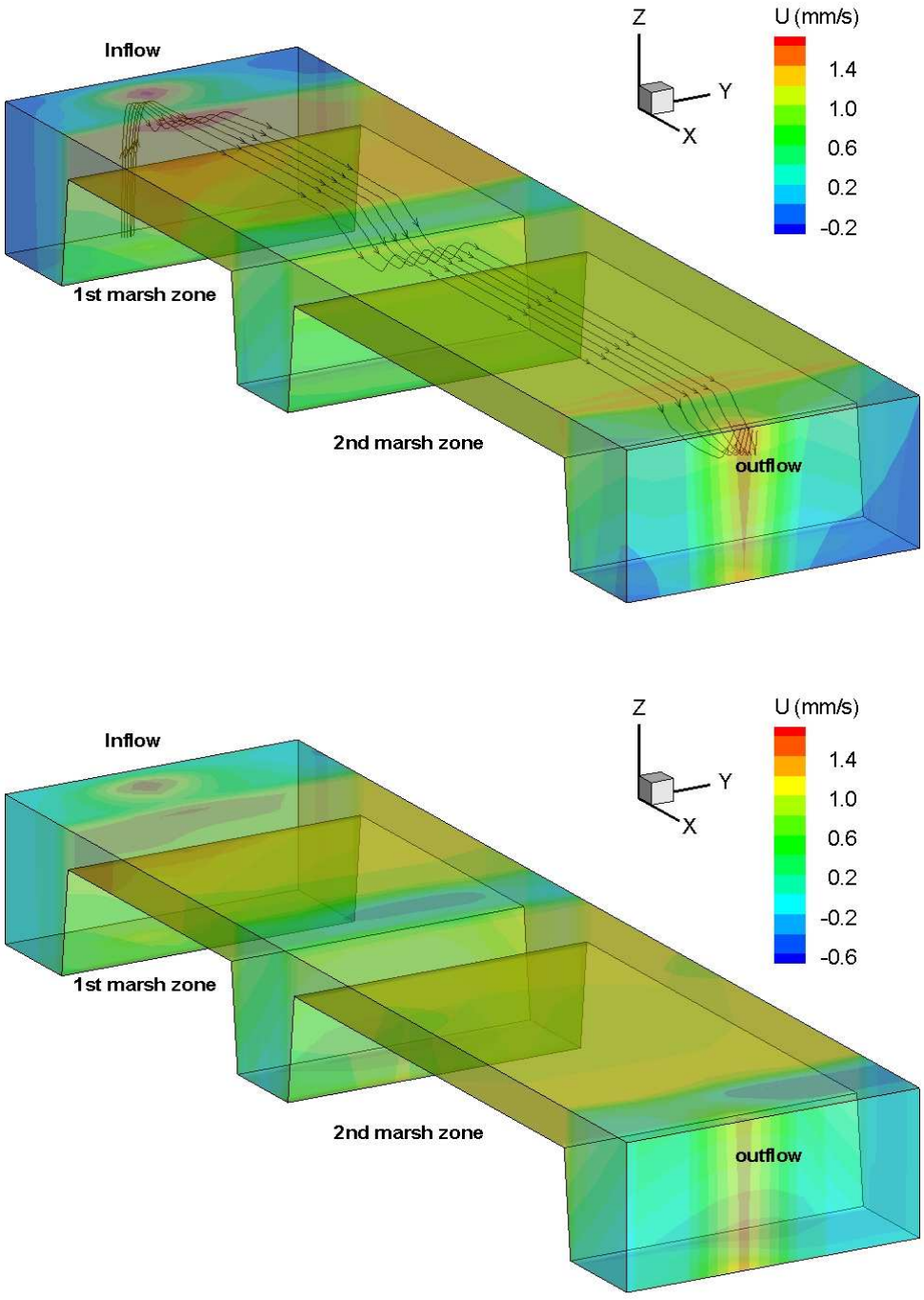

Figure 29a. Distribution of longitudinal velocity and streamline in Cell I-1 (top-5/29/09, bottom-6/12/09)

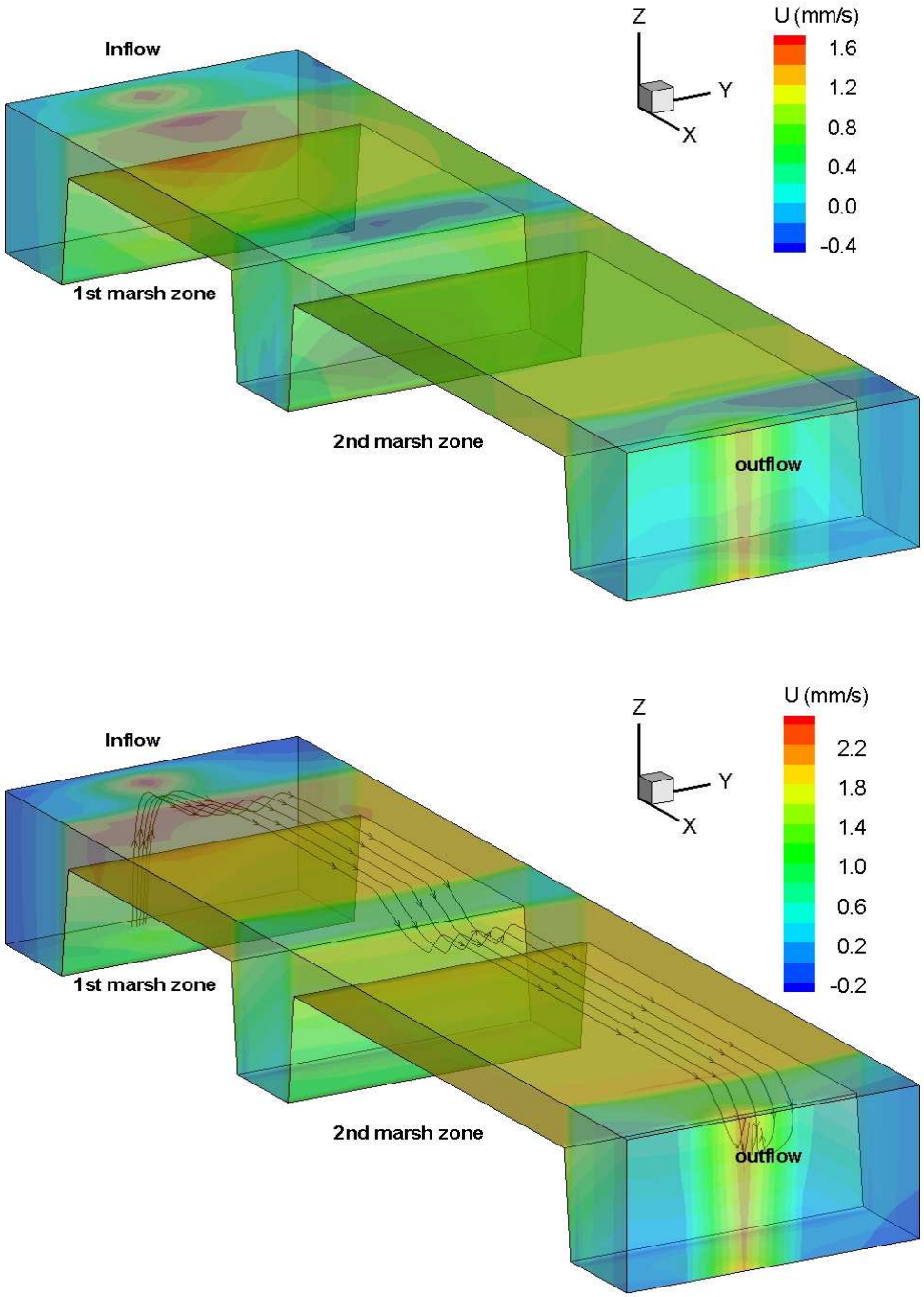

Figure 29b. Distribution of longitudinal velocity and streamlines in Cell I-1 (top-6/26/09, bottom-11/6/09)

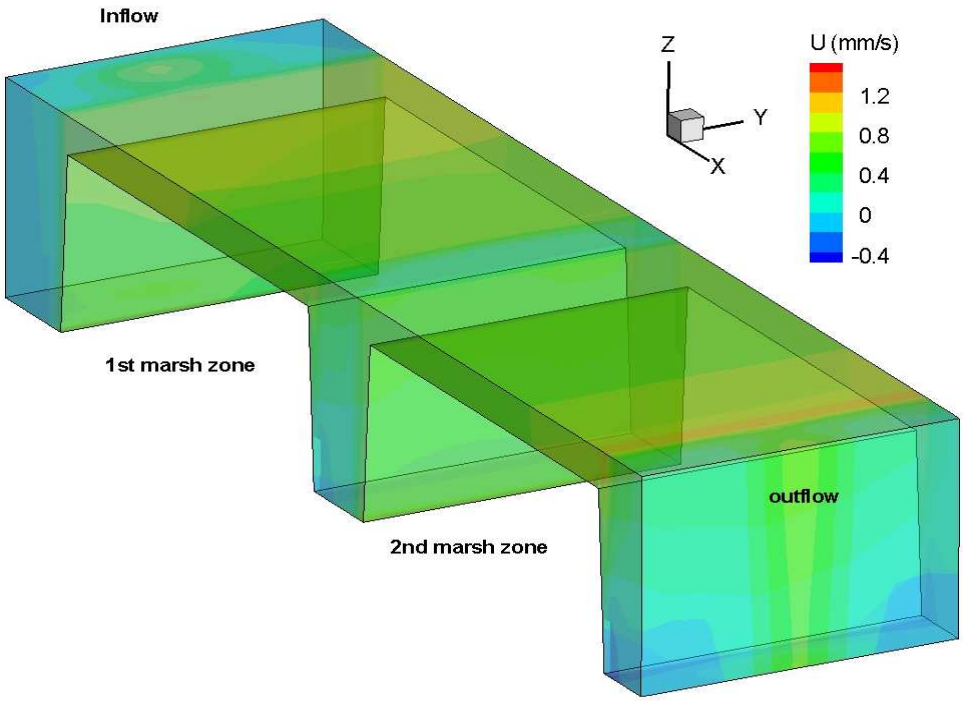

Figure 30. Distribution of longitudinal velocity in Cell H (6/12/09)

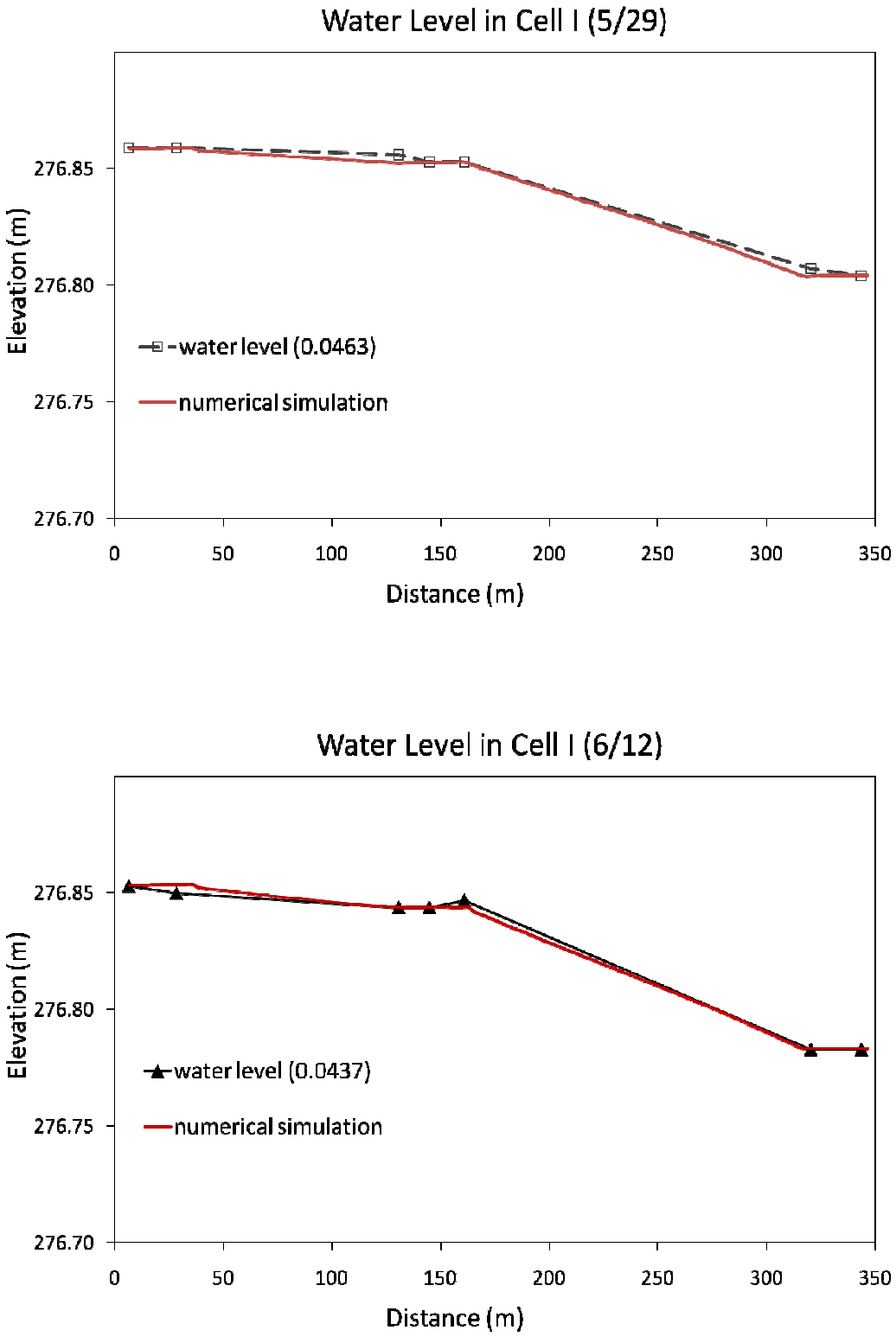

Figure 31a. Comparison of numerical result with water surface profile in constructed wetland (Cell I-1) (top-5/29/09, bottom-6/12/09)

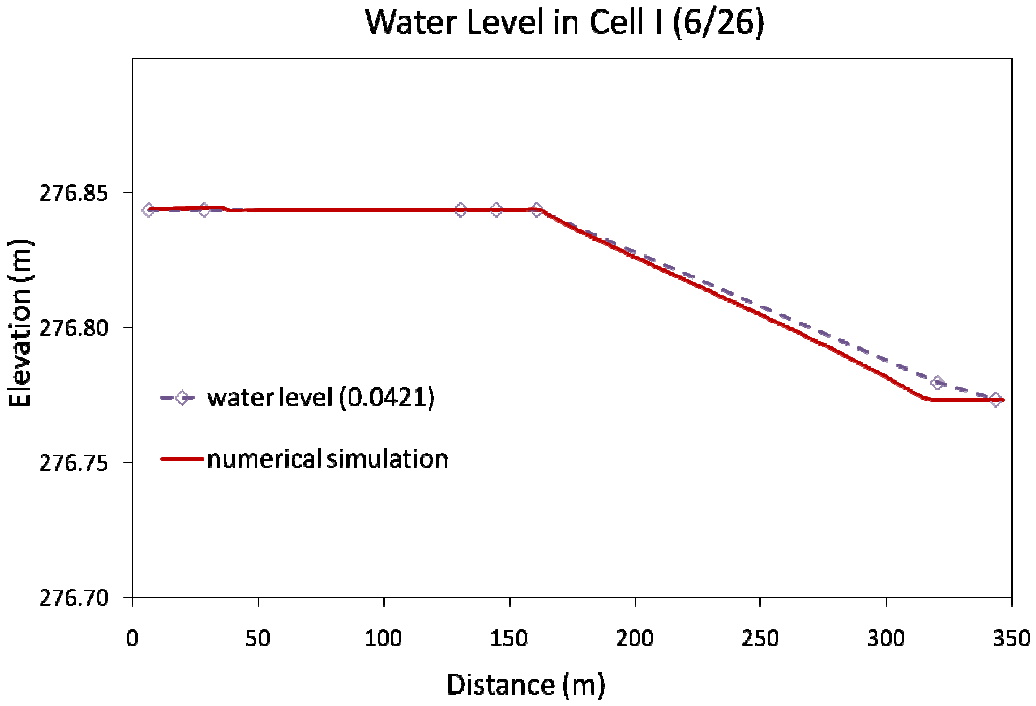

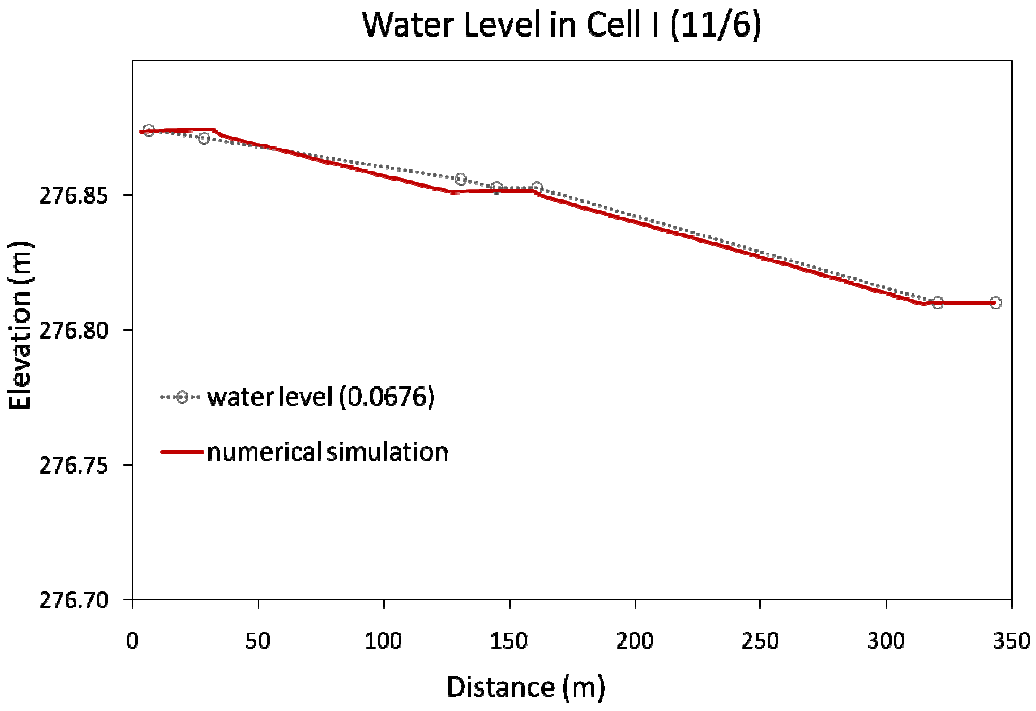

Figure 31b. Comparison of numerical result with water surface profile in constructed wetland (Cell I-1) (up-6/26/09, down-11/6/09)

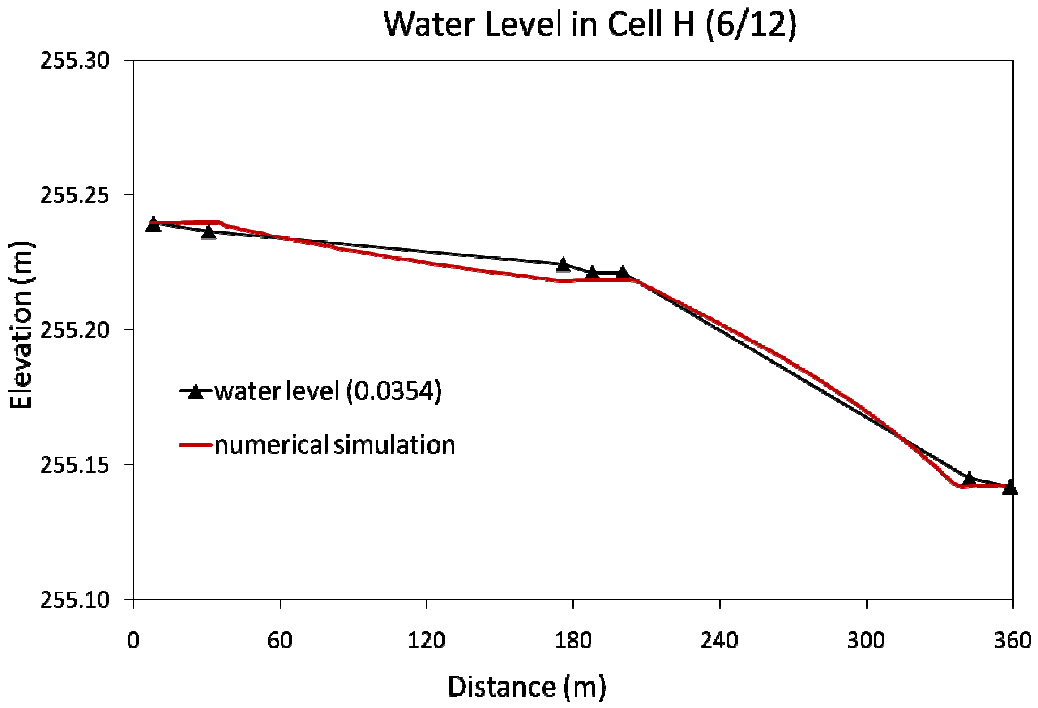

Figure 32. Comparison of numerical result with water surface profile in constructed wetland (Cell H) (6/12/09)

6. CONCLUSIONS AND RECOMMENDATIONS

A combination of field work and laboratory experiments was carried out to quantify flow resistance for Cattail, the most common vegetation in constructed wetlands. Typical densities and geometric properties of Cattail in two of the Clayton County Water Authoritie's wetland cells were determined through field work. Laboratory experiments were designed based on the determined quantities.

Measured water surface profiles in the field yielded different energy gradient lines in upstream and downstream marsh zones in each of the wetlands cells investigated even though vegetation density doesn't vary much between first and second marsh zone. The analysis of the measured water surface profiles in terms of flow resistance parameters yielded values that are far out of physically realistic bounds. The analysis of drag coefficients, generally accepted to be superior than Manning's n provided values that are up to 600 times higher than what would be expected for uniform flow. This is to be attributed to the effect of flow non-uniformity, being a result of zero bed slope in the cells and the addition of deep zones between upstream and downstream marsh zones.

The data from the laboratory experiment indicated that the vegetation density affects the flow resistance, especially under non-uniform conditions. Estimates of the drag coefficient of each flow condition in the laboratory are in line with previous findings and confirm the dependency of the drag on both density and cylinder Reynolds number. However, the effect of non-uniformity could not be adequately reproduced in the lab due to the setup of the laboratory conditions.

The numerical simulations of the laboratory using uncalibrated drag coefficients is rather satisfactory, however differences between observations and calculations were found. Particularly so when the conditions in the flume deviated from non-uniformity so that theoretically valid drag coefficients did not lead to the "correct" result.

The simulations of the CCWA wetland cells is both encouraging and discouraging. Encouraging because calculated and measured water surface profiles matched very well. However, these could only be obtained when calibrated (from measurements) roughness parameters were adopted.

The laboratory and numerical simulations showed that flow non-uniformity is the dominating influence on the flow resistance in wetlands that are constructed in a similar way than the ones of the Clayton County Water Authority. The effect of zero bedslope and strong variation in water depth between deep and marsh zone on flow resistance parameters requires further investigation. Therefore further laboratory experiments that model not only the vegetation parameters according to the field but also the flow nonuniformity are recommended.

REFERENCES

Bachand, P. A. M. and Horne, A. J. (2000). "Denitrification in constructed free-water surface wetlands: I. Very high nitrate removal rates in a macrocosm study." Ecological Engineering, 14: 9-15.

Brix, H. (1994). "Functions of macrophytes in constructed wetlands." Wat.Sci. & Tech., 29 (4): 71-78.

Cottam, G. and Curtis, J. T. (1956). "The use of distance measures in phytosociological sampling." Ecology, 37(3): 451-460.

Debusk, T. A., Laughlin, R. B., Jr, and Schwartz, L. N. (1996). "Retention and compartmentalization of lead and cadmium in wetland microcosms." Water Research, 30(11): 2702-2716.

Dix, R. L. (1961). "An application of the Point-Centered Quarter Method to the sampling of grassland vegetation." Journal of Range Management, 14(2): 63-39.

Dunn, C., Lopez F., and Garcia, M. H. (1996). Mean flow and turbulence in a laboratory channel with simulated vegetation. Hydraul. Engr. Series No. 51, UILU-ENG-96-2009, UIUC.

Elzinga, C. L., D. W. Salzer, and Willoughby, J. W. (1998). Measuring and Monitoring Plant Populations. Denver, Colorado.

Fairbanks, J. D. and Diplas, P. (1998). "Turbulence characteristics of flows through partially and fully submerged vegetation." Engineering Approaches to Ecosystem Restoration, Proc. Wetlands Engrg. and River Restoration Conf, ASCE, Denver, CO.

Fathi-Maghadam M. and Kouwen N. (1997). "Non-rigid, non-submerged, vegetative roughness on floodplains." ASCE Journal of Hydraulic Engineering, 123(1): 51-57.

Fischer-Antze, T., Stoesser, T., Bates, P. B., and Olsen, N. R. (2001). "3D Numerical modelling of open-channel flow with submerged vegetation." IAHR Journal of Hydraulic Research, 39: 303-310.

Kadlec, R. H., and Knight, R. L. (1996). Treatment Wetlands. CRC Press, Boca Raton, FL.

Kim, S. J. and Stoesser, T. (2009). "Drag forces on a staggered array of emergent cylinders in turbulent flow." Proceedings 33rd IAHR Congress. Vancouver. 9 – 14 Aug. 2009.

Lin, A. Y., Debroux, J-F., Cunningham, J. A., and Reinhard, M. (2003). "Comparison of rhodamine WT and bromide in the determination of hydraulic characteristics of constructed wetlands." Ecological Engineering, 20: 75-88.

Lopez, F. and Garcia, M. (1998). "Open-channel flow through simulated vegetation: Suspended sediment transport modelling." Water Resources Research, 34(9): 2341-2352.

Lopez, F. and Garcia, M. (2001). “Mean flow and turbulence structure of open-channel flow through non-emergent vegetation.” ASCE J. Hydraulic Engrg., 127(5): 392-402.

Lyon, L. J. (1968). “An evaluation of density sampling methods in a shrub community.” Journal of Range Management, 21(1): 16-20.

Malki, R., Wilson, C. A. M. E., and Edington, A. (2008). “The influence of plant morphology on velocity and turbulence structure.” River flow 2008, 2: 1487-1495.

Mitich, L. M. (2000). “Common cattail, Typha latifolia L.” Weed Technology. 14(2): 446-450.

Mueller-Dombois, D. and Ellenberg, H. (1974). Aims and Methods of Vegetation Ecology. New York. 547 pp

Neary, V. S. (2000). “Numerical model for open channel flow with vegetative resistance.” IAHR's 4th International Conference on Hydroinformatics, Cedar Rapids, Iowa, U.S.A., July 1-5, 2000.

Neumeier, U. (2005). “Quantification of vertical density variations of salt-marsh vegetation.” Estuarine, Coastal and Shelf Science, 63(4): 489-496.

O’Loughlin, E. J. and Burris, D. R. (1999). “Reductive dehalogenation of trichloroethene mediated by wetland DOC-transition metal complexes.” In: Means, J.L., Hinchee, R.E. (Eds.), Wetlands and Remediation: an International Conference, Salt Lake City, UT.

Olsen, N. R. B. (2005). SSIIM User’s Manual. Department of Hydraulic and Environmental Engineering, The Norwegian University of Science and Technology. <http://www.ntnu.no/~nilsol/ssiimwin/manual3.pdf>

Pasche, E. and Rouve, G. (1985). “Overbank flow with vegetatively roughened flood plains.” Journal of Hydraulic Engineering 111: 1262-1278.

Patankar, S. V. (1980). Numerical Heat Transfer and Fluid Flow. Hemisphere Publishing Corporation. Mac Graw Hill. New York.

Persson, J., Somes, N. L. G., and Wong, T. H. F. (1999). “Hydraulics efficiency of constructed wetlands and ponds.” Water Science and Technology, 40(3): 291–289.

Petryk, S. and Bosmajian, G. (1975). “Analysis of flow through vegetation.” Journal of Hydraulic Engineering. 101(7): 871-884.

Reilly, J. F., Horne, A. J., and Miller, C. D. (2000). “Nitrate removal from a drinking water supply with large free-surface constructed wetlands prior to groundwater recharge.” Ecological Engineering, 14: 33-47.

Schlichting, H. and Gersten, K. (2000). Boundary Layer Theory (8th ed.). New York: Springer.

Schulz, R. and Peall, S. K. C. (2001). “Effectiveness of a constructed wetland for retention of nonpoint-source pesticide pollution in the Lourens River Catchment, South Africa.” Environmental Science and Technology, 35: 422-426.

Shimizu, Y. and Tsujimoto, T. (1994). “Numerical analysis of turbulent open-channel flow over vegetation layer using a k-turbulence model.” Journal of Hydroscience and Hydraulic Engineering, JSCE, 11(2): 57-67.

Sundaravadivel, M. and Vigneswaran, S. (2001). “Constructed wetlands for wastewater treatment.” Critical Reviews in Environmental Science and Technology. 31(4): 351-409.

Stoesser, T. (2002). Development and Validation of a CFD Code for Open-Channel Flows. PhD Thesis. Department of Civil Engineering. University of Bristol.

Tanino, Y. and Nepf, H. M. (2008). “Laboratory investigation of mean drag in a random array of rigid, emergent cylinders.” Journal of Hydraulic Engineering, 134(1): 34-41.

Tsujimoto, T. and Kitamura, T. (1998). “A model for flow over flexible vegetation-covered bed.” Proceedings of International Water Resources Engineering Conference, ASCE, New York, 1380-1385.

Webb, J. S., McGinness, S., and Lappin-Scott, H. M. (1998). “Metal removal by sulphate-reducing bacteria from natural and constructed wetlands.” Journal of Applied Microbiology, 84 (2): 240-248.

Wilson, N. R. and Shaw, R. H. (1977). “A higher order closure model for canopy flow.” Journal of Applied Meteorology, 16(11): 1197-1205.

Wilson, C. A. M. E., T. Stoesser, and Bates, P. D. (2004). “Open channel flow through vegetation.” In: Computational Fluid Dynamics: Applications in Environmental Hydraulics, editors: Bates P. D., Lane S., Ferguson R., John Wiley & Sons, 395-428.

APPENDIX 1 – VEGETATION QUANTIFICATION SAMPLING DATA

Field Measurement Datasheet 1/3

		Sample No.	I-1
Date	5-May-09		
Member	Su Jin Kim, Brandon Harris, Brandon Strellis, Ingrid Duque		
Measuring location	(check or sketch the location on the picture below)		
Cell I-1		Cell H	

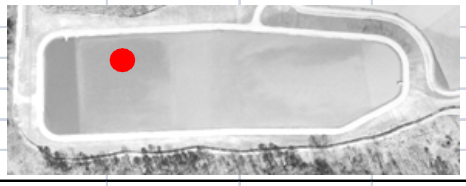

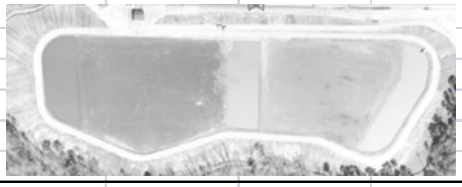

Discharge (inflow) _____ (cfs or cms)

Numbers of cattail in 1m x 1m 32

Sketch of 1m x 1m zone with distance between vegetion (1grid = 2.5 cm x 2.5 cm)

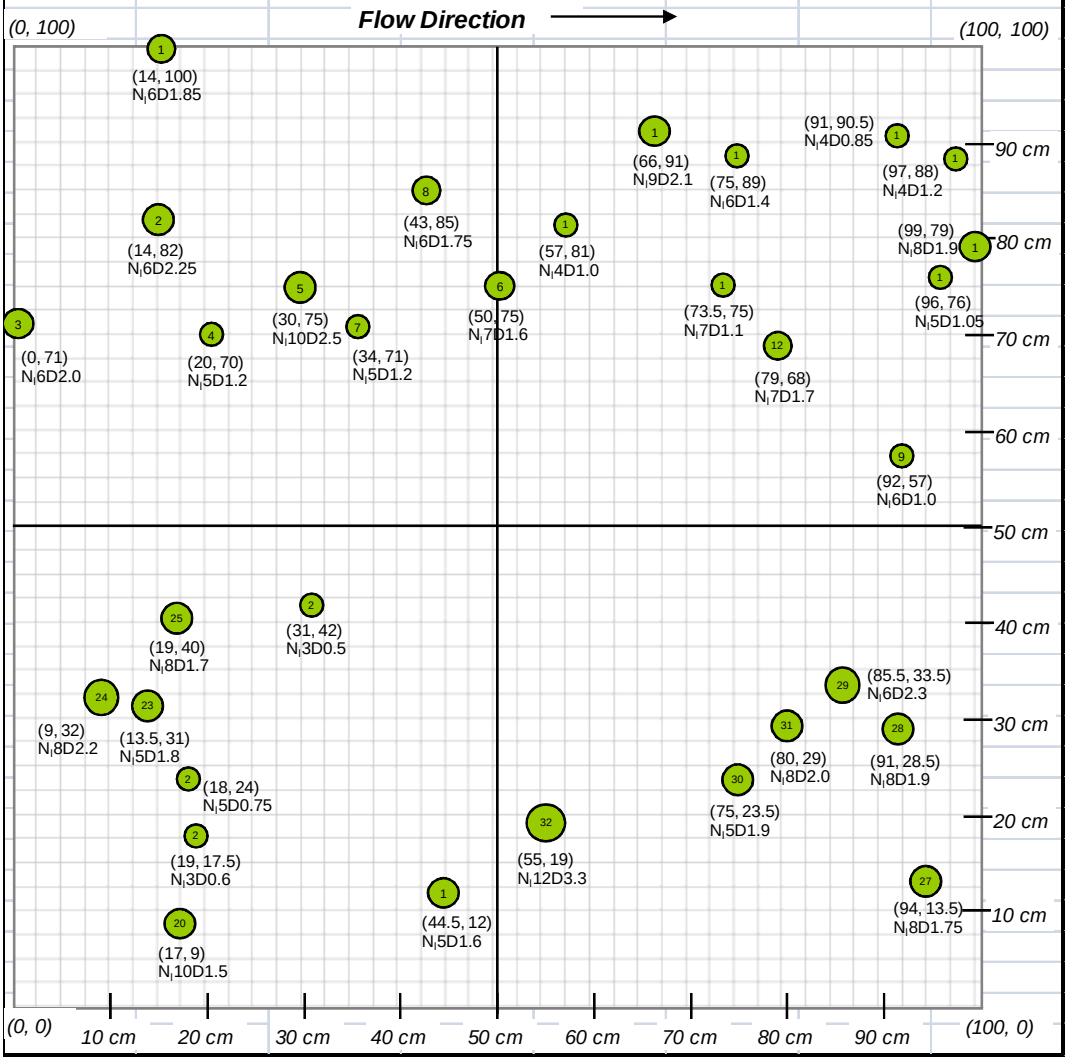

Field Measurement Datasheet 1/3

Sample No.	I-2
Date	5-May-09
Member	Su Jin Kim, Brandon Harris, Brandon Strellis, Ingrid Duque
Measuring location	(check or sketch the location on the picture below)

Cell I-1

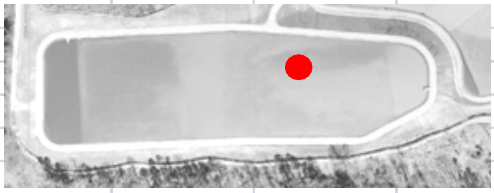

Cell H

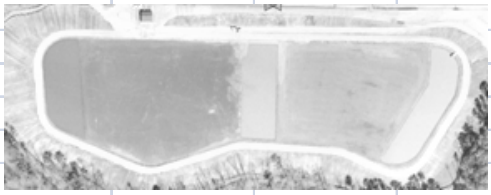

Discharge (inflow) _____ (cfs or cms)

Numbers of cattail in 1m x 1m 48

Sketch of 1m x 1m zone with distance between vegetion (1grid = 2.5 cm x 2.5 cm)

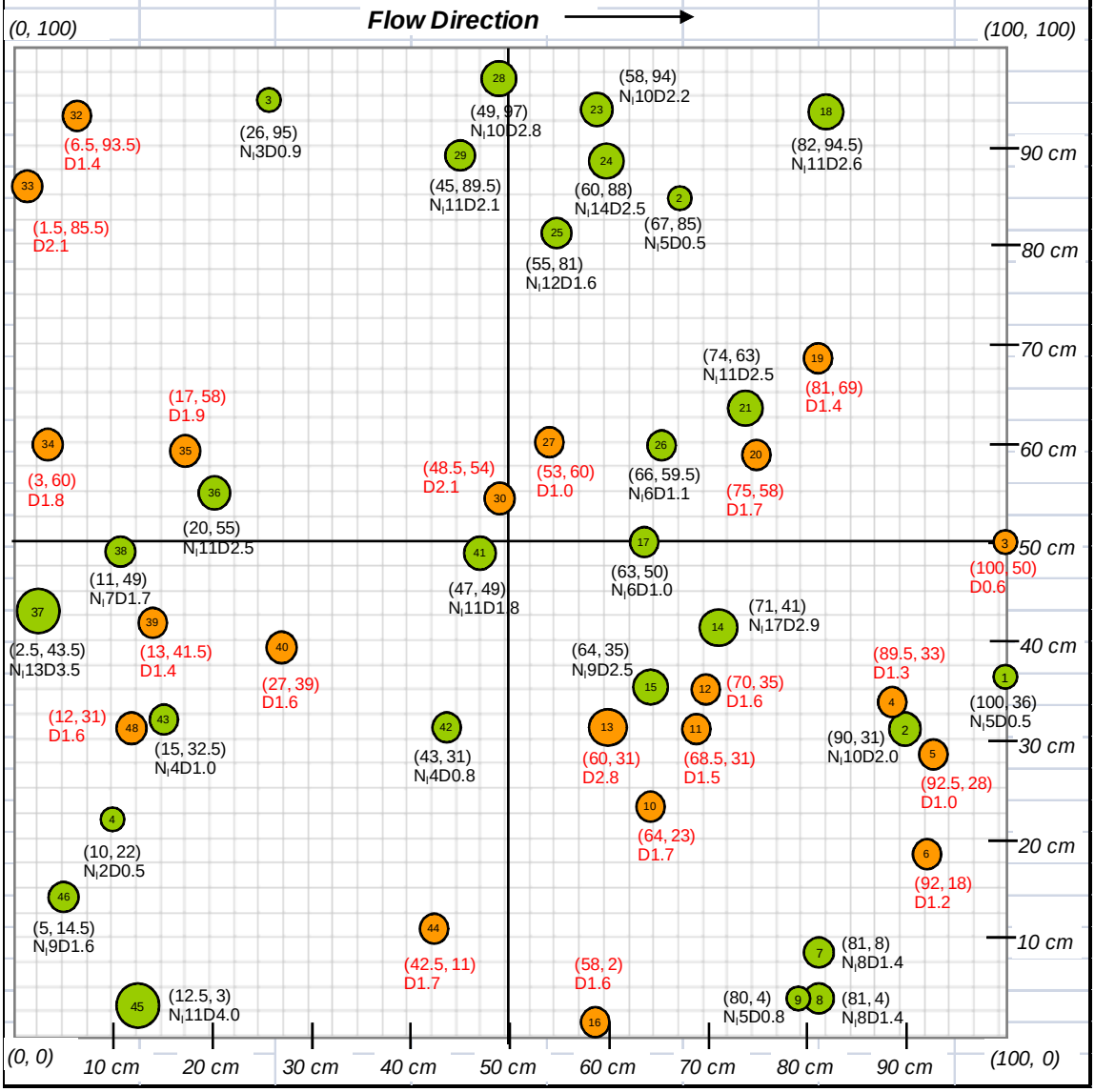

Field Measurement Datasheet 1/3

Sample No.	I-3
Date	14-May-09
Member	Su Jin Kim, Brandon Harris, Brandon Strellis, Ben Ioppolo, Emma
Measuring location	(check or sketch the location on the picture below)

Cell I-1

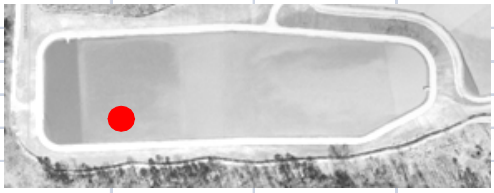

Cell H

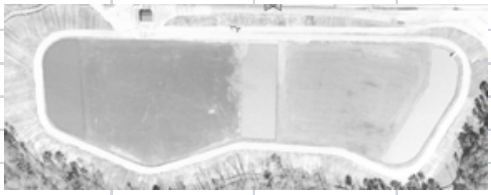

Discharge	(inflow)	(cfs or cms)
Numbers of cattail in 1m x 1m	37	

Sketch of 1m x 1m zone with distance between vegetion (1grid = 2.5 cm x 2.5 cm)

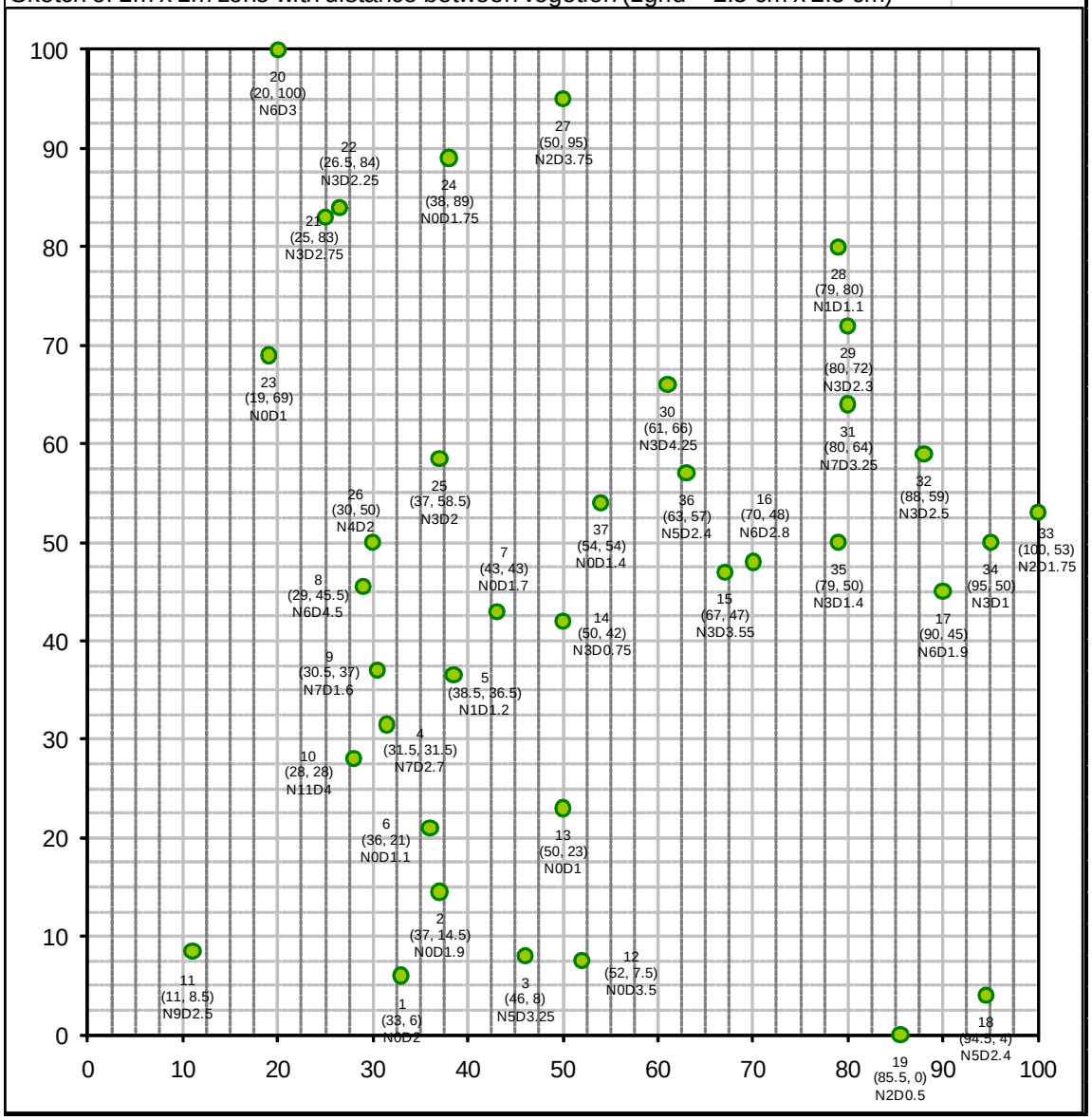

Field Measurement Datasheet 1/3

Sample No.	I-4
Date	14-May-09
Member	Su Jin Kim, Brandon Harris, Brandon Strellis, Ben Ioppolo, Emma
Measuring location	(check or sketch the location on the picture below)

Cell I-1

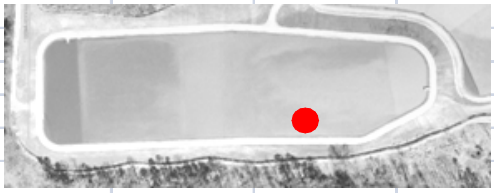

Cell H

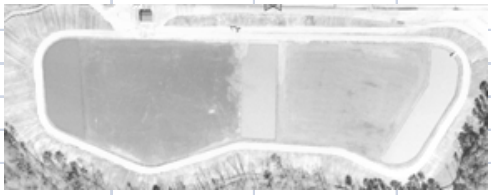

Discharge	(inflow)	(cfs or cms)
Numbers of cattail in 1m x 1m	53	

Sketch of 1m x 1m zone with distance between vegetion (1grid = 2.5 cm x 2.5 cm)

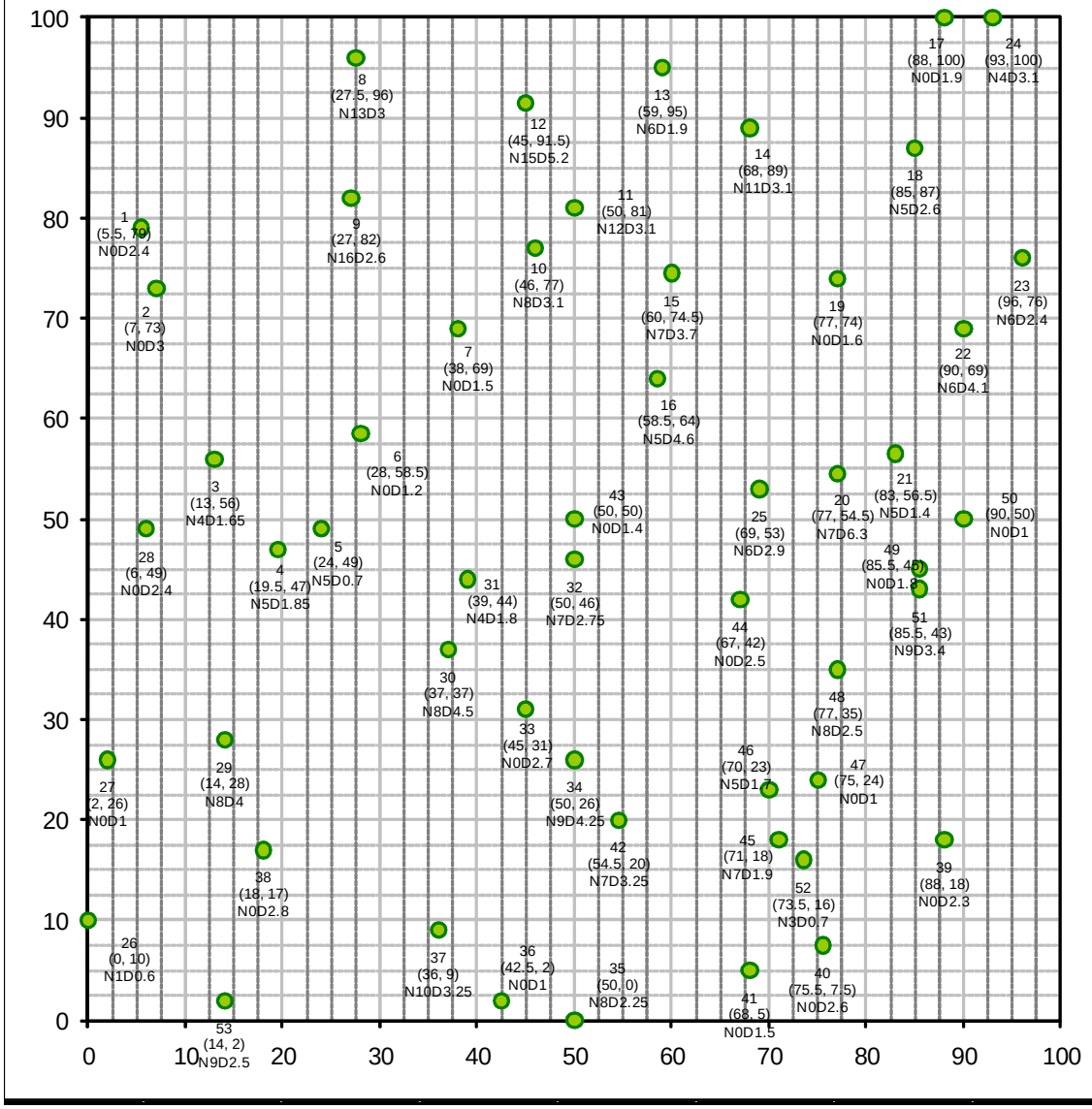

Field Measurement Datasheet 1/3

		Sample No.	I-5
Date	6-Nov-09		
Member	Su Jin Kim, Brandon Harris, Brandon Strellis, Ingrid Duque		
Measuring location	(check or sketch the location on the picture below)		
Cell I-1		Cell H	

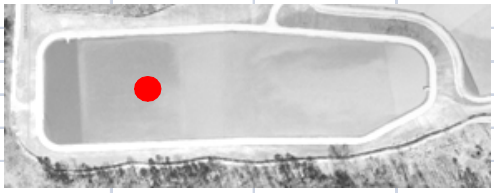

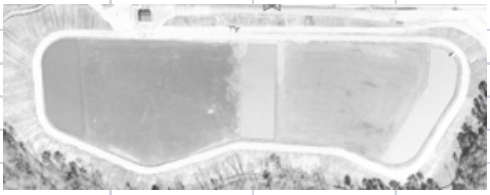

Discharge	(inflow)		(cfs or cms)
Numbers of cattail in 1m x 1m		43	

Sketch of 1m x 1m zone with distance between vegetion (1grid = 2.5 cm x 2.5 cm)

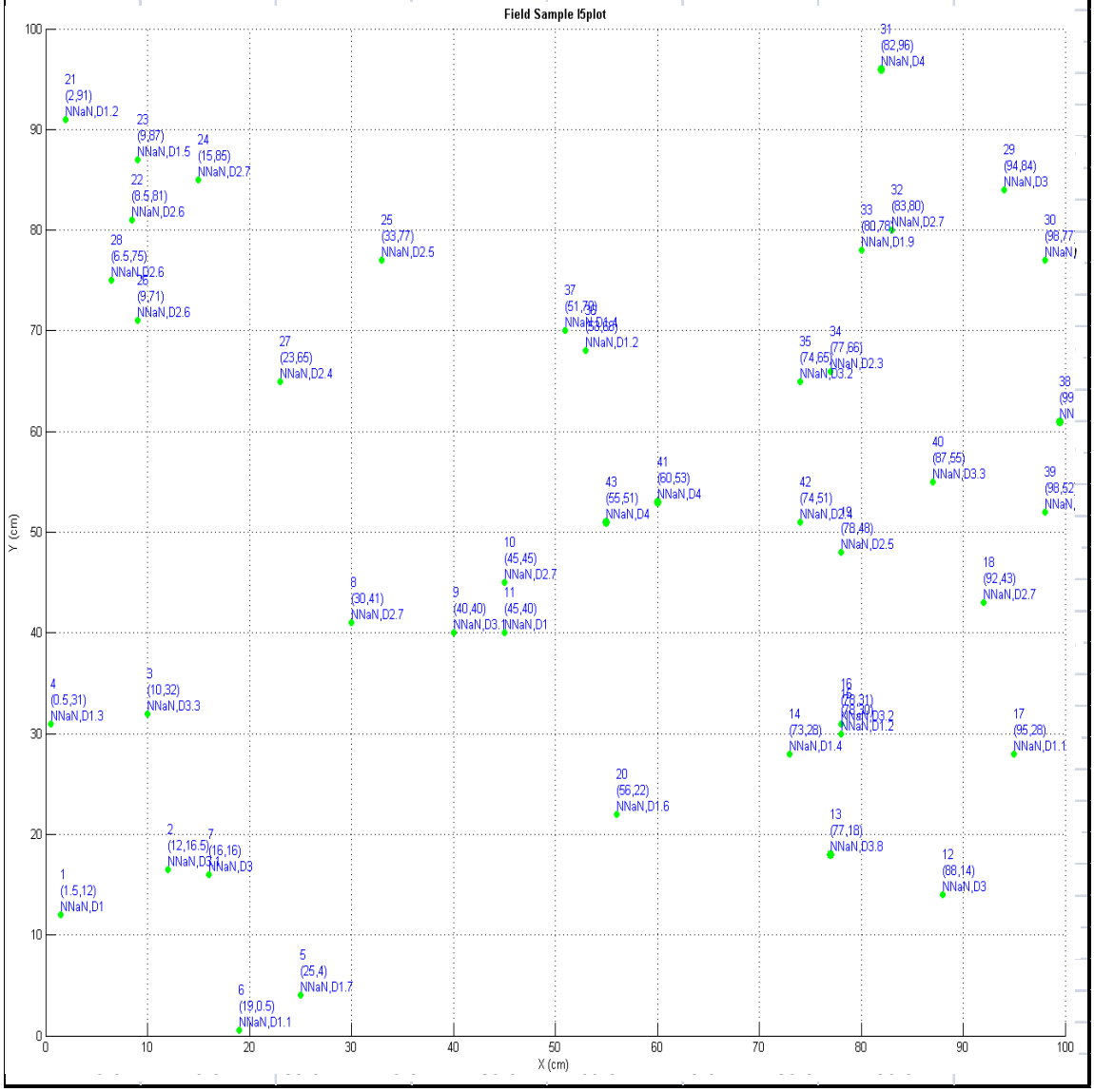

Field Measurement Datasheet 1/3

		Sample No.	I-6
Date	6-Nov-09		
Member	Su Jin Kim, Brandon Harris, Brandon Strellis, Ingrid Duque		
Measuring location	(check or sketch the location on the picture below)		
Cell I-1		Cell H	

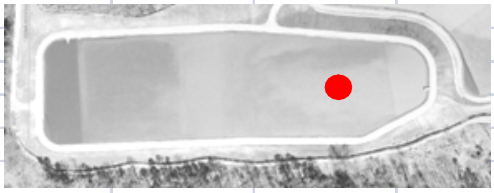

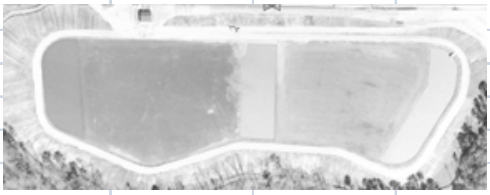

Discharge	(inflow)	(cfs or cms)
Numbers of cattail in 1m x 1m	37	

Sketch of 1m x 1m zone with distance between vegetion (1grid = 2.5 cm x 2.5 cm)

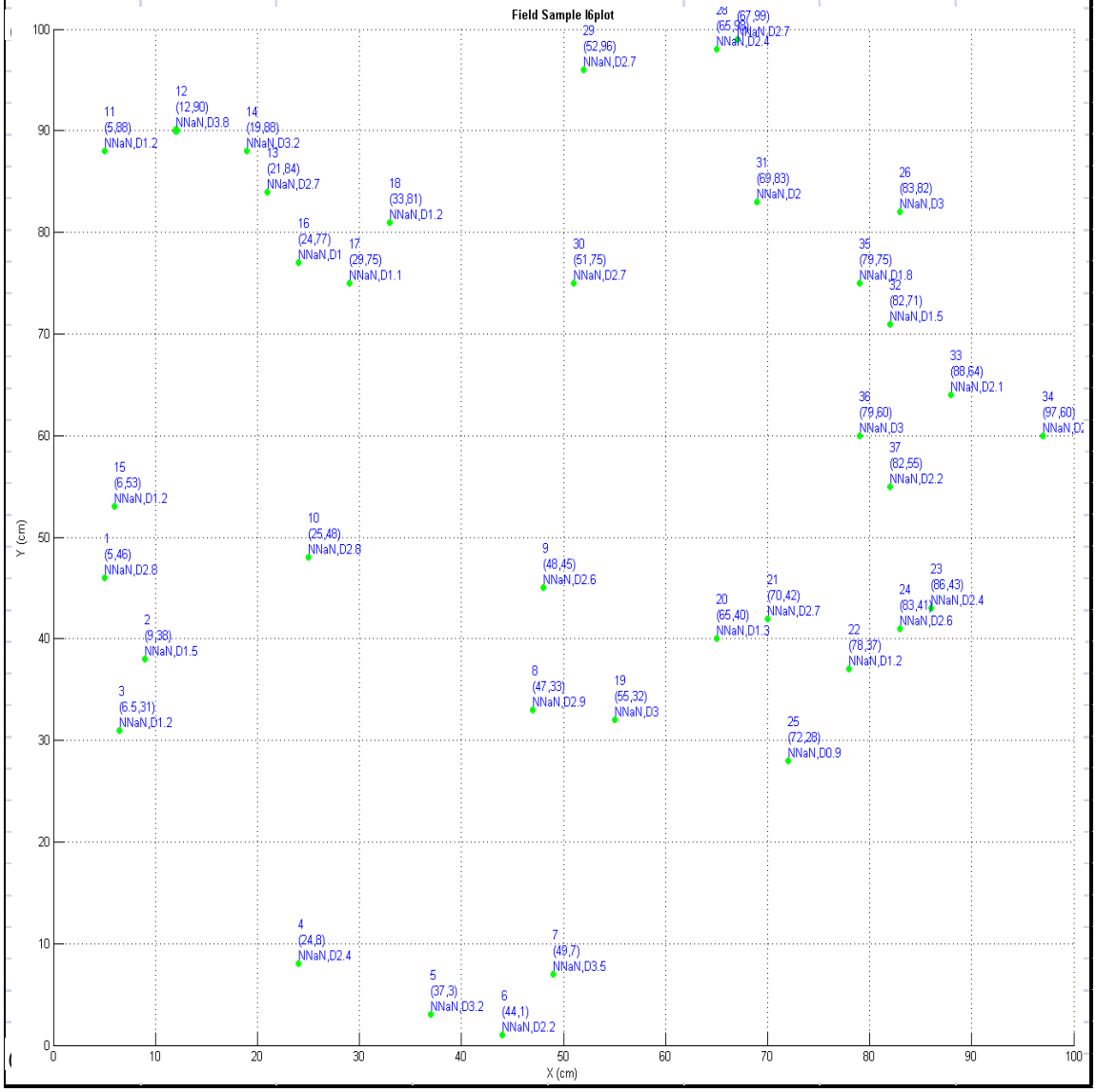

Field Measurement Datasheet 1/3

Sample No.	H-1
Date	5-May-09
Member	Su Jin Kim, Brandon Harris, Brandon Strellis, Ingrid Duque
Measuring location	(check or sketch the location on the picture below)

Cell I-1

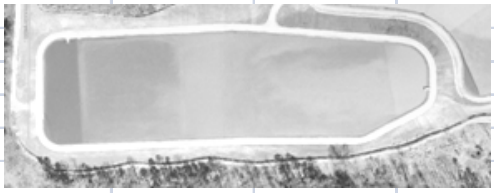

Cell H

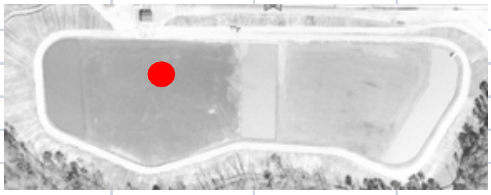

Discharge (inflow) _____ (cfs or cms)

Numbers of cattail in 1m x 1m 47

Sketch of 1m x 1m zone with distance between vegetion (1grid = 2.5 cm x 2.5 cm)

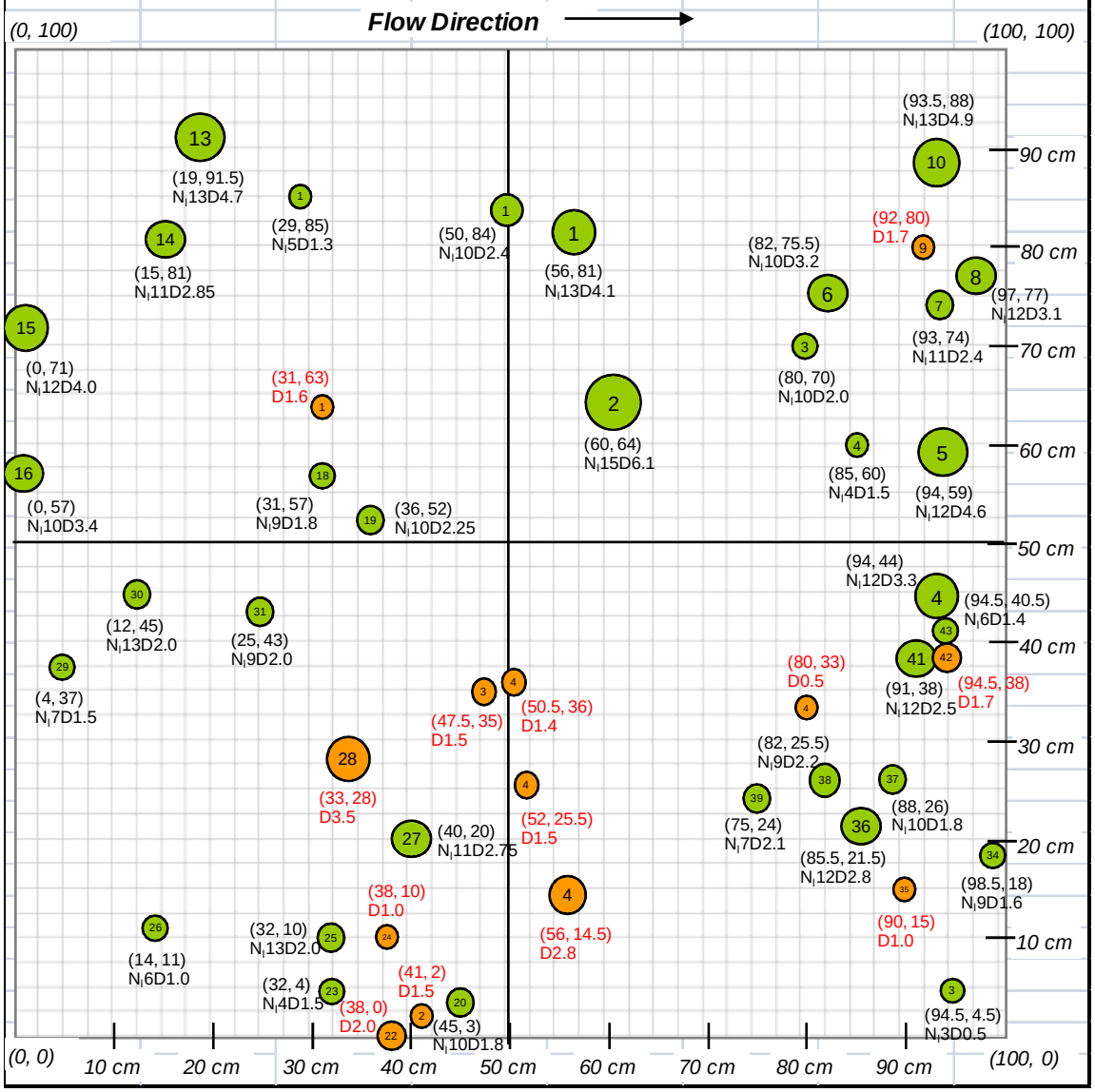

Field Measurement Datasheet 1/3

Sample No.	H-2
Date	5-May-09
Member	Su Jin Kim, Brandon Harris, Brandon Strellis, Ingrid Duque
Measuring location	(check or sketch the location on the picture below)

Cell I-1

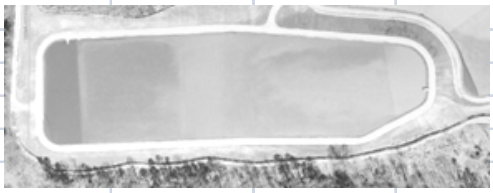

Cell H

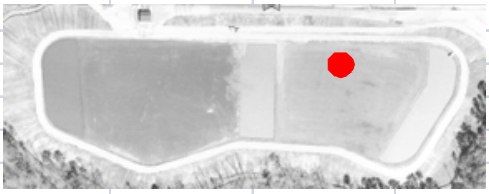

Discharge (inflow) _____ (cfs or cms)

Numbers of cattail in 1m x 1m 57

Sketch of 1m x 1m zone with distance between vegetion (1grid = 2.5 cm x 2.5 cm)

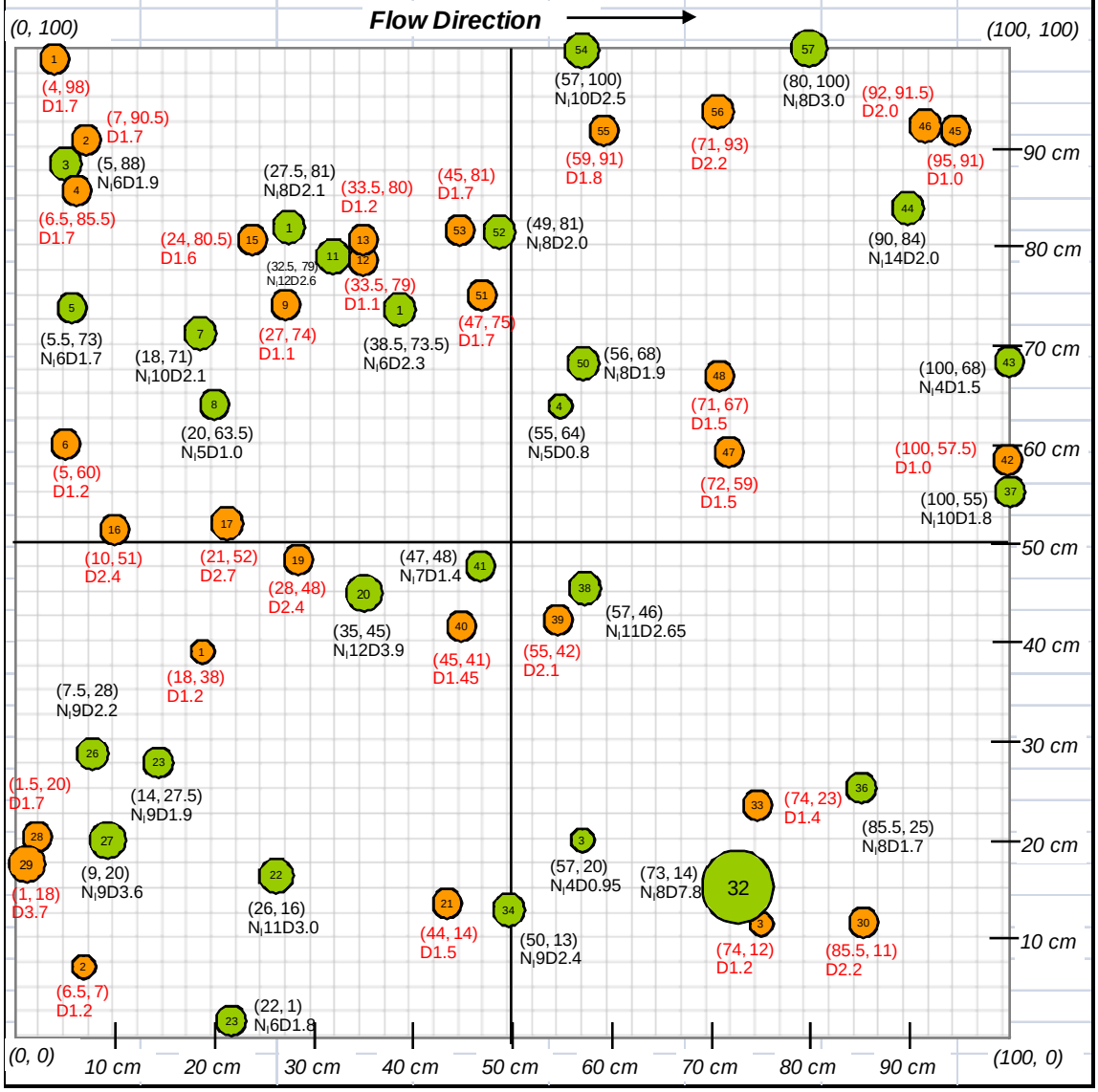

Field Measurement Datasheet 1/3

Sample No.	H-3
Date	14-May-09
Member	Su Jin Kim, Brandon Harris, Brandon Strellis, Ben Ioppolo, Emma
Measuring location	(check or sketch the location on the picture below)

Cell I-1

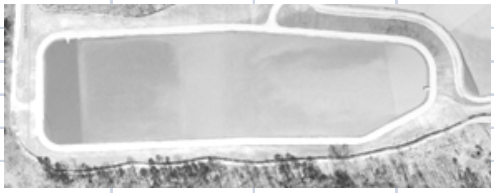

Cell H

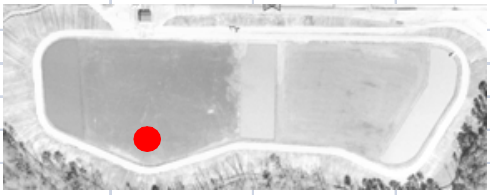

Discharge	(inflow)	(cfs or cms)
Numbers of cattail in 1m x 1m	60	

Sketch of 1m x 1m zone with distance between vegetion (1grid = 2.5 cm x 2.5 cm)

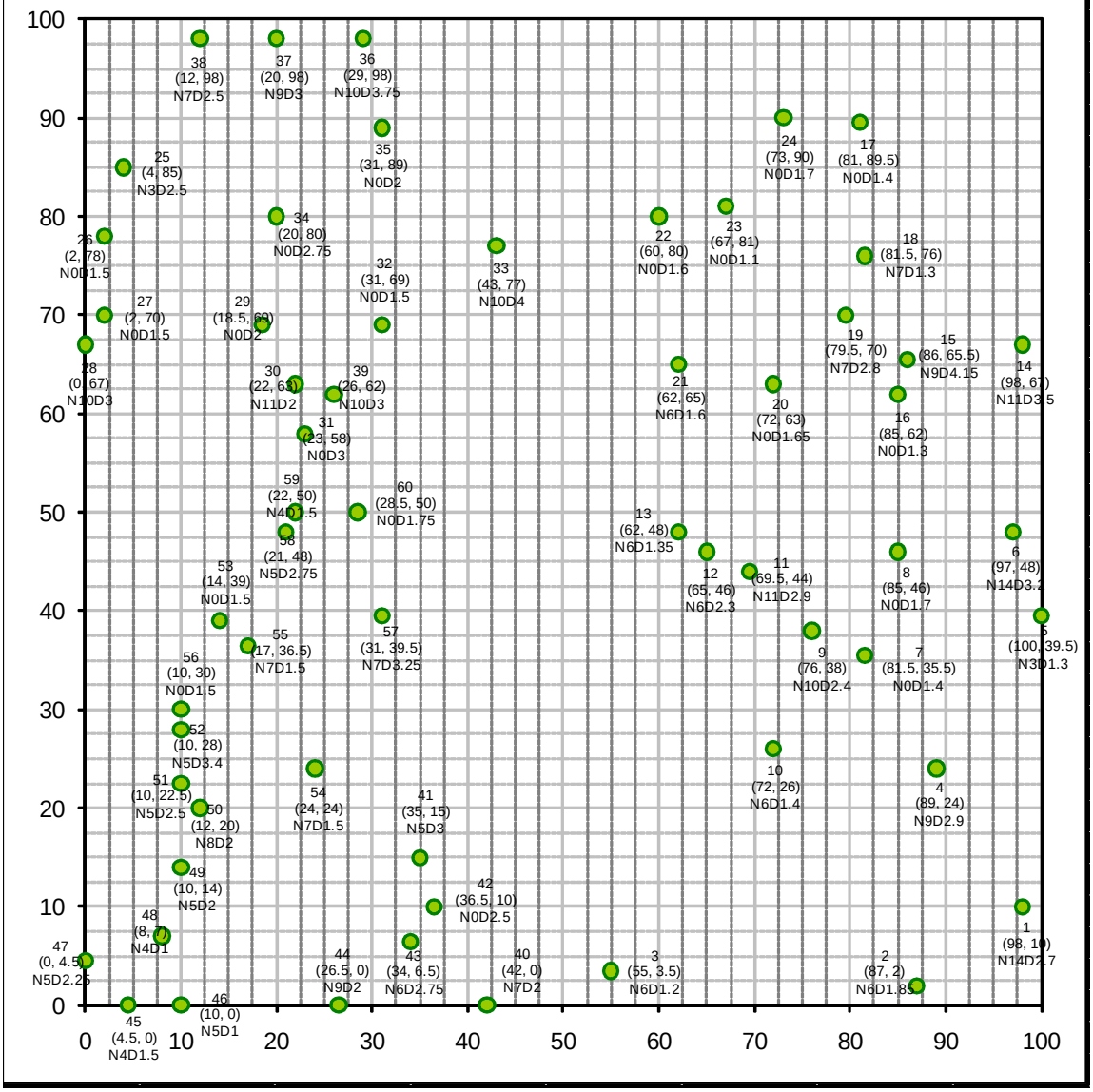

Field Measurement Datasheet 1/3

Sample No.	H-4
Date	14-May-09
Member	Su Jin Kim, Brandon Harris, Brandon Strellis, Ben Ioppolo, Emma
Measuring location	(check or sketch the location on the picture below)

Cell I-1

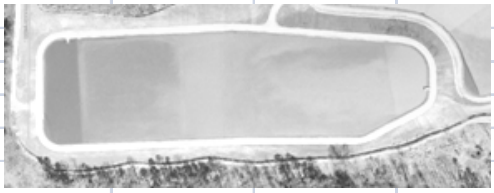

Cell H

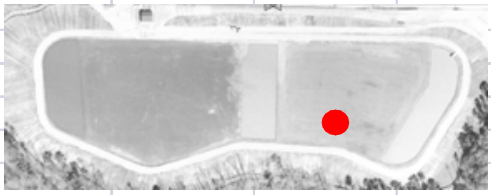

Discharge	(inflow)	(cfs or cms)
Numbers of cattail in 1m x 1m	58	

Sketch of 1m x 1m zone with distance between vegetion (1grid = 2.5 cm x 2.5 cm)

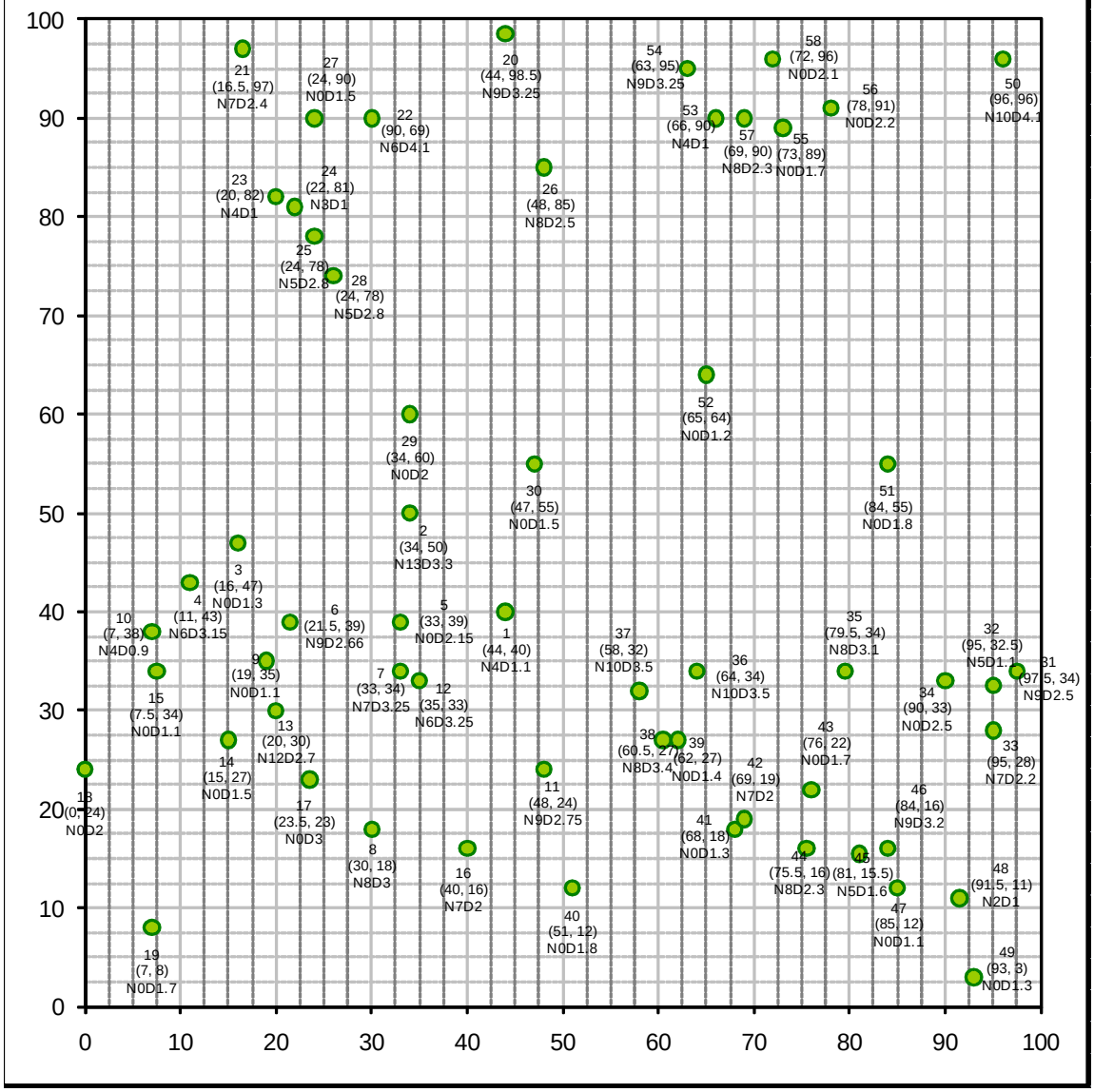

Field Measurement Datasheet 1/3

		Sample No.	H-5
Date	6-Nov-09		
Member	Su Jin Kim, Brandon Harris, Brandon Strellis, Ingrid Duque		
Measuring location	(check or sketch the location on the picture below)		
Cell I-1		Cell H	

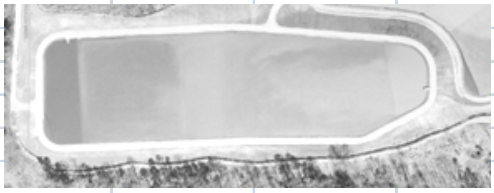

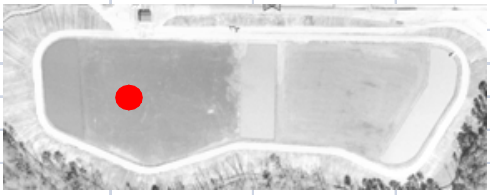

Discharge	(inflow)	(cfs or cms)
Numbers of cattail in 1m x 1m	21	

Sketch of 1m x 1m zone with distance between vegetion (1grid = 2.5 cm x 2.5 cm)

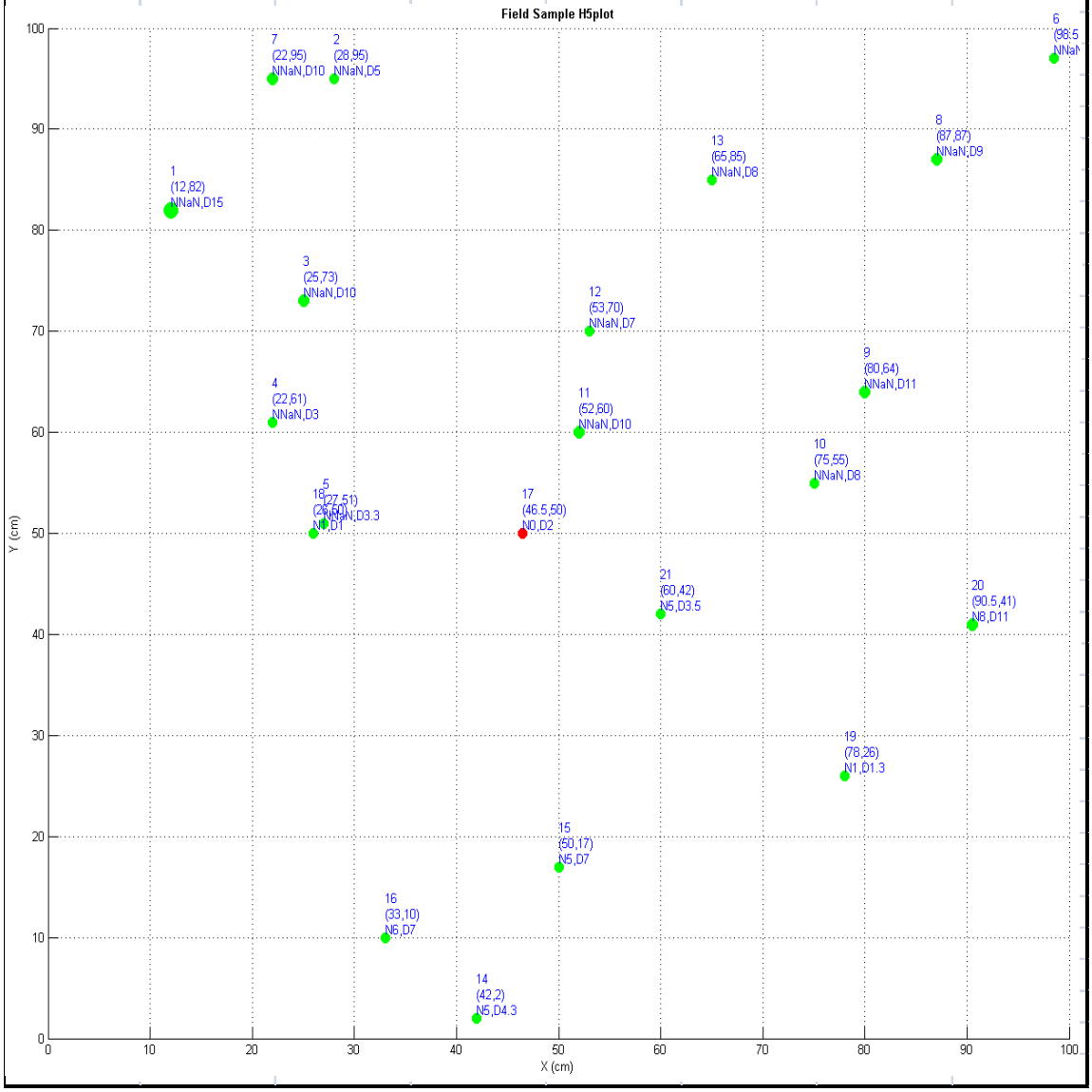

Field Measurement Datasheet 1/3

Sample No.	H-6
Date	6-Nov-09
Member	Su Jin Kim, Brandon Harris, Brandon Strellis, Ingrid Duque
Measuring location	(check or sketch the location on the picture below)

Cell I-1

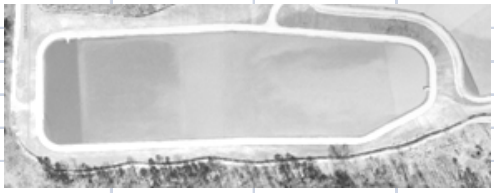

Cell H

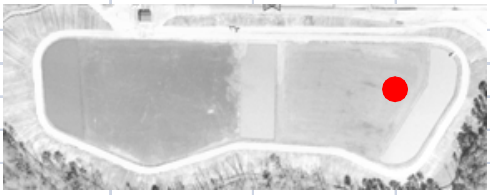

Discharge	(inflow)	(cfs or cms)
Numbers of cattail in 1m x 1m	35	

Sketch of 1m x 1m zone with distance between vegetion (1grid = 2.5 cm x 2.5 cm)

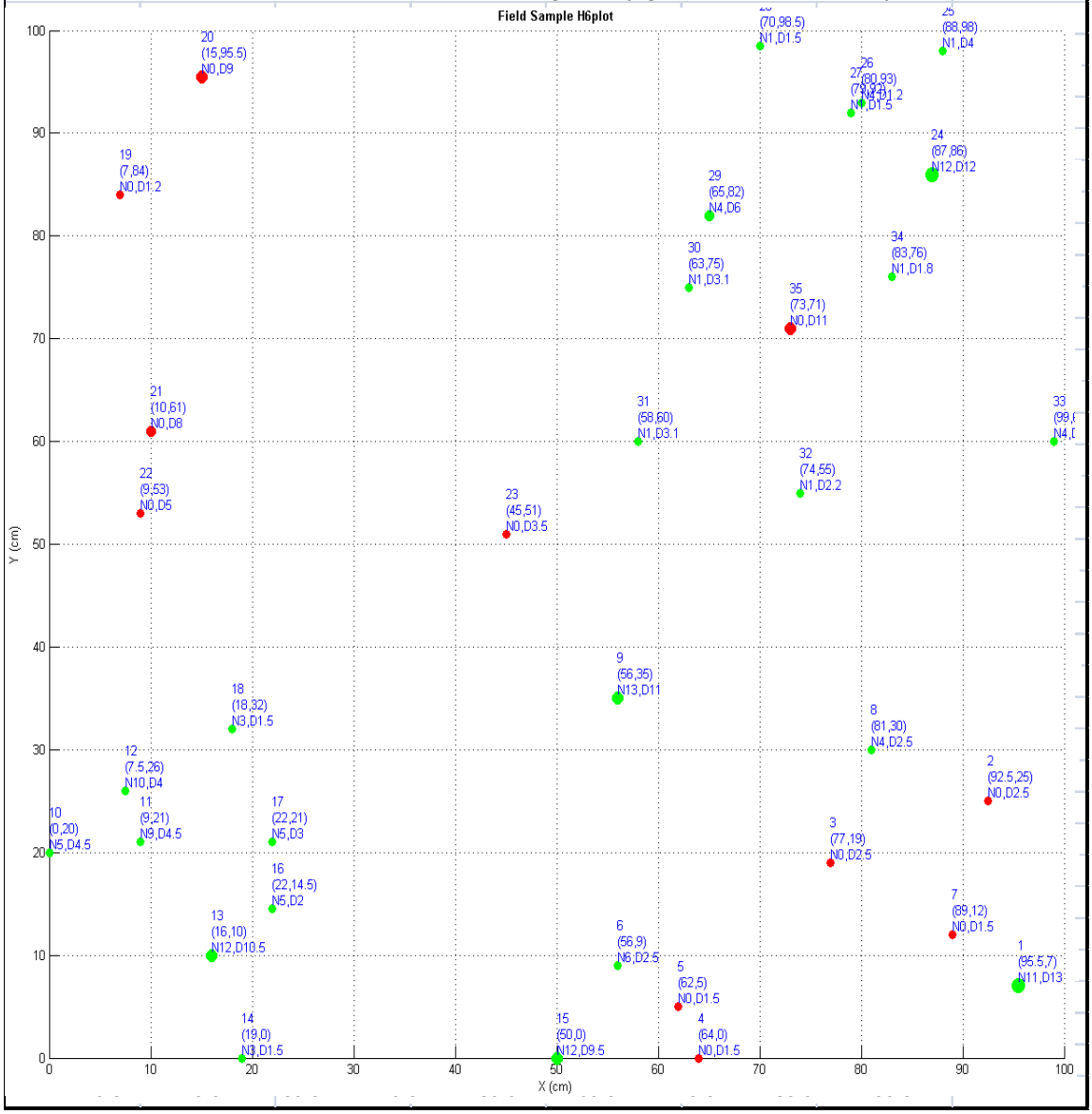

APPENDIX 2 – WATER LEVEL MEASUREMENT DATA

Field Measurement Datasheet

	No.	1

Date	29-May-09
Member	Su Jin Kim, Brandon Harris

Cell I-1

Cell H

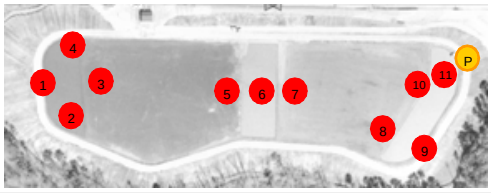

time	10:00 ~11:00 am			time	11:00 ~12:00 pm		
Survey Point ID	reference elevation	Water Level	Water depth (m)	Survey Point ID	reference elevation	Water Level	Water depth (m)
Sfe_113	278.26						
I-1	277.17	276.86	1.32	H-1	255.53	255.22	1.94
I-2	277.16	276.86	1.32	H-2	255.52	255.22	1.93
I-3	277.17	276.86	1.32	H-3	255.52	255.22	1.94
I-4	277.16	276.86	1.32	H-4	255.54	255.23	1.94
I-5	277.15	276.86	1.32	H-5	255.52	255.22	1.93
I-6	277.15	276.85	1.31	H-6	255.51	255.22	1.93
I-7	277.16	276.85	1.31	H-7	255.51	255.22	1.93
I-8	277.08	276.80	1.26	H-8	255.45	255.15	1.86
I-9	277.09	276.81	1.27	H-9	255.44	255.15	1.86
I-10	277.08	276.80	1.26	H-10	255.44	255.15	1.86
I-11	277.08	276.80	1.26	H-11	255.44	255.15	1.86
Pell	278.60	276.71	crest	Peh1	256.64	255.09	crest
	H=	0.09			H=	0.05	
	P=	1.170432			P=	1.801368	
bottom elev	275.54	m		bottom elev	253.29	m	

Field Measurement Datasheet

No.	2

Date	12-Jun-09
Member	Su Jin Kim, Ben Ioppolo

Cell I-1

Cell H

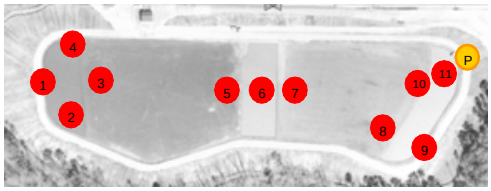

time	11:30 ~ 12:00 pm			time	12:00 ~ 12:30 pm		
Survey Point ID	reference elevation	Water Level	Water depth (m)	Survey Point ID	reference elevation	Water Level	Water depth (m)
Sfe_113	278.26						
I-1	277.17	276.85	1.31	H-1	255.53	255.24	1.95
I-2	277.16	276.85	1.31	H-2	255.52	255.24	1.95
I-3	277.17	276.85	1.31	H-3	255.52	255.24	1.95
I-4	277.16	276.85	1.31	H-4	255.54	255.24	1.95
I-5	277.15	276.84	1.30	H-5	255.52	255.22	1.94
I-6	277.15	276.84	1.30	H-6	255.51	255.22	1.93
I-7	277.16	276.85	1.31	H-7	255.51	255.22	1.93
I-8	277.08	276.77	1.23	H-8	255.45	255.15	1.86
I-9	277.09	276.78	1.24	H-9	255.44	255.15	1.86
I-10	277.08	276.77	1.23	H-10	255.44	255.15	1.86
I-11	277.08	276.78	1.24	H-11	255.44	255.14	1.85
Pell	278.60	276.71	crest	Peh1	256.64	255.09	crest
	H=	0.07			H=	0.05	
	P=	1.170432			P=	1.801368	
bottom elev	275.5392	m		bottom elev	253.2888	m	

Field Measurement Datasheet

No.	3

Date	26-Jun-09
Member	Su Jin Kim, Ben Ioppolo

Cell I-1

Cell H

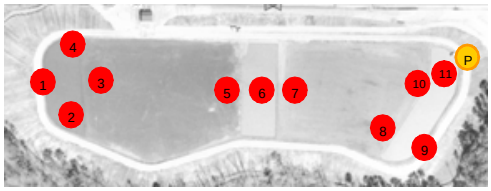

time	12:00 ~ 12:30 pm			time	12:30 ~ 1:00 pm		
Survey Point ID	reference elevation	Water Level	Water depth (m)	Survey Point ID	reference elevation	Water Level	Water depth (m)
Sfe_113	278.26	277.12	crest				
I-1	277.17	276.84	1.30	H-1	255.53	255.24	1.95
I-2	277.16	276.84	1.30	H-2	255.52	255.23	1.94
I-3	277.17	276.84	1.30	H-3	255.52	255.23	1.94
I-4	277.16	276.84	1.30	H-4	255.54	255.24	1.95
I-5	277.15	276.84	1.30	H-5	255.52	255.23	1.94
I-6	277.15	276.84	1.30	H-6	255.51	255.23	1.94
I-7	277.16	276.84	1.30	H-7	255.51	255.22	1.94
I-8	277.08	276.77	1.23	H-8	255.45	255.16	1.87
I-9	277.09	276.78	1.24	H-9	255.44	255.16	1.87
I-10	277.08	276.77	1.23	H-10	255.44	255.16	1.87
I-11	277.08	276.77	1.23	H-11	255.44	255.15	1.86
Pell	278.60	276.71	crest	Peh1	256.64	255.09	crest
	H=	0.13			H=	0.15	
	P=	1.17			P=	1.801368	
bottom elev	275.5392	m		bottom elev	253.2888	m	

Field Measurement Datasheet

No.	4

Date	6-Nov-09
Member	Su Jin Kim, Brandon Harris

Cell I-1

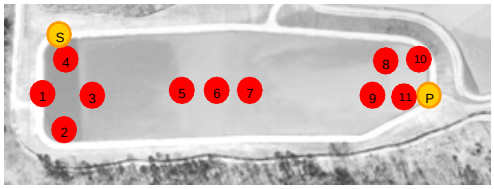

Cell H

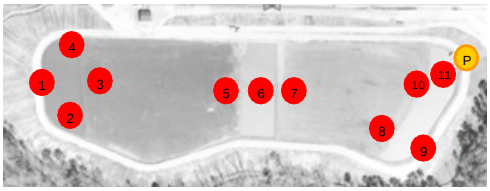

time	2:00 ~ 3:00 pm			time	3:00 ~ 4:00 pm		
Survey Point ID	reference elevation	Water Level	Water depth (m)	Survey Point ID	reference elevation	Water Level	Water depth (m)
Sfe_113	278.26	277.12	crest				
I-1	277.17	276.87	1.34	H-1	255.53	255.22	1.93548
I-2	277.16	276.87	1.33	H-2	255.52	255.22	1.93
I-3	277.17	276.87	1.33	H-3	255.52	255.22	1.93
I-4	277.16	276.87	1.33	H-4	255.54	255.22	1.94
I-5	277.15	276.86	1.32	H-5	255.52	255.20	1.91
I-6	277.15	276.85	1.31	H-6	255.51	255.20	1.91
I-7	277.16	276.85	1.31	H-7	255.51	255.20	1.91
I-8	277.08	276.80	1.26	H-8	255.45	255.16	1.87
I-9	277.09	276.81	1.27	H-9	255.44	255.15	1.87
I-10	277.08	276.82	1.28	H-10	255.44	255.15	1.86
I-11	277.08	276.81	1.27	H-11	255.44	255.15	1.86
Pell	278.60	276.71	crest	Peh1	256.64	255.09	crest
	H=	0.16			H=	0.13	
	P=	1.17			P=	1.80	
bottom elev	275.5392	m		bottom elev	253.2888	m	

Identifying Locations of High Connectivity between Floridan Aquifer Water and Surface Waters at Lineament Intersections with Tributaries of the Lower Flint River

Basic Information

Title:	Identifying Locations of High Connectivity between Floridan Aquifer Water and Surface Waters at Lineament Intersections with Tributaries of the Lower Flint River
Project Number:	2009GA201B
Start Date:	3/1/2009
End Date:	2/28/2010
Funding Source:	104B
Congressional District:	10
Research Category:	Ground-water Flow and Transport
Focus Category:	Hydrology, Hydrogeochemistry, Irrigation
Descriptors:	None
Principal Investigators:	Charles Rhett Jackson, Charles Rhett Jackson

Publications

1. Rugel, K, J. Romeis, C. R. Jackson, S. W. Golladay, D. W. Hicks, and J. F. Dowd. 2009. Long-term Effects of Center Pivot Irrigation on Streamflows in a Karst Environment: Lower Flint River Basin, Georgia, USA
2. Rugel, K, J. Romeis, C. R. Jackson, S. W. Golladay, D. W. Hicks, and J. F. Dowd. 2009. Use of historic data to evaluate effects of pumping stress on streams in southwest Georgia. Pages 140-143 in G. D. Carroll (ed.) In Proceedings of the 2009 Georgia Water Resources Conference. Institute of Ecology, University of Georgia, Athens, Georgia
3. Jackson, C.R. 2010. Applying a broad view of hydrologic connectivity to ACF water resource issues. UF Water Institute Sypmosium, February 24-25, Gainesville, FL.
4. Jackson, C.R. 2010. Water quality, flowpath, and hydrologic modeling issues related to intensified forestry for producing cellulosic biofuels. Watershed Perspective on Bioenergy Sustainability Workshop, Oak Ridge National Laboratory, February 3-4, Oak Ridge, TN.

Report as of FY2010 for 2009GA201B: "Identifying Locations of High Connectivity between Floridan Aquifer Water and Surface Waters at Lineament Intersections with Tributaries of the Lower Flint River"

Principal Investigator: C. Rhett Jackson
Co-Principal Investigator: Kathleen Rugel
Activity Period: March 1, 2009 through February 28, 2010

Publications and Presentations

Proceedings

Rugel, K, J. Romeis, C. R. Jackson, S. W. Golladay, D. W. Hicks, and J. F. Dowd. 2009. Use of historic data to evaluate effects of pumping stress on streams in southwest Georgia. Pages 140-143 in G. D. Carroll (ed.) *In* Proceedings of the 2009 Georgia Water Resources Conference. Institute of Ecology, University of Georgia, Athens, Georgia

Presentations

Jackson, C.R. 2010. Applying a broad view of hydrologic connectivity to ACF water resource issues. UF Water Institute Sypmosium, February 24-25, Gainesville, FL.

Jackson, C.R. 2010. Water quality, flowpath, and hydrologic modeling issues related to intensified forestry for producing cellulosic biofuels. Watershed Perspective on Bioenergy Sustainability Workshop, Oak Ridge National Laboratory, February 3-4, Oak Ridge, TN.

Journal Manuscripts In Preparation
*(*projected submission date: June 2010; target publication: *Hydrological Processes)*

Rugel, K, J. Romeis, C. R. Jackson, S. W. Golladay, D. W. Hicks, and J. F. Dowd. 2009. Long-term Effects of Center Pivot Irrigation on Streamflows in a Karst Environment: Lower Flint River Basin, Georgia, USA

Report Follows

Report as of FY2010 for 2009GA201B: "Identifying Locations of High Connectivity between Floridan Aquifer Water and Surface Waters at Lineament Intersections with Tributaries of the Lower Flint River"

Background

Groundwater withdrawals for irrigation increased over 100% between 1970 and 1976 in the lower Flint River Basin in southwest Georgia when cable tow irrigation systems were replaced by more efficient center pivot irrigation systems (Pierce et al., 1984). Irrigation in this region has allowed for the implementation of intensive farming practices including multiple harvests per year. Pumping of up to 3.4 BGD of groundwater is currently permitted from the Upper Floridan aquifer in the Dougherty Plain of southwest Georgia (Couch and McDowell 2006) which maintains the highest agricultural production in the state (McKissick 2004). The karstic aquifer in this region is shallow, often outcropping to the surface, and streams such as Ichawaynochaway and Spring Creek have incised through surficial deposits directly into underlying limestone resulting in a close hydrologic association of surface and sub-surface systems. Extraction of groundwater resources from the Upper Floridan aquifer has substantially reduced baseflows and altered low flow metrics in streams flowing through the lower Flint River Basin since irrigation intensified (Stamey 1996, Golladay et al 2007, Rugel et al 2009). Significant reductions in flow duration have been found in the post-irrigation record (1980-2008) for streamflow at Ichawaynochaway Creek at Milford, GA, and Spring Creek near Iron City, GA (Figure 1), including a decrease by an order of magnitude for 98% exceedance flows at Spring Creek compared to pre-irrigation years. Eight-day early summer and annual baseflow recession curves have become steeper in the post-irrigation period for Ichawaynochaway Creek and both Ichawaynochaway and Spring Creek revealed significant reductions in 1-, 7-, and 14-day flows suggesting that groundwater resources have been depleted more rapidly in the post-pumping years (Rugel et al 2009).

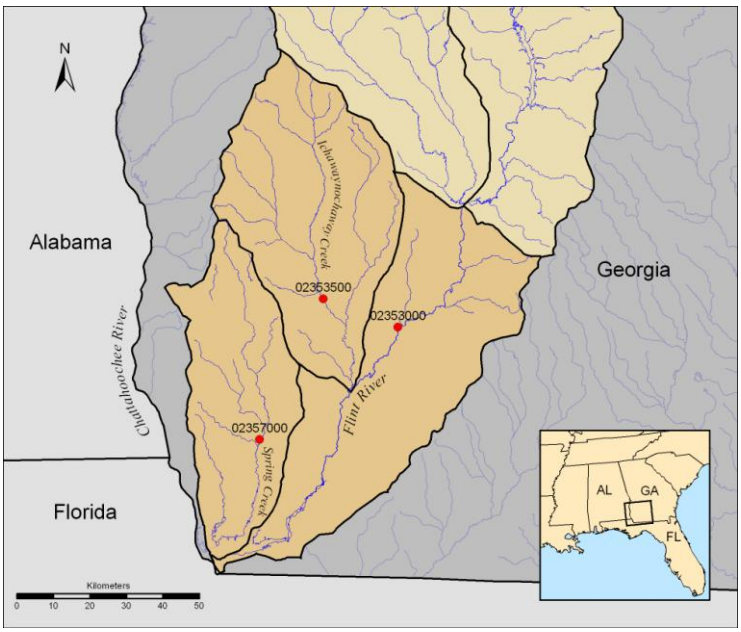

Figure 1. Sub-basins of the lower Flint River Basin in southwest Georgia and USGS stream gaging stations on the Ichawaynochaway and Spring Creeks and the Flint River

Prior to implementation of center-pivot irrigation, a relatively strong relationship existed between winter minimum flows and summer minimum flows, such that flow conditions in February could be used to estimate the probability of extreme low flow conditions in August. Irrigation has disrupted this relationship and in the post-pumping period it has become weak and insignificant making it difficult to gage the likelihood of late summer critical flow conditions based on hydrologic conditions in winter months (Figure 2). Our current analysis of low flow data and recession behavior is consistent with previous interpretations by USGS of pumping effects on streams in the lower FRB (Albertson and Torak 2002). Previous USGS MODFLOW modeling has indicated a lag time of approximately 100 days between the peak of pumping and the maximum negative effect on streamflows (Albertson and Torak 2002). The result of seasonal groundwater removal on already-reduced summer streamflow has increased low flow and no flow conditions in previously perennial streams in this area. While repeated droughts have occurred in the last decade, there has been no reduction in average precipitation during post-irrigation years, indicating that lowered flows in this region are not a result of altered climate patterns (Rose 2009, Rugel et al 2009, Seagar et al 2009).

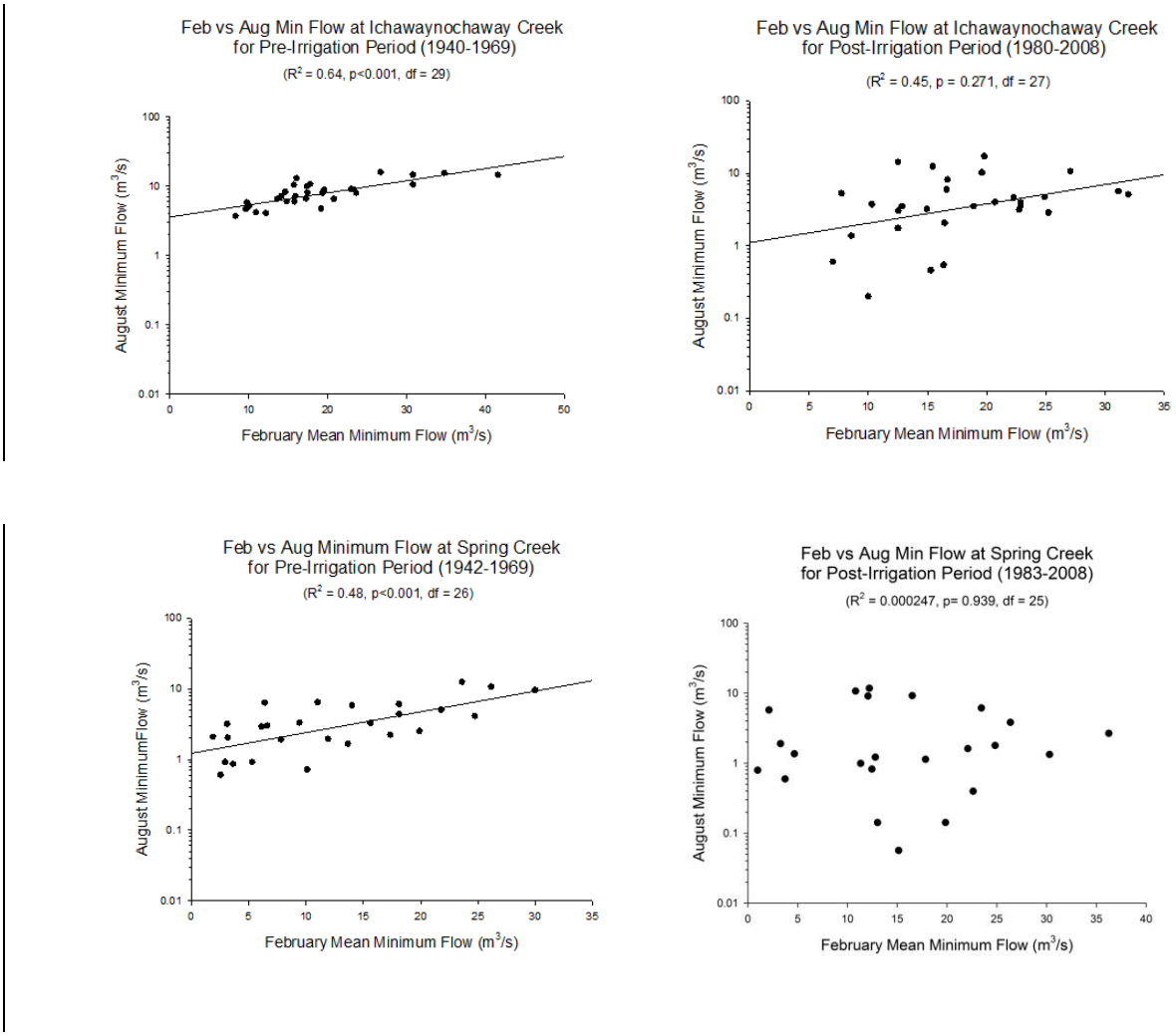

Figure 2. Comparison of winter (February) and summer (August) minimum flows at USGS stream gaging stations on the Ichawaynochaway Creek (02353500) and Spring Creek (02357000) in the pre- and post-irrigation period (Rugel, unpublished data)

Reduced streamflow has resulted in lower levels of dissolved oxygen and higher stream temperatures creating anoxic conditions which have been shown to threaten aquatic species in these waters (Zale et al. 1990; Golladay et al. 2004, Peterson 2006). Currently there are seven species of unionids listed as threatened or endangered in the lower Flint River Basin. Following severe drought between 1998 and 2000 Golladay and others (2004) reported significant declines in mussel taxa richness and stable species abundance within mid-stream reaches of Spring Creek, >50% reduction in total mussel abundance, and lowered or absent populations of species of special concern in no-flow reaches. Downstream ecosystems, as well as fishing, shrimping and shellfish industries in the Apalachicola Bay, also depend on upstream inputs of fresh water in order to maintain adequate levels of nutrients and salinity vital to estuarine and marine function (Elder and Cairnes, 1982; Gillanders and Kingsford, 2002). Stamey (1996) reported reduced downstream inputs to and outputs from Lake Seminole following the implementation of intensive irrigation practices.

Fracturing and dissolution of the Ocala Limestone Formation which underlies the Dougherty Plain in southwest Georgia has led to the development of secondary flow paths which connect some tributaries of the lower Flint River Basin hydraulically to the Upper Floridan aquifer (Torak and Painter 2006). Physiographic features and lateral drainage components throughout the Dougherty Plains, including escarpments, ridges, stream beds and lineaments, direct the development of dissolution paths between surface and sub-surface aquatic systems in this system. Lineaments, sinkholes, and other geologic surface features can be identified from aerial photos and satellite imagery and have been used to predict areas of high-yielding groundwater for development. Brook and Sun (1982) showed that variability in specific capacity of wells in the Albany, Georgia area was explained 89% of the time by distance to the nearest fracture trace (identified in aerial photos). Hyatt and Jacobs (1996) also found that 312 sinkholes in the Albany, GA area which collapsed following Tropical Storm Alberto, followed joint-controlled linear trends. Using a variety of tracers and chemical species, which included Cl^-, $\delta^{18}O$, and δ^2H, Plummer and others (1998) identified younger fractions of water in the Upper Floridan groundwater originating from sinkholes within the Withlacoochee River bed near Valdosta, Georgia.

Streams in karstic systems which share a close hydraulic connection with the underlying aquifer develop unique chemical signatures from exposure to the karst environment including increased calcium and specific conductivity, decreased temperature, isotopic depletion of water during fractionation, and higher nitrate concentrations from anthropogenic sources. Previous research by Li (2006) indicated that pH and specific conductivity differentiated between groundwater and stream water in the Fall Line Hills and Dougherty Plain. We hypothesize that stream characteristics such as solute concentration, isotopic composition and other physiochemical components of stream water will be explained by proximity of stream reaches to fractures and fracture intersections as a result of stream/groundwater interaction. Stream topology along Ichawaynochaway Creek strongly suggests locations of lineament connections, and preliminary sampling of the stream above, within, and below the identified direct connections is proceeding. Identifying and understanding the hydrological as well as biological interaction of the Floridan Aquifer with the stream system via fracture flow will be immediately useful for establishing protections for limited water resources in this region.

Objectives

In this research we will:

1) Locate and document lineament features using remote sensing data and GIS tools. We will use these surface features, including creek bearing, creek deflection (turn angle), elevation, wetland and vegetation patterns, to predict the occurrence of underlying fractures within the lower Flint River Basin where increased stream/aquifer exchange may be occurring.

2) Identify chemical signatures which differentiate precipitation and groundwater in the Ichawaynochaway sub-basin. Physiochemical parameters of interest will include isotopic composition (oxygen and deuterium), pH, temperature, specific conductivity, calcium and nitrate concentration.

3) Quantify contribution of hydrologic components (groundwater, precipitation) to streamflow generation within Ichawaynochaway Creek using stream chemistry data in two-member mixing model and mass balance equations

4) Use stream chemistry, visual reconnaissance and statistical analysis to verify presence of hydrological connections between stream and underlying aquifer in the lower Flint River Basin

5) Compare and contrast the usefulness of these methods for locating and predicting basin-wide flow exchange in this and other karstic systems.

Methods and Results

GIS Site Selection: Remote sensing data sets for the lower Flint River Basin have been obtained from the Georgia GIS Clearinghouse website (https://gis1.state.ga.us, accessed 2009), including USDA National Agriculture Imagery Program (NAIP) data (2007, 1 meter pixel resolution, natural color, leaf-on), USGS Digital Ortho Quarter Quads (DOQQ) (1999, 1:12,000, color infrared, leaf-off), USGS 7 ½ min.digital elevation models (DEMs), and National Wetland Inventory (NWI) datasets. Using NAIP, DOQQ, and NWI we have identified surface features, lineaments, escarpments, vegetation patterns, and stream and river beds within and in proximity to the lower Flint River Basin. Using ArcMap 9.1 we produced a surface feature layer (shape file) which was overlain onto existing remote sensing data layers of Spring Creek and Ichawaynochaway Creek to delineate regions of possible underlying fracturing. Due to challenges acquiring land access as well as difficulty in navigating reaches along Spring Creek at baseflow conditions, we have limited the scope of our research to the Ichawaynochaway Creek between Morgan, Georgia, and the confluence of the Ichawaynochaway with the Flint River.

Custom GIS Tool: We created a custom ArcMap tool based on the Boundary Convexity Tool (BCT) to delineate a line, or route, along the Ichawaynochaway Creek (Figure 3) from Morgan, Georgia, to the Flint River confluence. With this tool we have generated information on convexity or concavity (sinuosity) along the creek route, as well as other attribute data including creek turn angle, bearing of stream segments, and GIS coordinates (Figure 4). We have obtained data at variable stream segment lengths in order to potentially evaluate changes in attributes at multiple scales. We downloaded creek routes from ArcMap document into a Garmin Oregon 550 hand-held GPS to produce a route along Ichawaynochaway Creek. Experimental and control sites will be chosen along stream route at selected intervals following pre-sampling to determine

appropriate scale. Stream samples will be collected at experimental and control sites (see field collection section) and analyzed for multiple physiochemical parameters. Results will be evaluated using multi-ring proximity buffers in ArcMap in order to determine if proximity of changing creek turn angle, directional bearing of stream segments, presence of wetlands (and other surface features visible in remote sensing data) explains differences in stream physiochemistry (evaluated using principal components analysis).

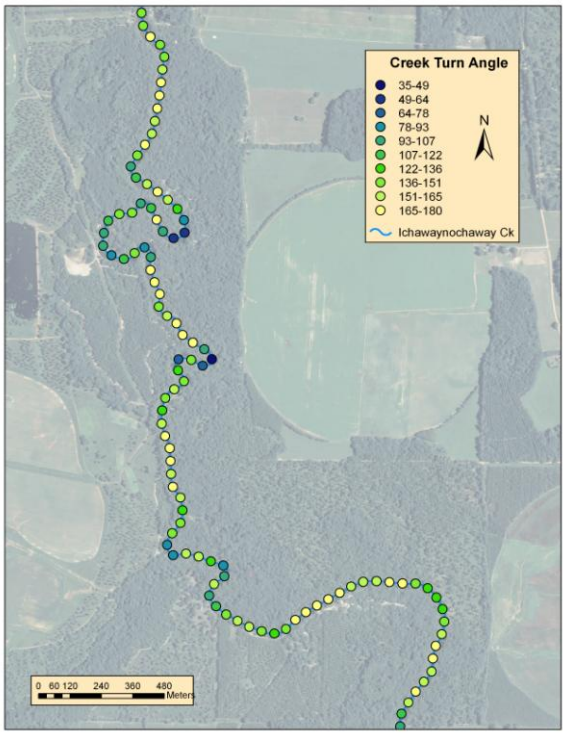

Figure 3. Portion of schematic for identification of creek turn angle along Ichawaynochaway Creek in the lower Flint River Basin, Baker County, Georgia, generated by custom boundary convexity tool

FID	Shape*	OBJECT	RID	Meas	StepLe	TurnAngle	Bearin	Directio	Beari	Directi
0	Point ZM	841	Ichaw aynochaw ay Creek	42175	250	156.000000	83	N	107	N
1	Point ZM	478	Ichaw aynochaw ay Creek	24025	250	133.000000	95	N	48	NE
2	Point ZM	618	Ichaw aynochaw ay Creek	31025	250	72.000000	113	NW	5	E
3	Point ZM	623	Ichaw aynochaw ay Creek	31275	250	127.000000	106	N	159	W
4	Point ZM	723	Ichaw aynochaw ay Creek	36275	250	177.000000	128	NW	125	NW
5	Point ZM	728	Ichaw aynochaw ay Creek	36525	250	94.000000	47	NE	133	NW
6	Point ZM	461	Ichaw aynochaw ay Creek	23175	250	104.000000	48	NE	124	NW
7	Point ZM	466	Ichaw aynochaw ay Creek	23425	250	180.000000	117	NW	118	NW
8	Point ZM	604	Ichaw aynochaw ay Creek	30325	250	156.000000	144	NW	121	NW
9	Point ZM	609	Ichaw aynochaw ay Creek	30575	250	171.000000	133	NW	124	NW
10	Point ZM	707	Ichaw aynochaw ay Creek	35475	250	177.000000	111	N	114	NW
11	Point ZM	712	Ichaw aynochaw ay Creek	35725	250	144.000000	98	N	134	NW

Figure 4. Attribute table identifying creek turn angle and bearing of creek along 50 meter intervals within Ichawaynochaway Creek, Baker County, Georgia

Field collections: Uncertain stream conditions due to excessive precipitation during collection months (late summer and winter 2009) prohibited access to Ichawaynochaway Creek and confounded attempts to sample under baseflow conditions. Current results reflect field collection which has been limited to sampling of groundwater and precipitation and preliminary samples collected in 2007 from Ichawaynochaway Creek. Stream sampling is expected to resume when low flow stream conditions return in summer and fall months 2010 and will be repeated in 2011.

Groundwater samples were collected from 35 wells throughout the Ichawaynochaway sub-basin of the lower Flint River Basin within an approximate 1 mile buffer of the Ichawaynochaway Creek. Water was purged from wellheads or spigots for approximately 10 minutes to clear pipes and to insure a representative sampling of groundwater. Samples were collected in 20 ml glass scintillation bottles, capped with nipple caps and sealed with tape to prevent air gaps and possible atmospheric contamination and returned to lab for evaluation of cation and anion concentration (NO_3^- and Ca^+).. Two samples from each collection site were sent to the University of Georgia's Center for Applied Isotope Studies in Athens, GA, for stable isotope analysis of $\delta^{18}O$, and $\delta^{2}H$. GPS data points were taken at each wellhead using a Garmin Oregon 550, hand-held GPS. Eight precipitation events were sampled using an acid-washed, 5x8 inch Pyrex glass pan placed 20 inches above the ground in open area near the Joseph W. Jones Ecological Research Center laboratory facilities. Collection was allowed to continue for approximately two hours at which time the precipitation sample was transferred to 20 ml glass scintillation bottles, sealed and analyzed as above (groundwater samples). Atmospheric conditions including temperature, relative humidity, wind speed and direction, and antecedent rain conditions were recorded at each precipitation event. Stream samples were collected at mid-reach and mid-depth 8 reaches along the Ichawaynochaway Creek in 2007 in 20 ml glass scintillation bottles, capped with nipple caps and sealed with tape to prevent air gaps and possible atmospheric contamination. Samples were returned to lab for evaluation of cation and anion analysis. Two samples from each collection were sent to the University of Georgia's Center for Applied Isotope Studies in Athens, GA, for stable isotope analysis on $\delta^{18}O$, and $\delta^{2}H$. GPS data points were taken at each collection site using a Garmin Oregon 550, hand-held GPS.

Future stream sampling: Future study and control reaches are expected to be approximately 100 meters in length (50 meters above and below study sites) depending on results of pre-sampling for determination of appropriate reach scale. A 16 ft. Coleman Scanoe has been obtained along with a 2.5 4-stroke outboard motor to navigate from downstream to upstream within Ichawaynochaway Creek when stream discharge returns to appropriate levels for sampling. Measurements will be made along the thalweg at each collection site in order to determine stream depth. A Hydrolab Quanta Water Quality Sampler has been purchased to measure pH, specific conductivity, and temperature. All measurements and collections will be performed at 6/10 depth along 10 meter intervals. Whole water samples (approximately 200 ml) will be collected in acid-washed Nalgene® polycarbonate bottles at selected intervals using a Little Giant® pump through Teflon® tubing. Whole water samples will be divided into 20 ml glass scintillation vials on site then returned to lab for anion and cation analysis. Additional 20 ml samples will be collected at each site in glass scintillation bottles, capped with nipple caps and sealed with tape to prevent atmospheric contamination, and sent to the University of Georgia's Center for Applied Isotope Studies in Athens, GA, for stable isotope analysis of $\delta^{18}O$, and $\delta^{2}H$. GPS data points will be taken with Garmin Oregon 550 hand-held GPS at the upper, middle, and lower end of each sample reach. Sampling will be conducted in mid-summer (July) and late fall (November) 2010 - 2011.

Sample analysis: Cation analyses (Ca^{+}) has been performed on current samples at the Joseph W. Jones Ecological Research Center (JERC) in Newton, Georgia, by flame atomic absorption analysis (3500-Ca B. Atomic Absorption Spectrometric Method) on a Perkin Elmer 5100. Anion analyses (NO_3^-) will be performed at the JERC using Lachat methods. Isotopic composition of samples are being evaluated by University of Georgia's Center for Applied Isotope Studies in Athens, GA. Isotopic composition is reported in parts per thousand: δ_{sample} ($^0/_{00}$) = 1000 (R_{sample} – $R_{standard}$/ $R_{standard}$), where R is $^{18}O/^{16}O$ or D/H abundance ratio (Craig, 1961). Standard is Vienna Standard Mean Ocean Water (V-SMOV) (Coplen 1994).

Results: Our preliminary analyses of pH, Ca^{+}, specific conductivity, $\delta^{18}O$, and $\delta^{2}H$, in samples of surface water, groundwater and precipitation showed that streams in this region fall along a continuum between two originating end members, groundwater and precipitation. Ca^{+} concentrations and effectively distinguished groundwater and precipitation, with a mean groundwater Ca^{+} of 54.13 ± 10.5 mg/L and mean Ca^{+} for precipitation of 0.3 ± 0.1 mg/L. Cursory sampling from Ichawaynochaway Creek indicated a mean Ca^{+} of 27.6 ± 11.9 mg/L (Fig. 5). High dissolved calcium in Ichawaynochaway Creek compared to precipitation suggested a significant interaction between this stream and the underlying carbonate aquifer.

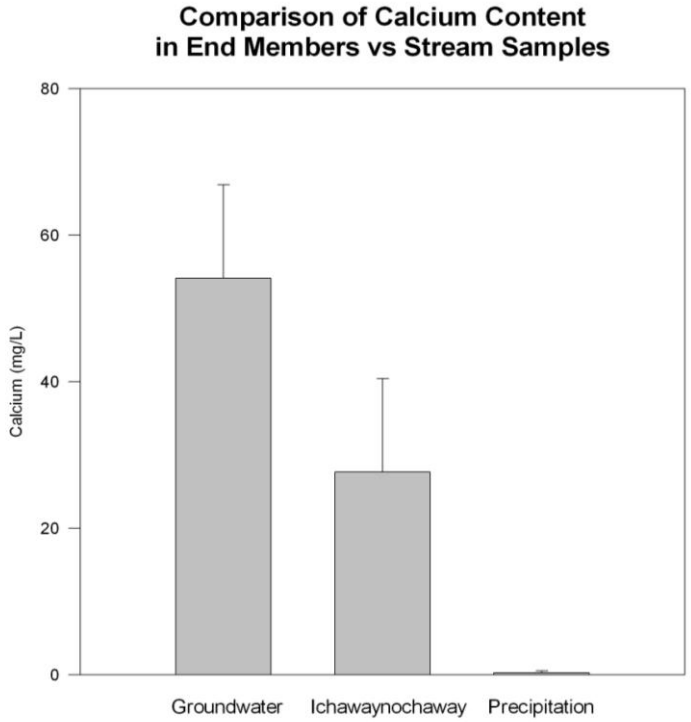

Figure 5. Results of preliminary sampling showing mean Ca^{+} composition of groundwater, precipitation, and stream samples collected from Ichawaynochaway Creek, Baker County, Georgia.

Analysis of groundwater, precipitation and stream water from Ichawaynochaway Creek indicated a strong correlation between D/H and $^{18}O/^{16}O$ and all samples fell along the local

meteoric water line (LMWL) (Kendall and McDonnell 1998). However, stream samples showed more oxygen enrichment compared to groundwater and precipitation (end members), most likely due to interaction of surface water with dissolved calcium or other species known to affect isotopic enrichment in a karst environment such as the Dougherty Plain. Other species such as nitrates and sulfates, found within this agricultural region, may also cause enrichment of oxygen in stream samples (Randy Culp, personal communication).Comparison of $\delta^{18}O$ and calcium concentration reveals distinguishable signatures between end members and streams samples within this basin (Fig. 6).

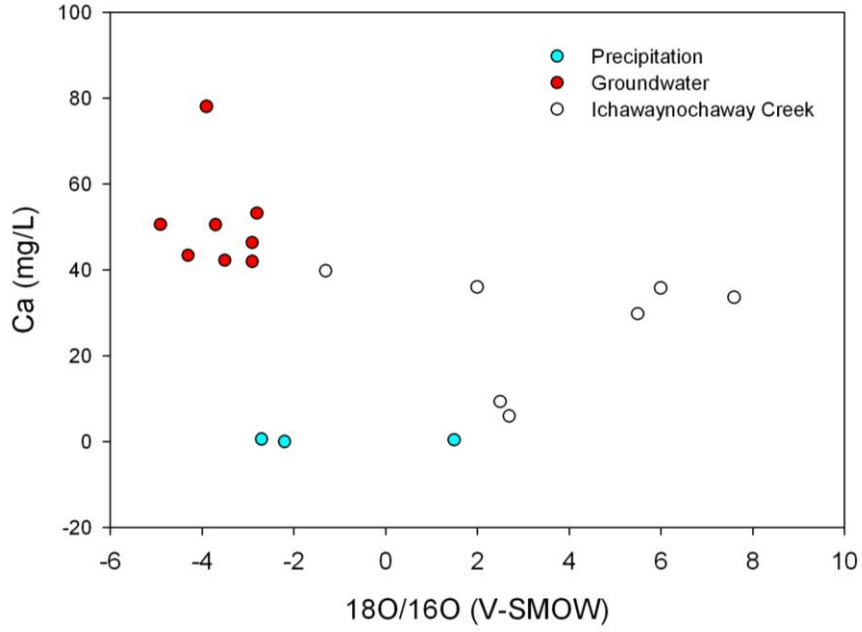

Figure 6. Calcium concentration vs isotopic composition ($\delta^{18}O$) of stream samples collected from Ichawaynochaway Creek to regional groundwater and precipitation (end members) samples. Isotopic composition is reported in parts per thousand: δ_{sample} ($^{0}/_{00}$) = 1000 ($R_{sample} - R_{standard}/ R_{standard}$) against Vienna Standard Mean Ocean Water (V-SMOW) standard

Conclusions

Hydrologic connectivity within catchments is dependent on local factors such as hydraulic conductance of streambed and aquifer materials, hydraulic gradient, and heterogeneous flow paths which can be challenging to delineate. Karst development is known to occur along joints and horizontal bedding planes where percolating water is preferentially transmitted to underground formations (Hicks et al.1987). In addition to larger flow paths such as limestone outcroppings and blue holes (large spring conduits), groundwater and surface water exchange directly through the streambed (hyporheos) to varying degrees (Brunke and Gosner 1997, Mosner 2002, Opsahl et al 2007). The locations and magnitude of these hydrologic exchanges cumulatively affect quantity and quality of surface waters and groundwater in the lower Flint River Basin. Easily obtainable geographical information systems (GIS) information and multi-

parameter physiochemical data can be used to locate surface fracture features which suggest areas of high stream/aquifer interaction. The location of these connections as well as how they are affected by natural and anthropogenic influences has not been fully investigated. This research can be conducted at relatively low costs compared to borehole or monitoring well procedures and may offer a more precise picture of where streamflow capture is occurring during drought and intense irrigation periods in these watersheds.

Using remote sensing data sets and GIS tools we have successfully identified lineaments and other surface features which suggest underlying fracture patterns within the Ichawaynochaway sub-basin in the lower Flint River Basin of southwest Georgia. Preliminary analyses of Ca^{+}, specific conductivity, and oxygen and hydrogen isotopes in groundwater, precipitation and stream samples has revealed distinct physiochemical characteristics of end members, with stream samples indicating a strong interaction with the underlying Upper Floridan aquifer. Unraveling the complex movement of water between surface and sub-surface systems, particularly in the Ichawaynochaway sub-basin, should be immediately useful for updating and improving current hydrologic models in this region and predicting and protecting the locations of these interactions on a basin-wide scale.

Acknowledgements

Special thanks to Jean Brock of the Joseph W. Jones Ecological Research Center for endless GIS technical support and to Shannon Albeke of the Warnell School of Forestry and Natural Resources, University of Georgia, for efforts to produce custom Boundary Convexity Tool. Thanks also to Randy Culp of the University of Georgia's Center for Applied Isotope Studies for isotopic analysis and helpful consultation.

References

Albertson PN, and Torak LJ. 2002. Simulated Effects of Ground-Water Pumpage on Stream-Aquifer Flow in the Vicinity of Federally Protected Species of Freshwater Mussels in the Lower Apalachicola-Chattahoochee-Flint River Basin (Subarea 4), Southeastern Alabama, Northeastern Florida, and Southwestern, Georgia. U.S. Geological Survey Water Investigations Report 02-4016.

Couch CA and McDowell RD. 2006. Flint River Basin Regional Water Development and Conservation Plan. Georgia Department of Natural Resources-Environmental Protection Division.

Craig H. 1961. Isotopic variations in meteoric waters. *Science* **133**: 1702.

Golladay SW, Gagon P, Kearns M, Battle JM, and Hicks DW. 2004. Response of Freshwater Mussel Assemblages (Bivalve:Unionidae) to Record Drought in the Gulf Coastal Plain of Southwest Georgia. Journal of the North American Ethological Society **23**: 494-506.

Hicks DW, Gill HE, and Longsworth SA. 1987. Hydrogeology, Chemical Quality, and Availability of Ground Water in the Upper Floridan Aquifer, Albany Area, GA. U.S. Geological Survey, Water-Resources Investigations Report 87-4145.

Kendall C and McDonnell JJ. 1998. Isotopic Tracers in Catchment Hydrology. Elsevier: Amsterdam, The Netherlands.

Li, G. 2006. Stream Temperature and Dissolved Oxygen Modeling in the Lower Flint River Basin, GA. PhD Dissertation. University of Georgia, Athens, GA.

McKissick JC. 2004, The Economic Importance of Irrigated Food and Fiber Production: A Spotlight on Georgia's Flint River Basin: Athens, GA, The University of Georgia Center for Agribusiness and Economic Development.

Mosner MS. 2002. Stream-Aquifer Relations in the Potentiometric Surface of the Upper Floridan Aquifer in the Lower Apalachicola-Chattahoochee-Flint River Basin in Parts of Florida, Georgia, and Alabama, 1999-2000. Hydrolic Atlas 22.

Opsahl S, Chapal SE, Hicks DW, and Wheeler CK. 2007. Evaluation for Ground-Water and Surface-Water Exchanges Using Streamflow Difference Analyses. Journal of the American Water Resources Association **43**: 1132-1141.

Pierce RR, Barber NL, and Stiles HR. 1984. Georgia irrigation, 1970-1980: a decade of growth. U.S. Geological Survey, Water Resources Investigations Report 83-4177.

Rose S. 2009. Rainfall-runoff trends in the south-eastern USA: 1938-2005. *Hydrological Processes* **23**: 1105-1118.

Seager R, Tzanova A, and Nakamura J. 2009. Drought in the Southeastern United States: Causes, Variability over the last Millennium, and the Potential for Future Hydroclimate Change. *Journal of Climate* **Vol 22**: 5021-5045.

Stamey TC. 1996. Streamflow Characteristics at Selected Sites in Southwestern Georgia, Southeastern Alabama, and Northwestern Florida, Near Lake Seminole. U.S. Geologic Survey Open File Report 95-455, Atlanta, Georgia,

Zale AV, Wiechman JD, Lochmiller RL, and Burroughs J. 1990. Limnological conditions associated with summer mortality of striped bass in Keystone Reservoir, Oklahoma. Transactions of American Fisheries Society **119**: 72-76.

Information Transfer Program Introduction

None.

USGS Summer Intern Program

None.

Student Support					
Category	**Section 104 Base Grant**	**Section 104 NCGP Award**	**NIWR-USGS Internship**	**Supplemental Awards**	**Total**
Undergraduate	5	0	0	0	5
Masters	1	0	0	0	1
Ph.D.	2	1	0	0	3
Post-Doc.	0	0	0	0	0
Total	8	1	0	0	9

Notable Awards and Achievements

Publications from Prior Years